

Auroral Arc Electrodynamics  
with FAST Satellite and Optical Data

Von der Gemeinsamen Naturwissenschaftlichen Fakultät  
der Technischen Universität Carolo-Wilhelmina  
zu Braunschweig

zur Erlangung des Grades eines  
Doktors der Naturwissenschaften  
(Dr. rer. nat.)

genehmigte  
D i s s e r t a t i o n

von  
Octav Marghitu  
aus Bukarest, Rumänien

1. Referent: Prof. Dr. Gerhard Haerendel  
2. Referent: Prof. Dr. Karl-Heinz Glaßmeier  
eingereicht am: 18. Dezember 2002  
mündliche Prüfung am: 6. Mai 2003  
2003

To my Mother



Credit: Jan Curtis, <http://climate.gi.alaska.edu/Curtis/curtis.html>



# Abstract

The present work is devoted to the examination of a wide, stable, wintertime evening arc. Particle and field data measured by the FAST satellite at  $\sim 4000$  km altitude, as well as ground optical data, are used to get a detailed description of the arc electrodynamics. By processing the particle data one can evaluate the ionospheric conductance, while the magnetic field data allows the calculation of the field-aligned current. The electric field measurements can be mapped to the ionosphere as long as the magnetic field lines below the satellite are equipotential and otherwise serve to determine the average ionospheric electric field.

In the vicinity of the arc FAST detects several ion beams, indicating field-aligned potential drop below the satellite, which precludes the mapping of the measured electric field to the ionosphere. In order to derive the ionospheric electric field we develop a new method, based on the current continuity at ionospheric level and on a parametric arc model. The simplest representation of an arc consists of a homogeneous block of increased conductance, infinitely extended in longitudinal direction; field-aligned current sheets that flow in and out of the ionosphere at the boundaries of the arc are connected through Pedersen current across the arc, while the electrojet that flows along the arc as Hall current is divergence free. The parameters, which are determined by numerical fit, express the departure from such an ideal model. We find that the minimum set of parameters necessary to obtain consistent results includes polarization, a longitudinal electric field constant across the arc, and coupling between the field-aligned current and the electrojet.

Once the conductance and the electric field are calculated we check for the configuration of the current, which proves to be completely atypical. Because the convection reversal is very close to the boundary between the downward and upward currents only a negligible fraction of the downward current returns to the magnetosphere as upward current. The upward current is fed by the westward electrojet while most of the downward current feeds the eastward electrojet; a small part of the downward current crosses the convection reversal and joins the westward electrojet. Although the magnetic field signature suggests the common pattern, with upward and downward field-aligned current sheets connected through ionospheric Pedersen current, a careful investigation shows that the two current sheets are actually decoupled in the ionosphere.

The results obtained in this case-study point to the prospect of performing a systematic surveillance of the high-latitude ionosphere by medium altitude satellites, including time intervals when the measured electric field cannot be mapped to the ionosphere. By extending the application of the method developed here other peculiar auroral features might be unraveled.



# Contents

<b>Chapter 1</b>	<b>Introduction</b>	<b>1</b>
1.1	A historical perspective . . . . .	1
1.2	The auroral arc and the auroral acceleration region . . . . .	4
1.2.1	Ground data . . . . .	4
1.2.2	In-situ data . . . . .	6
1.3	Goal and plan of the work . . . . .	9
<b>Chapter 2</b>	<b>Experimental setup</b>	<b>11</b>
2.1	Satellite payload . . . . .	11
2.1.1	Particle instruments . . . . .	13
2.1.2	Field instruments . . . . .	17
2.2	Data analysis software . . . . .	19
2.3	Ground optical equipment . . . . .	20
<b>Chapter 3</b>	<b>A satellite auroral overpass: FAST orbit 1859</b>	<b>23</b>
3.1	Geophysical conditions . . . . .	23
3.2	FAST data . . . . .	26
3.3	Optical data . . . . .	39
3.4	Summary . . . . .	44
<b>Chapter 4</b>	<b>Ionospheric conductance</b>	<b>45</b>
4.1	General considerations . . . . .	45
4.2	Conductivity induced by particle precipitation . . . . .	50
4.2.1	Electron precipitation . . . . .	50
4.2.2	Proton precipitation . . . . .	54
4.3	Ionospheric conductances during ion beam events . . . . .	58
4.3.1	Choice of the integration domain . . . . .	58
4.3.2	Numerical results . . . . .	60

4.4	Errors in the evaluation of conductances . . . . .	64
4.4.1	Methodological errors . . . . .	64
4.4.2	Measurement errors . . . . .	66
4.5	Summary . . . . .	69
<b>Chapter 5</b>	<b>Ionospheric electrodynamics. The auroral arc</b>	<b>70</b>
5.1	Previous work . . . . .	70
5.1.1	Ground based methods to infer ionospheric electrodynamics . . . . .	70
5.1.2	Electric field vs. magnetic field variation pattern . . . . .	73
5.1.3	The electric field in the vicinity of auroral arcs . . . . .	73
5.2	Comments . . . . .	79
5.3	Qualitative evaluation of the simplifying assumptions . . . . .	81
5.4	Ionospheric electric field from satellite data . . . . .	82
5.4.1	Current closure in cartesian coordinates . . . . .	83
5.4.2	Determination of the IEF for the infinite straight arc . . . . .	85
5.4.3	Parametrization of the FAC–electrojet coupling . . . . .	89
5.5	Summary . . . . .	90
<b>Chapter 6</b>	<b>Electric field and current close to the arc</b>	<b>91</b>
6.1	Preliminaries . . . . .	92
6.1.1	The ionospheric potential drop . . . . .	92
6.1.2	The fit procedure . . . . .	93
6.2	The infinite straight arc: calculations . . . . .	95
6.2.1	Non-polarized arc . . . . .	95
6.2.2	Determination of $\mathbf{n}_x$ . . . . .	96
6.2.3	Polarized arc . . . . .	96
6.3	The infinite straight arc: discussion . . . . .	100
6.3.1	Discussion of the parameters . . . . .	101
6.3.2	Consistency check: optical observations . . . . .	105
6.3.3	Internal consistency of the model YPYH . . . . .	105
6.4	Models with FAC–electrojet coupling . . . . .	108
6.4.1	Results obtained with the non-linear models . . . . .	108
6.4.2	Model YPYHX: Dependence of the results on the conductance pattern . . . . .	115
6.4.3	Model YPYHX: Dependence of the results on the fit formula . . . . .	117
6.4.4	Deriving $\tan \theta$ from magnetic field data . . . . .	120
6.4.5	The linear model YPYHXL . . . . .	121



6.5	Further discussion of the models YPYHX and YPYHXL . . . . .	125
6.5.1	The dependence on $\eta$ of the constant $\alpha_0$ . . . . .	125
6.5.2	$E_y$ : Fit results vs. optical evidence . . . . .	125
6.5.3	Boundary effects . . . . .	126
6.5.4	Extensions of the fit procedure . . . . .	127
6.6	Current configuration . . . . .	129
6.6.1	Current closure along FAST ionospheric footprint . . . . .	129
6.6.2	The uncommon topology of the current flow . . . . .	134
6.7	Summary . . . . .	139
<b>Chapter 7 Summary and future work</b>		<b>140</b>
<b>Appendix A Software tools</b>		<b>144</b>
A.1	Science Data Tool (SDT) and Data Manager (DM) . . . . .	144
A.2	General IDL routines . . . . .	145
A.3	Specific IDL code . . . . .	147
<b>Appendix B Geometric calibration of optical data</b>		<b>149</b>
<b>Appendix C Errors associated with conductance calculation</b>		<b>151</b>
C.1	Methodological errors: The assumption of stationarity . . . . .	151
C.2	Measurement errors . . . . .	154
C.2.1	Computation of $J_N$ and $J_E$ from the experimental data . . . . .	154
C.2.2	Calculation of the errors in $J_E$ , $J_N$ , and $\overline{E}$ . . . . .	157
C.2.3	Calculation of the errors in $\Sigma_P$ and $\Sigma_H$ . . . . .	158
<b>Appendix D Current closure in curvilinear coordinates</b>		<b>159</b>
<b>Appendix E Orthogonal polynomials</b>		<b>162</b>
E.1	Brief review . . . . .	162
E.2	Numerical results: Jacobi vs. Legendre polynomials . . . . .	165
<b>Appendix F Arc models: the numerical fit</b>		<b>167</b>
F.1	The Method of least squares and the goodness-of-fit test. . . . .	167
F.2	Numerical minimization . . . . .	169
<b>Appendix G Variance analysis</b>		<b>173</b>



# Chapter 1

## Introduction

The roots of the auroral physics can be traced back to more than 400 years ago. At that time Galileo Galilei mentioned “aurora borealis” in his work, Rene Descartes tried to explain it by reflection of sun light on ice crystals, and Georg Hartmann measured the variation of magnetic declination between Rome and Nürnberg. In 1600 William Gilbert, the physician of the Queen Elizabeth I, compared for the first time the Earth with a huge magnet in his book “De Magnetae”.

We shall begin by giving a brief account on the evolution of the auroral research, starting with early discoveries of rather qualitative nature, and concluding with sophisticated contemporary investigations. Because of the accumulation of knowledge and technological progress, the study of the aurora evolved from mainly addressing problems of a global nature to investigating details as small as the transverse 1km scale of the discrete arc. In the last Section we present the plan of the work and point out the goals to be achieved in each Chapter.

Part of the information in the first two Sections comes from the review papers of Stern (1989, 1996) and from the book “The Northern Light — from mythology to space research” of Brekke and Egeland (1983).

### 1.1 A historical perspective

In 1741 Hiorter and Celsius discovered that the magnetic needle was disturbed at time of auroras. It was realized for the first time that geomagnetic activity (this term had not been introduced at that time) and auroras are somehow connected. At the beginning of the 19th century Gauss and Weber established the first network of magnetic observatories, in order to accomplish systematic observations of the magnetic perturbations. Later on Schwabe discovered the sunspot cycle (in the 1840’s), Sabine found that the number of sunspots and the frequency of magnetic storms are correlated (in the 1850’s), and in 1859 two astronomers, Carrington and Hodgson, observed a huge

“solar flare” (another modern term) 17 hours before a brilliant aurora that could be seen even from London. In about 100 years were thus discovered the key relationships between solar activity, magnetic perturbations, and auroral light.

Starting with the last part of the 19th century the understanding began to move from rather qualitative to more quantitative. In 1896 Birkeland set up his famous “terrella” experiment: by sending cathode rays (electrons) against a magnetized sphere he was able to produce an artificial aurora - bright rings encircling the poles of the sphere - and consequently he suggested that aurora could be created by electron streams coming from the Sun. The experimental work of Birkeland was complemented by the theoretical investigations of Poincare, who studied the motion of the charge in a magnetic monopole field, and by Størmer, who extended the research to the dipole field. Poincare found that the particles are “guided” along the magnetic field, while Størmer discovered that the particles coming from infinity (from the Sun) can only reach the Earth at high latitudes, whereas at mid and low latitudes they are trapped by the Earth’s magnetic field.

Birkeland’s theory was criticized by Schuster in 1911, who showed that, because of internal electrostatic repulsion, no electron stream of solar origin could reach the Earth. To solve the problem Lindemann suggested in 1919 that the particle stream should be electrically neutral. Chapman and Ferraro used the image method of Maxwell to prove that the interaction of a neutral beam (later named solar wind), consisting of electrons and ions, with the magnetic field of the Earth, could lead to magnetic disturbances at the surface of the Earth. In a famous suite of papers, published in 1931, they showed that a magnetic cavity is formed around the Earth, and suggested that the magnetic disturbances could result from currents flowing at the surface of this cavity. This early view proved remarkably correct, even if a large number of refinements was added since that time. The Chapman-Ferraro cavity was named *magnetosphere* (Gold, 1959) and the global map of this region, as it is known today, is presented as Fig. 1.1.

The study of a fluid consisting of positive and negative charges, that balance each other so that charge neutrality is preserved (like the solar wind), was undertaken in a systematic manner by Langmuir and his collaborators, Mott-Smith and Tonks, through classic work done between 1925 and 1930 (Mott-Smith and Langmuir, 1926; Tonks and Langmuir, 1929; Langmuir, 1929). They named such a collection of charged particles *plasma*, in close analogy with the blood plasma — an electrolyte with positive and negative ions in dynamic equilibrium. The electrolyte behavior had been studied by Debye and Hückel (1923) who showed that outside of a sphere with radius  $\lambda_D = \sqrt{\epsilon_0 kT / ne^2}$  the departure from charge neutrality becomes vanishingly small. Likewise, the positive ions in a plasma are in equilibrium with the electrons and the plasma can be considered neutral on spatial scales larger than the Debye length.

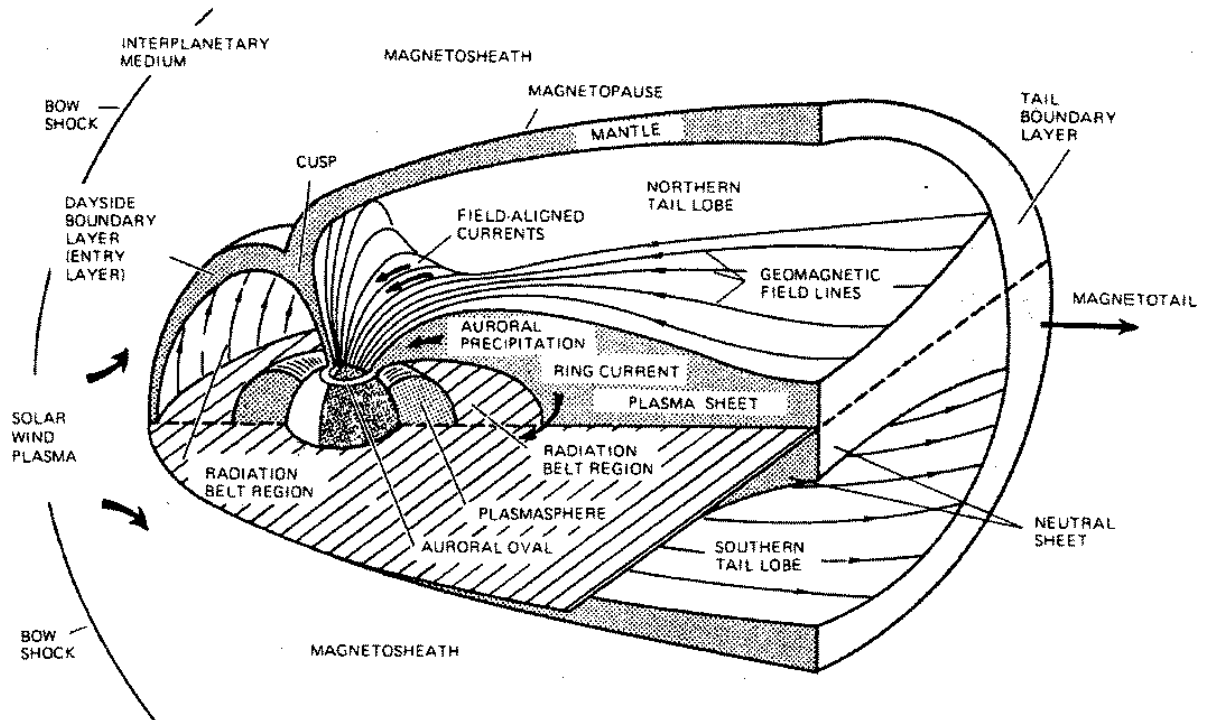


Figure 1.1: The global map of the magnetosphere. Figure 1.13 from Kelley (1989).

The basic analytical tools for plasma investigation were developed in the next few years by Vlasov, Chapman, and Alfvén. Vlasov (1938) wrote a classical paper where he showed that in many cases a good description of the plasma is provided if the collision term in the Boltzmann equation is neglected. By solving the resulting equation together with the Maxwell equations he obtained basic expressions for transverse and longitudinal oscillations in a plasma. Chapman laid the kinetic theory on a sound foundation through work presented in compact form in the book written together with Cowling, Chapman and Cowling (1939). Alfvén (1940a) invented in 1940 the one particle plasma theory, in relation with his work on magnetic storms (Alfvén, 1939, 1940b). Two years later Alfvén (1942) wrote the first paper on magneto-hydrodynamics, originating in his desire to understand the energy propagation within sunspots.

The plasma physics came to a rapid development after the world war II, mainly motivated by the efforts to obtain controlled fusion. Space physics readily took advantage of this opportunity: Beginning with the 1950's rockets and satellites collected a continuously increasing body of data. Analyzed by means of the new plasma physics tools, they boosted the understanding of the *solar wind – magnetosphere – ionosphere* system. In the next Section we shall give a more detailed account on the various types of data used in the investigation of the magnetosphere and ionosphere, in particular of the auroral arc.

## 1.2 The auroral arc and the auroral acceleration region

The auroral phenomena are studied by using both ground and in-situ data. Ground data are provided by optical instruments, magnetic observatories, and radar facilities; in-situ data are collected by rockets and satellites.

### 1.2.1 Ground data

#### Optical observations

During the first half of the 20th century the advance of the photographic and spectroscopic techniques found numerous applications in the auroral research, like: mapping the aurora distribution in height and geographical coordinates, the classification of auroral forms, and the detailed characterization of auroral spectra (including an evaluation of the collision mechanisms between charged and neutral atmospheric constituents). Extended presentations of such topics can be found in Chamberlain (1961) and references therein.

A significant progress in the optical observation of aurora was achieved at the middle of the 1950's, with the invention of the all-sky-camera (ASC), by which pictures covering the sky from horizon to horizon could be taken. The morphological studies of the aurora, following its development both in space and in time, greatly benefited from the ASC pictures. By examining an extended set of images, taken during the International Geophysical Year (IGY, 1957–1958), Akasofu (1964) managed to provide the first systematic description of the auroral substorm.

The photographic techniques require an exposure time of the order of a few seconds to 1 minute. This is not appropriate for highly dynamic auroral features, developing on short temporal and small spatial scales. This limitation was overcome at the middle of the 1960's, with the development of low light TV cameras. By using such an equipment Maggs and Davis (1968) measured with high accuracy the width of auroral arcs, while Hallinan and Davis (1970) studied the motion of auroral folds and curls. They found that many times the curls travel with high horizontal velocities, often in opposite directions along adjacent arc elements, and interpreted this motion as  $\mathbf{E} \times \mathbf{B}$  plasma drift. From the fast curl motions Hallinan and Davis (1970) inferred the existence of large electric fields ( $\sim 0.5$ – $1$  V/m) above auroras, perpendicular to the arc alignment and changing the sign across the arc. Such values are about one order of magnitude larger than those measured in the ionosphere, which are normally in the range  $0.01$ – $0.1$  V/m. In order to explain the existence of intense electric fields at higher altitudes Carlqvist and Boström (1970) suggested for the first time the “U”-shaped potential structure.

Ground optical data are also used to supply information in conjunction with rocket, satellite, and radar measurements. While rockets, satellites, and radars provide a 1D cut through the space-time continuum, the optical observations cover the evolution of the auroral luminosity over large 2D domains, adding valuable knowledge for understanding the in-situ data. As an example, the connection between discrete/diffuse aurora and upward/downward currents was established by combining Triad satellite and ground optical data. Optical observations in conjunction with rocket and radar data also allowed a comprehensive characterization of the electric field and current in the vicinity of auroral arcs (see Section 5.1.3).

### **Magnetic field observations**

As already mentioned, the first ground magnetic observatories were established at the beginning of the 19th century. At times of geomagnetic activity, currents flowing in the ionosphere, at about 110km altitude, or far away in the magnetosphere, perturb the geomagnetic field. By analyzing the magnetic perturbation pattern one can extract information about the intensity, location, and geometry of the current flow.

The current system associated with an auroral arc can be roughly divided in two sub-systems (see Section 5.1.2):

- The *field-aligned currents* (FACs) flow along the magnetic field lines and close in the ionosphere through Pedersen currents, parallel to the electric field.
- The *electrojets* flow in the ionosphere as Hall currents, perpendicular to the electric field.

Fukushima (1976) showed that the magnetic perturbations measured at the ground are essentially produced by the electrojets. In order to characterize the current distribution of the auroral electrojets, and to follow their development in space and time, meridian chains of magnetometers were set up in regions of intense auroral activity, over the polar part of the northern hemisphere.

### **Radar observations**

The radar investigation of aurora developed quickly with the advance of the incoherent scatter technique. Whereas the classical ionosonde can gather information only up to the altitude of the highest electron density (the F layer maximum, around 250-300km), by using incoherent scatter radars (ISRs) a full set of ionospheric parameters can be collected, up to altitudes of about 500-600km. Large ISR facilities close to the auroral zone are the European Incoherent SCATter radar (EISCAT), in northern Scandinavia, and the Sondrestrom radar (which was moved from Chatanika, Alaska, at the beginning of the 1980's), in southern Greenland.

Besides altitudinal profiles of electron density the ISRs also provide ion composition, ion and neutral wind velocity, electron, ion, and neutral temperatures. These can be further used to derive important parameters, like Pedersen and Hall conductivities, electric fields, perpendicular and parallel currents, as well as precipitating particle and energy fluxes. More information on results achieved by using ISRs is given in Sections 5.1.1 and 5.1.3.

## 1.2.2 In-situ data

### Rocket data

Collection of in-situ data started shortly after the world war II, when the first sounding rockets were launched into ionosphere. Reaching at the beginning only modest heights ( $\sim 100$ km), they evolved to more than 1000km nowadays.

A large fraction of the basic knowledge that we have about auroras was achieved by rocket experiments. Using a rocket particle detector McIlwain (1960) found that the discrete auroras are produced mainly by  $\sim 1$ – $10$ keV electrons and interpreted the shape of the particle distribution as suggesting the presence of electric fields parallel to the magnetic field lines — which had been theoretically anticipated by Alfvén (1958). The pioneering work of McIlwain (1960) was followed by other studies based on rocket data (e. g. Albert, 1967; Hoffman and Evans, 1968), which represented significant contributions in this early phase of in-situ auroral research. Work on auroral arc electrodynamics based on rocket data is discussed in Section 5.1.3.

Rockets were not only used for passive experiments, i. e. for just measuring various plasma and field quantities, but also as platform for active experiments. Some of the first determinations of the electric field in the ionosphere were accomplished by measuring the velocity of ion clouds released from rockets at  $\sim 100$ km altitude (e. g. Haerendel, 1972, and references therein). By using this technique it was also possible to obtain direct evidence for the existence of parallel electric fields above auroral arcs (e. g. Haerendel et al., 1976).

Rocket measurements are still heavily used by the auroral community, because of the possibility to obtain very high resolution data and the freedom in choosing the launch time, so that a rocket flight can be tuned to a particular type of event. Neither satellites, nor radars can compare to rockets in these respects, although recent missions, like Freja and FAST, have considerably diminished the gap. They provide measurement resolutions close to those obtained with rockets, while the continuous coverage results in large databases, that offer a large selection of individual events.



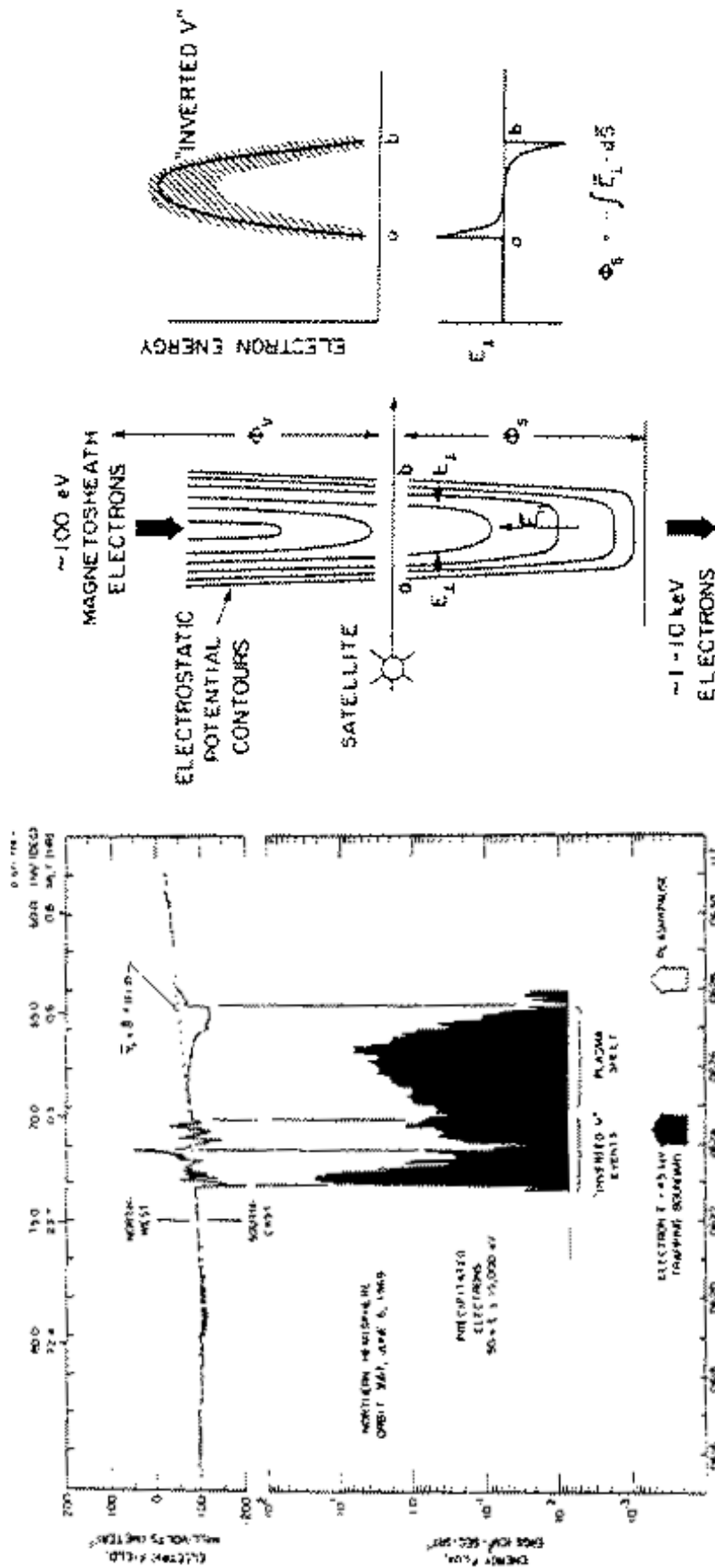


Figure 1.2: Electron inverted- $V$ , electric field reversal, and the associated potential structure. Figures 9 (left) and 10 (right) from Gurnett (1972).

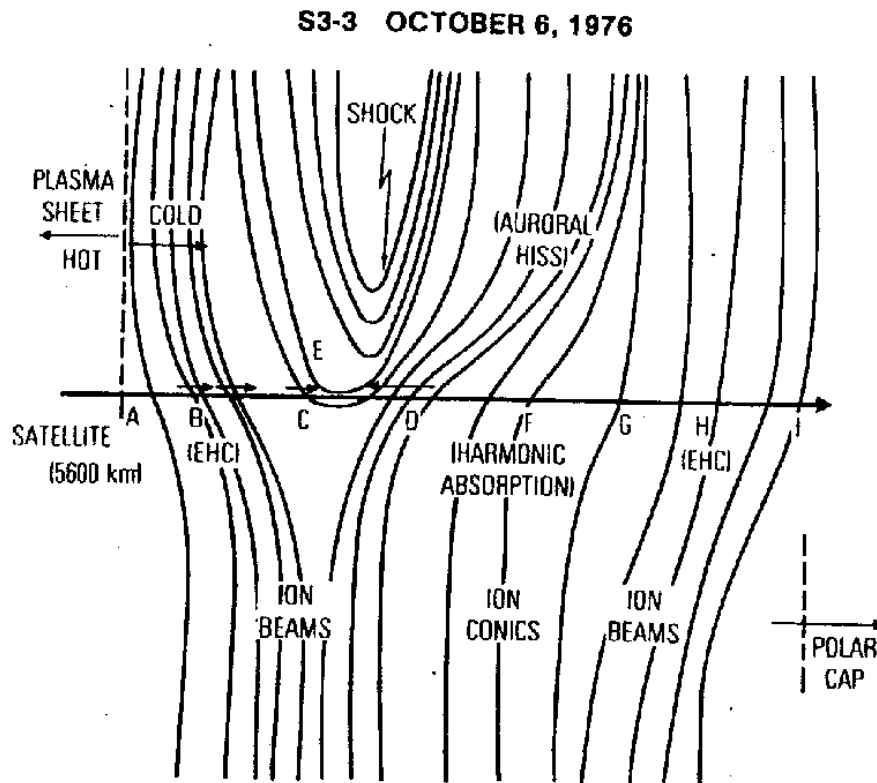


Figure 1.3: The geometry of the auroral acceleration region as revealed by S3-3. From Mizera et al. (1982).

### Satellite data

The continuous coverage made possible by satellites is of paramount importance for recognizing typical features. Without a large collection of data one could hardly guess if a certain feature is the exception or the rule.

At the end of the 1960's satellite measurements brought the peremptory proof for solving the old controversy on the existence of field aligned currents (Zmuda et al., 1970, and references therein). The discovery of characteristic auroral signatures, like the inverted-V pattern in time-energy electron spectrograms (Frank and Ackerson, 1971), and the association between inverted-V events and electric field reversals (Gurnett and Frank, 1973), were also possible due to satellite data. Gurnett (1972) suggested that an "U"-shaped potential structure — very similar to the configuration formerly imagined by Carlqvist and Boström (1970) — would explain both the inverted-V character of the electron precipitation and the associated electric field reversal (Fig.1.2).

Convincing experimental evidence that the structure sketched in Fig.1.2 really exists came with the USAF satellite S3-3, that discovered its location "almost accidentally" (cf. Fälthammar, 1983). Equipped with a full set of instruments to measure particles and fields, S3-3, with apogee at 8000km, provided the first systematic description of the auroral acceleration region (AAR).

Many of the characteristic features associated with this key region — ion beams (Shelley et al., 1976) and conics (Sharp et al., 1977), electrostatic shocks (Mozer et al., 1977), weak double layers (Temerin et al., 1982), ion cyclotron waves (Kintner et al., 1978) collocated with ion beams (Kintner et al., 1979) and FACs (Cattell, 1981) — were discovered by S3-3. The AAR map, as resulted from S3-3, is shown here in Fig. 1.3. For a full account of S3-3 achievements and extended references the reader is directed to the reviews of Mozer et al. (1980) and Chiu et al. (1983).

The discoveries of S3-3 were further substantiated by missions like DE, Viking, and Akebono, with apogees above 10000km, that fully confirmed the original picture and added further refinements through increased time resolution and exploration of different altitude ranges. More recently Freja, with apogee at 1700km, and FAST, with apogee at 4000km, resolved a large variety of small scale structures below and at the bottom side of the AAR.

### 1.3 Goal and plan of the work

The main goal of this work is to provide a good electrodynamic characterization of an auroral arc, based on high resolution satellite measurements and ground optical images. The satellite data we use come from the NASA auroral mission FAST (Carlson et al., 1998a). The images were recorded with a TV camera of Max-Planck-Institut für extraterrestrische Physik (Frey et al., 1996).

We shall develop a general frame for studies of arc electrodynamics, by building a realistic model, which incorporates the ionospheric polarization, the Hall contribution to the FAC closure across the arc, and the coupling between the FAC and the electrojet. Plasma and DC (electric and magnetic) field data, measured well above the current closure region, will be used to examine several instances of the model.

By means of the information provided by the ground images we shall check the consistency of the results derived from satellite data. However, the frame assembled in this work is, in principle, independent from ground measurements. If proved to be valid, it only relies on satellite data. The method we suggest could become a valuable tool for the investigation of arc electrodynamics under various auroral conditions.

The present work is organized as follows:

*Chapter 2:* Description of the satellite payload and of the ground optical equipment. The software packages used to process the data are also briefly introduced.

*Chapter 3:* Data corresponding to a FAST overpass, in conjunction with optical observations, are presented in detail. Geophysical parameters and ground magnetograms, illustrating the ambient conditions, are also included. The multi-scale approach possible with FAST, encompassing convection, field-aligned currents, inverted-Vs, and ion beams, is emphasized.

*Chapter 4:* Pedersen and Hall conductances are derived from particle data, by using approximate formulas, taken from literature. The evaluation of conductances during ion beam events is given special attention. We also discuss the errors associated with conductance determination, related both to the method used and to the measurement technique.

*Chapter 5:* We start with a review of ionospheric electrodynamics that emphasizes work done on the auroral arc. Some published experimental facts are briefly introduced. Several idealized features of the proposed models are commented and shown to be incompatible with our data. We conclude by building more realistic models whose parameters can be determined by fit.

*Chapter 6:* The results of Chapters 3, 4, and 5 are used to find the electric field and current along the ionospheric footprint of our case-study FAST orbit. A step by step evaluation of the arc model is performed, which shows that only the fully developed instance is reasonably consistent with the complete set of experimental data. The most promising results are used to discuss the 3D current configuration, which is found to differ substantially from the common pattern.

*Chapter 7:* Summary of the work and prospects for future development.

# Chapter 2

## Experimental setup

The forefather of Fast Auroral SnapshoT (FAST) is S3-3. About 25 years ago S3-3 discovered the AAR, taking full advantage from a complete payload of field and particle experiments.

The FAST mission, devoted to the investigation of the small scale structure of AAR, was developed under the SMall EXplorer (SMEX) program of NASA. The PI institution for FAST is the Space Science Laboratory (SSL) of the University of California at Berkeley (UCB). UCB/SSL has been heavily involved in auroral rocket and satellite projects (among them S3-3) since more than three decades.

At the beginning of 1997, shortly after the FAST launch, an auroral campaign supported FAST measurements with optical observations taken from a jet aircraft and from the ground. The ground observation was conducted by the Max-Planck-Institut für extraterrestrische Physik (MPE) and the jet aircraft by the Geophysical Institute of the University of Alaska at Fairbanks. In this work we shall use data from one of the MPE's TV cameras.

The first Section introduces the satellite and its payload. Next, the FAST data processing software is briefly described. In the last Section we present the MPE's optical equipment.

### 2.1 Satellite payload

The FAST satellite was launched on August 21, 1996, in a polar orbit ( $83^\circ$  inclination), with apogee at 4200km and perigee at 350km. The satellite has a reverse cartwheel motion, with a spin period of 5s and the spin axis perpendicular to the orbit plane. As an important consequence of the orbit and spin geometry, the magnetic field line is always close to the spin plane (typically within  $5^\circ$ ). A FAST crossing of the AAR, together with some characteristic phenomena in this region, is sketched on the left side of Fig. 2.1 (not to scale).

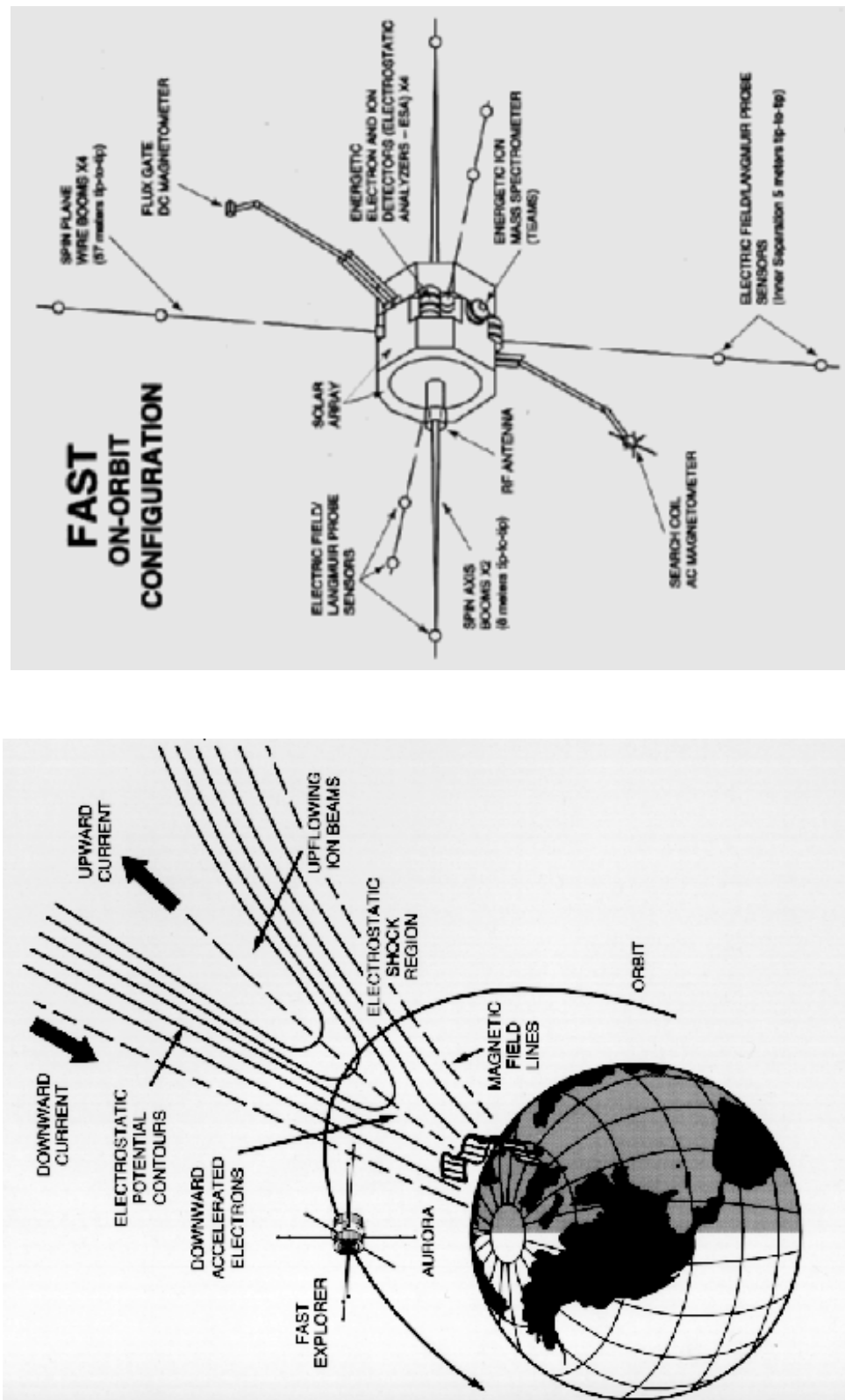


Figure 2.1: **Left:** Schematic view of FAST crossing the AAR (not to scale). **Right:** FAST payload. From <http://www-ssc.igpp.ucla.edu/fast>.

An important feature of FAST is the flexible data acquisition rate, depending on the satellite mode and on the selected Particle and Field modes. At low and medium latitudes the instruments are switched off, except for the magnetic field which is sampled at a rate of  $8\text{s}^{-1}$ . The satellite is switched to Slow Survey mode when it crosses  $60^\circ$  invariant latitude (the exact time is pre-determined by orbit calculation; see p.27 for the definition of the invariant latitude). Particle and field data collected in this mode are resolved at a rate comparable to that achieved by previous missions. In Fast Survey mode, triggered by the enhancement of the auroral activity (visible in the electron energy flux), the data rate increases by about one order of magnitude, and compares to the highest burst rates achieved by missions before FAST. The most intense events are selected for storing in Burst mode, according to another set of trigger algorithms, that depend on the scientific goal. The Burst data typically span 10–30s and allow the detailed investigation of the small scale structure of the AAR. The highest data rate available on FAST is High Speed Burst Memory (HSBM), for capturing waveforms up to 1 MHz (covering  $\sim 1\text{s}$  intervals). The present study is mainly based on Fast Survey data; Burst data, acquired during ion beam events, are also used.

FAST was designed as one integrated measuring unit, with the different instruments acting as sensors for the different data types. This concept is best reflected by the existence of a unique *Integrated Data Processing Unit (IDPU)*, taking care of all the scientific processing onboard FAST. A schematic representation of the satellite and its payload is shown on the right side of Fig.2.1. Extended descriptions can be found on the FAST web page, <http://sprg.ssl.berkeley.edu/fast>, and were published in a recent issue of Space Science Reviews, Vol.98(1-2), August 2001 (for an overview see Pfaff et al. (2001)). In addition, useful information was published in the AGU monographs *Measurement Techniques in Space Plasmas* (Pfaff et al., 1998a,b). The Tables 2.1 and 2.2 below are taken from McFadden et al. (1999). The following two Sections are intended just as an outline; the reader is directed to the mentioned references for details.

### 2.1.1 Particle instruments

There are 4 particle instruments onboard FAST: A mass spectrometer (TEAMS), an ion spectrometer without mass resolution (IESA), an electron spectrometer (EESA), and a high time resolution electron spectrograph (SESA). Table 2.1 shows the main characteristics of the particle instruments. A common feature is the large geometric factor (the last column), making possible the achievement of statistically significant results for short sampling times (column 4). This is very important for revealing the small scale structure of the AAR.

Table 2.1: FAST Particle Detectors. From McFadden et al. (1999)

Measurement	Energy per Charge Range	$\Delta E/E$	Sampling Reduction	Field of View	Angular Resolution	Sample Array	Geom. Factor ( $\text{cm}^2 \text{sr}^{-1} \text{E/E}$ )
Ion Mass Spectrometer	1eV/e – 12keV/e	0.13	2.50 s (3-D) 78 ms (2-D)	$360^\circ \times 10^\circ$	$22.5^\circ \times 10^\circ$	$4\text{M} \times 48\text{E} \times 64\Omega$ $4\text{M} \times 48\text{E} \times 16\alpha$	0.015
Ion Spectrometer	3eV/e – 25keV/e	0.20	78 ms	$360^\circ \times 12^\circ$ <sup>a</sup>	$11.2^\circ \times 12^\circ$	$48\text{E} \times 32\alpha$	0.014
Electron Spectrometer	4eV/e – 30keV/e	0.15	78 ms	$360^\circ \times 10^\circ$ <sup>a</sup>	$11.2^\circ \times 10^\circ$	$48\text{E} \times 32\alpha$	0.005
Electron Spectrograph	4eV/e – 30keV/e	0.15	1.6 ms	$360^\circ \times 10^\circ$	$22.5^\circ \times 10^\circ$	$6\text{E} \times 16\alpha$ <sup>b</sup>	0.005

<sup>a</sup>Field of view can be deflected  $\pm 10^\circ$  from the center angle.<sup>b</sup>A larger energy sample array can be achieved with poorer time resolution.



In this work we shall use Fast Survey and Burst data from the EESA and IESA instruments in the presentation of the AAR crossing (Chapter 3) and to calculate ionospheric conductances (Chapter 4). The Fast Survey TEAMS data (Chapter 3) show that the ion beams' composition agrees with the general geophysical conditions.

### **The Mass Spectrometer TEAMS**

The Time Energy Angle Mass Spectrometer (TEAMS) consists of:

- An electrostatic energy filter of top-hat design (Carlson et al., 1983), covering an energy per charge range of 1eV/e–12keV/e, divided into 48 logarithmic steps. An energy sweep takes typically 78 ms, 1.6 ms for each step. Behind the electrostatic analyzer the ions are accelerated by a selectable voltage of -15kV to -25kV.
- A time-of-flight (TOF) section able to resolve atomic and molecular ions with mass per charge between 1 and 64 a.u./e (in cooperation with the electrostatic analyzer); the major ionospheric ions, H<sup>+</sup>, O<sup>+</sup>, He<sup>+</sup>, are thus readily detected. For minor constituents longer accumulation times (several spin periods) are necessary.
- A detection unit based on Micro-Channel Plates (MCP) which images the incoming particles on 16 anodes, each of them covering a 22.5° sector.

The instrument axis is perpendicular to the spin axis, so that full 3D distributions can be obtained. The unit sphere is divided into 64 solid angles, symmetric with respect to the spin plane. Each hemisphere is divided into four belts, evenly spaced in polar angle (the middle polar angles for the belts of the positive hemisphere are equal to 11.25°, 33.75°, 56.25°, and 78.75°). Each belt, in its turn, is evenly divided in azimuthal sectors: 16 for the equatorial belts, 8 at lower mid latitudes, and 4 at upper mid latitudes and around the poles. The polar and azimuthal angle refer to the satellite spin axis.

In Fast Survey mode a full 3D distribution is collected every half spin (2.5s) for H<sup>+</sup> and O<sup>+</sup>, and every spin (5s) for He<sup>+</sup>. In Burst mode 2D distributions are also stored, 64 distributions per spin (corresponding to a 78 ms energy sweep: 5s/78ms=64). However, unlike the IESA and EESA plasma detectors, the magnetic field line lies in the TEAMS viewing plane only two times per spin. Consequently, pitch-angle spectra can only be obtained with half-spin (H<sup>+</sup>, O<sup>+</sup>) or spin resolution (He<sup>+</sup>). Other data products are also available, like mass spectra and high resolution data from the polar sectors of the instrument (which look all the time perpendicular to the magnetic field line and thus can offer information about transverse ion energization). See Klumpar et al. (2001) for further details.

### The plasma spectrometers IESA, EESA, and SESA

The ion spectrometer (IESA), the electron spectrometer (EESA), and the stepped electron spectrograph (SESA) are packed together in 4 stacks of 4 top-hat electrostatic analyzers (ESA) each, symmetrically distributed around the spacecraft. Each ESA has a field of view (FoV) of  $180^\circ$ , in the spin plane of the satellite, and opposite ESAs are paired to obtain  $360^\circ$  FoV; one ESA pair is used for IESA, one for EESA, and the rest of six for SESA. Additionally, the FoV can be deflected within  $10^\circ$  from the spin plane, in order to include the magnetic field line in the viewing plane. Consequently, *for each energy step the full pitch-angle distribution is measured* and complete energy–pitch-angle distributions are available at high rates. The specific rate for each instrument, as well as the energy range and the angular resolution are given below. For a detailed description see Carlson et al. (2001).

- The ion spectrometer, IESA, covers the energy per charge range  $3\text{eV/e}–25\text{keV/e}$  divided, as for TEAMS, in 48 logarithmic steps; the typical energy sweep takes 78 ms. In Fast Survey mode 4 energy sweeps are collected together while in Burst mode each sweep is recorded separately. The angular resolution is  $5.6^\circ$  for Fast Survey data and  $11.2^\circ$  for Burst data.
- The electron spectrometer, EESA, has similar characteristics as IESA, except for the energy coverage which is  $4\text{eV/e}–30\text{keV/e}$ .
- The electron spectrograph, SESA, can be set to achieve maximum time resolution, 1.6 ms, with 6 fixed energies, or maximum energy resolution, 48 levels, with a time resolution of  $8 \times 1.6 = 12.8\text{ms}$ . A trade-off between energy and time resolution is also possible. The SESA angular resolution of is  $22.5^\circ$ .

It is a useful exercise to evaluate the spatial scale associated with the particle measurements. At and near the apogee (as it is the case for this work) FAST velocity is  $\sim 5.6\text{km/s}$ . In Burst mode a full IESA/EESA distribution is collected in 78ms, which transforms to a distance of  $\sim 440\text{m}$ . In Survey mode the accumulation time is 4 times longer, which leads to  $\sim 1760\text{m}$ . The magnetic field at 4000km altitude is  $\sim 4$  times smaller than at 110km ionospheric level. Consequently, the mapping factor from FAST altitude to the ionosphere is  $\sim 0.5$  (considering isotropic mapping, which is a reasonable assumption for this altitude range) and the distances above correspond to  $\sim 220\text{m}$  and  $\sim 880\text{m}$  respectively, at ionospheric level, comparable to the width of thin discrete arcs. For SESA, the ionospheric distance between two measuring points is  $\sim 5\text{m}–40\text{m}$ .

### 2.1.2 Field instruments

The field measurements are very well represented onboard FAST, as one can easily notice by inspecting Table 2.2. Extended instrument presentations can be found in Ergun et al. (2001) (electric field) and Elphic et al. (2001) (magnetic field). The field data to be used later in this study cover only the DC part of the spectrum, for both the magnetic and the electric field. Nevertheless, AC data are also introduced in Section 3.2, to offer a broader perspective on the event under study.

The low frequency magnetic field is measured with a fluxgate magnetometer, mounted on a boom at 2m from the satellite body (see Fig. 2.1). The satellite is magnetically clean (Elphic et al., 2001) which allows high accuracy data. The sampling frequency is 128Hz and the signal is filtered to 50Hz, below the 64Hz Nyquist frequency. The measured magnetic field is further passed through a 16-bit analog-to-digital converter (ADC). The magnetometer covers the full  $\pm 65000\text{nT}$  range of the Earth's background field, with a resolution of  $\pm 2\text{nT}$ .

The electric field is measured by using the double probe technique. FAST is equipped with 4 wire booms in the spin plane and with 2 rigid booms along the spin axis; each spin plane boom carries 2 spherical probes, at 23m, respectively 28m from the satellite body; a probe is also mounted on each axial boom, 3m away from the satellite. The more distant radial probes can only work in voltage mode. The radial probes closer to the satellite, as well as the axial ones, can work both in voltage and in current mode; they either measure the electric field, or the electron density and temperature, according to the selected field mode.

The electric field booms came to an in-flight configuration different from the planned one. One of the radial wires did not deploy and, in order to preserve a good satellite dynamics, it was decided to deploy only one of the two axial booms. Because of the proximity of one axial probe to the spacecraft body and the lack of spin signals necessary to estimate gains and offsets, the electric field along the spin axis of the satellite (roughly E–W direction) is not measured in the DC range (details at [http://sprg.ssl.berkeley.edu/fast/scienceops/fast\\_fields\\_help.html](http://sprg.ssl.berkeley.edu/fast/scienceops/fast_fields_help.html)).

The data from the spin plane probes can still be processed to obtain the electric field components parallel/perpendicular to the spacecraft velocity. Due to the geometry of the orbit, when the satellite is close to apogee the two components are nearly perpendicular/parallel to the magnetic field; we designate them accordingly as  $E_{\perp}$  and  $E_{\parallel}$ . By integrating  $E_{\perp}$  one can obtain potential differences along the satellite path; this procedure will be detailed in Section 3.2 and further used in Chapter 6. As far as  $E_{\parallel}$  is concerned, it should be mentioned that this is *not* the exact value of the electric field component parallel to the magnetic field. A reliable determination of the parallel electric field requires serious precautions (see the discussion at p.35).

Table 2.2: FAST Field Instruments. From McFadden et al. (1999)

Measurement	Components	Frequency Range	Sampling Reduction	Measurement Range	Measurement Resolution, bit
<i>Electric field</i>					
DC E-field	3-axis	0–300 Hz	30 $\mu$ s	$\pm 1.6$ V/m	16
Wave E-field	3-axis	0.30–16 kHz	30 $\mu$ s	$\pm 200$ mV/m <sup>a</sup>	16
Swept frequency receiver <sup>b</sup>	3-E 1-B	0–2 MHz 0–2 MHz	32 ms 32 ms	$10^{-15}$ – $10^{-5}$ (V/m) <sup>2</sup> /Hz $10^{-12}$ – $10^{-5}$ nT <sup>2</sup> /Hz	8
E-field rectifier/filters	3-axis	0.10–2 MHz	30 $\mu$ s	0.1 mV/m – 1 V/m <sup>c</sup>	8
High-speed burst memory	3-E 1-B	0–1 MHz 0–500 kHz	0.5 $\mu$ s 0.5 $\mu$ s	$\pm 200$ mV/m $\pm 1$ nT	10
Density	2-point	0–250 Hz	0.5 ms	$1$ – $6 \times 10^4$ nA	8
<i>Magnetic field</i>					
Fluxgate	3-axis	0–50 Hz	2 ms	$\pm 6 \times 10^4$ nT	16
Search coil	2-axis 1-axis	50 Hz – 4 kHz 10 Hz – 16 kHz	30 $\mu$ s	$10^{-1}$ – $10^4$ nT $4 \times 10^{-2}$ – $4 \times 10^3$ nT	16 16

<sup>a</sup>The amplitude range increases for short wavelength (less than boom length) waves up to 1.6 V/m.<sup>b</sup>Frequency resolution, 15 kHz.<sup>c</sup>Selectable gain, range varies with antenna length.

AC electric and magnetic fields are measured over a frequency range extending from DC to 2MHz. The electric field sensors are the spherical probes mentioned above, while for the magnetic field a second, search coil magnetometer, was necessary. The various signals are processed both onboard and on the ground.

Continuous on-line monitoring of the ELF/VLF (DC to 16kHz) and HF ( $\sim 10$ kHz to 2MHz) power spectral densities is achieved through a Digital Signal Processor (DSP) and a Swept Frequency Analyzer (SFA) respectively. Averaged spectra, with frequency resolution of 32Hz (DSP) and 15kHz (SFA) are recorded typically every 4/0.25s in Slow/Fast Survey mode. In Burst mode SFA spectra can be obtained every 31.25ms. In addition, a Plasma Wave Tracker, a Wave-Particle Correlator, and a High Speed Burst Memory unit (able to collect  $\sim 1$ s of 1MHz waveform data), are active in Burst mode.

The off-line ground processing is performed by applying Fast Fourier Transform (FFT) to the captured waveforms. In Fast Survey mode the frequency range extends to 1kHz, while in Burst mode the upper frequency limit is either 4kHz or 16kHz (depending on the sensor and on the instrument mode). The data used later in this work to provide the average ionospheric electric field are low-pass filtered to the 10Hz Burst resolution of the particle experiment.

## 2.2 Data analysis software

The data presented in this work was analyzed by using three categories of software (for a more extended description see Appendix A):

1. A quick look program, Science Data Tool (SDT), which brings the data from the Level Zero Processing (LZP) files to the computer screen, for visual inspection, and in either disk or memory buffers for further processing. SDT cooperates with a Data Manager (DM) program, which communicates with the main FAST database at UCB/SSL. If a required file is not found on the host computer DM takes care of downloading that file, without extra trouble to the user.
2. A voluminous package of general IDL routines, covering tasks like:
  - Getting and plotting the satellite orbit .
  - Loading the data from the SDT buffers into IDL.
  - Getting despun components of the magnetic and electric field.
  - Obtaining energy and pitch-angle particle spectrograms.

- Obtaining frequency spectra for the electric and magnetic field.
- Computing moments of the particle distributions.
- Plotting (multi)line and spectrogram data.
- Viewing particle distributions in various formats.

The list is just indicative and biased according to the necessities of this study.

3. Specific IDL routines and add-ons to the existing code, required by the present work. A short selection includes:

- Reading the MPE image file format (IFF).
- Computing the ionospheric conductances and electric field.
- Adding error calculation sections to the code computing particle moments.

The quick look and data manager programs, together with the associated libraries, were developed at UCB/SSL and are described to some detail in McFadden et al. (2001). Documentation files on installing and configuring SDT and DM are provided within the package. Some information can also be found at [http://sprg.ssl.berkeley.edu/fast/scienceops/fast\\_sdt\\_help.html](http://sprg.ssl.berkeley.edu/fast/scienceops/fast_sdt_help.html). The general IDL package was contributed by UCB/SSL and by some of the CoI institutions: University of California at Los Angeles (UCLA) for the magnetic field code and University of New Hampshire for parts of the TEAMS code. The full package, containing SDT, DM, and general IDL routines, is available at the FAST ftp site: [ftp://juneau.ssl.berkeley.edu/pub/software\\_releases](ftp://juneau.ssl.berkeley.edu/pub/software_releases).

## 2.3 Ground optical equipment

The origin of the MPE interest in optical observations can be traced back to the rocket ion release experiments started in the 1960's (e.g. Föppl et al., 1967). The motion of the ion clouds was first recorded with photographic cameras and later by using low light TV systems. More recently, three low-light CCD TV cameras were developed at MPE in order to study small scale auroral structures (see Frey et al., 1996, for a detailed description). They can be equipped with either wide angle ( $86^\circ \times 64^\circ$ ) or narrow angle ( $21^\circ \times 16^\circ$ ) optics, and can be used either with filters (577nm and 630nm narrow band, or  $\geq 650$ nm pass band) or in white light.

Figure 2.2 shows the ground experimental setup during the auroral campaign from January–February 1997. The N–S and E–W directions are indicated at the top of the picture. The building at the rear is the field station that housed the electronics and the research team.

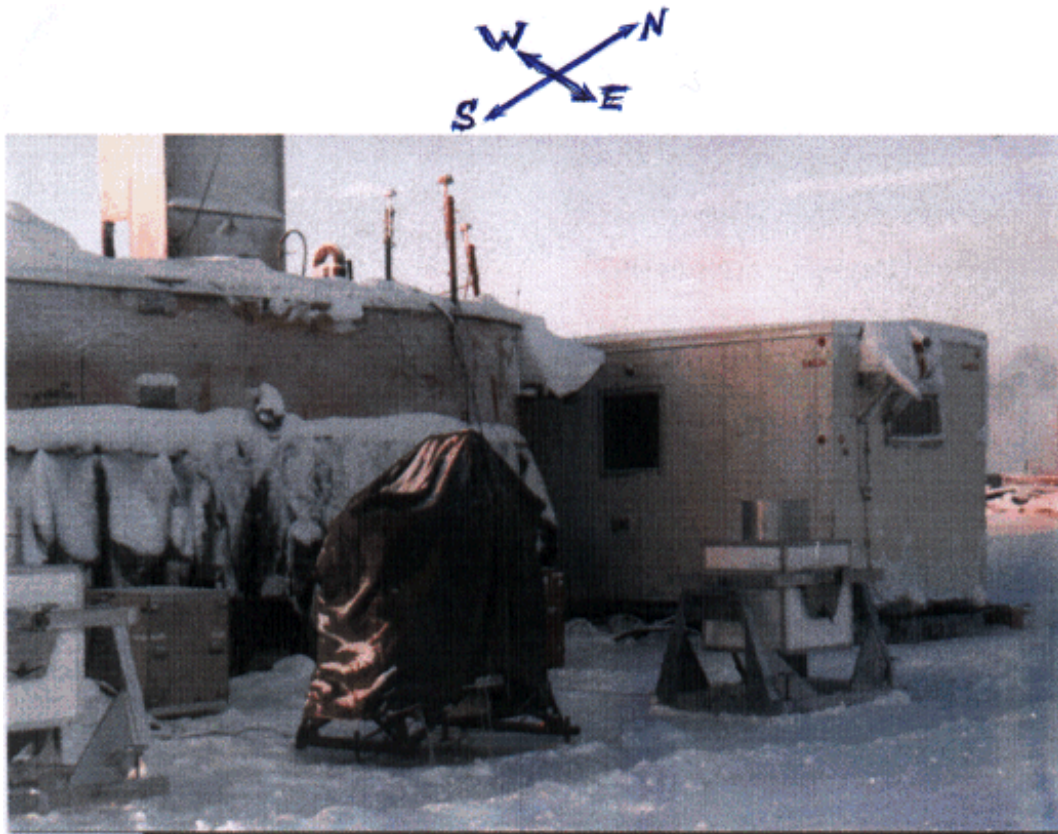


Figure 2.2: Ground optical equipment during the January–February 1997 campaign. At the rear is the field station, housing the team and the electronics to control the cameras, which are visible in the front plane. The side cameras are equipped with wide-angle and the middle one with narrow-angle optics. The cameras are N–S aligned, with the South at the left. The data used in this work come from the southward, only partially visible camera. (Courtesy W. Lieb)

The three cameras are visible in the front plane. The two cameras at the sides are equipped with wide-angle optics and fixed in cardanic mounting, that allows rotation around two axes (in this case N–S and E–W), in order to get the best view of the auroral form. The camera in the middle (under the black cover) is equipped with narrow-angle optics. The data we use in this work comes from the southward camera (which is only partially visible). During the observation the camera was rotated  $30^\circ$  around the N–S axis and  $25^\circ$  around the E–W axis (information from the campaign log-book, maintained by H. Frey), and was equipped with the pass band filter.

The exposure time of the cameras can be varied from 40ms, the standard PAL TV norm, by multiplication/division with/through powers of 2. The images are recorded on commercial video tapes. At MPE the images are digitized to  $768 \times 576$  pixel arrays (corresponding to the CCD detector geometry), with 8 bit depth.

The digitized pixel value depends not only on the intensity of the auroral light coming from a certain direction, but also on: **a)** optical parameters, e. g. transmission coefficients and their dependence on wavelength; **b)** camera setup, e. g. exposure time and electronic gain.

Obtaining the absolute light intensity is, in principle, possible, if the camera is optically calibrated for the respective spectral range, but such a procedure will not be attempted here. For the purpose of this work it is sufficient to calculate relative intensities (see Section 3.3). The accuracy of the results can be checked by comparing the position of the maximum brightness, along the satellite path, with the position of the maximum electron energy flux (Fig. 3.11). In order to compare the satellite measurements with the luminosity pattern exhibited by the ground images a geometrical calibration is also necessary. The reader is referred to Appendix B for the details of this procedure.



## Chapter 3

# A satellite auroral overpass: FAST orbit 1859

During the winter campaign from January–February 1997 optical data in conjunction with FAST measurements were obtained for several FAST orbits. The ground equipment was located at Deadhorse, in northern Alaska (Lat.  $70.22^\circ$ , Lon.  $211.61^\circ$ ). We present here FAST data from orbit 1859, collected on February 9, 1997, around 8:22 UT, while crossing the evening auroral oval, at about 21 MLT. The conjugated optical data are also discussed.

In the first Section the FAST crossing is placed in a more general context, derived from both geophysical indices and ground magnetograms. In the next two Sections the satellite and optical data are presented and discussed, with emphasis on the spatial and temporal scales available to observation. We conclude the Chapter by pointing out data features important for the further development of the work.

### 3.1 Geophysical conditions

The first half of the day of February 9, 1997, was relatively quiet in the auroral zone; the AE index is shown in Fig. 3.1. Nonetheless, the background was disturbed: a magnetic storm started on February 7 was in progress, reaching its maximum amplitude at the middle of February 10, with a  $D_{ST}$  of -72. The  $K_p$  index for UT 6–9 was 2, the minimum value during this storm period. On February 8 the  $K_p$  went up as high as 6- and on the evening of February 9 it reached 5+.

The satellite pass over the auroral oval and polar cap is shown at the left side of Fig. 3.2 (obtained by using the general IDL FAST package, see Appendix A). The figure is centered at the magnetic pole and has the magnetic noon at the top (although the magnetic pole is marked with

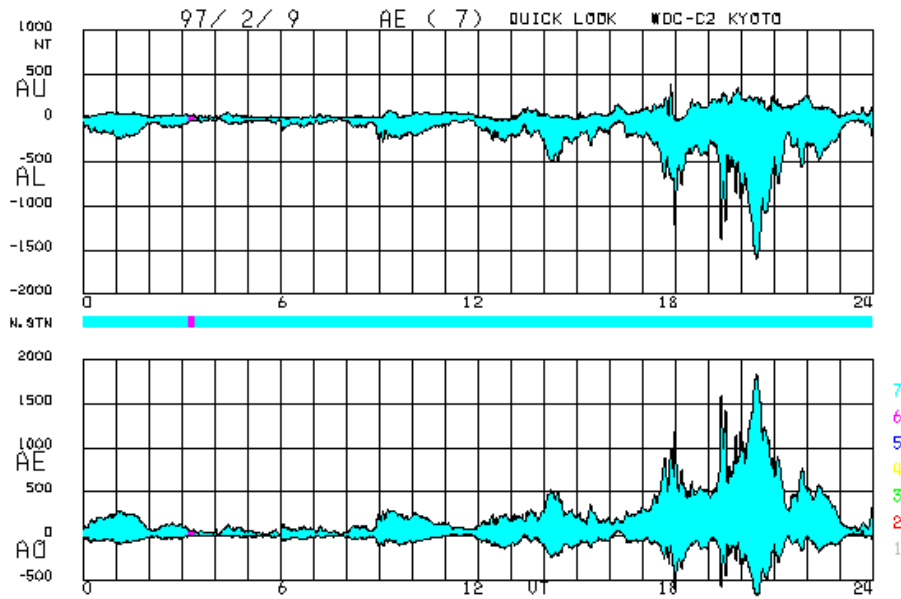


Figure 3.1: AE index for February 9, 1997. From World Data Center for Geomagnetism Kyoto, <http://swdcd.db.kugi.kyoto-u.ac.jp>.

'N', this is actually the magnetic South pole). Plotted in the figure are the satellite trajectory (the red curve joining the lower left and the upper right corners), the auroral oval, geographic fiducial lines, and the day–night terminator at 110km (the blue curve at the upper side). Note that FAST, at  $\sim 3900$ km, was continuously in sunlight. The figure also shows several magnetic observatories over Alaska and northern Canada, as well as Deadhorse, the site of the optical campaign.

The plotted auroral oval corresponds to an activity index  $Q=1$  (Holzworth and Meng, 1975), in agreement with the AE index around 8:22 (Fig. 3.1). The big 'X' close to the northern border of the oval shows the time 8:22:12 when FAST encountered the southern edge of the arc (see also Fig. 3.12). The width of the 'X' is a rough measure of the arc width. The '+' signs along the satellite path mark 5 minutes intervals. A more detailed view over the evening part of the oval is given at the right side of Fig. 3.2. One can compare the limits of the statistical oval with the convection, field-aligned current, and luminosity patterns (Sections 3.2 and 3.3). The agreement is reasonably good, with the oval extending somewhat north of the convection reversal.

To complete the picture of the geophysical context, magnetograms from 2 stations close to the arc, Barrow and College, are shown in Fig. 3.3. Each magnetogram shows the horizontal component,  $H$  [nT], the declination,  $D$  [0.1min], and the vertical component,  $Z$  [nT]. The main information one can extract from Fig. 3.3 is that around 8:22 the ground magnetic activity was reduced, both south (College) and northwest (Barrow) of the arc. However, shortly afterward the magnetic field within the oval got increasingly perturbed (this is also visible in the AE index).

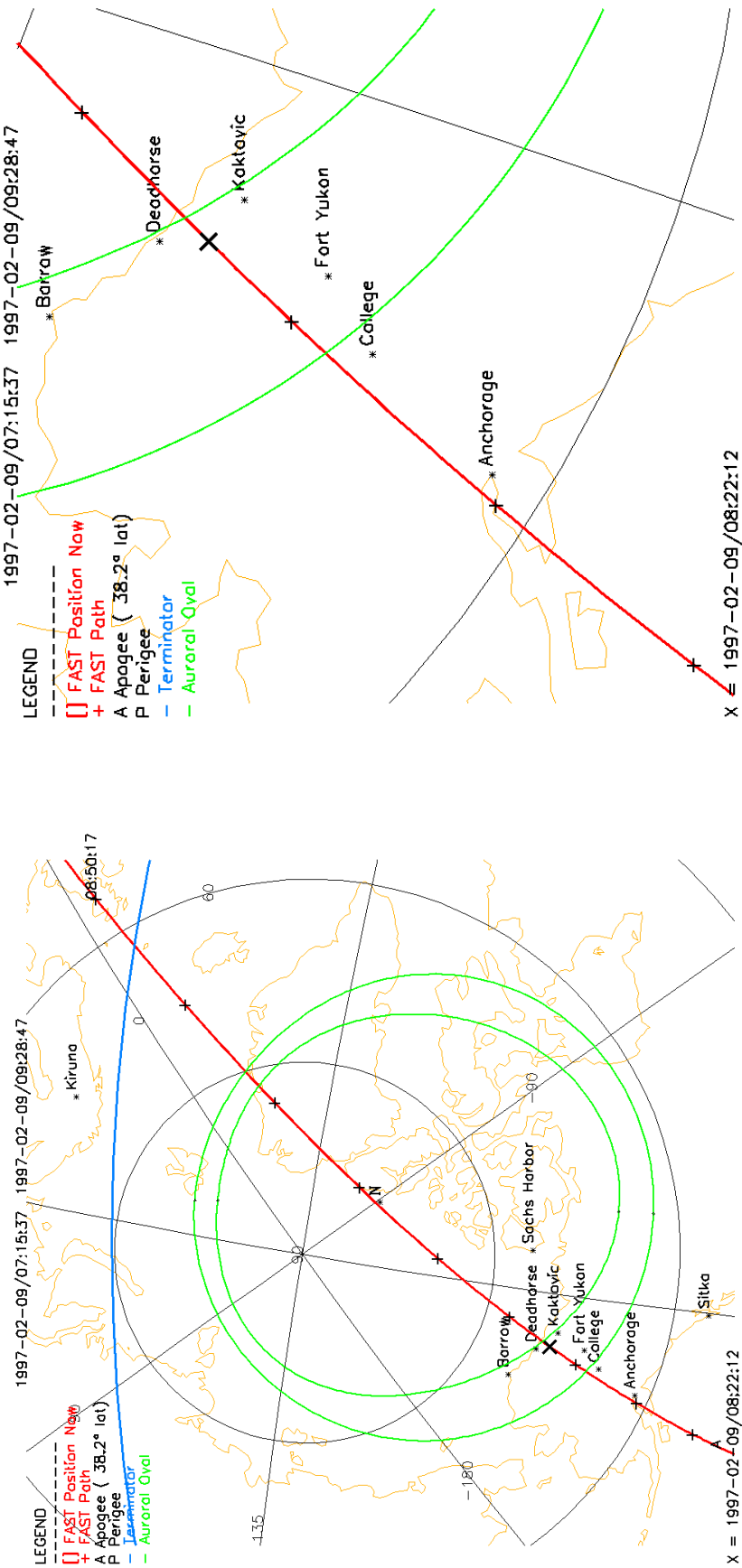


Figure 3.2: **Left:** FAST orbit 1859, over the northern auroral oval and polar cap, on February 9, 1997. The magnetic pole is at the center of the figure (marked with 'N') and the magnetic noon at the top. The satellite path crosses from bottom left to top right (red curve) and is marked with '+' every 5 minutes and with a big 'X' at the arc position (see also Fig. 3.12). The transverse blue curve at the top is the day-night terminator at 110km. The auroral oval (green) and geographic fiducial lines are also shown. **Right:** Detailed view of the FAST crossing over the evening side of the oval.

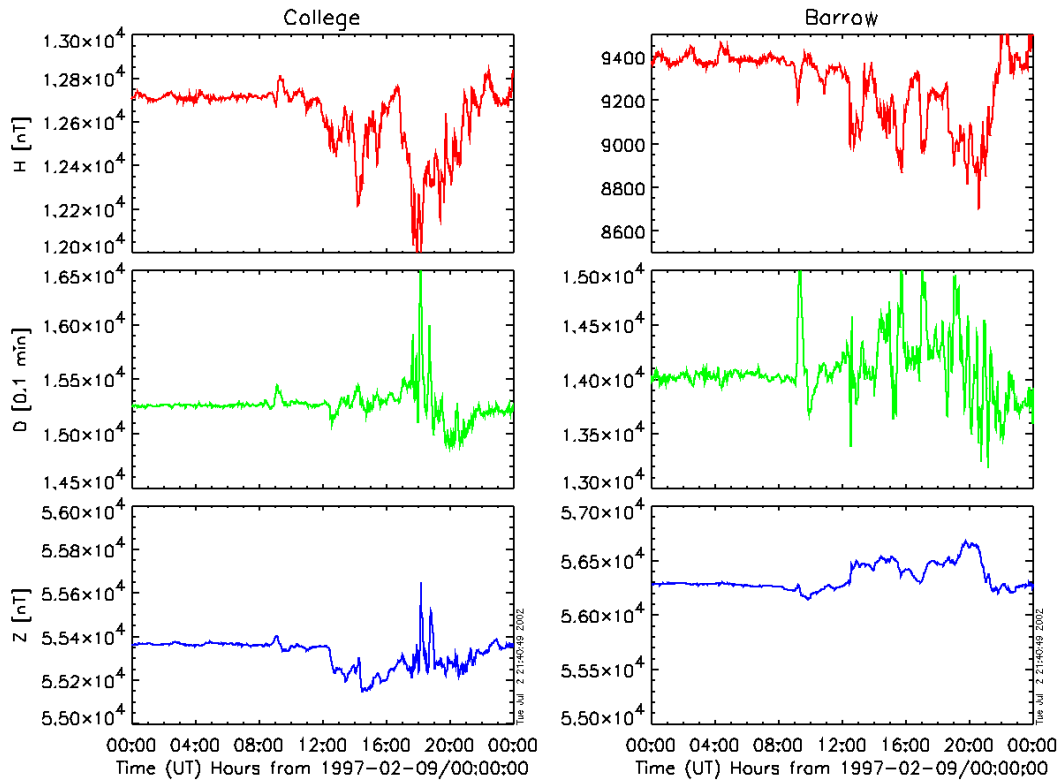


Figure 3.3: Ground magnetograms from College and Barrow. Data retrieved from Space Physics Interactive Data Resource, <http://spidr2.ips.gov.au/spidr>.

A strong westward electrojet progressively developed between College and Barrow, starting with  $\sim 9:00$  UT, as exhibited by the negative H component and by the change in the sign of the Z component from positive to negative.

We conclude that the data to be presented in the next two Sections were collected during the growth phase of a substorm, as seen both in the AE index and in the ground magnetograms.

### 3.2 FAST data

The satellite measurements are introduced according to a scale hierarchy. Large, medium, and small scale structures can be seen in the data. To understand the small scale features, which is the main goal of FAST, one has first to understand the frame within which these features develop.

As a first step, large scale electric and magnetic field data are shown in Fig. 3.4. The electric field was integrated along the satellite path, to get the potential drop, which reveals the large scale behavior better than the electric field itself. The potential is shown in the upper panel of Fig. 3.4 and its evolution illustrates the features of the convection pattern. Until 8:20, close to the southern border of the oval (Fig. 3.2), the plasma co-rotates with the Earth and convects antisunward (evening sector), the electric field is southward, and the potential increases.

From 8:20 to 8:22, across a large fraction of the oval, plasma convects sunward, the electric field is northward, and the potential decreases. At 8:22, close to the polar cap border, the potential starts to grow again, in good agreement with the general trend of dawn–dusk electric field and antisunward plasma flow over the polar cap. From 8:26 on the potential is roughly constant, allowing for a south-westward plasma flow (if any).

The middle panel of Fig. 3.4 shows the three components of the perturbation magnetic field in the Satellite Associated System (SAS), oriented as follows: the  $z$  axis along the model magnetic field  $\mathbf{B}_0$ , the  $y$  axis roughly to the east, along  $\mathbf{B}_0 \times \mathbf{v}$  ( $\mathbf{v}$  the satellite velocity), and the  $x$  axis roughly to the north, completing the right-handed orthogonal set (the  $x$  axis has the direction of  $(\mathbf{B}_0 \times \mathbf{v}) \times \mathbf{B}_0$ ). The magnetic field components are labeled as “x”, “y” and “z”. During the inverted-V event the SAS is practically identical with the Mean Field Aligned (MFA) system (Lühr et al., 1994). The MFA system has its  $z$  axis along  $\mathbf{B}_0$ , the  $y$  axis points eastward, perpendicular to the magnetic meridian, and the  $x$  axis completes the right-handed set, pointing predominantly northward. In general, MFA and SAS differ by a rotation around  $z$ .

At not too high altitudes ( $\lesssim 4 - 5R_E$ ) the magnetic field of the Earth is, to a good approximation, dipolar, with  $(82.7^\circ\text{LAT}, -92.0^\circ\text{LONG})$  and  $(-75.3^\circ\text{LAT}, 118.6^\circ\text{LONG})$  the coordinates of the magnetic South and North pole respectively (the magnetic poles are reversed as compared to the geographic ones). The poles are not symmetric because the best fit to the Earth’s magnetic field is obtained with an eccentric dipole ( $\sim 400\text{km}$  from the center of the Earth). The field lines that reach the Earth at high magnetic latitudes extend to large equatorial distances ( $> 10R_E$ ) and cease to be dipolar, due to the magnetic field produced by magnetospheric currents. The field lines can still be organized in  $L$ -shells of equal *invariant latitude*, ILAT. In the case of an ideal dipole field the intersection of the  $L$ -shell with the equatorial plane is a circle of radius  $r_{eq} = LR_E$  and  $\cos^2 \text{ILAT} = R_E/r_{eq} = 1/L$ . For the definition of the  $L$ -shell in a field which is not rigorously dipolar the reader is referred to McIlwain (1961). Using the concept of  $L$ -shell the MFA system is defined by the conditions that the  $z$  axis is parallel to  $\mathbf{B}_0$  and the  $y$ - $z$  plane is tangent to the  $L$ -shell.

The perturbation magnetic field measured by FAST exhibits the typical signature of double field-aligned current sheet, with downward current flowing at the south and upward current flowing at the north (Iijima and Potemra, 1978). The association of the double current sheet with the two convection reversals, visible in Fig. 3.4, is a consequence of processes that take place in the source region of the FACs, in the equatorial magnetosphere (e.g. Haerendel, 1990). A key feature of the data refers to the location of the convection reversal very close north of the boundary between the downward and upward FAC sheets. This leads to a quite special configuration of the 3D current flow, that will be explored in detail in Section 6.6.

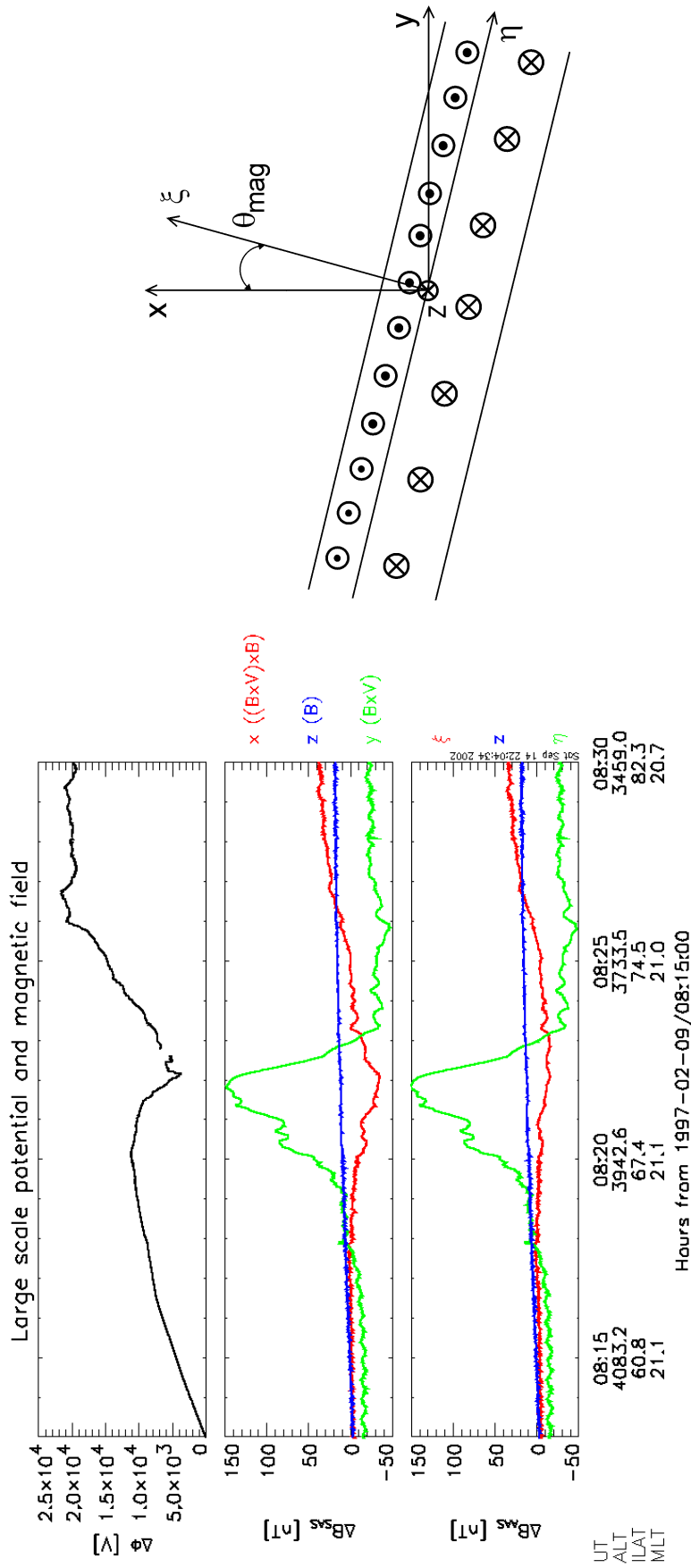


Figure 3.4: **Left:** Upper panel: large scale convection potential. There is a 10 second data gap at 8:22:37–8:22:47. For details on matching the potential after the data gap see p. 30. Middle panel: perturbation magnetic field in the Satellite Associated System (SAS). Lower panel: perturbation magnetic field in the Arc Associated System (AAS). For the labeling of the components and the definitions of the SAS and AAS see text. **Right:** Cartoon showing the orientation of the current sheets with respect to the SAS and AAS.

One can notice a small rotation,  $\theta_{mag} \simeq 8^\circ$  (calculation based on variance analysis, see Section 6.4.4 and Appendix G), between the satellite trajectory and the normal to the FAC sheets: the largest variation is in the “y” component, but there is some variation in the “x” component as well. This pattern is the result of a small clockwise rotation of the current sheets, as seen from above. The cartoon at the right of Fig. 3.4 shows the orientation of the current sheets with respect to the SAS, at FAST altitude. The  $(\xi, \eta)$  coordinates are associated with the current sheets and with the arc, and we shall accordingly call  $(\xi, \eta, z)$  the Arc Associated System (AAS). The cartoon also shows that the downward current is broader and, on average, less intense.

The lower panel in the left plot of Fig. 3.4 shows the AAS components of the magnetic field. As expected, the variation in  $B_\xi$  is smaller than the variation in  $B_x$ ; still,  $B_\xi \neq 0$ , which implies the variation of  $\theta_{mag}$  (stronger supported by the optical data, Fig 3.12) and/or an eccentric traversal of the current sheet. The variation of  $\theta_{mag}$  for the upward FAC will be further explored in Section 6.4.4.  $B_\eta$  is almost identical to  $B_y$  because  $\theta_{mag}$  is quite small.

There is also a small difference between the orientation of the upward current sheet and of the visible arc, as indicated by the magnetic and optical data, because the magnetic field of the Earth deviates from an ideal dipole. Strictly speaking, the AAS is not associated with the arc but with the FAC sheet at FAST altitude.

The medium scale, comparable to the transverse size of the oval, is dominated by downward and upward current signatures. They are visible not only in the magnetic field but also in the particle data, as seen in Fig. 3.5. The first panel shows again the magnetic field, for easy comparison with the particle data. The next four panels show electron data: energy spectrograms for downward (loss-cone), perpendicular (mirror) and upward (source-cone) electrons, as well as pitch-angle spectrogram. The presence of upward narrow bursts of medium energy electrons (up to  $\sim 1\text{keV}$ , panels 4 and 5) is the most prominent feature of the downward current region (Carlson et al., 1998b). During the satellite pass through the upward current region the electrons show a large inverted-V signature, relatively isotropic outside of the source-cone (panels 2, 3, and 5). Note that in the pitch-angle spectrogram the y axis extends from  $-90^\circ$  to  $270^\circ$ , corresponding to the  $360^\circ$  FoV of the plasma experiment. The angle range is shifted by  $90^\circ$ , to avoid having downward electrons split up among the upper and the lower borders of the plot. For a discussion of the electron velocity space, in the presence of a parallel electric field extending both above and below the satellite, the reader is referred to Section 4.3.1.

The last panel of Fig. 3.5 shows again the electric potential, to compare it with the ion energy and pitch-angle spectrograms in panels 6 and 7. As mentioned above, until 8:22:04 the potential decreases, corresponding to northward electric field and sunward convection. The ions

show mirroring plasma sheet distribution, both in the energy and in the pitch-angle spectrograms: the green area at the upper left half of panel 6 and the empty source-cone in panel 7. North of 8:22:04, which can be identified as the time of the convection reversal, the dominant ion feature is the sequence of beams and conics of ionospheric origin.

It is clearly visible that the beams are associated with holes under the inverted-V (panel 2) and with dips in the potential, consistent with the expectations implied by the “U” potential model. As long as the satellite is below the AAR, medium energy, backscattered, and secondary electrons (resulting from the interaction of the primary magnetospheric flux with the atmosphere), can reach the satellite either from below, or from above, after being reflected by the potential structure. When the satellite crosses the AAR the medium energy electrons are reflected down at lower altitudes, which explains the association of holes in the electron spectra with ion beams. The dips in the potential are an immediate consequence of the “U” shape of the AAR (Fig. 1.2).

The gap in the potential between 8:22:37 and 8:22:47 is due to bad quality electric field data, probably caused by the sensors’ saturation in low density plasma. The potential drop over the ion beam period,  $IALL = 8:22:03.8-8:22:57.5$ , was estimated at  $2000V \lesssim \Delta\Phi_{IALL} \lesssim 2250V$ , which implies a potential drop over the data gap  $1000V \lesssim \Delta\Phi_{gap} \lesssim 1250V$ . The calculation of  $\Delta\Phi_{IALL}$  is based on the fact that, outside of the ion beams, the magnetic field lines are equipotentials. The ionospheric potential drop can be determined on sub-intervals of IALL where data are available, yielding reasonable limits for the average ionospheric electric field,  $E_{\theta_x}$ , during the data gap. More details are given in Section 6.1.1.

AC electric and magnetic field data are presented in Fig. 3.6, in order to complete the view over a typical auroral event. The first six panels show electric field (panels 1–3) and magnetic field (panels 4–6) spectrograms in the HF ( $\sim 10\text{kHz}$  to  $2\text{MHz}$ ), VLF ( $2\text{kHz}$  to  $16\text{kHz}$ ), and ELF (DC to  $2\text{kHz}$ ) ranges. The electron cyclotron and proton cyclotron frequencies are overlaid in the HF and ELF panels, respectively. One recognizes the signature of the auroral kilometric radiation (AKR) in the HF panels. Broadband VLF electromagnetic emission is coincident with the more energetic part of the inverted-V electron distribution (compare with panel 2 in Fig. 3.5). The relationship between the ELF waves and the ion beams will be discussed later (p. 38).

The last three panels in Fig. 3.6 show the electric and magnetic energy densities,  $\frac{1}{2}\epsilon_0 E^2$  and  $\frac{1}{2}B^2/\mu_0$ , stored by the wave fields in the HF, VLF, and ELF frequency ranges. The high frequency AKR is electromagnetic and carries comparable magnetic and electric energies. The difference visible in panel 7 of Fig. 3.6 is caused presumably by instrument calibration. At low frequency (panels 8 and 9) the waves are essentially electrostatic, except for some electromagnetic contribution at 8:22:10–8:22:30. A more detailed view over the electric field spectra in the ELF



range is given in the panels 8 and 10 of Fig. 3.7 (to be discussed next). Note that, as documented at [http://sprg.ssl.berkeley.edu/fast/scienceops/fast\\_sdt\\_help.html](http://sprg.ssl.berkeley.edu/fast/scienceops/fast_sdt_help.html), the ELF and VLF DSP data are also affected by calibration errors: a factor of  $\sim 500$  for the electric component and of  $\sim 1/3160$  for the magnetic component.

Going to smaller scales, Fig. 3.7 zooms on the upward current region, dominated by a large inverted-V (panel 1). The more energetic part of the inverted-V is associated with a broad visible arc (Figs. 3.10 and 3.12), whose southern border is located at the sharp increase in the electron energy ( $\sim 8:22:12$ ). A particular feature of this arc is its position north of the convection reversal (as one can see by comparing panels 2 and 8 in Fig. 3.5). It is possible that the arc extends to the polar cap, as described by e. g. Meng and Akasofu (1976).

The position of the arc north of the convection reversal raises the problem of current closure. One modeling assumption frequently made (e. g. Boström, 1974), which is supported to a good extent by experimental data (Sugiura et al., 1982; Sugiura, 1984), is that the FACs close in the ionosphere through Pedersen currents and the Hall current is divergence free. This is obviously not the case here. The detailed consideration of this question is deferred to Chapters 5 and 6.

The panels 2–10 in Fig. 3.7 illustrate the small scale structure of the upward current region, which is typical for the measurements made by FAST during the winter months at the beginning of 1997 (McFadden et al., 1999). The most prominent feature is the repeated encounter with ion beams (panels 2–6), suggesting an altitude variation of the lower boundary of the AAR. In panels 2 and 3 we show IESA pitch-angle and energy spectrograms, while panels 4–6 present ion composition measurements achieved by TEAMS. The spectrogram pixels are wider for TEAMS because of the lower time resolution (Section 2.1).

In our case the dominant component is  $H^+$ , consistent with the relatively quiet conditions during FAST overpass. At disturbed times, however, the beams can be dominated by  $O^+$  ions: they are energized at low altitudes, transverse to the magnetic field, by wave–particle interactions, and can then reach the bottom side of the AAR overcoming the gravitational bound. The transverse motion transforms into parallel motion with the altitude increase, due to the conservation of energy and of the first adiabatic invariant,  $mv_{\perp}^2/2B$ , in the quasi-dipolar magnetic field of the Earth.

The presence of ion beams is accompanied by large spikes in  $E_{\perp}$  (panel 7), the so-called *electrostatic shocks* (Mozer et al., 1977). They can be either paired, as for the first ion beam, or unpaired, as it looks to be the case with the second ion beam. However, one has to take precautions for the second ion beam, because of the data gap: quite likely the potential recovers to a high level, in agreement with the evolution of ion energy (see Fig. 3.9), which implies a strong southward field, i. e. a negative spike, at the northern border of the beam.

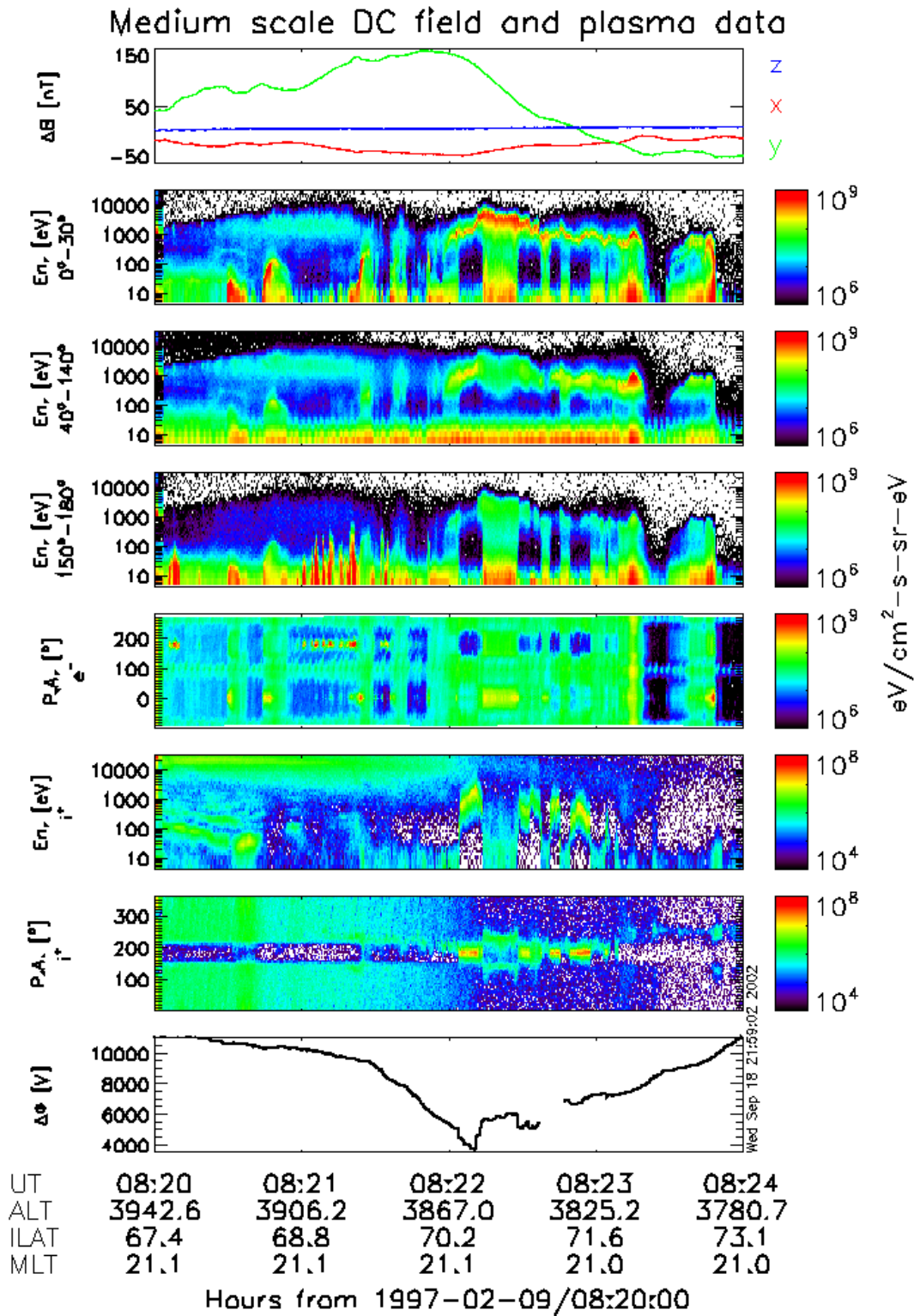


Figure 3.5: Medium scale DC electromagnetic field and particles. Panel 1: Perturbation magnetic field. Panels 2–4: Electron energy spectrograms for downward, transverse, and upward components. Panel 5: Electron pitch-angle spectrogram. Panels 6, 7: Ion energy and pitch-angle spectrograms. Panel 8: Electric potential; the data gap at 8:22:37–8:22:47 and the matching of the potential is discussed at p. 30.

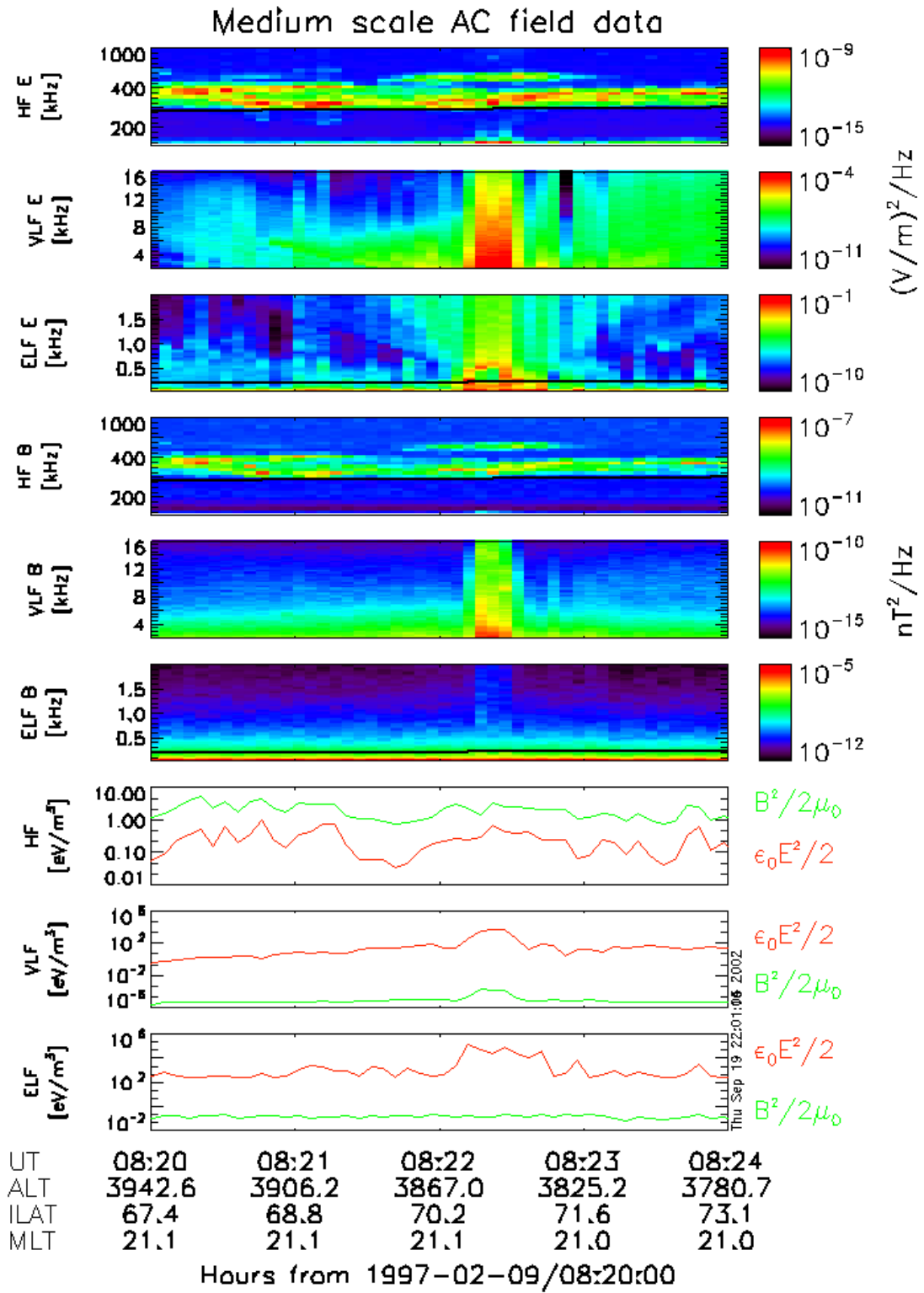


Figure 3.6: Medium scale AC electromagnetic field. Panels 1-3: Electric field spectra in the HF, VLF, and ELF ranges. The black lines overlaid in panels 1 and 3 show the electron cyclotron and proton cyclotron frequencies, respectively. Panels 4-6: Magnetic field spectra in the HF, VLF, and ELF ranges. Panels 7-9: Electric and magnetic energy density in the HF, VLF, and ELF ranges.

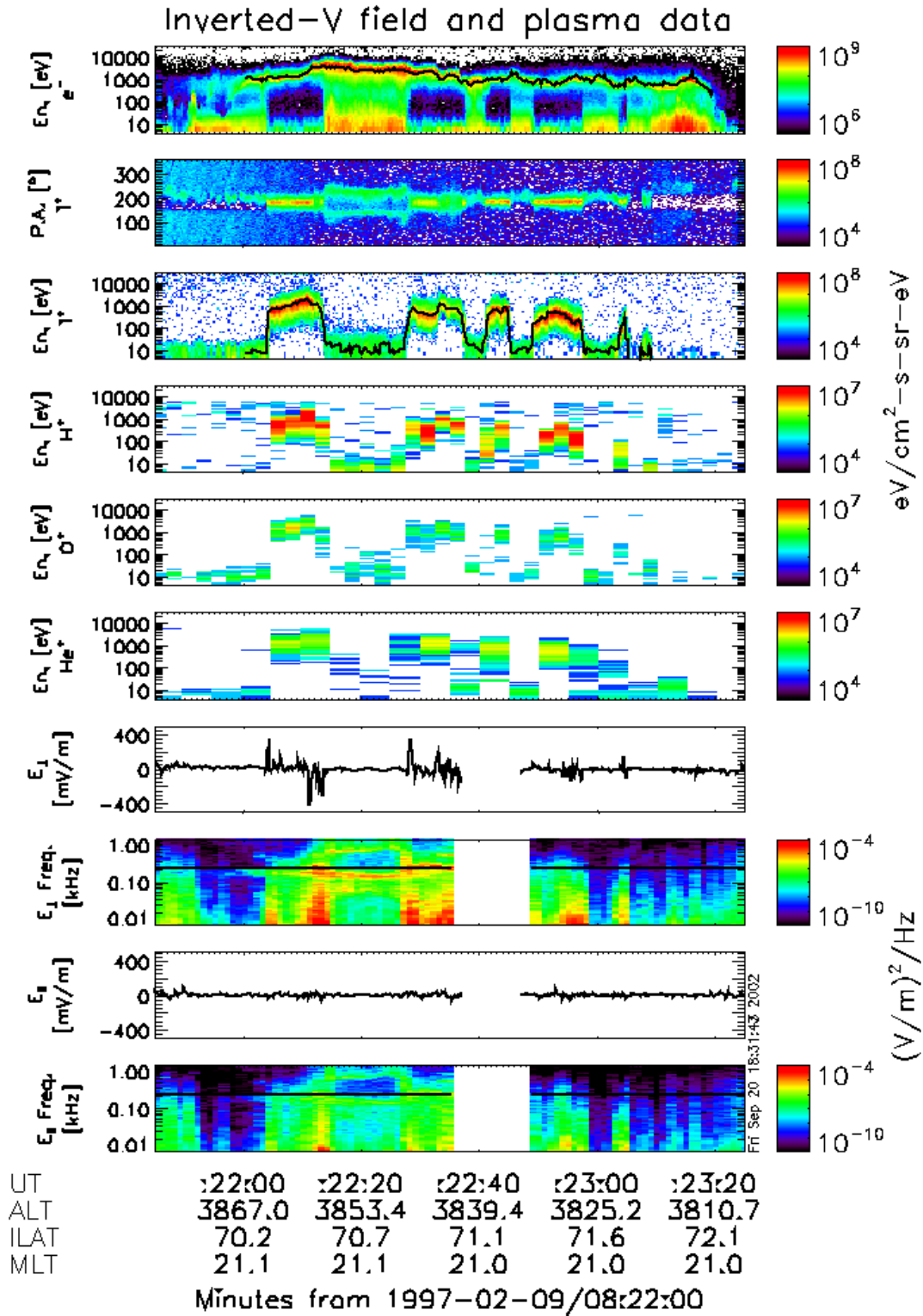


Figure 3.7: Inverted-V data. Panel 1: Downward electron energy spectrogram. Panel 2: Ion pitch-angle spectrogram. Panel 3: Upward ion energy spectrogram. Panels 4–6: Upward ion composition ( $H^+$ ,  $O^+$ ,  $He^+$ ) as measured by TEAMS. Panels 7, 9:  $E_{\parallel}$  and  $E_{\perp}$  filtered to 10Hz. Panels 8, 10: Spectra of  $E_{\parallel}$  and  $E_{\perp}$  (not filtered). The average electron and ion energy is overlaid in panels 1 and 3, respectively. The line in panels 8 and 10 show the proton cyclotron frequency.

The bipolar variation of the electric field is associated with the “U” geometry of the potential while the unipolar variation corresponds to the “S” geometry. When the bipolar variation is not balanced the resulting structure combines the two geometries, as illustrated by Figs.1.3 and 5.3.

The  $E_{\parallel}$  component of the electric field (panel 9) is seen to be about an order of magnitude smaller than  $E_{\perp}$  at times of electrostatic shocks. It is, however, quite difficult to precisely determine  $E_{\parallel}$ : the uncertainty, arising primarily from the inaccurate knowledge of the detector orientation, is comparable to or larger than the field itself.  $E_{\parallel}$  is rather a proxy for the error of the electric field measurement (R. Ergun, personal communication):

$$\sigma_E \approx \sqrt{\frac{\sum_{i=1}^N E_{\parallel i}^2}{N}} \quad (3.1)$$

Even if  $E_{\parallel}$  is large, comparable to  $E_{\perp}$  (not in our case), the validation of the measurement is not an easy task, because of the many potential error sources (e. g. Mozer and Kletzing, 1999).

Panels 8 and 10 in Fig. 3.7 show frequency spectra obtained by applying FFT to  $E_{\perp}$  and  $E_{\parallel}$ , respectively. The wave activity is mainly transverse to the magnetic field line. It consists of broadband extremely low frequency (BBELF) emissions, associated with ion beams, and electrostatic ion cyclotron (EIC) emissions near the proton cyclotron frequency, going along with both beams and conics. The energy exchange with waves contribute to the ion energy budget, in addition to the interaction with the AAR potential structure (see the discussion below).

High resolution particle measurements are illustrated with Burst data in Figs.3.8 and 3.9, showing the first two ion beam events. Each pixel in the particle spectrograms (downward electrons in panel 1 and upward ions in panel 2) represents 220m, if mapped at ionospheric level (p. 16). The transverse electric field and the high-altitude potential are shown in panels 3 and 4. Panel 5 compares the average ion energy, obtained as ratio of the energy flux to the number flux, with the field-aligned (FA) potential drop; the lower curve is the kinetic temperature. To obtain the FA potential drop we considered the ionospheric potential linearly variable across the beam and equal to the high-altitude potential at the beam boundaries. Accordingly:

$$\Delta\Phi_{\parallel} = \frac{x}{L}\Delta\Phi_{ionos} - \int_0^x -E_{\perp} ds = -\frac{x}{L} \int_0^L E_{\perp} ds + \int_0^x E_{\perp} ds \quad (3.2)$$

The calculation of  $\int_0^L E_{\perp} ds$  for the second ion beam cannot be rigorously performed because of the data gap. Details on the evaluation procedure are given in Section 6.1.1.

An obvious feature in Figs. 3.8 and 3.9 is the close agreement between the beam average energy and the electric potential, which supports the electrostatic model down to very small scales (McFadden et al., 1998). However, a closer inspection reveals discrepancies which are better visible for the second beam but can be noticed for the first beam as well. Even if most of the time

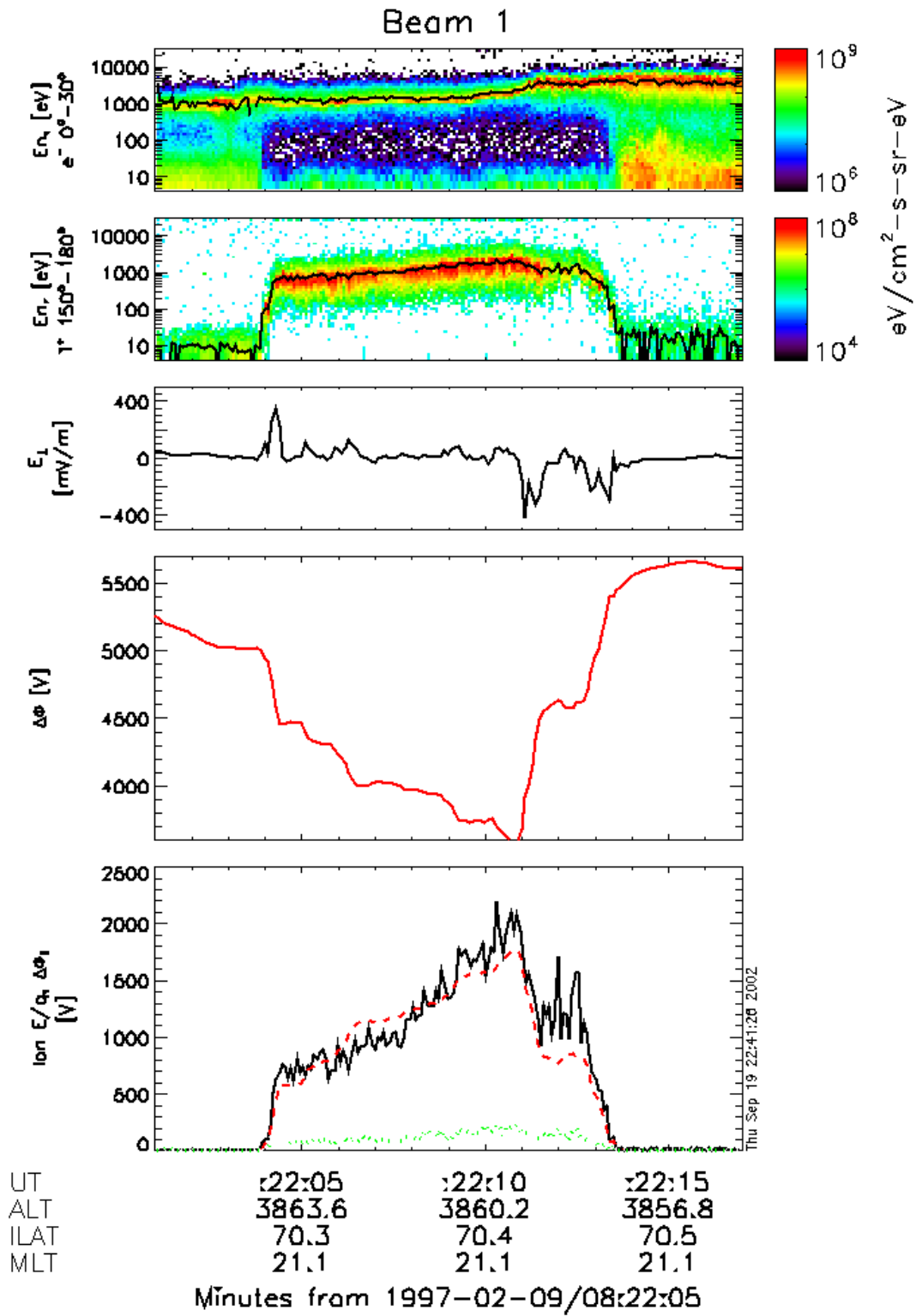


Figure 3.8: First beam event. Panels 1, 2: Downward electron and upward ion spectrograms. Panel 3: Transverse electric field. Panel 4: Electric potential. Panel 5: Ion average energy (black solid line), FA potential (red dashed line), and kinetic temperature (green dotted line).

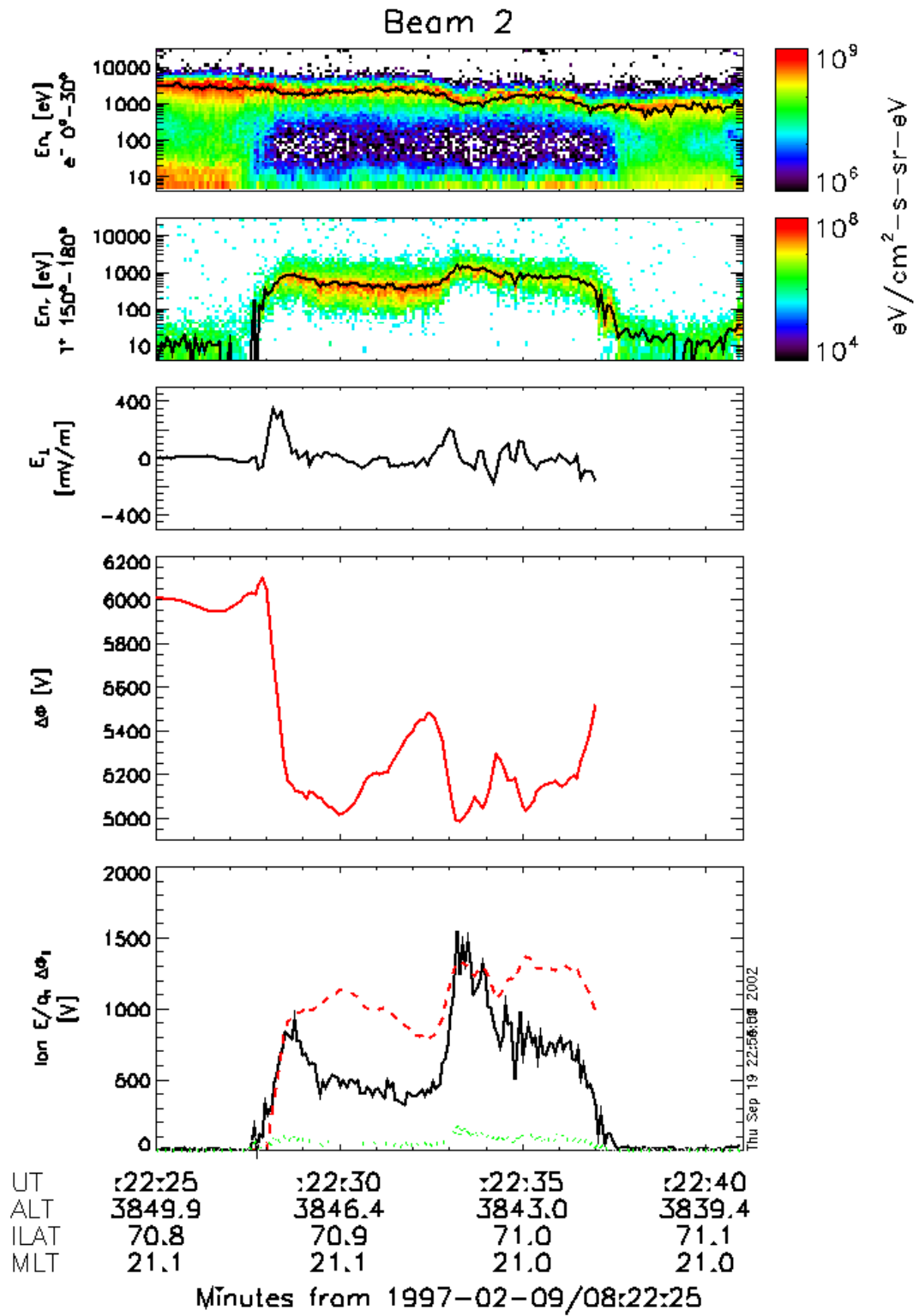


Figure 3.9: Second beam event. Same as Fig. 3.8.

the ion energy and the potential vary at the same pace, there are also times when the ion energy grows either slower or faster than the potential. In the first group we could pick up the intervals 8:22:06–8:22:06.5 and 8:22:29–8:22:30 (here the potential increases while the energy decreases) whereas in the second group we have 8:22:08–8:22:10 and, most striking, 8:22:32.9–8:22:33.1.

A detailed investigation of the origin of these discrepancies is beyond the scope of this work. We shall mention, however, some possible mechanisms leading to differences in the variation rate of the potential and of the beam energy:

- The ionospheric potential does not have a linear variation, i. e. the N–S electric field is not constant. This should not be very surprising, considering the fact that a 10s ion beam covers  $\sim 28$ km at ionospheric level, whereas the ionospheric Debye length and ion gyroradii are in the centimeter and meter ranges, respectively. However, as we will show in Chapter 6, the ionospheric electric field does not have large variations (at least for the data presented here) and the ionospheric potential does not deviate too much from a linear evolution. One cannot expect the non-linearity of the ionospheric potential to explain big disagreements between FA potential and ion energy.
- There are non-electrostatic mechanisms contributing to ion energization. It is a well known fact that ions get not only parallel energy, from the FA potential, but also transverse energy, by interacting with various wave modes (e. g. André et al., 1998; Lund et al., 1999). The transverse energy pumped by the waves can vary at a higher or slower rate, as compared to the field aligned potential; consequently, the variation of the total ion energy will not follow the variation of the potential. A good proxy for the non-electrostatic energization is the kinetic temperature: the ion temperature in the ionosphere is less than 0.2eV, whereas the ion beam temperature is typically in the 0.1–1keV range. It is more difficult to explain such a temperature increase by invoking only electrostatic interactions (although such model exists, e. g. Borovsky (1984)) and the simultaneous measurements of wave activity on auroral field lines suggests the wave–particle interactions to be the main cause. Nevertheless, for the two beam events discussed here the kinetic temperature is pretty low as compared to the average ion energy ( $\lesssim 10\%$ ) and can only explain small differences between beam energy and FA potential.
- Non-electrostatic interactions between ions and the electromagnetic field can originate in the development of anomalous resistivity. This happens, for example, when the FAC density overcomes a critical value,  $j_c$ . Plasma becomes unstable and the excited wave mode (e.g. ion cyclotron or ion acoustic) can generate anomalous resistivity through non-linear saturation.



In such a case the ion energy would increase slower than the potential, or even decrease when the potential increases. Our data show potential increase and ion energy decrease at 8:22:29–8:22:30, coincident with intense BBELF and EIC wave activity (panel 8 of Fig.3.7).

- It is also possible that the electric field is actually not electrostatic and the time variations are important. One can still try to preserve the electrostatic model by associating the time variations with motions of the potential structure along the field line (e. g. McFadden et al., 1998). A downward motion would lead to a variation in the beam energy higher than the variation in the potential (e. g. 8:22:32.9–8:22:33.1).

### 3.3 Optical data

Ground optical data enlarge the satellite perspective over the auroral phenomena. Whereas the satellite payload can measure in detail plasma and field parameters along the track, ground images give a better description of the aurora development, both in space and in time.

We focus further on images taken on February 9, 1997, during the interval UT 8:19–9:14. The conjunction with FAST did only last 2:20 minutes, between 8:21:00 and 8:23:20. However, inspection of the longer period of optical data provides the context for the shorter conjunction time. A sequence of 9 frames, 1 minute apart, centered on the conjunction interval, is shown in Fig. 3.10. Visual evaluation suggests that 1 minute is a reasonable time-scale for the change of the auroral display. The frames are sequentially numbered in the upper right corner. One can also read, in the upper left corner, the exposure time. As mentioned in Section 2.3 the exposure time can be varied. In particular, “00” means 40 ms and “-01” means 20 ms. Note that the exposure time doubles for the last frame.

For the time period when FAST crossed the camera’s FoV (frames 4,5,6) we indicated the satellite’s footprint at ionospheric level (110km). The instantaneous satellite position is shown as a square (see Appendix B for a brief description of the mapping procedure). One can check that the FAST footprint is at the right place by comparing the brightness profile along the satellite path with the electron energy flux derived from EESA data (Fig. 3.11, relative units). The two curves reach their maxima at about the same time, with a small separation  $\Delta t \approx 3s$ , the energy flux maximum coming first.  $\Delta t \neq 0$  could result from mapping the satellite position to a lower altitude, as compared to that of the light emission. In such a situation the corresponding elevation angle would be smaller than its real value and the image pixel associated with the maximum energy flux would be too far south, resulting in a smaller brightness than the real one.

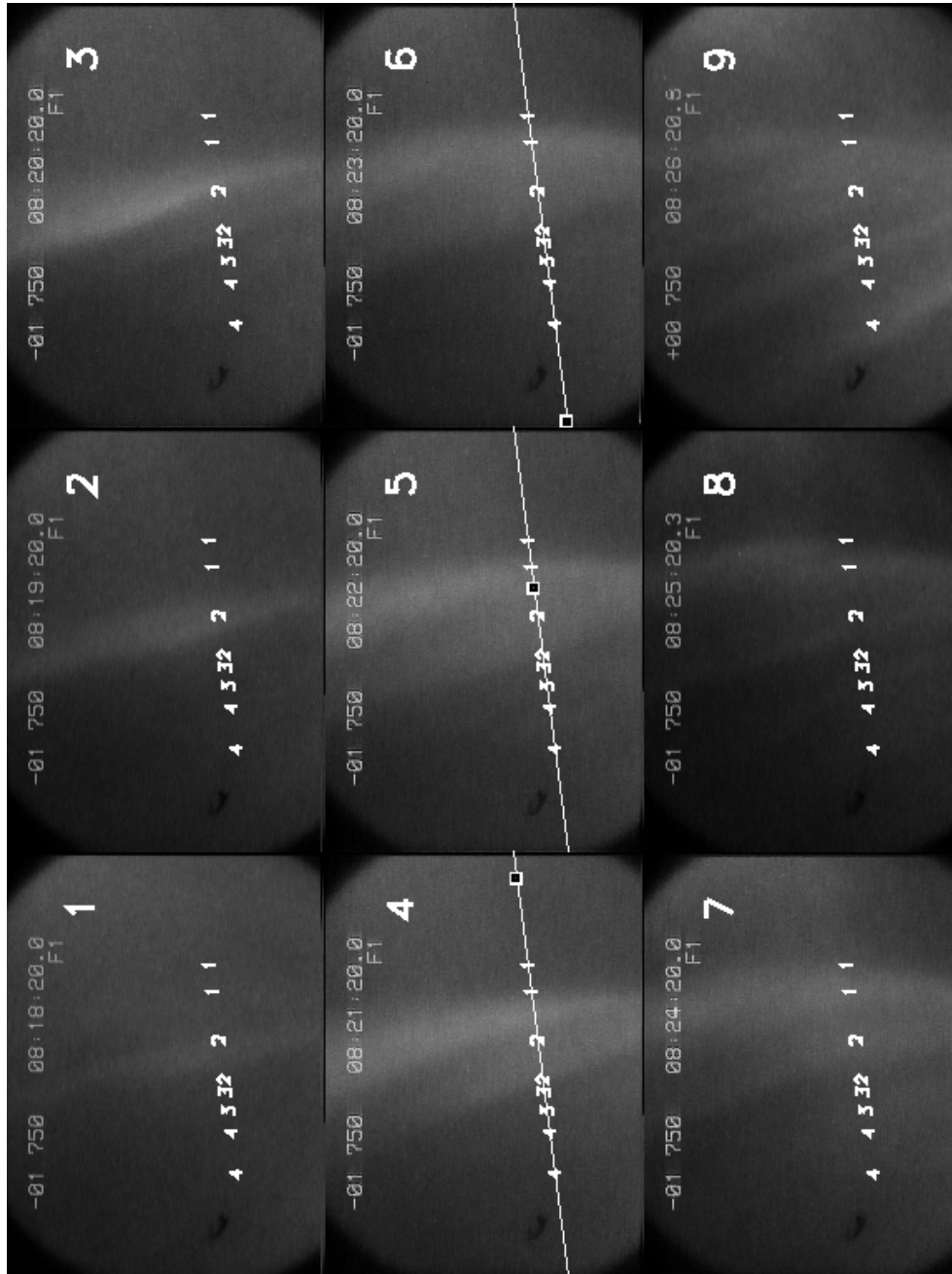


Figure 3.10: Selection of auroral images, 1 minute apart, taken on February 9, 1997, UT 8:18–8:26. The North and East directions point roughly to the left and to the bottom, respectively. For better identification the frames are numbered sequentially. FAST crosses the camera's FoV in the frames 4,5,6. For these frames the projection of the trajectory is indicated and the satellite's ionospheric footprint is shown as a square. The limits of the ion beams detected by FAST are overlaid in all the frames (see text).

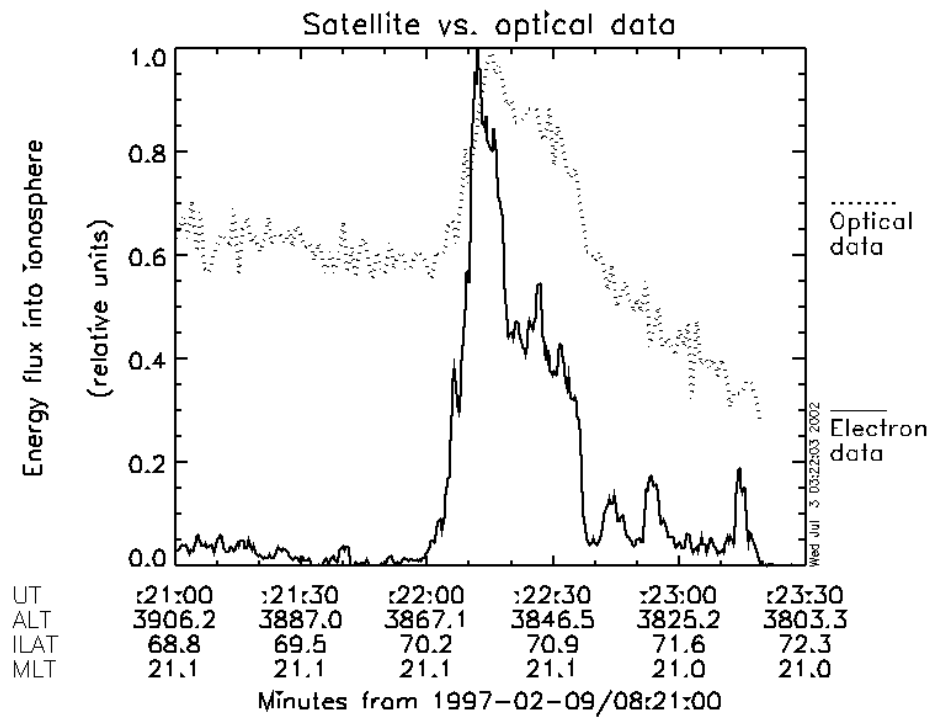


Figure 3.11: The energy flux resulting from optical data compared to the energy flux resulting from particle data. The fluxes are represented in relative units, scaled to the maximum value.

The large difference between brightness and electron energy flux in Fig. 3.11 (except for the position of the maxima) is probably related to a layer of background luminosity which decreases toward north. This view is supported by the higher value of this presumed background south of the arc, in a region of diffuse aurora. However, a direct comparison between the electron and the optical data is difficult, because of the difference between the elevation of the magnetic zenith,  $\alpha_M = 80^\circ$ , and of the ionospheric footprint of FAST,  $\alpha_F \leq 45^\circ$  (the elevation increases from  $31^\circ$  at 8:22 to  $45^\circ$  at 8:23 and then decreases to  $27^\circ$  at 8:24).

In each frame of Fig. 3.10 the ion beams' boundaries, as read in IESA data (Section 3.2), are identified with pairs of numbers between 1 and 4. Note that the satellite actually encounters ion beams between 8:22:04 and 8:22:57. Marking all the frames does not imply that ion beams are necessarily there and is just meant to provide a reference for the evolution of luminosity. Although there is no direct connection between auroral light and ion beams, the observational evidence supports the association of ion beams at lower altitudes with the development of visible arcs (Marghitu et al., 2001).

On the longer time scale of the optical observation one can see that the more energetic part of the inverted-V is relatively stable, denoting an equilibrium state along the respective flux tubes. On the other hand small enhancements in the energy flux (at  $\sim 8:22:42$  and  $\sim 8:22:52$ ) develop into

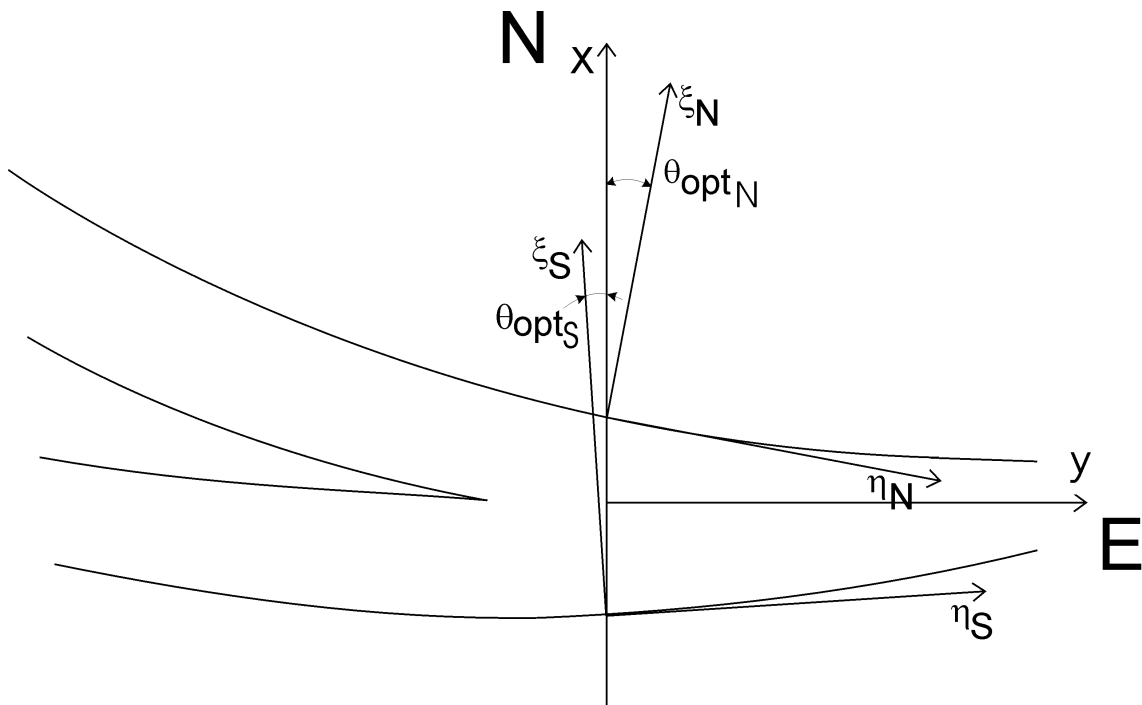
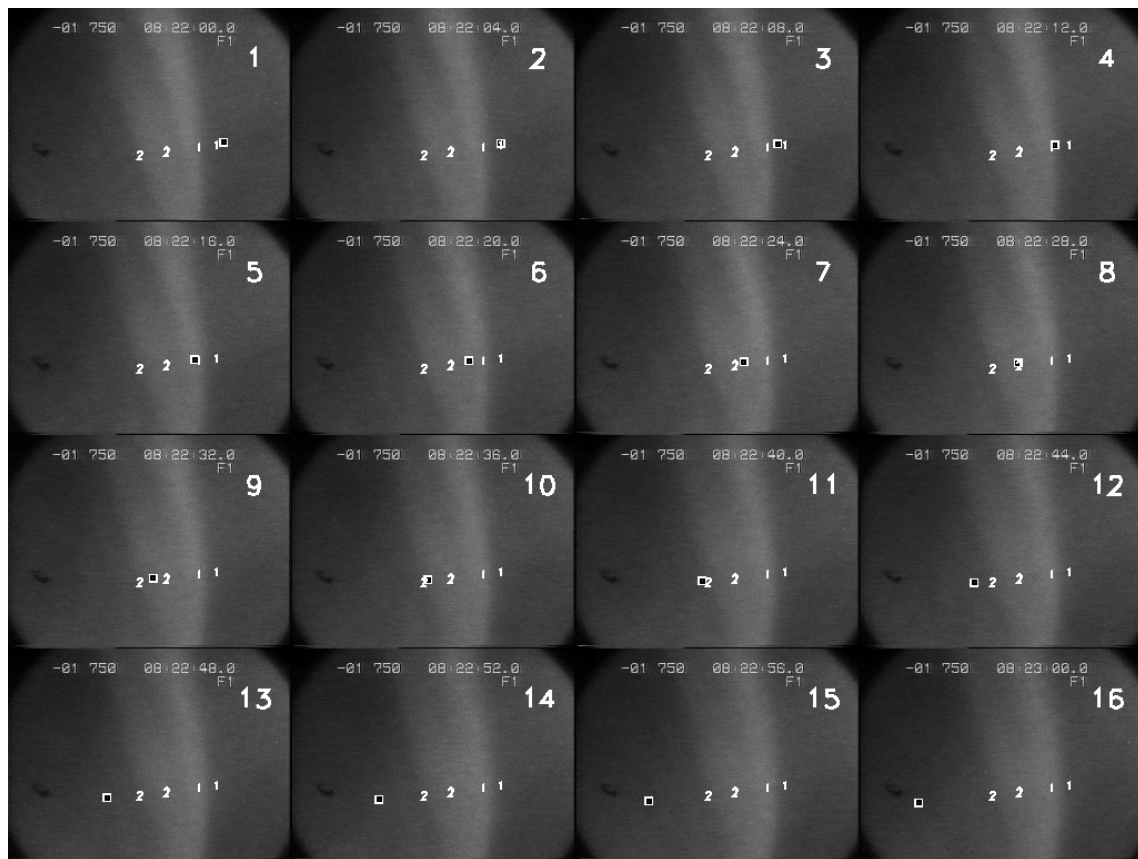


Figure 3.12: **Top:** Optical images 4s apart taken during the FAST overpass. The satellite is figured as a square and the limits of the first two ion beams are shown in each figure as '11' and '22'. North is at the left and East at the bottom, similar to Fig. 3.10. **Bottom:** Outline of the arc geometry with North at the top and East at the right. The reference systems associated with the southern and northern boundaries of the arc, at the points of intersection with the trajectory of FAST, are also shown.

visible arcs, consistent with a positive feedback mechanism (Sato, 1978). A peculiar feature is the association of ion beams (3–3 and 4–4 in Fig. 3.10) with these energy flux enhancements, and further with the visible arcs. This association supports recent simulation work by Ergun et al. (2000), who found that the altitude of the bottom side of the AAR is determined by the balance between backscattered and secondary electrons, and ionospheric ions. An increase in the energy flux results in a larger backscattered and secondary flux, which leads to the lowering of the bottom side of the AAR.

The optical behavior of the arc during the minute 8:22:00–8:23:00 is detailed in Fig. 3.12. At the top side is given a sequence of 16 frames, 4 seconds apart, each of them bearing markers for the satellite footprint and for the first two ion beams. One can easily notice the stability of the arc during the satellite overpass. The cartoon at the bottom side outlines the arc geometry. The plot gives the correct arc orientation, with North at the top and East at the right (the camera inverts East and West because of the optical system). The reference systems  $(\xi_S, \eta_S)$  and  $(\xi_N, \eta_N)$  are associated with the arc boundaries at the points of intersection with FAST trajectory. A careful inspection of the images provides useful information for the following Chapters:

- By comparing the position of the southern edge of the arc with the position of the first ion beam one can see that the arc has a slow, approximately uniform equatorward motion. The arc covers a distance roughly equal to the width of the beam in two minutes (frames 4 to 6 in Fig. 3.10) and half of this distance in one minute (first to last frame in Fig. 3.12). The beam width is  $5.6\text{km/s} \times 10\text{s} = 56\text{km}$  at FAST altitude, which maps to  $28\text{km}$  at ionospheric level. The resulting average arc velocity is  $\sim 200\text{m/s}$ . A slow equatorward motion is often observed during the growth phase of a substorm (e. g. Mozer, 1971).
- If the arc is frozen in the ionospheric plasma (possible deviations from this assumption are discussed in Section 6.5.2) its motion follows the plasma  $\mathbf{E} \times \mathbf{B}$  drift; the associated electric field points westward and has a magnitude  $E = |\mathbf{v} \times \mathbf{B}| \approx 10\text{mV/m}$ . A westward electric field drives a northward Hall current, that contributes to the ionospheric closure of the FAC.
- The arc is not straight and its borders are not parallel. The angle between FAST trajectory and the normal to the arc varies slightly across the arc (Fig. 3.12): at the southern border of the arc  $\theta_{opt_S} \lesssim 0$ , whereas at the northern border  $\theta_{opt_N} > 0$ . The frames in Fig. 3.12 show that the width of the arc decreases from top to bottom (West to East). This geometry suggests a coupling between the currents flowing transverse to the arc and the currents flowing along the arc, that is between the FAC system and the electrojet.

### 3.4 Summary

We presented ground magnetic data, in-situ measurements, and optical images, corresponding to FAST orbit 1859, from February 9, 1997. The information can be summarized as follows:

- The data were collected during the growth phase of a small substorm, in the most quiet period ( $K_p=2$ ) of a disturbed interval ( $K_p$  up to 6).
- An auroral arc  $\sim 70\text{km}$  wide is seen in the images. FAST data shows that the arc is situated north of the convection reversal and is associated with an upward Birkeland current sheet, carried by inverted-V electrons with energies up to  $\sim 5\text{keV}$ . The convection reversal is quite close to the downward current sheet, which flows south of the arc.
- The inverted-V associated with the arc encompasses several ion beams. For two of them Burst data are available, which allow a detailed examination of the relation between ion energy and FA potential drop. The two quantities track each other quite well, except for short intervals of disagreement.
- The arc is slowly moving equatorward, with a velocity of  $\sim 200\text{m/s}$ , corresponding to a westward electric field of  $\sim 10\text{mV/m}$  (if the arc proper motion is negligible).
- Both the magnetic and optical data indicate a slight rotation of the arc with respect to the SAS y axis. In addition, the optical data show that the arc edges are not parallel and the width of the arc decreases from West to East.

## Chapter 4

# Ionospheric conductance

An essential ingredient in deriving the full picture of the ionospheric electrodynamics, for either large, medium, or small scale phenomena, is the conductivity. By integrating it with respect to height one obtains the conductance. Satellite measurements, like those presented in the previous Chapter, allow the monitoring of the particle influx into the ionosphere and the subsequent determination of the conductance.

We begin with an overview of basic facts related to the conductivity of an anisotropic magnetic plasma. Next, we discuss in more detail the particle induced conductivity, which plays the major role during the winter nighttime auroral oval. As an example we use Survey data collected during the inverted-V period of orbit 1859 (Fig. 3.7). A separate Section is devoted to the evaluation of the conductance when the satellite detects ion beams; we illustrate it with Burst data collected during the two beam events presented in Figs. 3.8 and 3.9. In the last Section we address the methodological and measurement errors involved in conductance calculation.

### 4.1 General considerations

The ionospheric plasma is influenced by the magnetic field of the Earth and is strongly anisotropic. Both electron and ion motion, parallel and perpendicular to the electric field, contribute to the current conduction. Their relative importance is determined by the relation between electron-neutral ( $\nu_{en}$ ) and ion-neutral ( $\nu_{in}$ ) collision frequencies in the (upper) atmosphere, and the respective gyrofrequencies ( $\omega_{ge,gi} = eB/m_{e,i}$ ). We concentrate here on the high-latitude auroral region, where the magnetic field can be approximated as perpendicular to the ionosphere (the actual angle is  $\sim 75^\circ$  at auroral latitudes). This Section is only intended to provide a brief overview. For reviews devoted to high-latitude conductances see e. g. Reiff (1984), Brekke and Moen (1993).

By writing the equation of motion for electrons and ions, with neglect of pressure gradients and gravity force, one comes to the following form of Ohm's law, appropriate for the ionospheric plasma (e. g. Kertz, 1971; Brekke et al., 1974; Baumjohann and Treumann, 1996):

$$\mathbf{j} = \sigma_{\parallel} \mathbf{E}'_{\parallel} + \sigma_P \mathbf{E}'_{\perp} + \sigma_H \mathbf{e}_B \times \mathbf{E}'_{\perp}, \quad \mathbf{e}_B = \mathbf{B}/B \quad (4.1)$$

where  $\sigma_{\parallel}$ ,  $\sigma_P$ ,  $\sigma_H$  are respectively the parallel, Pedersen, and Hall conductivity ( $\mathbf{j}_P = \sigma_P \mathbf{E}'_{\perp}$  and  $\mathbf{j}_H = \sigma_H (\mathbf{B} \times \mathbf{E}'_{\perp})/B$  are the Pedersen and Hall current):

$$\begin{aligned} \sigma_{\parallel} &= \frac{ne}{B} \left( \frac{1}{\nu_{en}/\omega_{ge}} + \frac{1}{\nu_{in}/\omega_{gi}} \right) \\ \sigma_P &= \frac{ne}{B} \left( \frac{\nu_{en}/\omega_{ge}}{1 + (\nu_{en}/\omega_{ge})^2} + \frac{\nu_{in}/\omega_{gi}}{1 + (\nu_{in}/\omega_{gi})^2} \right) \\ \sigma_H &= \frac{ne}{B} \left( \frac{1}{1 + (\nu_{en}/\omega_{ge})^2} + \frac{1}{1 + (\nu_{in}/\omega_{gi})^2} \right) \end{aligned} \quad (4.2)$$

In the above formulas  $e$  is the electron charge,  $n$  is the plasma density, and the rest of the symbols have already been defined. At the altitude of the current flow the main ion constituents are  $\text{O}_2^+$  and  $\text{NO}^+$ . The mass difference between the two molecular ions is small, and can be neglected as a first approximation. The ionosphere can be represented by only one ion species, with density  $n_i$ , that has to be equal to the electron density,  $n_e$ , in order to keep the plasma neutral:  $n_i = n_e = n$ .

Typical variations of the conductivities with altitude, corresponding to mid latitudes at day time, are shown in Fig. 4.1. The high latitude profiles have similar shapes, with  $\sigma_{H_{max}} > \sigma_{P_{max}}$  and  $h_H < h_P$ , but the specific numerical values can differ. Above  $\sim 75\text{km}$   $\sigma_{\parallel}$  grows rapidly and is usually taken as infinite, equivalent to saying that the magnetic field lines in the ionosphere are equipotentials;  $\sigma_P$  and  $\sigma_H$  have maxima at  $\sim 100\text{--}125\text{km}$  altitude and vanish above  $\sim 200\text{--}250\text{km}$ .

As one can see by examining Eqs. 4.2 the conductivities depend on the ratios  $\nu_{en}/\omega_{ge}$ ,  $\nu_{in}/\omega_{gi}$ , and on the plasma density,  $n$ . The profiles in Fig. 4.1 reflect these two influences:

- The ratios  $\nu_{en}/\omega_{ge}$  and  $\nu_{in}/\omega_{gi}$  decrease with altitude, because of the decrease in the respective collision frequencies, which in turn depend mainly on the density of the neutral atmosphere. The gyrofrequencies can be considered constant over the altitudinal range of the current carrying ionosphere. At  $\sim 75\text{km}$   $\nu_{en}/\omega_{ge} = 1$  while at  $\sim 125\text{km}$   $\nu_{in}/\omega_{gi} = 1$ . Below  $\sim 75\text{km}$  the motion of the charged particles is predominantly collisional, generating current along the direction of the electric field. Between  $\sim 75\text{km}$  and  $\sim 125\text{km}$  the electron motion is governed by the  $\mathbf{E} \times \mathbf{B}$  drift and contributes mainly to the Hall current, while the ion motion is dominated by collisions, contributing mainly to the Pedersen current. Above  $\sim 125\text{km}$  the ion motion becomes also controlled by the magnetic field and the associated



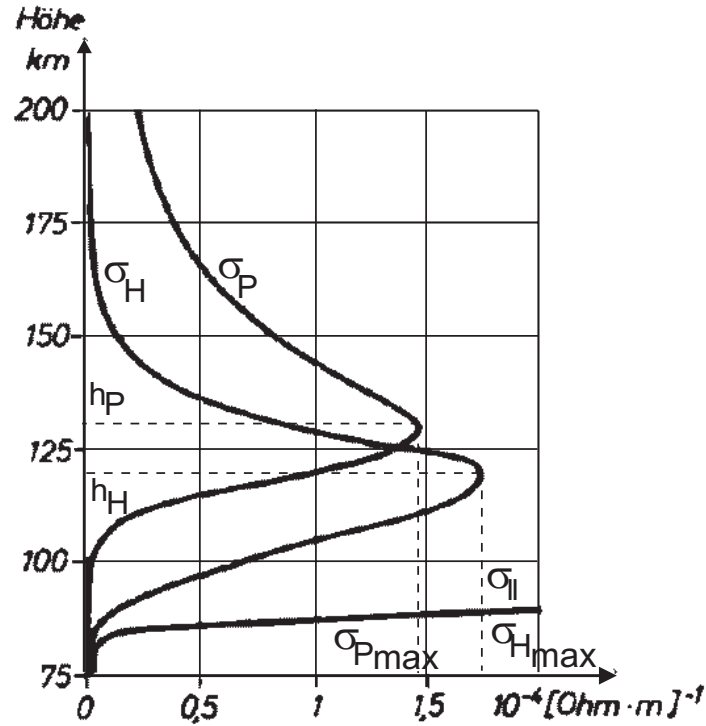


Figure 4.1: Variation of the conductivities with altitude. The profiles illustrate day time values at medium latitudes, with the conductivities produced by solar radiation. At high latitudes, where particle precipitation becomes important, the maxima,  $\sigma_{Pmax}$  and  $\sigma_{Hmax}$ , as well as their respective altitudes,  $h_P$  and  $h_H$ , can differ. Nevertheless, the relationships  $\sigma_{Hmax} > \sigma_{Pmax}$  and  $h_H < h_P$  remain valid. Adapted from Kertz (1971), Fig. 89.

current is opposite to the electron Hall current. From  $\sim 200$ – $250$  km up the plasma convects as a whole and the perpendicular current vanishes. The convection electric field reflects the balance between magnetospheric driving forces and ionospheric collisional drag forces.

- The plasma density,  $n$ , behaves as a weighting factor in Eqs. 4.2. In the  $D$  layer, below  $\sim 85$ – $90$  km,  $n$  is small and the contribution to current conduction is not significant.  $n$  comes to a maximum,  $n_{max}$ , in the  $E$  layer, at  $h_{nmax} \simeq 110$  km. In the case of particle induced conductivity  $n_{max}$  and  $h_{nmax}$  depend on the particle energy flux and on its spectral distribution. The plasma density increases again in the  $F$  layer, at  $\sim 150$ – $200$  km, but the bracketed terms in the expressions of  $\sigma_P$  and  $\sigma_H$  (Eqs. 4.2) take small values and the resulting (transverse) conductivities are small as well.

In Eq. 4.1  $\mathbf{E}'$  is the electric field in the reference system of the neutral atmosphere:  $\mathbf{E}' = \mathbf{E} + \mathbf{u} \times \mathbf{B}$ , where  $\mathbf{u}$  is the neutral wind velocity. For the following we disregard the potential influence of the neutral wind and consider  $\mathbf{E}' \equiv \mathbf{E}$ . This approximation is supported by the fact that  $E$  region neutral winds during reasonably quiet periods have typical velocities  $\lesssim 100$  m/s, which imply electric fields  $\lesssim 5$  mV/m (e. g. Brekke et al., 1973). Note that the neutral winds show a

strong height variation and can reach several 100m/s in the  $F$  region; however, as discussed above, the transverse current flowing in the  $F$  region is small and disregarding the  $F$  region neutral winds has little influence on the current closure. Neutral winds velocities as high as several 100m/s were also measured, at times, in the  $E$  region (e. g. Comfort et al., 1976), so that neglecting the  $E$  region neutral winds can be a serious source of errors. Nevertheless, since we have no information on these winds, we cannot take them into account.

The ionospheric perpendicular conductivities are significant in a very thin layer, when compared to the magnetospheric dimensions. The magnetic field (and the distance between magnetic field lines) can be considered as constant within this range. As the field lines are equipotentials the electric field is constant as well and the perpendicular part of equation 4.1 can be integrated with respect to altitude:

$$\mathbf{J}_\perp = \Sigma_P \mathbf{E}_\perp + \Sigma_H \mathbf{e}_B \times \mathbf{E}_\perp \quad (4.3)$$

where

$$\Sigma_P = \int \sigma_P dz, \quad \Sigma_H = \int \sigma_H dz$$

are the height-integrated Pedersen and Hall conductivities, or conductances. The most dynamic factor in causing variations of the conductances is the plasma density. The gyrofrequencies,  $\omega_{e,i}$ , are practically constant, both in space (over the height of the current carrying layer) and in time, while the neutral atmosphere, which determines the collision frequencies,  $\nu_{e,i}$ , was shown to have a reduced dynamic influence. Evans et al. (1977) found that the neutral atmosphere model considerably influences the altitude dependence of the conductivities, but drives just minor changes in the conductances.

The behavior of  $n$  is governed by the continuity equation (e. g. Atkinson, 1970):

$$\partial n / \partial t + \nabla \cdot (n \mathbf{v}) = q - \alpha (n^2 - n_0^2) \quad (4.4)$$

where  $\mathbf{v}$  is the plasma convection velocity,  $q$  is a source term,  $\alpha$  is the recombination coefficient, and  $n_0$  stands for the background ionization. The terms of Eq. 4.4 can be explained as follows:

- The second term on the l.h.s. can be approximated by considering the ionospheric plasma as incompressible and by replacing  $\mathbf{v}$  with the  $\mathbf{E} \times \mathbf{B}$  drift velocity. One obtains:

$$\nabla \cdot (n \mathbf{v}) = \frac{\mathbf{E} \times \mathbf{B}}{B^2} \cdot \nabla n \quad (4.5)$$

which represents ionization convected by plasma motion, e. g. from the dayside to the nightside. During precipitation events in the winter auroral region this contribution can be neglected, as long as the induced ionization is high.

- The first term on the r.h.s. stands for ionization production, which arises from two main contributions: the solar radiation and, in the high-latitude region, the particle precipitation. In the winter nighttime auroral region the contribution of the solar radiation is negligible (for ionization produced by solar radiation see Brekke and Moen (1993) and references therein).
- The second term on the r.h.s. represents ionization loss which, at  $E$  region altitudes, is mainly due to dissociative recombination (Kelley, 1989):  $O_2^+ + e^- \rightarrow O + O$ , and  $NO^+ + e^- \rightarrow N + O$ . The background ionization,  $n_0$ , results from atmospheric interaction with galactic EUV and cosmic radiation, as well as solar EUV scattered radiation (e. g. Wallis and Budzinski, 1981).

Under the assumptions made above Eq. 4.4 writes, for nighttime winter auroral events:

$$\partial n / \partial t = q - \alpha(n^2 - n_0^2) \quad (4.6)$$

with  $q$  produced by particle precipitation. Equation 4.6 is further simplified by assuming stationarity and neglecting the background contribution, which leads to the following expression for the ionization:

$$n(z) = \sqrt{\frac{q(z)}{\alpha(z)}} \quad (4.7)$$

where we have explicitly emphasized the dependence on altitude.

The assumption of stationarity is, broadly speaking, allowed for precipitation events longer than the recombination time,

$$\tau_{rec} = \frac{1}{\alpha n} \quad (4.8)$$

As  $1 \times 10^{-7} \lesssim \alpha \lesssim 3 \times 10^{-7}$  and  $10^5 \lesssim n \lesssim 10^6$ , a recombination time range  $3s \lesssim \tau_{rec} \lesssim 100s$  results. In Section 4.4.1 we shall discuss the errors related to the assumption of stationarity, in particular for our drifting stable arc.

The background ionization is not larger than  $10^4$ , which is small enough to be neglected when compared to the ionization inside the arc. Outside of the arc the background ionization can account for a significant fraction of the total ionization and neglecting it can lead to substantial errors in conductivity.

To proceed further one needs to know the recombination coefficient,  $\alpha$ , and the ion production rate,  $q$ . Tabulated values of  $\alpha$  can be found e. g. in Rishbeth and Garriott (1969), Evans et al. (1977), while  $q$  follows from the energy deposited by particle precipitation.

## 4.2 Conductivity induced by particle precipitation

Ionospheric energy deposition by precipitating particles has two sources: electrons and protons. Electron precipitation is the main contributor for discrete auroral forms, at the northern/southern side of the oval in the evening/morning sector. While the proton precipitation is substantially lower — the overall energetic contribution is  $\sim 15\%$  (Galand et al., 2001) — it can be important and even larger than the electron precipitation for certain time periods or localized areas, like the equatorward side of the evening oval (Galand et al., 2001). In this Section we discuss electron and proton induced conductances along the ionospheric footprint of the FAST orbit 1859 during the inverted-V event.

### 4.2.1 Electron precipitation

The ionization production  $q(z)$  in Eq. 4.7 depends on the energy deposition at altitude  $z$ . Computer codes based on the early work of Rees (1963) were developed (e. g. Vickrey et al., 1981) for the computation of  $q(z)$ , and further  $n(z)$ , on the condition that the stationarity assumption is valid. With  $n(z)$  known Eqs. 4.2 can be integrated with respect to  $z$  to obtain the conductances.

Processing of a large amount of radar, rocket, and satellite data, led to a faster procedure for evaluating  $\Sigma_P$  and  $\Sigma_H$ , which is based on the following facts:

- On average, the formation of an electron–ion pair requires 35eV. Consequently, one would expect  $q(z)$  to be proportional to the rate of the energy deposition at altitude  $z$ ; this rate should be equal, in turn, to the energy flux of the precipitating electrons,  $J_E$ , weighted by a factor dependent on the form of the electron distribution function. Note that “energy flux of the precipitating electrons” can be understood in two ways:
  - energy flux dissipated in the ionosphere, that is incoming minus backscattered flux
  - energy flux available at the top of the ionosphere, that is only incoming flux

We shall return to this point below.

- By performing rigorous calculations, with test distributions representative for auroral electrons, it was found that the particular shape of the distribution has a relatively small influence on the final result (Robinson et al., 1987, estimated it to  $\sim 25\%$ , for electrons with energies higher than  $\sim 1\text{keV}$ ). Consequently, one could characterize the distribution by a global parameter, the average energy,  $\overline{E}$  (Eq. 4.10), thus neglecting the deviation from a maxwellian having the same average energy.

- $\Sigma_P$  is expected to be small for very hard or very soft electrons and the integral of the weighting factor over  $z$  should follow the same variation pattern. For soft spectra the energy is deposited at high altitudes, where the collision rate is too small to support Pedersen conductivity. On the other hand for hard spectra the energy is deposited deep inside the  $E$ -layer, where the current is dominated by the electron Hall contribution.
- The ratio  $\sigma_H/\sigma_P$  only depends on altitude, via  $\nu_{i,e}$ , but not on  $n$  (an immediate result of Eqs. 4.2). One would expect the ratio of the integrals  $\Sigma_H/\Sigma_P = \int \sigma_H dz / \int \sigma_P dz$  to be mainly determined by  $\sigma_H/\sigma_P$  at the altitude where the energy deposition maximizes, which in turn depends on  $\overline{E}$ .

Robinson et al. (1987) found simple approximate formulas for  $\Sigma_H$  and  $\Sigma_P$ , from fitting the results obtained by Vickrey et al. (1981):

$$\begin{aligned}\Sigma_P &= \frac{40\overline{E}}{16 + \overline{E}^2} J_E^{1/2} \\ \frac{\Sigma_H}{\Sigma_P} &= 0.45\overline{E}^{0.85}\end{aligned}\tag{4.9}$$

$J_E$  is the energy flux, in erg/cm<sup>2</sup>s, and  $\overline{E}$  is the average energy, in keV.  $\overline{E}$  is calculated as ratio of the energy and number flux:

$$\overline{E} = \frac{\int_{E_{min}}^{E_{max}} E F(E) dE}{\int_{E_{min}}^{E_{max}} F(E) dE}\tag{4.10}$$

with  $F(E)$  the differential number flux and  $E_{min}$ ,  $E_{max}$  the lower and upper integration limits, that depend on the detector characteristics.  $E_{min}$  should not be too low, to avoid contamination with secondary electrons, while  $E_{max}$  has to be high enough, to cover the full energy distribution; if  $E_{max}$  is too low a correction factor is required. Following Robinson et al. (1987) we chose  $E_{min} = 500\text{eV}$  and  $E_{max} = 30\text{keV}$  (the upper limit of the detector). For the event under study no correction factor is necessary, as the electron energy is less than 5keV (panel 1 in the right plot of Fig. 4.2), considerably smaller than  $E_{max}$ .

We would like to shortly comment on the choice of the pitch-angle range to be used when calculating  $J_E$  and  $\overline{E}$ , which is not explicitly mentioned by Robinson et al. (1987). One can identify two different items related to this problem:

- The precipitating electrons, i. e. the electrons whose pitch-angle is less than 90° at the top of the ionosphere (in the northern hemisphere), do not deposit all their energy in the ionosphere. Part of this energy returns to the magnetosphere, carried by backscattered and secondary electrons. Rees (1963) predicted an energy backscatter ratio of 17% (for an

isotropic distribution), while Evans et al. (1977) found 18% from experimental data. Only the energy deposited in the ionosphere leads to ionization production and, further, to increased conductivity. In order to calculate ionospheric parameters one has to subtract the upward (energy and number) flux from the downward one. If the electron measurement is done at a higher altitude (as it is the case with FAST), it is only a fraction of the velocity space that contains particles reaching the ionosphere: the precipitating electrons fill up the loss-cone while the backscattered and the secondaries are to be found in the source-cone. The rest of the velocity space is populated with electrons that cannot reach the ionosphere because of the magnetic mirror force, part of them bouncing between the magnetic mirror from below and the electric potential mirror from above. The definition of the loss-cone and source-cone, as well as a detailed discussion of the electron velocity space in the presence of parallel potential drops both below and above the satellite, are given in Section 4.3.1. We will show there that the difference between the downward and the upward flux can be calculated by integration over the full velocity space, if the assumption of stationarity holds.

- Equations 4.9 depend on the variables  $J_E$  and  $J_N$  ( $\bar{E} = J_E/J_N$ ), that can be calculated either by integration over the loss-cone — yielding the fluxes of the precipitating electrons, available at the top of the ionosphere — or over the full distribution — yielding the fluxes that actually dissipate in the ionosphere (the two possible interpretations for the “flux of the precipitating electrons” were already mentioned at p.50; the discussion there refers to the energy flux, but it applies to the number flux as well). The values obtained are certainly different, nevertheless both sets are equally good to be used as independent variables when fitting the results obtained with an energy deposition computer code (as done by Robinson et al. (1987)). The numerical constants in Eqs. 4.9 (yielded by fit) depend on the integration domain used to calculate  $J_E$  and  $J_N$ . As Robinson et al. (1987) do not mention it explicitly, we chose to calculate the moments and conductances by both integration over the full distribution and over the loss-cone. Note that in integrating over the loss-cone we did not take into account the widening produced by the potential drop below the satellite (if such a potential drop exists; this is the case when ion beams are detected).

In the left plot of Fig. 4.2 we show the energy and number fluxes, as well as the average energy. All the quantities were mapped to ionosphere level, by using Eqs. 4.15. One can see that outside of the ion beams the integration over the loss-cone produces higher fluxes, whereas the opposite happens when ion beams are detected. For the first case the explanation is easy: by integrating over the full distribution the loss-cone results are diminished by the negative contribution

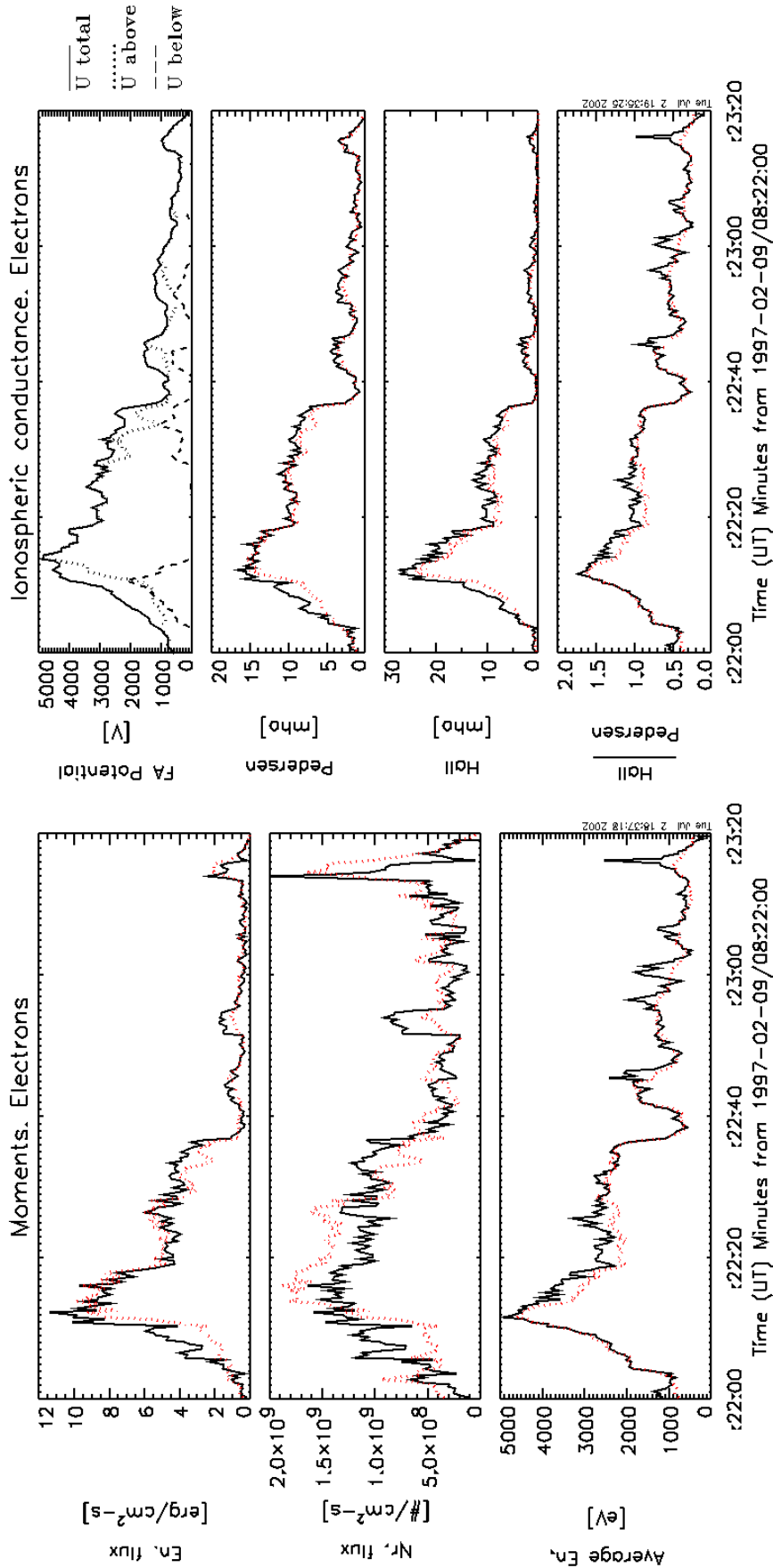


Figure 4.2: **Left:** Electron energy flux, number flux, and average energy, at ionospheric level, under the inverted-V. Black solid line: integration over the full velocity space. Red dotted line: integration over the loss-cone. **Right:** Panel 1: Potential drop above the satellite (dotted line), below (dashed line), and total (solid line). Panels 2-4:  $\Sigma_P$ ,  $\Sigma_H$ , and the ratio  $\Sigma_P/\Sigma_H$ , calculated with Eqs. 4.9 by using  $J_E$  and  $\bar{E}$  from the left plot.

of the source-cone, while the effect of the mirroring and trapped populations is negligible. In the second case the energy-dependent widening of the loss-cone compensates the fraction subtracted by the source-cone particles. This question is examined in more detail in Section 4.3.1. The average energy is not very sensitive to the integration domain during beam events, as the energy and number fluxes vary at roughly the same pace. Outside of the beams the increase in the source-cone number flux is larger than the increase in the energy flux (the backscattered and secondary electrons do not carry too much energy), so that the average energy obtained by integration over the full distribution is smaller.

The Pedersen and Hall conductances, as well as their ratio, are shown in the right plot of Fig. 4.2. During ion beam events the difference between the two sets of results can be significant, in particular when the potential drop below the satellite is comparable to the potential drop above. (see panel 1 in the right plot of Fig. 4.2 for the potentials). Nevertheless, we will show in Section 6.4.2 that the change in the conductance pattern associated with the choice of the integration domain has only a small influence on the calculated ionospheric electric field and current.

Except for the energetic part of the inverted-V, coincident with the visible arc, the conductances in Fig. 4.2 drop to low values, below  $\sim 5$  mho. In such a case the proton induced conductivity can, in principle, become important. This possibility is supported by the examination of the ion panels in Fig. 3.5. At the equatorward border of the arc there is significant high-energy proton precipitation, presumably of plasma-sheet origin. In the next Section we discuss proton precipitation and evaluate its contribution to the ionospheric conductance during FAST overpass.

### 4.2.2 Proton precipitation

Proton precipitation has been studied since decades, due to its importance for diffuse and red arc auroras (Eather, 1967). It was suggested in older conductance models that proton contribution could be taken into account by assimilating the proton distribution with an electron distribution of somewhat lower energy flux and average energy (e. g. Reiff, 1984). More recently Galand and Richmond (2001) undertook a detailed investigation of proton precipitation, similar to that performed by Robinson et al. (1987) for electrons. They used a transport code to calculate the ionization production  $q(z)$  and then fitted approximate formulas to the results. The transport code used by Galand and Richmond (2001) assumes a pure incident proton flux, isotropic over the downward hemisphere, at the top of the atmosphere (800 km), and takes into account the charge exchange between protons and the neutral atmosphere (the main reaction is  $\text{H}^+ + \text{O} \xrightarrow{\leftarrow} \text{H} + \text{O}^+$ ). As a result of the charge exchange the incident  $\text{H}^+$  beam transforms into a mixture of  $\text{H}^+$  and  $\text{H}$ ,



which diffuses across the field line (the H atoms motion is not impeded by the magnetic field), and the incident flux is reduced. When mapping the proton flux from the 4000km FAST altitude to the 800km top of the atmosphere one can disregard the charge exchange process because of the associated large mean free path.

The approximate formulas found by Galand and Richmond (2001) are good for protons (“p”) with average energies in the range 2–40keV:

$$\begin{aligned}\Sigma_P^p &= 5.7 J_E^{1/2} \\ \frac{\Sigma_H^p}{\Sigma_P^p} &= 0.45 \overline{E}^{0.3}\end{aligned}\tag{4.11}$$

The meaning of the symbols is similar to that in Eq.4.9. Galand and Richmond (2001) also derived a more complete form of the above equations, where the dependence on the magnetic field (which is shown to be important) is taken into account. However, as Eqs.4.11 are based on Chatanika (Alaska) data, and the FAST measurements analyzed here come from over Alaska, we can neglect the magnetic field dependence.

One striking difference between Eqs. 4.11 and Eqs. 4.9 is that  $\Sigma_P^p$  does not depend on the average energy. This can be explained as follows: for protons with higher energy the ionization cross-section grows, so that finally the energy is deposited roughly in the same altitude range. Higher energy electrons, on the contrary, penetrate to progressively larger ionospheric depths. For further discussion the reader is referred to the paper of Galand and Richmond (2001).

In the left plot of Fig. 4.3 we present the proton energy and number flux, as well as the average energy, obtained by integrating over the loss-cone, for the time interval 8:20 – 8:24. We chose a longer period to show that the proton precipitation only contributes the conductance at the southern edge of the inverted-V. Integration over the loss-cone is right for protons: there is no source-cone contribution to be subtracted from the loss-cone result, as the deposited energy is not altered by backscattering and secondary emissions. The source-cone population, which occasionally show up as beams (Fig. 3.7), is extracted from higher altitudes, not important for current conduction. One could still argue that the energy of the precipitating protons is reduced during beam events, because of the potential drop below the satellite. However, the associated potential energy is negligible when compared to the plasma-sheet proton energy (even if not, we would still obtain upper limits for the proton fluxes and energy). The proton induced conductance is shown in the right plot of Fig.4.3. Its relative contribution to the total conductance is seen to be significant only at the equatorward border of the arc (compare with the right plot of Fig.4.2). Our values are in good agreement with those obtained in the statistical study of Galand et al. (2001).

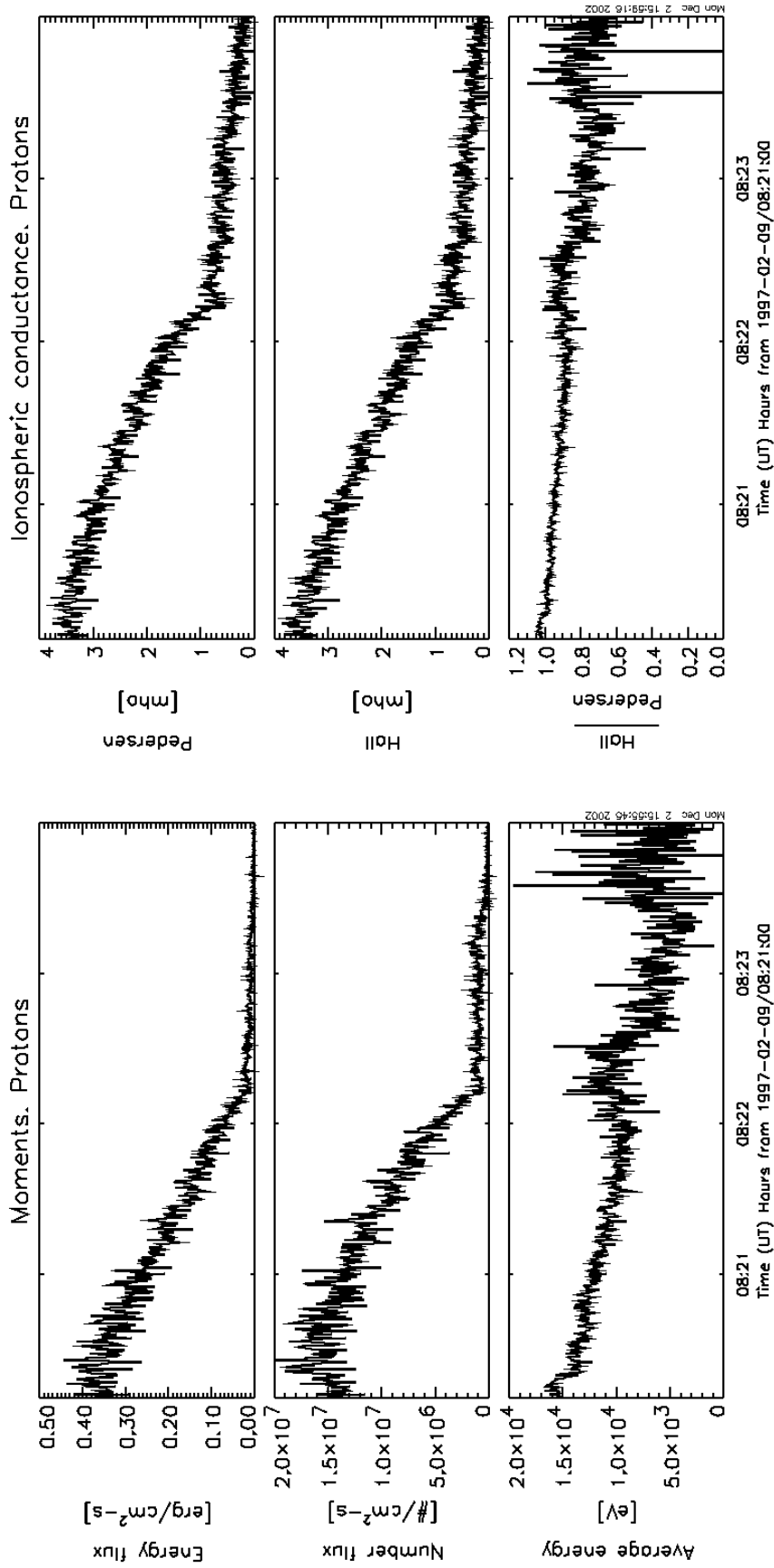


Figure 4.3: **Left:** Energy flux, number flux, and average energy of the protons, at ionospheric level. **Right:**  $\Sigma_P$ ,  $\Sigma_H$ , and the ratio  $\Sigma_P/\Sigma_H$ , calculated with Eqs. 4.11 by using  $J_E$  and  $\bar{E}$  from the left plot.

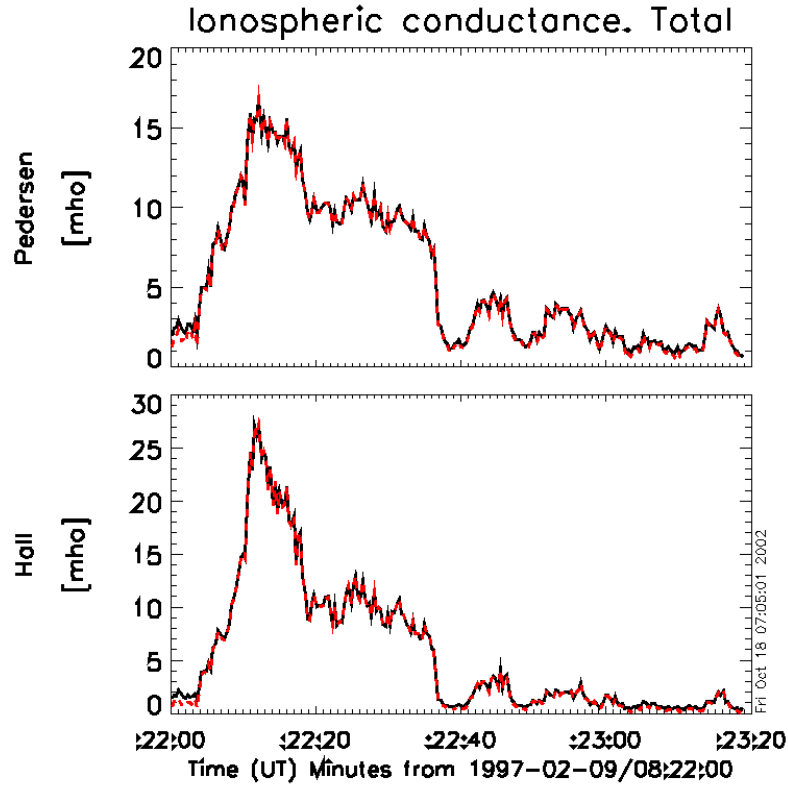


Figure 4.4: Pedersen and Hall conductances resulted from combined electron and proton precipitation,  $\Sigma = \sqrt{\Sigma^{e^2} + \Sigma^{p^2}}$  (black solid line). The electron induced conductances (red dashed line) are obtained by integration of  $(J_E, J_N)$  over the full distribution. One can see a difference between the two curves only at the beginning of the interval.

The combination of conductances resulting from different sources is not trivial. This problem was addressed by e. g. Wallis and Budzinski (1981) who showed that good results are obtained by writing the resulting conductance as:

$$\Sigma = \sqrt{\Sigma_1^2 + \Sigma_2^2} \quad (4.12)$$

Strictly speaking, Eq. 4.12 is valid only for similar altitudinal distributions of ionization (on the basis of Eq. 4.7). Wallis and Budzinski (1981) showed that Eq. 4.12 holds reasonably well for ionization induced by electron precipitation and solar radiation. Galand and Richmond (2001) checked that Eq. 4.12 can be also used when the ionizing sources are precipitating electrons and protons. Figure 4.4 shows the ionospheric conductances during the inverted-V event, due to both electron and proton precipitation. To emphasize the proton contribution at the equator side, the conductance obtained from electron data alone is plotted as well.

### 4.3 Ionospheric conductances during ion beam events

This Section provides a more detailed consideration of the conductance calculation when ion beams are detected. After a discussion regarding the integration domain, Burst data collected during the two beam events presented in Figs. 3.8 and 3.9 are used to calculate moments and conductances.

#### 4.3.1 Choice of the integration domain

To illustrate the discussion, Fig. 4.5 shows the boundaries that develop in the electron velocity space (azimuthal symmetry is assumed) in the presence of a parallel electric field extending both above and below the satellite (e. g. Knight, 1973; Chiu and Schulz, 1978). Particles going down to ionosphere have positive  $v_{\parallel}$ .

The hyperbola  $\mathcal{H}$  separates particles that either originate or get lost in the ionosphere from mirroring particles, that cannot reach the ionosphere. The ellipse  $\mathcal{E}$  separates particles that experience the full potential drop above the satellite, from particles that were or are going to be reflected by the potential. The dotted lines  $\mathcal{L}$  and  $\mathcal{S}$  show the loss-, respectively source-cone, that would develop in the absence of the potential drop below the satellite. The angle  $\theta_L$  ( $= \theta_S$ ),

$$\sin^2 \theta_L = \frac{B}{B_E}, \quad B_E \text{ the magnetic field on the same field line at } \sim 100\text{km} \quad (4.13)$$

results easily from the conservation of energy,  $mv^2/2$ , and of the first adiabatic invariant,  $mv_{\perp}^2/2B$ . At FAST altitude  $\theta_L \simeq 30^\circ$ . The potential drop enlarges the loss-/source- cones to the hyperboloid intersecting the  $(v_{\parallel}, v_{\perp})$  plane along  $\mathcal{H}$ .

For clarifying the difference between integration over the full velocity space and integration over the loss-cone, the various sub-domains bordered by  $\mathcal{H}$ ,  $\mathcal{E}$ ,  $\mathcal{L}$  and  $\mathcal{S}$  are labeled in Fig. 4.5 as  $D_1 \cdots D_{12}$ . The downward electrons in  $D_2, D_4, D_6$  are reflected by the potential above the satellite and, for a stationary situation, they should exactly mirror the upward electrons in  $D_{12}, D_{10}, D_8$  respectively, with  $D_6$  and  $D_8$  electrons bouncing between the upper electric and the lower magnetic mirrors (strictly speaking,  $D_2$  and  $D_4$  could be more populated than  $D_{12}$  and  $D_{10}$ , in case of suprathermal electron bursts; as there is no evidence for such events in our data we shall assume that the equality stated above holds). Similarly,  $D_5$  and  $D_7$  should balance each other: for a stationary case  $D_7$  electrons are just the mirror flux of  $D_5$ , going back to the magnetosphere.

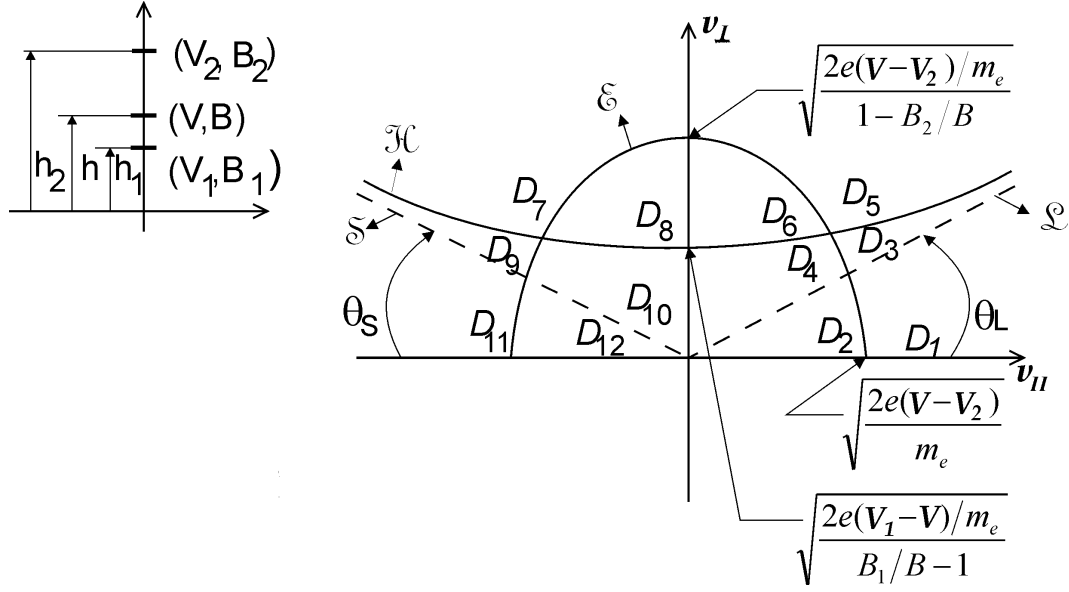


Figure 4.5: Electron velocity space domains at altitude  $h$ , inside the AAR, in the presence of a parallel electric field extending both above and below the satellite. See text for details. The geometry is sketched in the upper left corner:  $(V_1, B_1)$  and  $(V_2, B_2)$  are the potential and the magnetic field at the bottom and the top side of the AAR, at altitudes  $h_1$  and  $h_2$ , respectively.  $V$  and  $B$  are the potential and the magnetic field at altitude  $h$ .

Consequently, the integration over the full velocity space yields:

$$\begin{aligned}
 J_{N,E} &= \left( \int_{D_1} + \int_{D_3} + \int_{D_9} + \int_{D_{11}} \right) \cdots f(\mathbf{v}) d\mathbf{v} \\
 &= \left( \int_{D_1 \cup D_2} + \int_{D_3 \cup D_4} \right) \cdots f d\mathbf{v} - \left( \int_{D_{11} \cup D_{12}} + \int_{D_9 \cup D_{10}} \right) \cdots \tilde{f} d\mathbf{v} \\
 &= \left( \int_{\text{Loss-cone}_0} + \int_{\text{Loss-cone}_{\text{enh}}} \right) \cdots f d\mathbf{v} - \left( \int_{\text{Source-cone}_0} + \int_{\text{Source-cone}_{\text{enh}}} \right) \cdots \tilde{f} d\mathbf{v}
 \end{aligned} \tag{4.14}$$

where the last two forms explicitly show the negative contribution of the particles going away from the ionosphere. The index “0” stands for no potential drop below the satellite,  $U^{\text{below}} = 0$ , while “enh” indicates the enhancement of the loss-/source- cone when  $U^{\text{below}} \neq 0$ .

Equation 4.14 explains the difference between integration over the full velocity space and over the loss-cone alone. When there is a potential drop below the satellite, the enhancement of the loss-cone exceeds the negative contribution of the total source-cone (“0” + “enh”) and the integration over the full distribution gives a larger result compared to the integration over the loss-cone. The support rendered by the data to this qualitative explanation gives confidence that the assumed equality between incident and reflected fluxes is reasonably correct and further, that the hypothesis of stationarity is acceptable.

### 4.3.2 Numerical results

Equations 4.9 and 4.11 relate the conductances to the parameters  $\overline{E}$  and  $J_E$  calculated at ionospheric level. For the precipitating protons one can disregard the potential below the satellite, at least at FAST altitude (see the discussion in Section 4.2.2). However, this is not allowed for electrons. The extension of the potential structure below the satellite can add significant contributions to the energy flux and average energy of the electrons. Consequently, they are calculated with:

$$\begin{aligned} J_E^{ionos} &= \frac{B^{ionos}}{B^{sat}} \left( J_E^{sat} + J_N^{sat} e U^{below} \right) \\ \overline{E}^{ionos} &= \overline{E}^{sat} + e U^{below} \end{aligned} \quad (4.15)$$

The notations above are transparent. When  $U^{below} = 0$  Eqs. 4.15 reduce to the mapping required by the convergent magnetic field.

$U^{below}$  can be estimated by using ion data. If the ions in the beam interacted only with the electrostatic field the potential drop would be given by the peak energy. However, ion beams are a mixture of H<sup>+</sup>, O<sup>+</sup>, and He<sup>+</sup> (see panels 4–6 in Fig. 3.7), that can interact with each other, e. g. by two-stream instability. The heavy ions can be transferred a substantial amount of the H<sup>+</sup> energy, with the consequence that an ion spectrometer without mass resolution (as IESA) would see rather a plateaued than a peaked distribution, with the left wing of the plateau corresponding to H<sup>+</sup> and the higher energy part being increasingly populated with O<sup>+</sup> and occasionally with He<sup>+</sup> (J. McFadden, personal communication). In this case the peak energy under-estimates the potential drop. The average energy is a better estimate, on the condition that the ions only exchange energy one to each other. This condition, in its turn, is not rigorously valid. The extraction of the ionospheric ions frequently involves wave-particle interactions, which lead to the formation of ion conics. The ions, in particular the heavy ones, are given enough energy to reach the potential structure, escaping the gravitational bound and avoiding to get lost by charge-exchange with the H atoms. The average energy of the ions overestimates, to some extent, the FA potential drop. However, the ion conic energy is often below several 10eV (see e. g. the conic between 8:22:14 and 8:22:27 in the ion panels of Fig. 3.7), so that evaluating the ion average energy can still be a reasonable measure for the potential drop below the satellite.

Moments and electron induced conductances calculated for Beam 1 and Beam 2 by using Burst data are presented in Figs. 4.6 and 4.7 respectively. Proton contribution is not significant during the two beam events. Conductances obtained by using Burst and Survey data are compared in Fig. 4.8. As expected, they are similar, with some more variability in the Burst results.

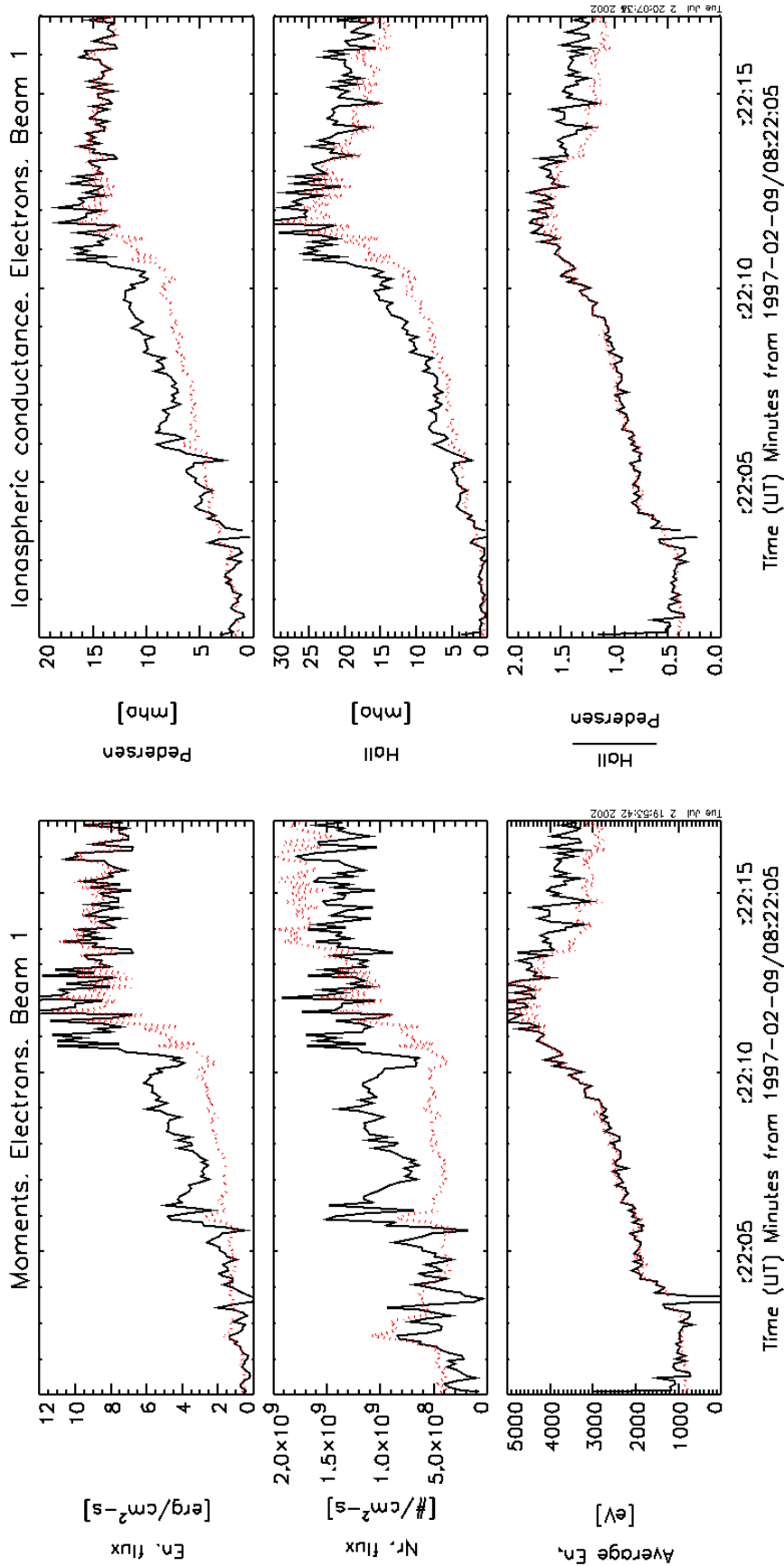


Figure 4.6: **Left:** Electron energy flux, number flux, and average energy during Beam 1, calculated from Burst data. **Right:** Electron induced conductances during Beam 1. Integration over the whole distribution (black solid line) and over the loss-cone (red dotted line). The beam covers the interval 8:22:03.8–8:22:13.8.

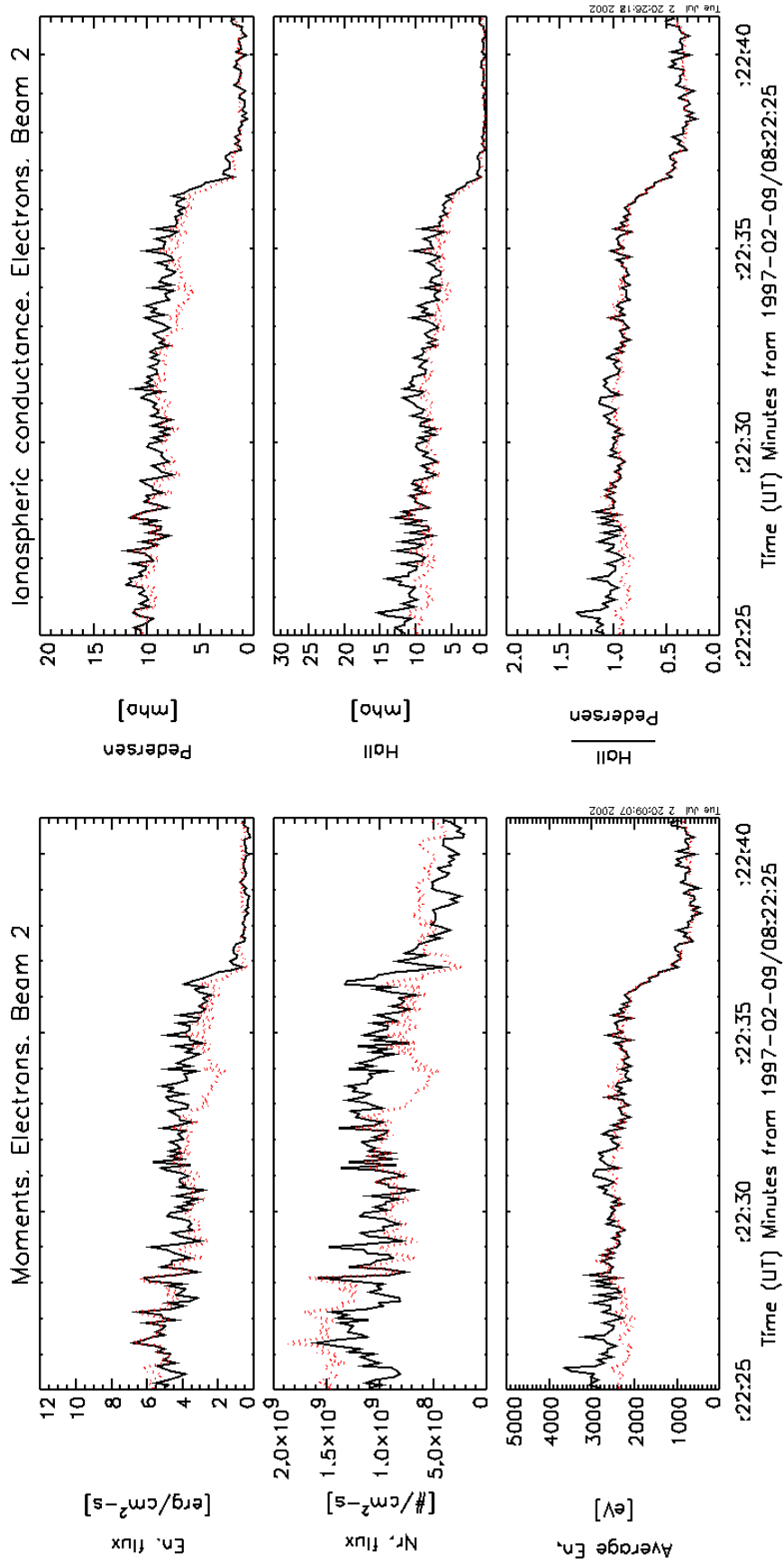


Figure 4.7: Moments and conductances during Beam 2, calculated from Burst data. Same format as Fig. 4.6. The beam covers the interval 8:22:26.9–8:22:37.5.



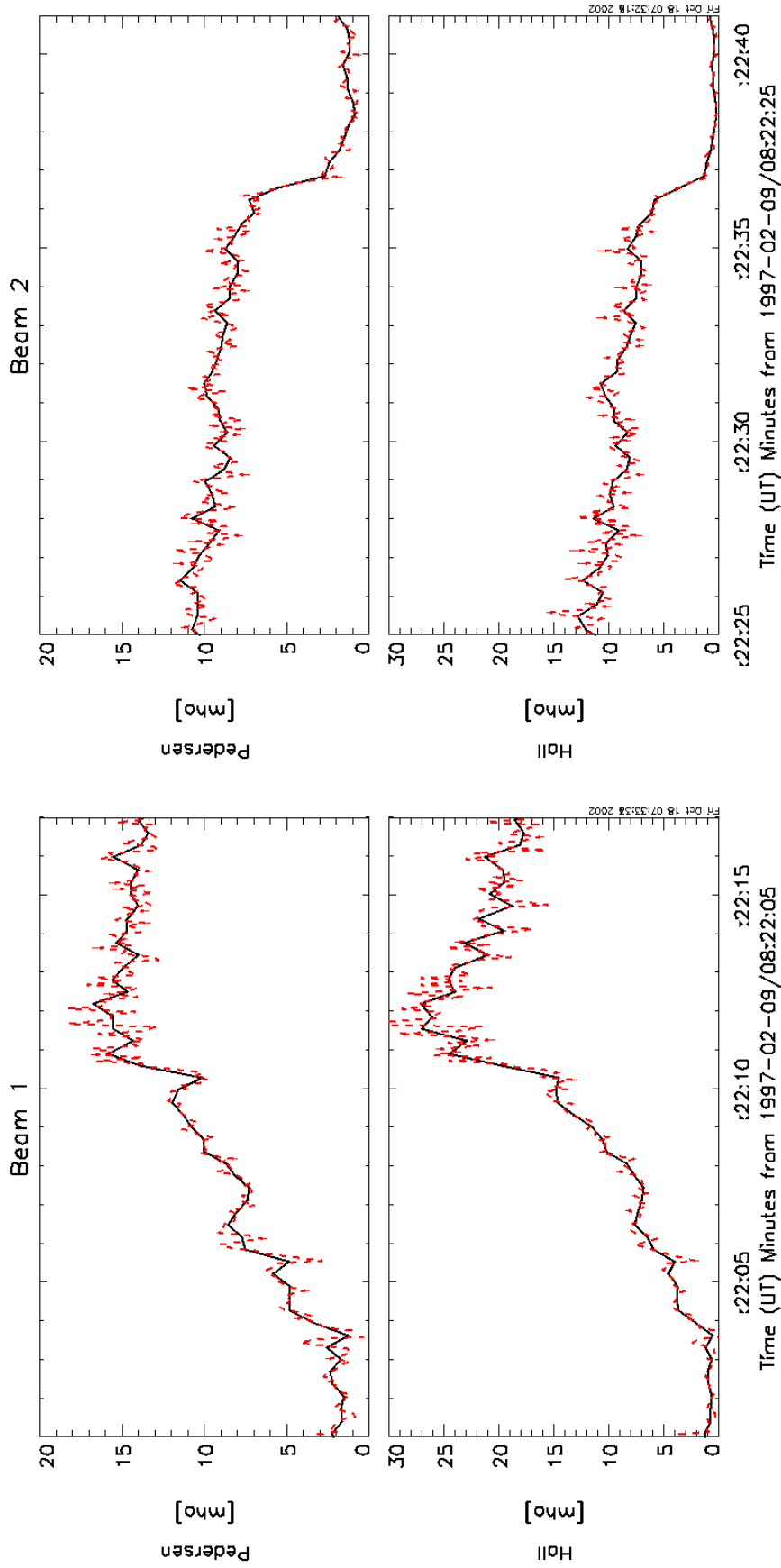


Figure 4.8: Conductances obtained by integration over the full distribution. Burst (red dashed line) and Survey (black solid line) data. **Left:** Beam 1. **Right:** Beam 2.

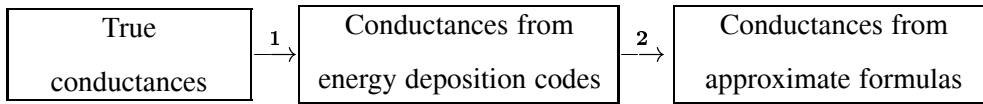
We conclude this Section by emphasizing once more that the two ion beams are located at the edges of the visible arc, where significant conductance gradients develop. One can be reasonably confident in the obtained results as long as the conductances do not drop below  $\sim 1\text{mho}$ . For smaller values the errors related to the measurement technique, to the approximate formulas used, and to the neglected ionization sources, become comparable to the results. The errors involved in the calculation of conductances are considered in more detail in the following Section.

## 4.4 Errors in the evaluation of conductances

An accurate electrodynamic description of the auroral arc depends essentially on the precision to which one can determine the conductances. First, we discuss carefully the sequence of steps leading to Eqs. 4.9 and 4.11, and try to evaluate the *methodological errors*. Next, we compute the *measurement errors*, originating in the statistical nature of the particle experiment and the discrete sampling of the energy and angle continua.

### 4.4.1 Methodological errors

The chain of approximations done in deriving Eqs. 4.9 and 4.11 can be summarized as follows:



By using energy deposition codes one implies the simplified form Eq. 4.7 for the continuity equation Eq. 4.4. This simplification is subject to errors because of:

- assuming stationarity and disregarding  $\partial n / \partial t$
- neglecting the convection term,  $\mathbf{v} \cdot \nabla n$ .
- neglecting the residual ionization,  $n_0$ .

For precipitation events in the winter nighttime auroral oval one would expect the errors due to ignoring the convection and the residual ionization to be small. However, assuming stationarity is a more serious source of errors, in particular at the leading and trailing edges of the arc.

Evans et al. (1977) addressed this problem for a pre-midnight auroral arc produced by  $\sim 10\text{keV}$  electrons. They found that the time constant associated with the growth/decay of the conductance at the leading/trailing edge of the arc is of the order of 15/70s. As their arc moved equatorward with  $\sim 100\text{m/s}$  these times transform to distances of 1.5/7km over which the conductances might have been out of equilibrium (higher at the leading edge of the arc and lower at the trailing edge, as compared to the real ones).

In our case the energy of the electrons is lower,  $\sim 5\text{keV}$  (Section 3.2), and the southward motion of the arc is faster,  $\sim 200\text{m/s}$  (Section 3.3). One can identify three intervals of precipitation gradient for the visible arc (Fig. 4.2):  $I_{12}=8:22:04-8:22:12$ ,  $I_{23}=8:22:12-8:22:19$ , and  $I_{31}=8:22:35-8:22:38$ , at the leading edge, in the middle of the arc, and at the trailing edge respectively. The indices are related to precipitation levels. As the satellite velocity is  $\sim 5.6\text{km/s}$  and the mapping factor  $\sim 0.5$  (p. 16), each second of FAST data corresponds to  $\sim 2.8\text{km}$  ionospheric distance. Consequently, the respective widths of the precipitation gradients are  $d_{12}^{(e)} = 22.4\text{km}$ ,  $d_{23}^{(e)} = 19.6\text{km}$ , and  $d_{31}^{(e)} = 8.4\text{km}$ . The time constants associated with the variations in conductance are  $t_{12}^{(i)} = 9\text{s}$ ,  $t_{23}^{(i)} = 23\text{s}$ , and  $t_{31}^{(i)} = 95\text{s}$ , which transform to  $d_{12}^{(i)} = 1.8\text{km}$ ,  $d_{23}^{(i)} = 4.6\text{km}$ , and  $d_{31}^{(i)} = 19\text{km}$  respectively. It results that the assumption of stationarity is reasonable at the leading edge and in the middle of the arc, but probably wrong at the trailing edge. To avoid confusion, the notations “*e*” and “*i*” above stand for “external” and “internal”. For the explanation of these notations and for computational details the reader is referred to Appendix C.1.

The time constants and the associated distances at the edges of the arc are in reasonable agreement with the values from Evans et al. (1977). The differences are presumably related not only to having other electron energies and arc velocity, but also to the less rigorous estimation procedure we used. Our results are derived by solving the time dependent Eq. 4.6 at the altitude  $z^*$ , where the ionization production maximizes. No height integration was performed. Additionally, except for using recombination coefficients corresponding to the actual height of maximum ionization, the variation of  $z^*$  with the change in precipitation was neglected.

The inaccurate knowledge of the recombination coefficient and/or of the loss mechanism(s) can further increase the error in  $n$ . If the electron precipitation is too hard/soft the energy is deposited at low/high altitude, where the dissociative recombination is no longer the dominant loss mechanism. In our case, however, the electrons have medium energies and we do not expect this error source to be important.

Other contributions to the error in conductances may come from the collision frequencies,  $\nu_{en}$  and  $\nu_{in}$ , that enter in Eqs. 4.2 and depend essentially on the neutral atmosphere. Evans et al. (1977) compared several models and estimated the associated uncertainties to be (+4%, -5%) for  $\Sigma_H$  and (+8%, -9%) for  $\Sigma_P$ . The integration of Eqs. 4.2 with respect to height levels out the differences between particular models.

Returning to the scheme at p. 64, we still have to discuss the errors associated with the use of the approximate formulas, based on just two parameters. To validate these formulas conductances produced by idealized maxwellian distributions were computed, both by using energy deposition codes and the approximations. The results were found to agree better than 20% for an

average energy  $\overline{E} < 10\text{keV}$  (Robinson et al., 1987). A serious source of errors can be the deviation from maxwellian of the real distribution. However, except for some extreme situations (e. g. monoenergetic), the results obtained for the equivalent maxwellian distribution agree fairly well with the results yielded by the energy deposition codes, for the actual distribution. Robinson et al. (1987) stated that for electrons with average energy  $\overline{E} > 1\text{keV}$ :

“(...) the assumption of the Maxwellian spectrum yields conductivities that are within about 25% of the actual values for the most common types of auroral distributions.”

Taking into account that our arc exhibits average electron precipitation we conclude that, by using the approximate formulas, fairly accurate conductance values are expected inside the visible arc. However, outside of the arc the errors are presumably of the same order with the calculated conductances, because of non-stationarity, residual ionization, and use of the approximate formulas with low energy electrons. In the next Section we show that the measurement errors have a similar evolution, i. e. reduced inside the arc and increased outside.

#### 4.4.2 Measurement errors

The measurement errors are related to the statistical nature of the particle experiment, to the limited energy and angle coverage, and to the necessary division of the continuous energy–angle domain into a finite number of channels, corresponding to a discrete sequence of energies and directions.

To find the errors associated with the conductances calculated from Eqs. 4.9 and 4.11 one has first to evaluate  $\sigma_{J_E}$  and  $\sigma_{\overline{E}}$ , the errors in  $J_E$  and  $\overline{E}$ . As  $\overline{E} = J_E/J_N$ , the primary errors that we need are  $\sigma_{J_E}$  and  $\sigma_{J_N}$ . A possible way to deal with this problem is described in Paschmann et al. (1998): One chooses maxwellian distributions of given density, temperature, and bulk velocity, computes the detector response, adds a Poisson error to the counting statistics, calculates the desired moments, and compares the results with the rigorously calculated moments of the maxwellian input data (this procedure is summarized in Fig. 6.2 of the cited reference).

Such an analysis can yield a reasonable estimate of the expected error ranges associated with typical plasma regimes, by the appropriate choice of the maxwellian parameters. However, one does not obtain the *actual* error, corresponding to a *measured* distribution, which may well be *non-maxwellian*. We used an alternative approach, based on applying the error propagation formula (e. g. Bevington and Robinson, 1992) to the measured distribution. The reader is referred to Appendix C.2 for details on the technical steps. This procedure relies on the assumption that the energy and angle windows of the detector are narrow enough to consider the distribution as uniform over each energy–angle bin. Its main advantage is that it is solely based on the actual

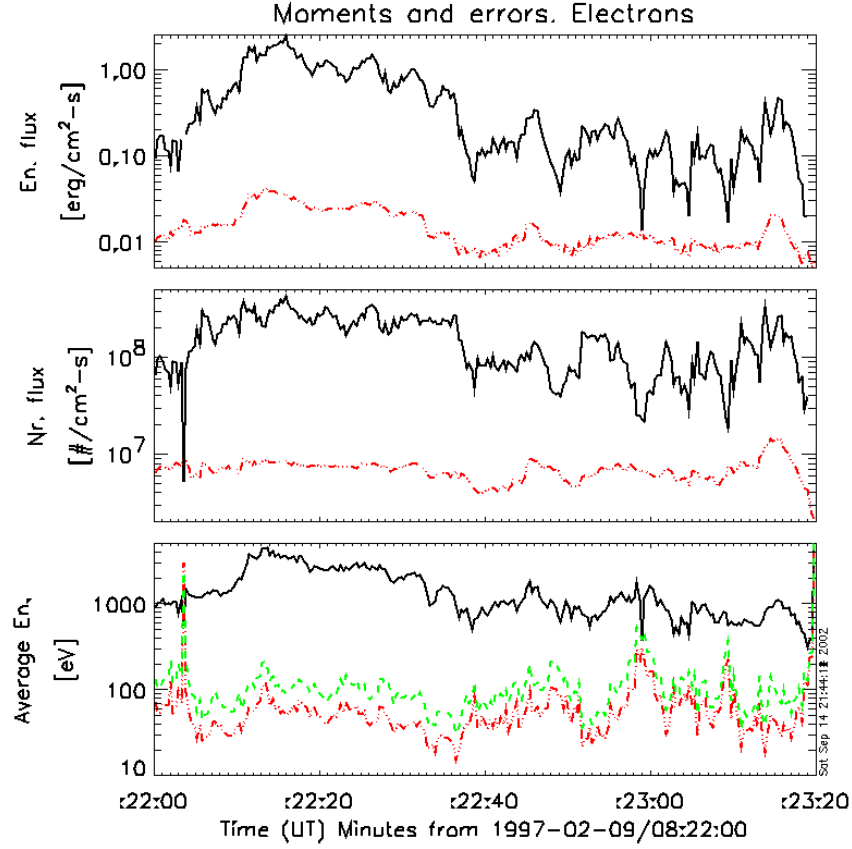


Figure 4.9: Number flux, energy flux, and average energy (black solid lines), together with their respective errors (red dash-dotted lines). In the average energy panel the green dashed line shows the error calculated by disregarding the correlation between  $J_E$  and  $J_N$ .

distribution. The assumption of uniformity has good chances to be reasonable; the present day detectors collect thousands of samples for each single distribution (for FAST the numbers are 1536 in Burst mode and 3072 in Survey mode).

Figure 4.9 shows  $J_N$ ,  $J_E$  and  $\bar{E}$  together with their respective errors. The scale is logarithmic, for better visibility of the error curves. As a general remark, the relative errors are quite small, below 10% for most of the time. The explanation can be found in the high geometric factor (see Table 2.1), providing a count rate,  $n_{ij}$ , typically higher than 100. As the relative error roughly scales with  $1/\sqrt{n_{ij}}$ , one can easily understand the results.

In the  $\bar{E}$  panel two error variations are given: The lower curve is calculated rigorously, by taking into account the positive correlation between the energy flux and the number flux:

$$\bar{E} = \frac{J_E}{J_N} \Rightarrow \frac{\sigma_{\bar{E}}^2}{\bar{E}^2} = \frac{\sigma_{J_E}^2}{J_E^2} + \frac{\sigma_{J_N}^2}{J_N^2} - 2 \frac{\sigma_{J_E J_N}}{J_E J_N} \quad (4.16)$$

The upper curve is calculated by disregarding the correlation, i. e. by neglecting the last term on the r.h.s. of Eq. 4.16. Still, the two curves track each other quite well, suggesting that the inexact calculation could be good enough to find the relative variation of the error along the satellite path.

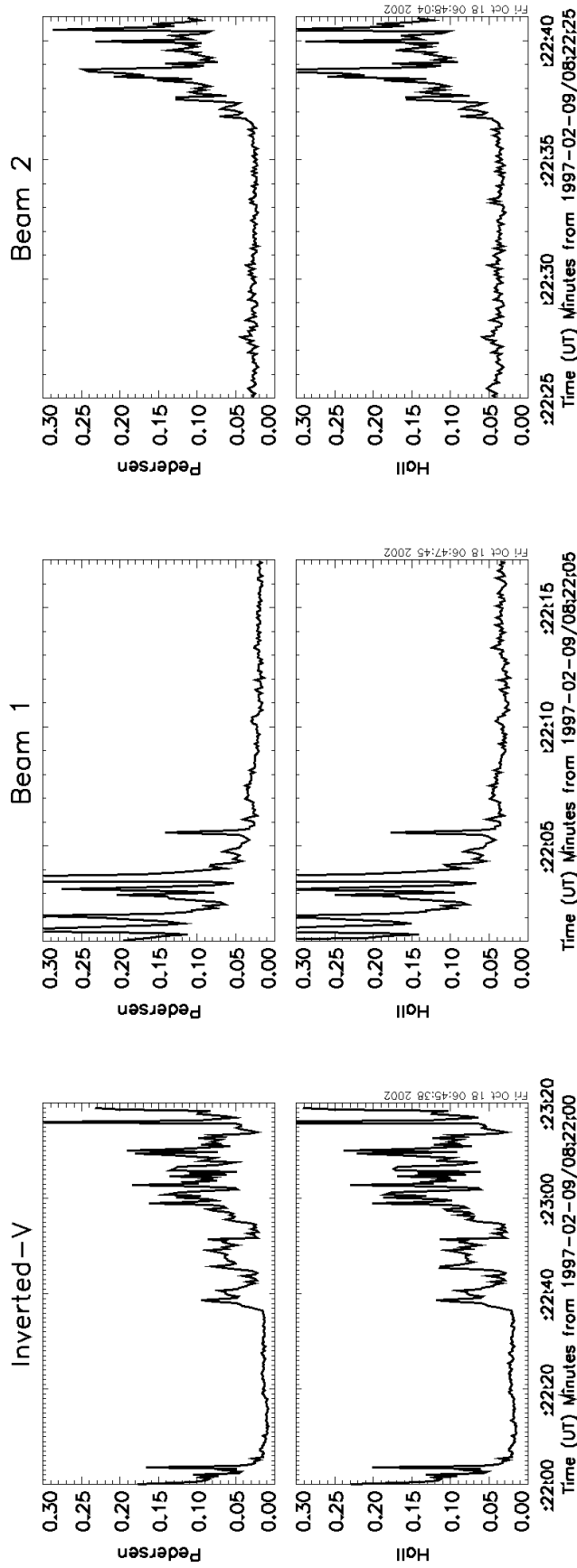


Figure 4.10: Relative errors in Pedersen and Hall conductances, calculated by neglecting the correlations. **Left:** Under the inverted-V (Survey data); **Middle and Right:** During Beam 1 and Beam 2 (Burst data).

This observation is useful when proceeding to evaluate the errors in conductances. A rigorous calculation would be extremely cumbersome in this case. Even if one neglects the proton induced conductance, the application of the error propagation formula to Eqs. 4.9, with  $J_E$  and  $\overline{E}$  from Eqs. 4.15, would imply a considerable amount of work (to measure this work one can follow the rigorous calculation of  $\sigma_{\overline{E}}$  in Appendix C.2.2).

The chance that this work would be worthwhile is, however, small. The measurement errors are most probably less important compared to the methodological errors, which are not as easy to evaluate quantitatively. One cannot expect, realistically speaking, to fully derive the magnitude of the errors implied by the conductance calculation. Still, by using the approximate procedure, which neglects the correlations between the involved quantities, one can hope to get a reasonable estimate for the variation of the error along the satellite path.

Figure 4.10 shows the relative errors obtained for the whole inverted-V interval and for the two beam events, by neglecting the correlations. The errors are quite small under the energetic part of the inverted-V, inside the visible arc, and increase at the edges. This behavior is similar to the expected variation of the methodological errors, which supports the use of these results as proxy for the error shape. The influence of the errors in the conductance pattern upon the calculated ionospheric electric field is checked in Sections 6.4.2 and 6.4.3.

## 4.5 Summary

This Chapter was devoted to evaluating ionospheric conductances from the satellite data. We concentrated on conductances induced by particle precipitation, which is the main ionization source in the winter nighttime auroral ionosphere. Simple approximate formulas were used to derive electron and proton induced conductances, during the inverted-V period, using Survey data, and during two ion beam events, using Burst data. The proton contribution was shown to be negligible for the time interval under study.

The calculation of conductances during ion beam events was discussed in more detail in Section 4.3. In particular, we commented on the choice of the integration domain to be used for computing the energy and number flux. Because of some ambiguity in the derivation of the approximate formulas, we decided to perform the numerical evaluations for both the full distribution and the loss-cone population alone.

The errors in conductances were investigated in Section 4.4. Both methodological and measurement errors were considered. We suggested that, although a reliable magnitude of the errors is difficult to obtain, a simplified evaluation of the measurement error could provide a reasonable estimate for the relative variation of the total error along the satellite path.

## Chapter 5

# Ionospheric electrodynamics with emphasis on the auroral arc

The ionospheric electrodynamics is investigated by using both ground-based and in-situ data. In the first Section we review some of the methods developed to study the electrical parameters of the ionosphere and outline important findings, in particular with respect to the auroral arc. Some simplifying assumptions often made are discussed in the second Section and qualitatively evaluated with respect to our data in the third Section. In the last Section a new method, developed for the arc study and based on high resolution satellite data, is introduced.

### 5.1 Previous work

Ionospheric electrodynamics is investigated on multiple scales: different types of data, with different spatial and temporal resolution, are used to understand both global and local phenomena. Similar to the logic of data presentation in Chapter 3, we begin by looking to methods based on ground data, more adequate for describing large to medium scale patterns. Next, the relationship between magnetic perturbation and electric field in the Birkeland current region, as revealed by satellite data, is discussed. The review of the previous work is concluded with a more extended Section devoted to the electrodynamics of the auroral arc.

#### 5.1.1 Ground based methods to infer ionospheric electrodynamics

The main advantage of using ground data is the 2D coverage. Extended networks of magnetometers, ionosondes, coherent and incoherent scatter radars, photometers and all-sky cameras cover large areas in the polar part of the northern hemisphere. The methods addressing ionospheric



electrodynamics are mainly based on measuring the ground perturbations in the magnetic field produced by the ionospheric currents, as well as the ionospheric electric field (IEF). The auroral images provide information on the geometry and dynamics of the luminosity pattern.

The basic relations underlying the ground based methods are (Glassmeier, 1987):

The Ohm's law in the ionosphere:

$$\mathbf{J}_\perp = \Sigma_P \mathbf{E} + \Sigma_H \mathbf{e}_B \times \mathbf{E} \quad (5.1)$$

The decomposition of the ionospheric current density into a source-free and an irrotational part, according to Helmholtz theorem:

$$\mathbf{J}_\perp = \mathbf{J}_{sf} + \mathbf{J}_{irr} \quad (5.2)$$

The dependence of the magnetic field perturbation,  $\mathbf{B}_{hor}$ , below the current-carrying layer, on  $\mathbf{J}_{sf}$ :

$$\mathbf{J}_{sf} = \frac{2}{\mu_0} \mathbf{e}_B \times \mathbf{B}_{hor} \quad (5.3)$$

The dependence of the FAC,  $j_\parallel$ , on  $\mathbf{J}_{irr}$ :

$$j_\parallel = \nabla_h \cdot \mathbf{J}_{irr} \quad (5.4)$$

where the subscript  $h$  denotes differentiation with respect to the horizontal coordinates.

Considering the IEF to be electrostatic,  $\mathbf{E} = -\nabla_h \phi$ , one can process Eqs. 5.1–5.4 further.

By applying  $(\text{rot})_z$  to Eqs. 5.1 and 5.3 one obtains:

$$\left( \frac{\partial \Sigma_H}{\partial x} - \frac{\partial \Sigma_P}{\partial y} \right) \frac{\partial \phi}{\partial x} + \left( \frac{\partial \Sigma_P}{\partial x} + \frac{\partial \Sigma_H}{\partial y} \right) \frac{\partial \phi}{\partial y} + \Sigma_H \nabla_h^2 \phi + \frac{2}{\mu_0} \nabla_h \cdot \mathbf{B}_{hor} = 0 \quad (5.5)$$

By applying  $(\text{div})_h$  to Eqs. 5.1 and 5.4 it results:

$$\left( \frac{\partial \Sigma_P}{\partial x} + \frac{\partial \Sigma_H}{\partial y} \right) \frac{\partial \phi}{\partial x} - \left( \frac{\partial \Sigma_H}{\partial x} - \frac{\partial \Sigma_P}{\partial y} \right) \frac{\partial \phi}{\partial y} + \Sigma_P \nabla_h^2 \phi + j_\parallel = 0 \quad (5.6)$$

The two relations 5.5 and 5.6 are elliptic differential equations for  $\phi$ . The source term is related to the lower side of the ionosphere in Eq. 5.5 ( $\frac{2}{\mu_0} \nabla_h \cdot \mathbf{B}_{hor}$ ) and to the upper side in Eq. 5.6 ( $j_\parallel$ ). The methods based on ground data use mainly Eq. 5.5 and are discussed in more detail by e. g. Glassmeier (1987), Untiedt and Baumjohann (1993). Here we shall just mention them briefly:

- The KRM method (Kamide et al., 1981; Mishin et al., 1980) solves Eq. 5.5 for a model distribution of the conductances and with  $\mathbf{B}_{hor}$  derived by upward continuation of the ground magnetic perturbation. The method is suited to be applied on global scale (e. g. polar cap and auroral oval).

- The forward or 'trial and error' modeling uses electric field observations and assumed conductance distributions and calculates the associated disturbance in the ground magnetic field. The model conductances are iteratively changed until a good agreement between the measured and calculated magnetic perturbations is obtained. This method was applied to more local problems, e. g. auroral break-ups (Baumjohann et al., 1981) and Westward Traveling Surges (WTS; Opgenoorth et al., 1983).
- The Assimilative Mapping of Ionospheric Electrodynamics (AMIE; Richmond and Kamide, 1988) can use as many data sets as available and finds the ionospheric parameters that provide the best fit to the data, in a least square sense (e. g. Richmond et al., 1988). It is more appropriate for global problems.
- The "method of characteristics" (Inhester et al., 1992) originated with the Untiedt algorithm (see Glassmeier, 1987). It requires magnetic and electric field measurements and it only assumes the distribution of  $\alpha = \Sigma_H / \Sigma_P$ . An important achievement of this method is the possibility to assess the error, as well as to check the uniqueness of the solution. In a subsequent study Amm (1995) applied the method to some typical auroral situations and showed that the results are only weakly dependent on the error in  $\alpha$ . Later on, Amm (1998) generalized it to spherical coordinates.

A serious drawback of the ground-based methods is the relatively poor spatial resolution — some typical numbers are 100km for the magnetic field data (Küppers et al., 1979) and 20km for the electric field data (Greenwald et al., 1978). With the method of characteristics, which is best suited to smaller scales, one can obtain a good description of the WTS or of the Harang discontinuity (Amm, 1995), with a resolution of some 10km, but such a scale is normally too coarse for the discrete auroral arc.

A fundamental difference between the studies based on ground data and those based on in-situ data refers to the conductance distribution: while with ground data the conductance has to be, in general, either assumed or calculated, with in-situ experiments is usually possible to derive the conductance from the measured particle precipitation.

In the particular case of the discrete arc, having the length 1–2 orders of magnitude larger than the width, the variation of the physical parameters is substantially smaller along the arc than across the arc; high resolution 1D data, collected in-situ, can be more appropriate to investigate the arc than low resolution 2D ground measurements.

### 5.1.2 Electric field vs. magnetic field variation pattern

The correlation between the E–W magnetic perturbation ( $B_y$ ) and the N–S electric field ( $E_x$ ) in the FAC region was anticipated by Boström (1974) from an idealized treatment of the ionospheric current closure. Assuming homogeneous Pedersen and Hall conductances, and disregarding the E–W variations, one obtains easily the following relation (see Section 5.3 for the full derivation):

$$E_x = \frac{B_y}{\mu_0 \Sigma_P} + \text{const.} \quad (5.7)$$

$B_y$  can be measured above the ionosphere with satellite-borne magnetometers.

Surprisingly enough, this very simple model was validated by experimental evidence: Bythrow et al. (1980) used AE-C data, while Smiddy et al. (1980) and Rich et al. (1981) used S3-2 and S3-3 data, to show that indeed, there is a qualitative agreement between the E–W perturbation magnetic field and the N–S IEF. These results were substantiated by Sugiura et al. (1982), who found highly correlated DE-2 data sets, including a case with 0.996 correlation coefficient.

In a subsequent paper Sugiura (1984) extended the first results. He showed that even when the current sheet is not parallel to the E–W direction, the ionospheric closure of the FAC is achieved mainly through Pedersen current, perpendicular to the sheet, whereas the Hall current parallel to the sheet (driven by the perpendicular electric field) is essentially divergence free. This particular geometry had been already predicted by Boström (1964) as a possible magnetosphere–ionosphere (M–I) coupling mode.

Besides homogeneous conductance and neglect of the longitudinal variations Boström’s model also assumes that the FACs flow in thin sheets, at the southern and northern edges of the auroral oval. Later on, this model was used not only for large scale M–I coupling, but also for small scale structures, like the auroral arc. While one can emphasize basic physical mechanisms in this way, there are also features not properly described with such a model. We shall return to this point in Section 5.2.

### 5.1.3 The electric field in the vicinity of auroral arcs

Early observations (Evans et al. (1977), de la Beaujardière et al. (1977), and references therein) showed that for a large majority of the auroral arcs the IEF associated with the arc is either correlated or anti-correlated with the electron precipitation.

Using high quality rocket data, Evans et al. (1977) investigated in much detail an evening arc. They were able to compute the Pedersen and Hall conductances from the electron data and to show that a sharp decrease in the electric field corresponds to a sharp increase in conductance,

originating in the enhanced precipitation. Furthermore, they also showed that the atmospheric power inputs due to Joule dissipation and electron precipitation are anti-correlated, and inferred that the auroral form should be just the visible portion of a larger system. To explain the relationship between the IEF and the electron density Evans et al. (1977) suggested that either the magnetosphere acts like a current generator, or a high impedance along the magnetic field lines controls the current to close in the ionosphere, emphasizing the role played by the FACs.

de la Beaujardière et al. (1977) conducted a study based on radar data. They examined three different arcs, located in the evening, pre-midnight and post-midnight sectors respectively, and found that for the evening and pre-midnight arcs the electric field was anti-correlated with the electron density, whereas for the post-midnight arc the two quantities were positively correlated. Making use of the fact that the zonal component of the electric field was westward inside the arc in all the three cases, de la Beaujardière et al. (1977) suggested that both patterns originate in the build-up of polarization charges at the edges of the arc. The charges are carried by the northward Hall current driven by the westward electric field inside the high-conductivity arc channel. The plasma inside the arc is neutral and the conductivity is homogeneously enhanced. Although de la Beaujardière et al. (1977) computed the divergence of the ionospheric current, the FACs play just a secondary role in their polarization model. This can be contrasted with Evans et al. (1977). The difference might be related to the primary data used: a rocket experiment allows the direct detection of the precipitating particles, whereas a radar measures the induced ionospheric ionization.

The two configurations imagined by de la Beaujardière et al. (1977) are reproduced here as Fig. 5.1. On the evening side the polarization electric field is opposite to the large scale, northward convection field, resulting in a decrease of the field inside the arc. On the morning side the polarization electric field is again southward, but this time it adds to the southward convection field, enhancing the arc field. de la Beaujardière et al. (1977) attributed the E–W electric field a magnetospheric origin, but they did not address its large shear at the border of the arc. If the variations along the arc are neglected, as in the model of de la Beaujardière et al. (1977), the Faraday's law writes  $\partial E_\eta / \partial \xi = \partial B_z / \partial t$  and  $\Delta B_z \approx \Delta E_\eta / \Delta \xi \times \Delta t$ . With  $\Delta E_\eta = 20 \text{ mV/m}$ ,  $\Delta t = 100 \text{ s}$ , and  $\Delta \xi \leq 50 \text{ km}$ , one obtains  $\Delta B_z \geq 0.4 \text{ gauss}$ , a value comparable to the Earth's magnetic field (the numerical values correspond to the evening arc of de la Beaujardière et al. (1977)). The shear in the electric field also implies that the convection velocity is not divergence free, which is hard to explain, given that the magnetospheric plasma is practically incompressible. A solution to the difficulty raised by the shear in the electric field might be conceived in terms of measurement errors (from the evaluations of de la Beaujardière et al. (1977) one infers  $\delta E_\eta \gtrsim 7 \text{ mV/m}$  and consequently  $\delta \Delta E_\eta \gtrsim 14 \text{ mV/m}$ ), possibly combined with temporal and/or longitudinal variations.

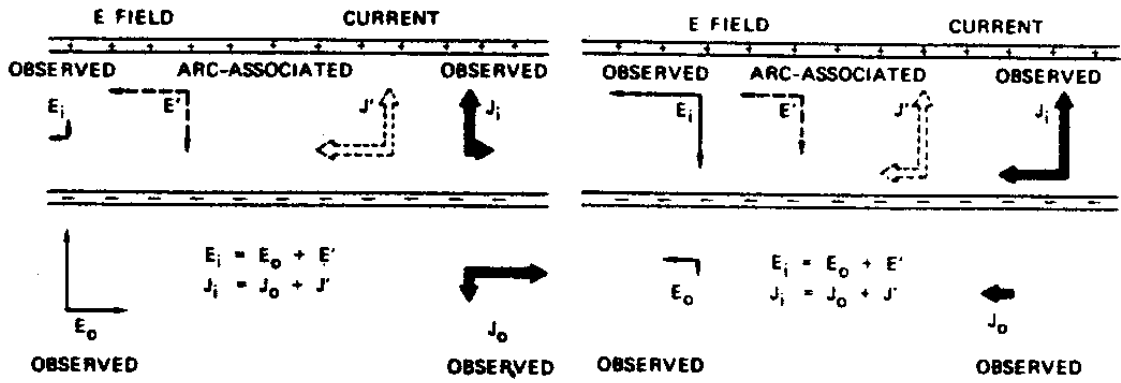


Figure 5.1: Electric field and current for a pre-midnight (left) and a post-midnight (right) arc.  $(E_o, J_o)$ ,  $(E_i, J_i)$ , and  $(E', J')$  are respectively the electric field and current outside the arc, inside the arc, and associated with the arc. Figures 15 and 16 from de la Beaujardière et al. (1977).

Later, de la Beaujardière et al. (1981) advanced the following arc classification:

1. anticorrelation type, when the N-ward electric field within the evening arc is decreased
2. asymmetric type, when the the N-ward electric field is decreased within the evening arc and remains low on the poleward side of the arc
3. reversal type, when the meridional electric field reverses within the arc
4. correlation type, when the S-ward electric field is increased within the morning arc

They also suggested that both polarization and field-aligned currents contribute to establishing the electric field configuration:

“When the electric field and the conductivities vary with latitude so that the current divergence is nonzero, then Birkeland currents may flow, and/or space charges may be induced so as to modify the ionospheric electric field. The balance between these two effects depends on the configuration of the large-scale circuit that links the resistive ionosphere to the magnetosphere via field lines where anomalous resistivity or double layers can modify the current.”

The aforementioned balance was expressed by de la Beaujardière et al. (1981) in the following equation (as compared to the original text  $x$  and  $y$  were changed to  $\eta$  and  $\xi$ , in order to agree with our reference system; the sign of  $J_{||}$  was also changed; for the rest of notations see Fig. 5.1):

$$E_{pol} = E_{\xi}^i - E_{\xi}^o = -E_{\xi}^o(1 - \Sigma_P^o/\Sigma_P^i) + E_{\eta}^o(\Sigma_H^i/\Sigma_P^i - \Sigma_H^o/\Sigma_P^o) + J_{||}/\Sigma_P^i \quad (5.8)$$

Equation 5.8 was derived by assuming that the E–W electric field is continuous:  $E_{\eta}^i = E_{\eta}^o$ . Note the block structure of the model, with homogeneous regions inside and outside of the arc.

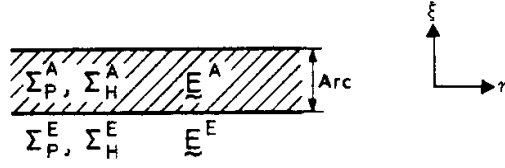


Figure 5.2: The arc and the neighboring ionosphere. Cartoon adapted from Marklund (1984).

An important paper for the arc classification was written by Marklund (1984). He undertook a comprehensive review of the work published until that time and came to the following scheme, resembling the suggestion of de la Beaujardière et al. (1981):

1. polarization arcs
2. Birkeland arcs
3. combination arcs

Still, Marklund's (1984) point of view is not identical to that of de la Beaujardière et al. (1981). For example, while de la Beaujardière et al. (1981) sees the combination arc as a low-altitude signature of a step like shear flow in the magnetosphere, Marklund (1984) considers it as a combination of polarization arc equatorward and Birkeland arc poleward, superposed on the decreasing convection field toward the reversal boundary.

For Marklund (1984) the classifying criterion is the mechanism providing the current continuity. He expresses the competition between Birkeland currents and polarization in an equation similar to that of de la Beaujardière et al. (1981):

$$E_{\xi}^A = E_0 + J_{\parallel} / \Sigma_P^A \quad (5.9)$$

with:

$$E_0 = \frac{\Sigma_P^E}{\Sigma_P^A} E_{\xi}^E + \left( \frac{\Sigma_H^A}{\Sigma_P^A} - \frac{\Sigma_H^E}{\Sigma_P^A} \right) E_{\eta}^E \quad (5.10)$$

Note that we changed the original notation,  $(x, y)$ , to  $(\xi, \eta)$ . The geometry assumed by Marklund (1984) is shown in Fig. 5.2. Idealizing assumptions are, again, a block structure of the ionosphere (inside and outside of the arc) and infinite extension along the  $\eta$  direction. The parallel currents flow in thin sheets at the steep borders that separate the arc from the rest of the ionosphere. The tangential component of the electric field is continuous,  $E_{\eta}^E = E_{\eta}^A$ , as required by Faraday's law.

When  $E_{\xi}^A$  is roughly equal to  $E_0$  in Eq. 5.9 the polarization mechanism prevails. Intuitively this can be understood by considering the first term in Eq. 5.10 to be dominant. Then  $E_{\xi}^A \cong E_0$  implies  $J_{\parallel} \ll \Sigma_P^E E_{\xi}^E$ , that is the parallel current is much smaller than the ambient ionospheric current. In such a case the parallel current cannot have a significant contribution to

keeping the ionospheric current continuous and the polarization plays the major role. Marklund (1984) concluded that most of the arcs — evening arcs showing anti-correlation, or morning arcs showing correlation between conductance and electric field — are polarization arcs. This point is further commented in Section 5.2.

It is appropriate to mention here that already Coroniti and Kennel (1972) discussed the close relationship between FACs and polarization as means to provide the current continuity in the auroral ionosphere. However, this early paper addresses the auroral oval as a whole and is more theoretically oriented. Marklund (1984) concentrates on the smaller scale arc features and relies on a large collection of data sets, that became available in the meanwhile.

The experimental facts and models reviewed up to this point dealt with the modification of the large scale convection electric field, due to increased electron density inside the arc produced by precipitation. A qualitatively new effect was emphasized by Opgenoorth et al. (1990) and Aikio et al. (1993). Both papers point out the presence of an increased electric field in the proximity of an arc, either at the equator edge in the evening sector, or at the polar edge in the morning sector. This overshoot was attributed to the low density region close to the arc, on the side where the downward return current flows. As this current is carried mainly by ionospheric electrons, a region of highly depleted plasma develops close to the arc. To compensate the low conductivity and preserve the current continuity a high electric field is necessary. Opgenoorth et al. (1990) measured increased E-region electron and F-region ion temperatures, which are proxies for intense electric fields, by using the EISCAT radar. Aikio et al. (1993) measured the electric field directly, by means of the STARE (Scandinavian Twin Auroral Radar Experiment) radar.

More recently Elphic et al. (1998) showed, by using FAST data, that the association of broad upward current regions, presumably connected to auroral arcs, with narrow intense downward currents flowing at the sides, is quite common for the auroral current circuit. Another experimental fact emphasized by Elphic et al. (1998) is the smooth character of the FAC, in contrast to the steep variations in the electron precipitation (and, consequently, conductance). Such a behavior suggests that the IEF adjusts itself so that the ionospheric current matches the input magnetospheric current — in other words that the magnetosphere acts rather as a current than as a voltage generator. This view is supported by a recent theoretical study of Vogt et al. (1999).

An additional contribution to the IEF comes from the high-altitude 'electrostatic shocks' (Mozer et al., 1977), that go along with the creation of the AAR. Although the largest part of this field is screened out by the parallel potential, a small fraction makes it to the ionosphere, because of the 'U'+ 'S' geometry (Fig. 1.3). The superposition of the AAR structure over the convection electric field results in deviations from the ideal 'U' configuration, as shown in Fig. 5.3.

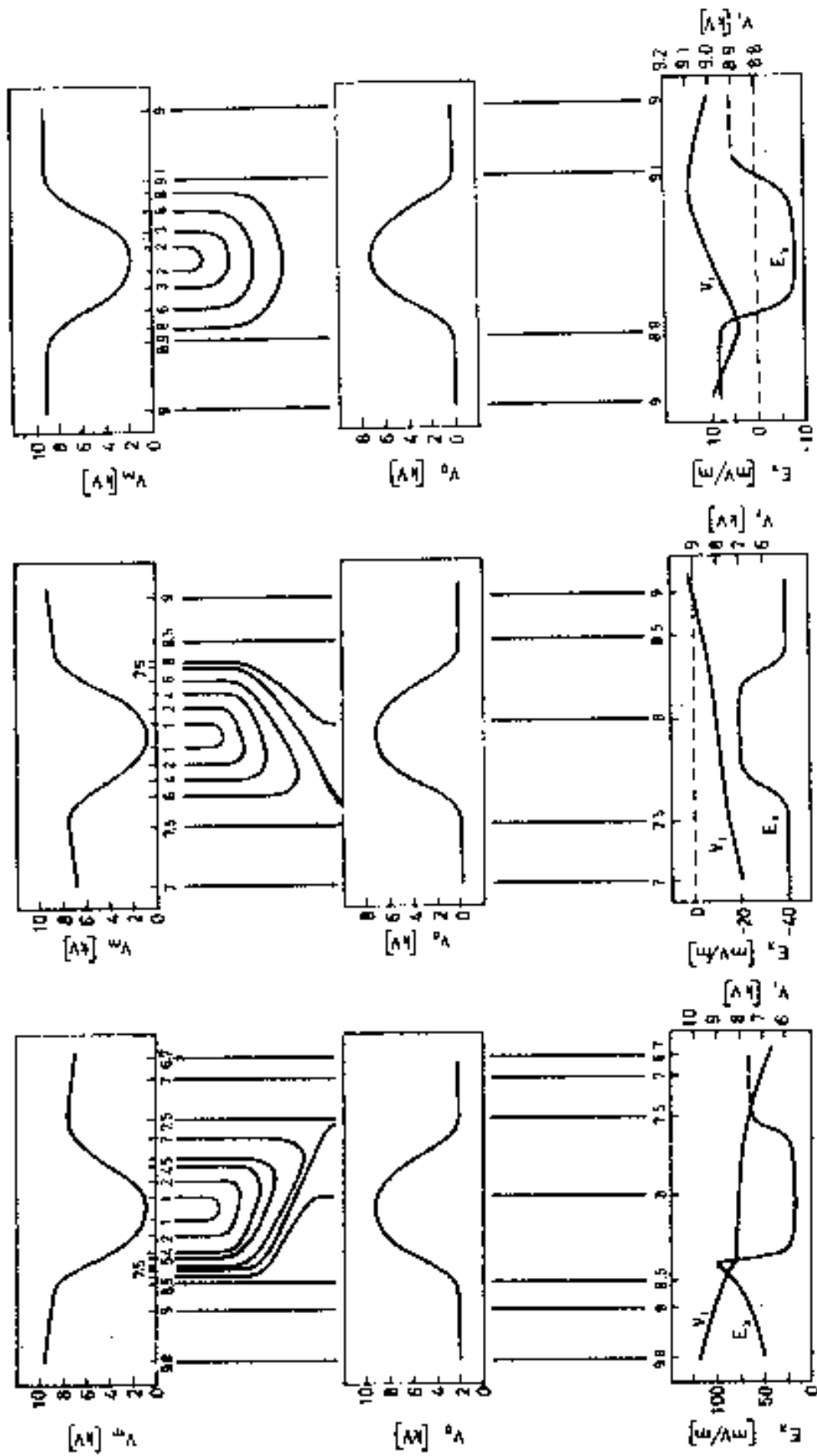


Figure 5.3: High-altitude and ionospheric potential together with the geometry of the AAR. **Left:** Evening arc embedded in northward convection field. **Middle:** Morning arc embedded in southward convection field. **Right:** Reversal arc. North is to the right. Figure 9 from Marklund (1984).



## 5.2 Comments

In the previous Section we outlined several relationships between quantities relevant to ionospheric electrodynamics, with emphasis on the auroral arc. We also described models which help to understand these relationships. Here we shall discuss in more detail the idealizing assumptions associated with these models.

We start by writing the current closure equation at the top of the ionosphere (in Section 5.4 we shall concentrate on an alternative form):

$$j_{\parallel} = \nabla \cdot \mathbf{J}_{\perp} = \frac{\partial}{\partial \xi} (\Sigma_P E_{\xi} - \Sigma_H E_{\eta}) + \frac{\partial}{\partial \eta} (\Sigma_H E_{\xi} + \Sigma_P E_{\eta}) \quad (5.11)$$

which can be easily transformed into:

$$\begin{aligned} j_{\parallel} = & \underbrace{E_{\xi} \left( \frac{\partial \Sigma_P}{\partial \xi} + \frac{\partial \Sigma_H}{\partial \eta} \right)}_{T_1} + \underbrace{E_{\eta} \left( \frac{\partial \Sigma_P}{\partial \eta} - \frac{\partial \Sigma_H}{\partial \xi} \right)}_{T_2} + \\ & \underbrace{\Sigma_P \left( \frac{\partial E_{\xi}}{\partial \xi} + \frac{\partial E_{\eta}}{\partial \eta} \right)}_{T_3} + \underbrace{\Sigma_H \left( \frac{\partial E_{\xi}}{\partial \eta} - \frac{\partial E_{\eta}}{\partial \xi} \right)}_{T_4} \end{aligned} \quad (5.12)$$

The two equations above are written in the Arc Associated System (see Fig. 3.4) and the symbols have their usual meaning. Before proceeding to explore possible simplifications, we would like to comment on the significance of the 4 terms above.

We start with  $T_4$ , which is usually neglected:

$$\frac{T_4}{\Sigma_H} = (\nabla \times \mathbf{E})_z = \frac{\partial B_z}{\partial t} = 0 \quad (5.13)$$

One can estimate how fast the variation of  $B_z$  should be, in order to make  $(\nabla \times \mathbf{E})_z \neq 0$ . By approximating  $(\nabla \times \mathbf{E})_z \simeq \Delta E/L$  and  $\partial B_z/\partial t \simeq \Delta B_z/T$ , we find that  $\partial B_z/\partial t$  becomes significant only for a time scale  $T \lesssim L \Delta B_z / \Delta E$ . With some typical values,  $\Delta E = 50 \text{ mV/m}$ ,  $L = 5 \text{ km}$ , and  $\Delta B_z = 500 \text{ nT} \approx 0.01 B_{Earth}$ , one obtains  $T \lesssim 5 \cdot 10^{-2} \text{ s}$ , which is much shorter than the duration of most auroral events.

For the other three terms in Eq. 5.12, one can look at them from different viewpoints:

- A possibility is to regard  $T_1$  and  $T_2$  as being of magnetospheric, and  $T_3$  of ionospheric origin.  $T_1$  and  $T_2$  arise because of inhomogeneous ionospheric conductance, mainly caused by magnetospheric electron precipitation. On the other hand, if we disregard  $\partial E_k / \partial z$ , which is legitimate in the ionosphere,  $T_3$  can be related to the ionospheric polarization,  $T_3 / \Sigma_P \equiv \nabla \cdot \mathbf{E} = \rho_e / \epsilon_0$ .

- Boström (1974) associated opposite meanings with  $(T_1, T_2)$  and  $T_3$ . He considered that  $T_1$  and  $T_2$  to be of ionospheric origin, because they express the variation of ionospheric conductances, while  $T_3$  has magnetospheric origin, because the variation of the IEF is related to the magnetospheric convection. Boström's view was adopted by many other authors (more recently e. g. Sato et al., 1995; Sofko et al., 1995). However, these papers address the medium scale Birkeland currents region. When discussing about the auroral arc, rather in the small scale range, one would expect that the changes in the electric field originate mainly in the polarization and not so much in the variation of the magnetospheric convection.
- Another option is to use the labels 'magnetospheric' or 'ionospheric' depending on the orientation of the respective partial current as related to the electric field: if  $\mathbf{J} \cdot \mathbf{E} > 0$  the ionosphere behaves like a load, dissipating magnetospheric energy, while for  $\mathbf{J} \cdot \mathbf{E} < 0$  the ionosphere behaves like a dynamo, pumping energy into magnetosphere. Let us consider an ideal configuration: the magnetosphere imposes the field  $E_\eta$ , along the arc, while  $E_\xi$  develops transverse to the arc, so that the associated Pedersen current balances the Hall current driven by  $E_\eta$ . According to the above criterion, emphasized by e. g. Haerendel (1990), only half of  $T_2$ , that is  $-E_\eta \partial \Sigma_H / \partial \xi$ , can be termed as 'ionospheric'.

To conclude this discussion, we tend to support the idea that, in the coupled M-I system, it is better to avoid labeling the terms in Eq. 5.12 (see also Kosch et al. (2000) in this sense).

The current closure Eq. 5.12 is suited to discuss the arc classification scheme of Marklund (1984). By disregarding  $T_4$  one can re-write Eq. 5.12 as:

$$T_1 + T_2 = j_{||} - T_3 \quad (5.14)$$

In this form it is evident that electron precipitation excess has to be absorbed by either polarization or FACs. To evaluate the relative contribution of the two mechanisms Rothwell et al. (1984) introduced the phenomenological parameter  $\alpha$  in a WTS study. Later, Lysak (1986) was able to express  $\alpha$  in terms of other parameters — basically conductances — characterizing the coupled M-I system, and investigated its variation for typical values of these parameters. As Lysak's (1986) results are not geometry dependent (in particular his Fig. 1) they can be used in the arc case to show that for a Pedersen conductance larger than  $\sim 2 \text{ mho}$  the arc is almost completely polarized.

Such a statement seems to contradict the common sense and to disagree with the classification from Marklund (1984): The auroral arcs are normally associated with FACs, which provide the continuity mechanism for Birkeland arcs. However, even the intense FACs are usually small when compared to the ionospheric currents. Consequently, they take over only a reduced fraction of the current that would develop in the absence of polarization (see also the discussion at p.77).

Considering this fact, one would expect to find Birkeland arcs only reasonably close to the convection reversal, where the ambient ionospheric electric field (and current) is small enough. One should also add that the balance between polarization and FAC is intrinsically continuous and cannot be fully captured with a model based on several homogeneous regions.

### 5.3 Qualitative evaluation of the simplifying assumptions

We concentrate further on the possible simplifications of Eq. 5.12 and check, at a qualitative level, whether they are appropriate to fit our data (Chapters 3 and 4). We start by assuming that:

1. the field configuration is stationary,  $T_4 = 0$
2. there is no variation along the arc,  $\partial/\partial\eta = 0$
3. there is no Hall current perpendicular to the arc,  $E_\eta = 0$
4. the conductance distribution is homogeneous not only along but also across the arc

Altogether, Eq. 5.12 reduces to:

$$j_{||} = \Sigma_P \frac{dE_\xi}{d\xi} \quad (5.15)$$

Taking into account that for sheet geometry the Ampere's law writes:

$$j_{||} = 1/\mu_0 \cdot dB_\eta/d\xi \quad (5.16)$$

Eq. 5.15 can be integrated to:

$$B_\eta = \mu_0 \Sigma_P E_\xi + \text{const.} \quad (5.17)$$

which is the same as Eq. 5.7, as long as  $\Sigma_P = \text{const.}$

The assumption that the conductance is constant across the arc is obviously not correct, as one can guess by looking at the electron energy flux (Fig. 3.11). The computation (Fig. 4.4) confirms this evaluation. Even if Eq. 5.17 holds,  $\Sigma_P$  cannot be taken as constant.

Further, we check the assumption that only the Pedersen current closes the FAC in the ionosphere. For the purpose of this preliminary discussion we neglect the small rotation of the AAS with respect to the SAS (Fig. 3.4) and loosely take  $x \equiv \xi$ . Disregarding the Hall current is not supported by the data. The southward drift of the arc stands for a westward component of the electric field (Section 3.3), in a reference frame related to the ground (in the plasma frame the electric field can vanish, i. e. the arc can be 'frozen' into the plasma). In the presence of a non-homogeneous Hall conductance the westward electric field — which is constant, by Faraday's law, as long as we neglect temporal variations and consider the arc to be longitudinally homogeneous — drives a Hall current in the N–S direction whose divergence is not zero.

On the other hand, as the arc is north of the convection reversal, the Pedersen current flows southward. It would be difficult to close the FAC circuit in the absence of a Hall current flowing to the north. As the data are obtained in the winter time, current contributions coming from outside the auroral oval, in particular from the polar cap, are potentially not very substantial.

An important piece of information which was not used yet is the optical evidence that the width of the arc is not constant. Consequently, the intensity of the electrojet associated with the arc might have a longitudinal variation. An arc model that takes into account the coupling between the FAC and the electrojet would have better chances to fit the experimental data.

The discussion up to this point can be summarized as follows: To explain the data one has, as a minimum, to give up the assumptions of homogeneous conductance perpendicular to the arc, and vanishing electric field parallel to the arc. In such a case — still idealized — the FAC closes perpendicular to the arc, through Pedersen and Hall currents, and this current system is not coupled with the electrojet. One can proceed further relatively easy and parametrize this coupling as well. The formulation of a strategy able to provide the variation of  $E_\xi$  across the arc, the constant value of  $E_\eta$ , and a proper parametrization of the coupling between the FAC and the electrojet is the object of the next Section. This strategy is applied to our case-study data in Chapter 6.

There are two more steps possible, in order to get a fully realistic arc model:

1. taking into account non-potential electric fields,  $\partial E_\xi / \partial \eta \neq \partial E_\eta / \partial \xi \Leftrightarrow \partial B_z / \partial t \neq 0$
2. giving up the arc symmetry, which is based on cartesian coordinates

Step 1 would be appropriate for auroral forms with rapid variations of intensity (see the discussion at p. 79). Step 2 would open the possibility to investigate 2D structures, like the WTS or omega band, but could lead to a more accurate modeling of the arc as well.

## 5.4 Ionospheric electric field from satellite data

Deriving the IEF from satellite measurements is in principle trivial, as long as the magnetic field line below the satellite is equipotential. One has just to map the satellite measured field to ionospheric level. This is no longer possible when the satellite crosses the AAR. For such cases, when there is a potential drop below the satellite, one has to use additional data to find the IEF. One possibility would be to add the ion average energy to the high-altitude potential, in order to estimate the ionospheric potential and further the IEF. However, the ion average energy reflects not only the potential difference between the ionosphere and the measuring point, but also non-potential energization by e. g. wave-particle interactions. A better method for the evaluation of the IEF would be desirable.

We begin by casting the current closure equation in cartesian coordinates in a form suited for processing satellite data input (a more general expression, valid in arbitrary orthogonal curvilinear coordinates, is derived in Appendix D). Next, we examine possible solutions of this equation for an infinite straight arc. In this case the coupling between the FAC system and the electrojet is implicitly disregarded. Finally, we show how this coupling can be taken into account by just slightly extending the formalism developed for the infinite straight arc.

### 5.4.1 Current closure in cartesian coordinates

We give the full derivation, step by step, in order to make clear the generality of the result. The choice of the reference system is unimportant, as long as the  $z$  axis is parallel to the magnetic field; we neglect the small inclination,  $\sim 15^\circ$ , of the auroral magnetic field lines, with respect to the direction perpendicular to ionosphere.

Charge conservation is expressed by the continuity equation:

$$\frac{\partial \rho}{\partial t} + \nabla \cdot \mathbf{j} = 0 \quad (5.18)$$

Because of the very high conductivity of the plasma along the magnetic field (see Fig.4.1) the time dependent term in Eq. 5.18 can be disregarded and the charge conservation turns into the current continuity equation (for a proof that  $\partial \rho / \partial t$  is indeed much smaller than  $\nabla \cdot \mathbf{j}$  see Akhiezer et al. (1975), Chap. 1):

$$\nabla \cdot \mathbf{j} = 0 \Rightarrow \partial j_{\parallel} / \partial z = -(\partial j_x / \partial x + \partial j_y / \partial y) \quad (5.19)$$

Further we integrate between the top and the bottom of the ionosphere. These are not sharp boundaries, but the transverse conductivity is concentrated mostly in the altitude range 90–150km and is negligible below 70km and above 250km (e. g. Brekke and Moen, 1993). With respect to current closure one can consider these heights as the appropriate 'bottom' and 'top' of the ionosphere, respectively.

Integrating Eq. 5.19 between 'top' and 'bottom' ( $z = 0$  and  $z = z_0$  in our reference system) and taking into account that no significant FAC flows below 'bottom', in the neutral atmosphere, one obtains for the l.h.s. term:

$$\int_0^{z_0} \partial j_{\parallel} / \partial z = j(z_0) - j(0) = -j(0) \equiv -j_{\parallel}^{top} \quad (5.20)$$

where  $j_{\parallel}^{top}$  designates the downward parallel current at the 'top' of the ionosphere.

For the r.h.s. of Eq. 5.19, we express  $j_x$  and  $j_y$  according to Ohm's law (Eq. 5.1) and neglecting the neutral winds (p. 47). In our coordinate system  $j_x$  and  $j_y$  write:

$$\begin{aligned} j_x &= \sigma_P E_x - \sigma_H E_y \\ j_y &= \sigma_H E_x + \sigma_P E_y \end{aligned} \quad (5.21)$$

By integration along  $z$  and neglecting the variation of the electric field with the altitude (which is allowed due to the very high parallel conductivity) one obtains:

$$\begin{aligned} J_x &= \Sigma_P E_x - \Sigma_H E_y \\ J_y &= \Sigma_H E_x + \Sigma_P E_y \end{aligned} \quad (5.22)$$

and

$$j_{\parallel}^{top} = \frac{\partial J_x}{\partial x} + \frac{\partial J_y}{\partial y} \equiv \frac{\partial}{\partial x}(\Sigma_P E_x - \Sigma_H E_y) + \frac{\partial}{\partial y}(\Sigma_H E_x + \Sigma_P E_y) \quad (5.23)$$

with  $J_x, J_y$  the height-integrated ionospheric currents and  $\Sigma_P, \Sigma_H$  the height-integrated Pedersen and Hall conductivities (Section 4.1).

We express  $j_{\parallel}^{top}$  by using Ampere's law and neglecting the displacement current,  $\partial D / \partial t$  (neglecting the displacement current in the Ampere's law is of the same order with neglecting  $\partial \rho / \partial t$  in Eq. 5.18 — see Akhiezer et al. (1975), Chap. 1):

$$j_{\parallel} = \frac{1}{\mu_0} \left( \frac{\partial \Delta B_y^{ionos}}{\partial x} - \frac{\partial \Delta B_x^{ionos}}{\partial y} \right) \quad (5.24)$$

where by the notation  $\Delta B^{ionos}$  we emphasize the perturbative character of the transverse magnetic field and the fact that the perturbation is mapped to ionospheric level. With  $H \equiv \frac{\Delta B^{ionos}}{\mu_0}$  we finally obtain:

$$\begin{aligned} \frac{\partial}{\partial x}(H_y - J_x) &= \frac{\partial}{\partial y}(H_x + J_y) \quad \text{or} \\ \frac{\partial}{\partial x}(H_y - \Sigma_P E_x + \Sigma_H E_y) &= \frac{\partial}{\partial y}(H_x + \Sigma_H E_x + \Sigma_P E_y) \end{aligned} \quad (5.25)$$

In arc coordinates Eq. 5.25 writes:

$$\frac{\partial}{\partial \xi}(H_{\eta} - J_{\xi}) = \frac{\partial}{\partial \eta}(H_{\xi} + J_{\eta}) \quad (5.26)$$

Equation 5.25 represents the most general expression of the current continuity equation; no approximation was done, except for neglecting the displacement current and the charge density variation which presumably amounts to negligible errors for the ionospheric plasma. This statement could be false only for very dynamic transients. As already stated, the equation is equally valid in any cartesian coordinate system with the  $z$  axis parallel to  $\mathbf{B}$  — no particular use was made of the  $x$  and  $y$  orientations. Equation 5.26 illustrates this point.

Equation 5.26 is completely equivalent to Eq. 5.12. The two equations do express, however, different viewpoints: while Eq. 5.12 shows in detail the *local* balance between the FA and the ionospheric current, Eq. 5.26 is more appropriate to investigate the FAC sheet and its ionospheric continuation as a *whole*. Equation 5.26 expresses the coupling between the FAC system and the electrojet. The  $H_\xi$  component of the magnetic field is small in AAS coordinates (e. g. Fig. 3.4; for an infinite current sheet  $H_\xi = 0$ ) and  $\partial H_\xi / \partial \eta$  can be neglected when compared to  $\partial J_\eta / \partial \eta$  if the variation length scales of  $J_\eta$  and  $H_\xi$  are not too different (which is presumably true when the satellite crosses the current sheet close enough to its center). In this case the r.h.s. of Eq. 5.26 reduces to  $\partial J_\eta / \partial \eta$ , roughly equal to the longitudinal derivative of the electrojet current. Equation 5.26 says that the FAC closes not only transverse to the arc, but also along the arc.

We note that Sugiura (1984) expressed the current continuity in the form Eq. 5.25. However, he only used this form to show that Eq 5.7 is valid not only for E–W aligned FAC sheets but can be regarded as a general M–I coupling mode. With high resolution data, like that coming from FAST, one can try to use Eq. 5.26 to find small scale IEF solutions, corresponding to certain events. The next Section deals with the particular case of an auroral arc that can be reasonably described by assuming longitudinal homogeneity.

#### 5.4.2 Determination of the IEF for the infinite straight arc

Consideration of an infinite straight arc reduces Eq. 5.26 to:

$$H_\eta - J_\xi = \text{const.} = c_0 \quad (5.27)$$

If the AAS is rotated by the angle  $\theta$  with respect to the SAS then:

$$v_\xi = v_x \cos \theta + v_y \sin \theta, \quad v_\eta = -v_x \sin \theta + v_y \cos \theta \quad (5.28)$$

where  $\mathbf{v}$  is an arbitrary vector. Equation 5.27 transforms to:

$$H_y - H_x \tan \theta - J_x - J_y \tan \theta = \frac{c_0}{\cos \theta} \quad (5.29)$$

or

$$H_x \tan \theta + (\Sigma_P + \Sigma_H \tan \theta) E_x + (-\Sigma_H + \Sigma_P \tan \theta) E_y + \frac{c_0}{\cos \theta} = H_y \quad (5.30)$$

The unknown quantities in Eq. 5.30 are  $\tan \theta$ ,  $E_x$ ,  $E_y$  and  $c_0$ .  $H_x$ ,  $H_y$  are measured and  $\Sigma_P$ ,  $\Sigma_H$  can be determined from the measured particle distributions (see Chapter 4). The angle  $\theta$  can also be determined from magnetic field and/or optical data, but for the time being we shall consider it as unknown. This provides an additional degree of freedom, in order to accommodate situations

when the electrojet is not parallel to the arc; the experimental data show that this is not unusual (e. g. Evans et al., 1977). It has to be emphasized here the following distinction:

- For an ideal case the equations above state that the arc is homogeneous along the direction  $\theta$  and all the physical quantities are constant along this direction.
- In the case of a real arc, described with real data, we can still try to use Eq.5.27 as starting point, but the angle  $\theta$  to be determined by fit just shows the flow direction of the electrojet, which in turn is not an exact result. When deriving  $\theta$ , i. e. one parameter, we impose the electrojet an invariant flow direction. This approximation may be good enough for arcs, but not for auroral forms with more complicated geometries.

In the next Chapter we shall complete this discussion with results based on experimental data. In particular, in Section 6.4.5 we shall check how these results change when using  $\theta$  as provided by the magnetic data, instead of considering it as an unknown parameter. Note that for the calculations to follow by  $(\xi, \eta)$  we understand the coordinates  $(\xi_F, \eta_F)$  provided by fit, which are not identical to the AAS coordinates (Fig. 3.4).

To get a reasonably well defined physical problem one has to add to Eq.5.30 the condition Eq. 5.13 that the field is electrostatic:

$$\frac{\partial E_\eta}{\partial \xi} = \frac{\partial E_\xi}{\partial \eta} \quad (5.31)$$

This condition has two consequences:

1. One can define an electric potential, and evaluate it by integrating the measured electric field along the satellite path. Even when the satellite crosses ion beams, one can still integrate between the start and the end of the beam. Assuming that the magnetic field lines at the boundaries of the beam are equipotentials, one obtains the potential drop at ionospheric level and, consequently, the average IEF,  $E_{0x}$ :

$$\int_{s_1}^{s_2} E_x ds = \int_{s_1}^{s_2} E_{0x} ds = E_{0x}(s_2 - s_1) \equiv E_{0x}L = -\Delta\Phi \Rightarrow E_{0x} = -\Delta\Phi/L \quad (5.32)$$

2. Because of the assumed homogeneity along the arc,  $\partial E_\xi / \partial \eta \equiv 0$ , and by using Eq. 5.31 we get

$$E_\eta = \text{const.} = b(\eta) \quad (5.33)$$

In the following we shall take  $b(\eta) \equiv b_0 = \text{const.}$  This assumption is further discussed in Section 6.5.4. From  $-E_x \sin \theta + E_y \cos \theta = E_\eta = b_0$  it results

$$E_y = E_x \tan \theta + b_0 / \cos \theta \quad (5.34)$$



By introducing Eq. 5.34 in Eq. 5.30 we obtain:

$$H_x \tan \theta + \Sigma_P (1 + \tan^2 \theta) E_x + (-\Sigma_H + \Sigma_P \tan \theta) \frac{b_0}{\cos \theta} + \frac{c_0}{\cos \theta} = H_y \quad (5.35)$$

It is convenient to write  $E_x$  as:

$$E_x = E_{0_x} + \delta E_x \quad (5.36)$$

where  $\delta E_x$  is the deviation from the average, not necessarily small. We require that the integral of  $\delta E_x$  over the satellite path vanishes:

$$\int_{s_1}^{s_2} \delta E_x ds = 0 \quad (5.37)$$

A natural parametrization of  $\delta E_x$  is achieved by using orthogonal polynomials (Appendix E). In our case the proper choice is represented by either Legendre polynomials,  $(P_n)$ , or Jacobi polynomials belonging to the weight function  $p(x) = 1$ , from now on termed just Jacobi polynomials,  $(J_n)$ . Both of them satisfy by definition Eq. 5.37. As  $(P_n)$  and  $(J_n)$  are equivalent,  $P_n(x) = J_n(\frac{1-x}{2})$ , the results should not depend on which of the two systems is used. The practical confirmation of this theory (see Appendix E) provides support for the correctness of the numerical results to be derived in Chapter 6.

For the time being we just write the expression of  $\delta E_x$  without specifying whether we use Jacobi or Legendre polynomials:

$$\delta E_x = \sum_{i=1}^{i=n_x} a_i G_i \quad (5.38)$$

The summation in 5.38 starts from index 1 because the constant term, corresponding to index 0, was explicitly written as  $E_{0_x}$ . We shall return in Section 6.2.2 to the determination of  $n_x$ .

Introducing the parametrization 5.38 in Eq. 5.35 we finally obtain:

$$H_x \tan \theta + \Sigma_P E_{0_x} \tan^2 \theta + \Sigma_P (1 + \tan^2 \theta) \sum_{i=1}^{n_x} a_i G_i + (-\Sigma_H + \Sigma_P \tan \theta) b_0 \sqrt{1 + \tan^2 \theta} + c_0 \sqrt{1 + \tan^2 \theta} = H_y - \Sigma_P E_{0_x} \quad (5.39)$$

The l.h.s. of Eq. 5.39 depends on the unknown parameters  $\tan \theta, a_1, \dots, a_{n_x}, b_0, c_0$ , whereas the r.h.s. is fully determined by experimental measurements. In the most general case the unknown parameters can be found by non-linear minimization of a  $\chi^2$  type expression (Eq. 6.2). Equation 5.39 can be written in condensed form as:

$$y_{ft_k} = y_{ms_k} \quad (5.40)$$

where the indices “ft” and “ms” express that the l.h.s. contains parameters to be found by numerical fit, whereas the r.h.s. results from measurements. The index “k” emphasizes the fact that Eq. 5.40 is written for every measurement point,  $P_k$ .

A full consideration of the numerical fit problem is the object of Chapter 6. Here we shall only add a brief discussion on possible simplifications of Eq. 5.39. By setting some of the unknown coefficients in Eq. 5.39 equal to 0 we can model a polarized or non-polarized arc, considering or not the Hall contribution to the current closure. For each of the following models a linear version is obtained if the electrojet is assumed to flow parallel to the arc and  $\tan \theta$  derived from the magnetic data is used. The bracketed “L” in the name indicates the possible linear model.

1. Model NPNH(L) (No Polarization No Hall): With  $E_\eta = 0$  and  $E_\xi = \text{const.}$ , which implies  $b_0 = 0$  and all the terms  $a_i G_i = 0$ , we have the simplest model: a non-polarized arc,  $\nabla \cdot \mathbf{E} = 0$ , without Hall current. The ionospheric closure of the FAC is achieved by Pedersen current only. Equation 5.39 becomes:

$$H_x \tan \theta + \Sigma_P E_{0x} \tan^2 \theta + c_0 \sqrt{1 + \tan^2 \theta} = H_y - \Sigma_P E_{0x} \quad (5.41)$$

In this case there are two parameters to be found,  $\tan \theta$  and the constant  $c_0$ .

2. Model NPYH(L) (No Polarization Yes Hall): If  $E_\xi = \text{const.}$  and  $E_\eta \neq 0$  the arc is still unpolarized but the Hall current contributes to the closure of the FAC and Eq. 5.39 becomes:

$$H_x \tan \theta + \Sigma_P E_{0x} \tan^2 \theta + (-\Sigma_H + \Sigma_P \tan \theta) b_0 \sqrt{1 + \tan^2 \theta} + c_0 \sqrt{1 + \tan^2 \theta} = H_y - \Sigma_P E_{0x} \quad (5.42)$$

The parameters to be found are  $\tan \theta$ ,  $b_0$ ,  $c_0$ .

3. Model YPNH(L) (Yes Polarization No Hall): With  $E_\eta = 0$  and  $E_\xi$  variable one models a polarized arc,  $\nabla \cdot \mathbf{E} \neq 0$ , where the FAC closes through Pedersen current; no Hall current is present. Equation 5.39 becomes:

$$H_x \tan \theta + \Sigma_P E_{0x} \tan^2 \theta + \Sigma_P (1 + \tan^2 \theta) \sum_{i=1}^{n_x} a_i G_i + c_0 \sqrt{1 + \tan^2 \theta} = H_y - \Sigma_P E_{0x} \quad (5.43)$$

There are  $n+2$  parameters to be found:  $\tan \theta$ , the coefficients  $a_1 \cdots a_n$ , and the constant  $c_0$ .

4. Model YPYH(L) (Yes Polarization Yes Hall): Last possibility is to let Eq. 5.39 as it is, i. e. consider  $E_\xi \neq \text{const.}$  and  $E_\eta \neq 0$ . This means that both the arc polarization and the Hall current are allowed to contribute the ionospheric closure of the FAC. This is the most general form of the current closure equation that can be obtained by disregarding the variations along the arc, and implicitly neglecting the coupling between the FAC system and the electrojet. We shall see in Section 6.3.3 that even for quiet, pre-breakup arcs, Eq. 5.39 is still too idealized to get consistent results.

### 5.4.3 Parametrization of the FAC–electrojet coupling

The easiest way to model the coupling between the FAC system and the arc associated electrojet is to set the r.h.s. of Eq. 5.26 equal to a constant  $\tilde{c}_1$ :

$$\frac{\partial}{\partial \eta}(H_\xi + J_\eta) = \tilde{c}_1 \quad (5.44)$$

As discussed at p. 85, if  $(\xi_A, \eta_A)$  are the AAS coordinates,  $\partial H_{\xi_A}/\partial \eta_A$  may, in general, be neglected. However, in the  $(\xi_F, \eta_F)$  system  $\partial H_{\xi_F}/\partial \eta_F$  is not necessarily negligible. By considering the transform Eq. 5.28, with the rotation angle  $\theta_{AF} = \theta_F - \theta_A$  ( $\theta_A \equiv \theta_{mag}$ ), one obtains:

$$\frac{\partial H_{\xi_F}}{\partial \eta_F} = \cos^2 \theta_{AF} \frac{\partial H_{\xi_A}}{\partial \eta_A} + \sin \theta_{AF} \cos \theta_{AF} \frac{\partial H_{\eta_A}}{\partial \eta_A} - \sin \theta_{AF} \cos \theta_{AF} \frac{\partial H_{\xi_A}}{\partial \xi_A} - \sin^2 \theta_{AF} \frac{\partial H_{\eta_A}}{\partial \xi_A} \quad (5.45)$$

Because of the sheet geometry the dominant term in Eq. 5.45 is the last one:

$$\frac{\partial H_{\xi_F}}{\partial \eta_F} \approx -\sin^2 \theta_{AF} \cdot \frac{\partial H_{\eta_A}}{\partial \xi_A} \approx -\sin^2 \theta_{AF} \cdot j_{||} \quad (5.46)$$

Note that, in the upward current region,  $j_{||} < 0$  and  $\partial H_{\xi_F}/\partial \eta_F > 0$ .

Equation 5.44 provides an estimation for the longitudinal length scale of the electrojet,  $L_\eta$ :

$$\left| \frac{\partial J_\eta}{\partial \eta} \right| \approx \frac{|J_\eta|}{L_\eta} \Rightarrow L_\eta \approx \left| \frac{J_\eta}{c_1 - \partial H_{\xi_F}/\partial \eta_F} \right| \approx \left| \frac{J_\eta}{c_1 + \sin^2 \theta_{AF} \cdot j_{||}} \right| \quad (5.47)$$

which reduces to

$$L_\eta \approx \left| \frac{J_\eta}{c_1} \right| \quad (5.48)$$

if  $\sin^2 \theta_{AF} \cdot j_{||}$  is negligible. In Section 6.4.1 we shall evaluate  $L_\eta$  and the relative importance of  $\partial H_{\xi_F}/\partial \eta_F$  from the experimental data.  $L_\eta$  will be shown to be in the range of several 100km, in good agreement with the expectations.

If we introduce Eq. 5.44 in Eq. 5.26 we get:

$$\frac{\partial}{\partial \xi}(H_\eta - J_\xi) = \tilde{c}_1 \quad (5.49)$$

which integrates to:

$$H_\eta - J_\xi = c(\eta) + \tilde{c}_1 \xi \quad (5.50)$$

In the following we shall disregard the dependence of  $c$  on  $\eta$  and set  $c(\eta) \equiv c_0 = \text{const.}$  This assumption implies that the variation in  $\eta$  associated with the arc crossing is small as compared to  $L_\eta$  and will be further discussed in Section 6.5.1. By writing Eq. 5.50 in SAS we get:

$$H_y - H_x \tan \theta - J_x - J_y \tan \theta = \frac{c_0 + \tilde{c}_1 \cos \theta x}{\cos \theta} = \frac{c_0 + c_1 x}{\cos \theta} \quad (5.51)$$

with  $y = 0$  along the satellite trajectory and  $\xi = x \cos \theta$ . Equation 5.51 is identical to Eq. 5.29, except for the term  $c_1 x$  on its r.h.s. Consequently, the fit formula Eq. 5.39 transforms to:

$$H_x \tan \theta + \Sigma_P E_{0_x} \tan^2 \theta + \Sigma_P (1 + \tan^2 \theta) \sum_{i=1}^{n_x} a_i G_i + (-\Sigma_H + \Sigma_P \tan \theta) b_0 \sqrt{1 + \tan^2 \theta} + (c_0 + c_1 x) \sqrt{1 + \tan^2 \theta} = H_y - \Sigma_P E_{0_x} \quad (5.52)$$

We shall associate Eq. 5.52 with the model YPYHX(L). The models NPNHX(L), NPYHX(L), and YPNHX(L) are obtained from NPNH(L), NPYH(L), and YPNH(L) by just changing  $c_0$  with  $c_0 + c_1 x$  in Eqs. 5.41, 5.42 and 5.43, respectively. Figure 6.21 in Section 6.6 could help to a better visualization of the models described above.

## 5.5 Summary

In this Chapter we reviewed some of the work done on ionospheric electrodynamics and discussed several of the frequently used approximations. It appears that a highly idealized model, consisting of regions with homogeneous conductance, and disregarding the Hall contribution to the current closure, is not appropriate for the data we have.

A new method to process the data was introduced, leading to the characterization of the ionosphere status along the footprint of the satellite path. By this method one can evaluate the longitudinal component of the IEF and the ionosphere polarization during intervals when ion beams are detected. The IEF was assumed as electrostatic and a cartesian coordinate system was used.

Two families of models were developed: For the first family the variations along the arc were disregarded and the coupling between the FAC system and the electrojet implicitly neglected. For the second family this coupling was taken into account through a coefficient which was shown to be related to the longitudinal length scale of the electrojet. Each model can be formulated either linearly, by assuming that the arc associated electrojet is parallel to the arc, or non-linearly, by including the electrojet orientation among the parameters to be found by fit.

As a last remark, one can note the similarities that exist between the AMIE and the method introduced here: both aim to finding the IEF by using multiple data sets. However, while the AMIE is appropriate for large scale problems and is mainly based on low resolution ground data, our method is oriented to small scale structures and is based on high resolution satellite data.

## Chapter 6

# FAST Orbit 1859: Electric field and current close to the arc

We concentrate further on the electrodynamics of the arc presented in Chapter 3. A large fraction of the Chapter is devoted to the derivation of the IEF during the ion beam period of orbit 1859. After some preliminaries (Section 6.1), we discuss the IEF obtained with the models NPNH, NPYH, YPNH, and YPYH (Sections 6.2 and 6.3). Although an improvement is visible with the increase in the complexity of the model some inconsistencies persist, because of neglecting the coupling between the electrojet and the FAC system. The results obtained with the models YPYHX and YPYHXL (Section 6.4), which take this coupling into account, are significantly better. The discussion of the two models is extended in Section 6.5.

Finally, in Section 6.6, we examine the 3D current flow which reveals an interesting and infrequent configuration: the transverse current that connects the downward and upward FAC sheets is very small and the FACs are continued in the ionosphere essentially parallel to the arc. This feature is related to the position of the convection reversal close to the boundary between the two current sheets, already pointed out in Section 3.2. Because the upward FAC is electrically decoupled from the downward FAC it is possible to treat the ion beam period as an independent unit, which is implicitly assumed in the first part of the Chapter. The southern boundary of this interval coincides with the convection reversal, as witnessed by the large scale potential (Fig. 6.22).

The underlying theoretical basis for the analysis presented here is the current conservation at ionospheric level, where the FAC is balanced by Pedersen and Hall currents, flowing both transverse and parallel to the auroral arc. We emphasize that although the auroral arcs are quite homogeneous in longitudinal direction, the coupling between the FAC and the electrojet should not be disregarded. This issue is particularly important for our atypical case.

## 6.1 Preliminaries

Before proceeding to show numerical calculations for the particular models we note that the fit problem posed by Eqs. 5.39 and 5.52 has the same quantity on its r.h.s., independent of the choice of the model. This quantity is:

$$y_{ms} = H_y - \Sigma_P E_{0_x} \quad (6.1)$$

We can regard the two terms involved in  $y_{ms}$  as the 'forcing' exerted by the magnetosphere on the ionosphere. It is particularly appropriate to say this in our case, as the SAS and MFA reference systems are practically identical (p. 27) during the inverted-V.  $H_y$  stands for the current pumped into the ionosphere, whereas  $E_{0_x}$  depends on the potential across the arc, mainly controlled by the magnetosphere.  $\Sigma_P$  imposes a structure over the quite flat  $H_y$ . This view, which is convenient here at least for practical reasons, leads to the following interpretation of the fit problem: given the 'forcing' of the magnetosphere, one tries to find, in a least-square sense, how the ionosphere changes to accommodate this forcing. To avoid confusion we should mention that the three quantities on the r.h.s. of Eq. 6.1 are not independent; their relationship is investigated in M-I coupling studies (e.g. Lysak, 1990, and references therein).

### 6.1.1 The ionospheric potential drop

As already noticed (Section 3.2) the electric field data is not usable during the time 8:22:37–8:22:47. This raises the question about how to estimate  $E_{0_x}$  for the time interval IALL=8:22:03.8–8:22:57.5, when ion beams are detected (Fig. 3.7).

To answer it we note first that IALL consists of an alternation of ion beams (IB) and ion conics (ICo) and can be naturally divided in five sub-intervals. The first and second column of Table 6.1 show the identifier of the ion beam or conic and the respective time period. The time origin is  $t_0 \equiv 8:22:00$ . ICo2, IB3, and ICo3 were grouped together under the identifier I4 because of a scale reason: the corresponding time stretch is 10.8s, comparable to the other four time intervals. Column 3 of the table shows the length of the satellite path projected at ionospheric level.

Table 6.1: Ion beams and conics during Orbit 1859

Id	$\Delta t$	$L[km]$	$\Delta \Phi[V]$	$E_{0_x}[mV/m]$
I1 (IB1)	03.8–13.8	28.5	482	-16.9
I2 (ICo1)	13.8–26.9	36.7	455	-12.4
I3 (IB2)	26.9–37.7	30.5	(500, 350)	(-16.4, -11.5)
I4 (ICo2, IB3, ICo3)	37.7–48.5	30.5	(500, 350)	(-16.4, -11.5)
I5 (IB4)	48.5–57.5	26.1	292	-11.2
IALL	03.8–57.5	152.3	(2229, 1929)	(-14.6, -12.7)

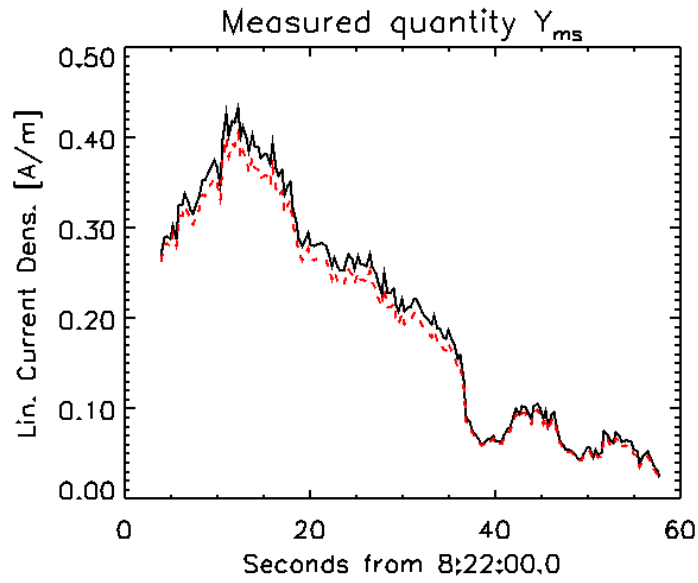


Figure 6.1:  $Y_{ms}$ , the quantity on the r.h.s. of Eqs. 5.39 and 5.52, fully determined from the experimental data. The black solid line corresponds to an ionospheric potential  $\Delta\Phi = 2250\text{V}$ , the red dotted line to  $\Delta\Phi = 2000\text{V}$ .

Columns 4 and 5 show the potential difference across each path segment and the corresponding  $E_{0_x}$ . For I3 and I4 some reasonable upper and lower limits are suggested, based on the values for the other three intervals.

Figure 6.1 shows the variation of  $y_{ms}$  for the time interval IALL. The upper curve corresponds to  $E_{0_x} = -14.8\text{mV/m}$ , the lower one to  $E_{0_x} = -13.1\text{mV/m}$ . The first value of  $E_{0_x}$  was obtained for an ionospheric potential drop  $\Delta\Phi = 2250\text{V}$ , which results by rounding off the sum of potentials in column 4 of Table 6.1, with the upper limit taken for I3 and I4. For the second value of  $E_{0_x}$  a total potential drop  $\Delta\Phi = 2000\text{V}$  was used, with the potential drop over I3 and I4 close to its lower limit.

### 6.1.2 The fit procedure

The fit procedure consists in minimizing a  $\chi^2$  type expression:

$$f = \sum_{k=1}^N \frac{(y_{ms_k} - y_{ft_k})^2}{\sigma_k^2} \quad (6.2)$$

with both  $y_{ms_k}$  and  $y_{ft_k}$  introduced first in Eq. 5.40.  $N$  is the total number of measuring points;  $N = 171$  for fitting over IALL. For an interval of  $\sim 10$  s, comparable to the duration of the 'units' I1...I5, FAST Survey data provides  $N \approx 33$  points. The minimum of  $f$  is found by a numerical algorithm. More details on the statistical significance of  $f$ , on the minimization procedure, and on the computer implementation of this procedure are presented in Appendix F.

**The weighting factor  $1/\sigma_k^2$** 

In Eq. 6.2  $\sigma_k$  is the error of the measurement  $y_{ms_k}$ . By applying the error propagation formula we get:

$$\sigma_k^2 = \sigma_{H_y}^2 + E_{0_x}^2 \sigma_{\Sigma_P}^2 + \sigma_{E_{0_x}}^2 \Sigma_P^2 \quad (6.3)$$

One has to look how the error terms compare. For the first term we have to take into account that  $\mathbf{B}$  is obtained as the difference between a measured and a model field,  $\mathbf{B} = \mathbf{B}_{ms} - \mathbf{B}_{model}$ , and consequently:

$$\sigma_{B_y}^2 = \sigma_{B_{ms}}^2 + \sigma_{B_{model}}^2 \quad (6.4)$$

The measurement error is mainly the quantization error, amounting to  $\sim 2\text{nT}$  (see Section 2.1.2). Since  $H$  is obtained from  $B$  by dividing through  $\mu_0 \equiv 4\pi \cdot 10^{-7}$ , it results  $\sigma_{H_{ms}} \approx 2 \times 10^{-2} / 4\pi \approx 2 \times 10^{-3} \text{ A/m}$ . When FAST is near the apogee, this number should be multiplied by a factor of  $\sim 2$  in order to get  $\sigma_{H_{ms}}$  at ionospheric level. The result is still quite small, when compared to the typical values of the ionospheric currents, of several 0.1 A/m.

The model error is, however, more important. The reason is the inaccurate knowledge provided by the IGRF (IGRF95 in our case). A discussion of the error sources in the IGRF models is given at <http://www.ngdc.noaa.gov/IAGA/wg8/igrfhw.html>. Based on this, we shall take as a typical error in the  $B_y$  component the value of 10nT. By dividing through  $\mu_0$  we get  $\sim 10^{-2} \text{ A/m}$ , a value comparable to the other error terms, as we shall see.

The evaluation of the second error term was basically done in the previous Chapter. Assuming a typical Pedersen conductance of  $\sim 10\text{mho}$  and a relative error of  $\sim 10\%$  we get  $\sigma_{\Sigma_P} \approx 1\text{mho}$ . With an electric field of  $\sim 10\text{mV/m}$  a rough estimation for the error contributed by the conductance term amounts also to  $\sim 10^{-2} \text{ A/m}$ .

For the third term, the discussion in Section 6.1.1 suggests an imprecision in  $\Delta\Phi$ , and consequently in  $E_{0_x}$ , of about 10%. With  $E_{0_x} \approx 10\text{mV/m}$  and  $\Sigma_P \approx 10\text{mho}$ , we get once more an error of  $\sim 10^{-2} \text{ A/m}$ .

By adding the 3 terms in Eq. 6.3 and taking the square root we get a total error  $\sigma_k \approx 2 \cdot 10^{-2} \text{ A/m}$ . However, instead of keeping all the three error terms in  $\sigma_k$ , which would be the rigorous approach, we shall discard the imprecision due to the errors in the magnetic and electric field and keep only the conductance term. This influences the actual minimum value of  $f$  in Eq. 6.2 but presumably not too much the parameter values. We shall check the dependence of the results on the assumed error in the second unit of Section 6.4.3.



## 6.2 The infinite straight arc: calculations

We explore next the models introduced in Section 5.4.2. We only discuss the non-linear models: NPNH, NPYH, YPNH, and YPYH. The results obtained with the linear instances are not substantially different. For each model we will show the currents  $J_{par}$  and  $J_{ion}$ , as well as the components of the IEF,  $E_x$  and  $E_y$ .  $J_{par}$  and  $J_{ion}$  are obtained from  $y_{ms}$  and  $y_{ft}$  respectively, by adding  $(\Sigma_P E_{0x} - H_x \tan \theta)$  and multiplying the result with  $\cos \theta$ :

$$J_{par} = (H_y - H_x \tan \theta) \cos \theta = H_y \cos \theta - H_x \sin \theta \equiv H_\eta \quad (6.5)$$

$$\begin{aligned} J_{ion} &= (y_{ft} + \Sigma_P E_{0x} - H_x \tan \theta) \cos \theta \\ &= (\Sigma_P E_x (1 + \tan^2 \theta) + (-\Sigma_H + \Sigma_P \tan \theta) \frac{b_0}{\cos \theta} + \frac{c_0}{\cos \theta}) \cos \theta \\ &= (\Sigma_P (E_x + E_y \tan \theta) - \Sigma_H (-E_x \tan \theta + E_y)) \cos \theta + c_0 \\ &= \Sigma_P E_\xi - \Sigma_H E_\eta + c_0 = J_\xi + c_0 \end{aligned} \quad (6.6)$$

To get Eq. 6.6 we introduced Eqs. 5.28 and 5.34 on the l.h.s. of Eq. 5.39. If one measured an ideal, infinite and parallel FAC sheet,  $H_\eta$  would be the linear density of the FA current and  $J_{ion}$  the ionospheric current transverse to the arc, plus the constant  $c_0$ . As we work with real data, the directions  $\xi$  and  $\eta$  are not related to the FAC sheet, but to the flow direction of the ionospheric electrojet (see the discussion at p. 86). Note that the figures to come show  $J_\xi + c_0$  instead of  $J_\xi$ , in order to make clear how good is the agreement between the experimental data and the fit.

The non-polarized arc models, NPNH and NPYH, are presented first. Then, as a preparation for the polarized models, the limit imposed by the data to the expansion in orthogonal polynomials is discussed. Section 6.2.3 presents the results from the models YPNH and YPYH. The fitted parameters are listed in Table 6.2 and discussed in detail in Section 6.3.1.

### 6.2.1 Non-polarized arc

The model NPNH, Eq. 5.41, disregards the Hall current and depends on just 2 parameters,  $\tan \theta$  and  $c_0$ . The model NPYH, Eq. 5.42, takes into account the Hall term by adding the parameter  $b_0$ .

#### Hall term = 0

The top panels of Fig. 6.2 show the results obtained for the model NPNH. As expected, there is a substantial difference between  $J_{par}$  and  $J_{ion}$ . The electric field components,  $E_x$  and  $E_y$ , are both constant.  $E_y$  is not 0 because the modeled current sheet is not aligned with the SAS  $y$  axis.

### Hall term $\neq 0$

The results are substantially better when the Hall term is included in the fit (bottom panels of Fig. 6.2).  $E_y$  is close to 0 because  $E_x \tan \theta$  and  $b_0 / \cos \theta$  balance each other in Eq. 5.34.

### 6.2.2 Determination of $n_x$

The results in the previous Section are illustrative for the necessity to take into account the ionospheric polarization. This means that  $E_x$  is no longer considered constant and the coefficients of the series  $\delta E_x$  (Eq. 5.38) have to be determined. In principle, the numerical procedure allows one to get to any order, even higher than the number of data points,  $N$ . This does not make sense and a first question is to find a reasonable criterion for cutting the series, i. e. to decide what should be  $n_x$ . Physically,  $n_x$  corresponds to the polarization length scale. This interpretation is particularly appropriate with orthogonal polynomials, due to their quasi-periodic variation (see AppendixE).

A good estimation of the required  $n_x$  is provided by fitting  $y_{ms}$  with progressively higher order expansions. The dependence of  $\chi_r^2$  on the order of the expansion is shown in the top left panel of Fig. 6.3. One can see that the decrease of  $\chi_r^2$  saturates for  $n_x \gtrsim 18$ ;  $y_{ms}$  was normalized by dividing it through 0.01, roughly equal to its estimated error. For higher orders the improvement in the representation of  $y_{ms}$  is small. The right top panel of Fig. 6.3 shows  $y_{ms}$  together with the approximations obtained for  $n_x = 7, 18, 36$ .

The higher order (smaller scale) variability in  $y_{ms}$  results from the electron precipitation. This can be read in the bottom panels of Fig. 6.3: the left panel shows the dependence  $\chi_r^2(n_x)$  for  $H_y$ , the right panel for  $\Sigma_P$ . The decrease of  $\chi_r^2$  saturates at  $n_x \approx 4$  for  $H_y$  and at  $n_x \approx 18$  for  $\Sigma_P$ .

### 6.2.3 Polarized arc

As compared to the non-polarized arc models we shall examine in addition the influence of the polarization length scale. Each plot shows results obtained for  $n_x = 7, 18, 36$ . The fields will be seen to converge with increasing  $n_x$ , which provides a double-check for the numerical algorithm.

### Hall term = 0

The currents and electric fields for the model YPNH, Eq. 5.43, are shown in the top panels of Fig. 6.4. The fit is considerably better as compared to model NPNH (Fig. 6.2, top panels). However, the improvement as compared to model NPYH (Fig. 6.2, bottom panels) is not very substantial, although with model YPNH we have a much larger number of parameters. This is a good hint for the importance of the Hall term.

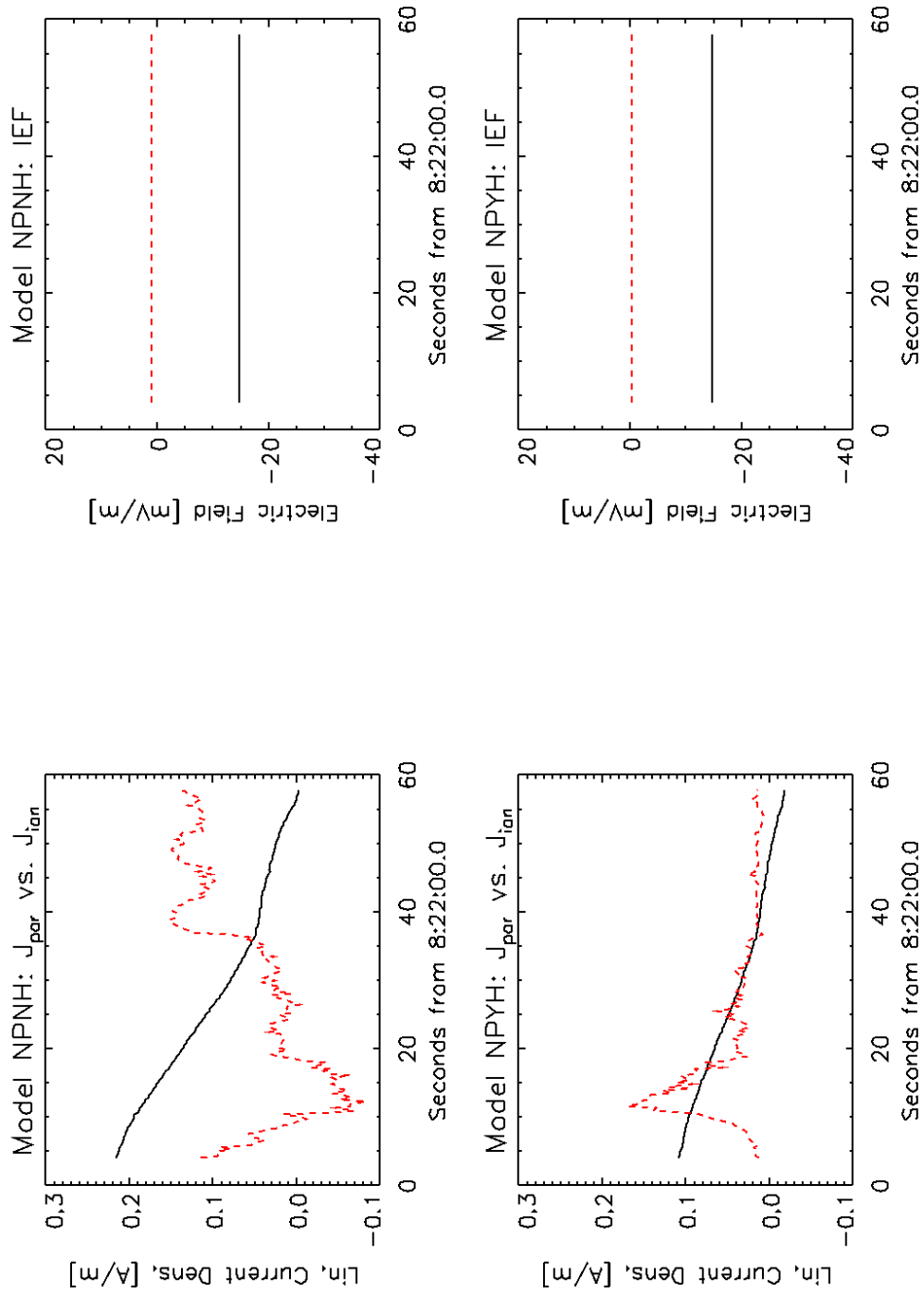


Figure 6.2: **TOP** Model NPNH. **Left:** Parallel/Ionspheric current (black solid line/red dashed line). Here and in the following figures the constant  $c_0$  was added to  $J_{ion}$ , in order to make easier the comparison with  $J_{par}$  (see also p. 95). **Right:**  $E_x/E_y$  (black solid line/red dashed line). **BOTTOM** Model NPYH. Same as for model NPNH.

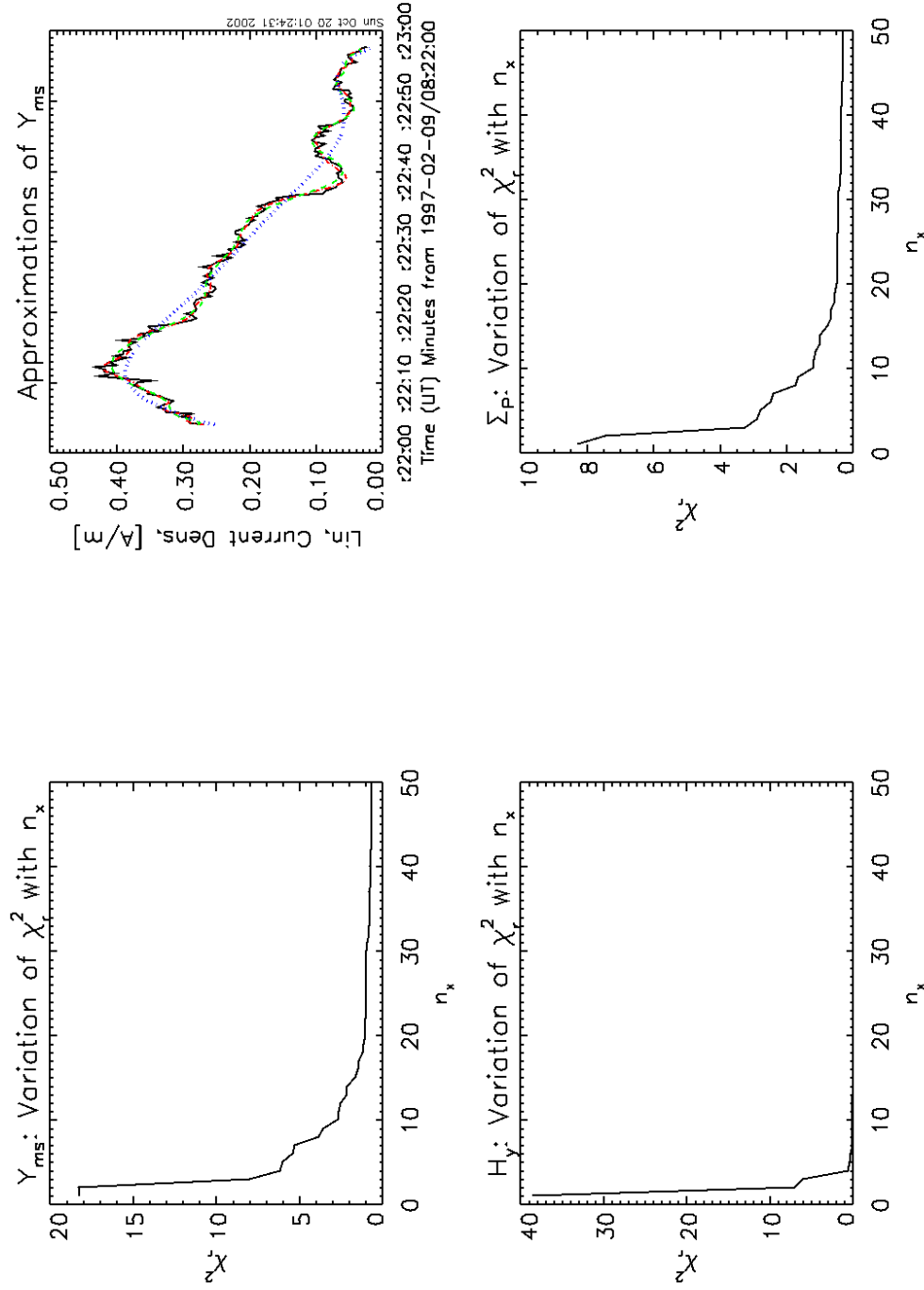


Figure 6.3: **TOP Left:** Dependence of  $\chi_r^2$  on the expansion order for  $y_{ms}$ . **Right:** Approximations of the measured data,  $y_{ms}$  (black solid line), with orthogonal polynomials (blue dotted line/green dashed line/red dash-dotted line for  $n_x = 7/18/36$ ). **BOTTOM** Dependence of  $\chi_r^2$  on the expansion order. **Left:**  $H_y$ . **Right:**  $\Sigma_P$ .

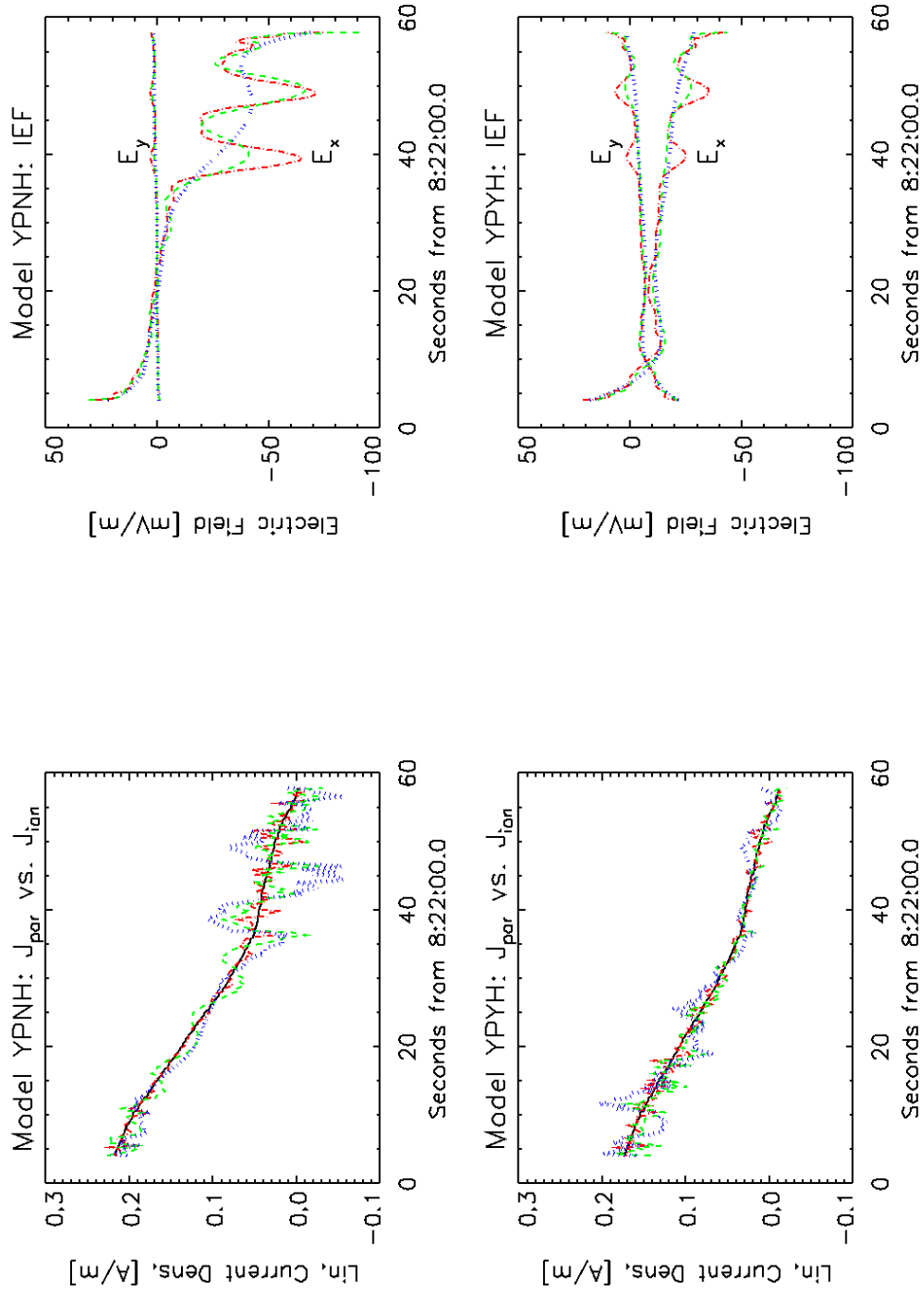


Figure 6.4: **TOP** Model YPNH,  $n_x = 7/18/36$  (blue dotted line/green dashed line/red dash-dotted line). **Left:** Parallel (black solid line) and Ionospheric current; **Right:**  $E_x$  and  $E_y$ . **BOTTOM** Model YPYH. Same as for model YPNH.

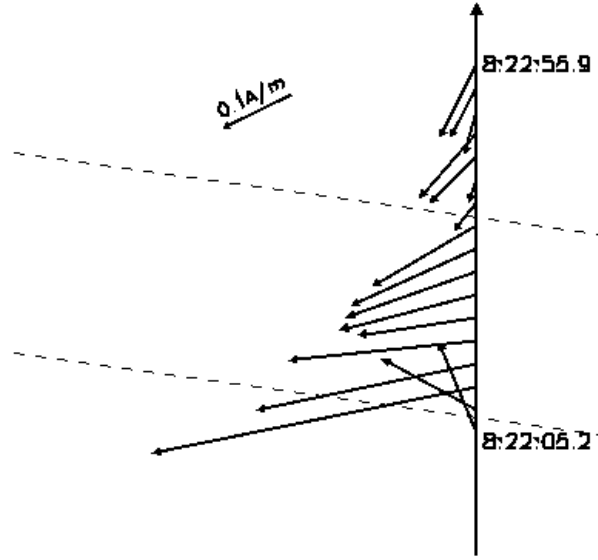


Figure 6.5: The current along the ionospheric footprint of FAST for model YPYH36. The dashed lines indicate the approximate location of the visible arc edges. The reference arrow at the top shows the flow direction of the electrojet as determined by fit.

### Hall term $\neq 0$

The best fit to the data, assuming no variation along the straight and parallel arc, is obtained by taking into account both the polarization and the Hall term. The bottom panels of Fig.6.4 show the results obtained with the model YPYH. The main difference as compared to model YPNH is seen in the electric field, whose values are considerably smaller in the second half of the interval. The agreement between  $J_{par}$  and  $J_{ion}$  is also better. However, the model YPYH still has a serious flaw, that will be pointed out in Section 6.3.3.

Figure 6.5 shows the ionospheric current vector, obtained via Eqs.5.22, with  $E_x$  and  $E_y$  resulted from the fit procedure. Note that, inside the visible arc, the direction of the current is not very different from the fitted electrojet direction. However, the current is strongly divergent at the arc edges, in particular at the southern one.

## 6.3 The infinite straight arc: discussion

We shall analyze the results presented in a graphical form in the previous Section. First, we shall tabulate the computed parameters and point out several peculiar features. Next, we shall check the agreement with the optical information. We shall conclude with a careful examination of the internal consistency of the results. Before proceeding to the discussion we emphasize that assuming an infinite straight arc model, which implies no variation along the arc, has the important side-effect that the coupling between FAC and electrojet is neglected.

### 6.3.1 Discussion of the parameters

The parameters resulting from the infinite straight arc models are summarized in Table 6.2, for both  $\Delta\Phi = 2000\text{V}$  (left column) and  $\Delta\Phi = 2250\text{V}$  (right column). For the models with polarization the value of  $n_x$  is indicated in the name of the model. Thus, e. g. YPYH36 stands for model YPYH with  $n_x = 36$ . Only  $\tan\theta$ ,  $b_0$  (for models NPYH and YPYH), and  $c_0$  are listed. The coefficients  $a_i$  are not given in the table: although they substantially contribute to the agreement between data and model, their particular values are not of prime importance for the discussion to follow. When trying to model the ionosphere status the important option is whether to take or not into account the polarization. Choosing a certain polarization order is important for small scale changes in the field distribution, but has just a small influence on the global parameters  $\tan\theta$ ,  $b_0$ , and  $c_0$ . We shall return to this point below.

The last column of the table shows the reduced  $\chi_r^2$ , obtained as  $\chi_r^2 = f/(N - M)$ , with  $N$  the number of data points and  $M$  the number of model parameters;  $M$  is equal to either  $n_x + 3$  or  $n_x + 2$ , depending whether the Hall term is considered or not. For the two cases without polarization (NPNH and NPYH)  $n_x = 0$ . Both the start value (before minimization) and the minimum found are given for  $\chi_r^2$ . As starting point for the search of the minimum we chose, as a rule, the origin of the parameter space. This is equivalent to an  $L$ -shell aligned homogeneous arc, with no ionospheric current flowing into (or out of) the auroral oval (other starting points were also tried, to make sure that the minimum found is not just a local one). With a good model the minimum obtained for  $\chi_r^2$  should be close to 1, on the condition that the errors in Eq. 6.2 are correctly evaluated (see Appendix F). As we only have a limited knowledge on the error, we can only say that the chance for a model to be better is higher when  $\chi_r^2$  is smaller.

By examining the Table 6.2 one notes systematic trends that deserve to be commented:

- The angle  $\theta$  is close to 0 when the Hall term is disregarded. This can be explained by considering the symmetry of the problem. With  $b_0 = 0$  the Hall conductance is not included in the fit (Eqs. 5.41 and 5.43). The angle  $\theta$  is not exactly 0 because the FAC sheet is not rigorously aligned with the  $L$ -shell and  $H_x \neq 0$  (Fig. 3.4). If this were the case the models NPNH and YPNH would imply FAC closure through Pedersen current along  $x$  (perpendicular to the  $L$ -shell,  $\tan\theta = 0$ ) and a constant current density electrojet in the  $-y$  direction.

When the Hall term is taken into account  $\tan\theta < 0$ . The negative value of  $\tan\theta$  for the models NPYH and YPYH indicates that the flow direction of the electrojet is different from the orientation of the current sheet. This possibility was already mentioned at p.86 and is essentially related to the dependence of the electrojet direction not only on the conductance,

Table 6.2: Infinite straight arc: Summary of results

Model	$\tan \theta$	$b_0$ [mV/m]	$c_0$ [A/m]	$\chi_{r,i}^2 / \chi_{r,o}^2$
NPNH	-0.079	-	0.156	16481/5463
NPYH	-1.220	-9.9	0.018	16579/ 742
YPNH3	-0.045	-	0.123	16779/ 569
YPNH7	-0.037	-	0.119	17193/ 400
YPNH12	-0.036	-	0.117	11741/ 366
YPNH18	-0.043	-	0.114	18446/ 155
YPNH36	-0.054	-	0.113	20941/ 44
YPYH3	-0.484	-7.7	0.061	16880/ 314
YPYH7	-0.506	-10.0	0.046	17300/ 105
YPYH12	-0.594	-10.2	0.037	17854/ 45
YPYH18	-0.579	-9.9	0.040	18569/ 37
YPYH36	-0.523	-8.6	0.050	21101/ 21

Table 6.3: Model YPYH: Parameters for the whole interval and for sub-intervals

Interval	$n_x$	$\tan \theta$	$\Phi_{sub}$ [V]	$\Phi_{all}$ [V]	$b_0$ [mV/m]	$c_0$ [A/m]	$\chi_{r,i}^2 / \chi_{r,o}^2$
IALL	36	-0.523	-	2000	-8.6	0.050	21101/21.0
I1S	7	-0.319	482	69	-10.3	0.200	38517/7.4
I1B	28	-0.306	482	69	-9.9	0.210	7798/3.0
I2	7	-0.185	455	323	-4.9	0.194	35013/3.8
I3S	7	-0.435	400	369	-10.1	0.054	18115/ 5.1
I3B	28	-0.341	400	369	-8.5	0.078	4560/ 2.0
I4	7	-0.374	400	616	-10.2	0.038	4406/ 0.8
I5	7	-0.434	292	699	-9.6	0.012	2523/1.1



but also on the IEF. While the conductance is, indeed, closely connected to the FAC, the IEF reflects the large scale balance between magnetospheric driving forces and ionospheric drag forces, which are not in a direct relationship with the FAC.

As already noted above,  $\tan \theta$  is not very sensitive to the polarization order (except for the case  $n_x = 0$ ). The small influence of the polarization order can be understood if we think that the parameter  $\tan \theta$  — as well as  $b_0$  and  $c_0$  — is global, depending mainly on the average values of the measured physical quantities. The polarization order can only reveal small scale features, associated with the conductivity pattern, but not modify too much the derived flow direction of the electrojet.

- The value of the parameter  $b_0$  is only slightly influenced by the polarization order (even if  $n_x = 0$ , model NPYH) and scales with the total potential drop across the arc: an increase of  $\sim 10\%$  in  $\Delta\Phi$  (from 2000V to 2250V) leads to an increase of  $\sim 10\%$  in  $|b_0|$  (e. g. from 8.6 to 9.6, model YPYH36). We shall try to explain the values obtained for  $b_0$  based on the geometry presented in Fig. 6.6.

Once the direction  $\theta_J$  of the ionospheric current  $J$  is known, the direction of the electric field is fixed by:

$$\tan \theta_{JE} = \Sigma_H / \Sigma_P \quad (6.7)$$

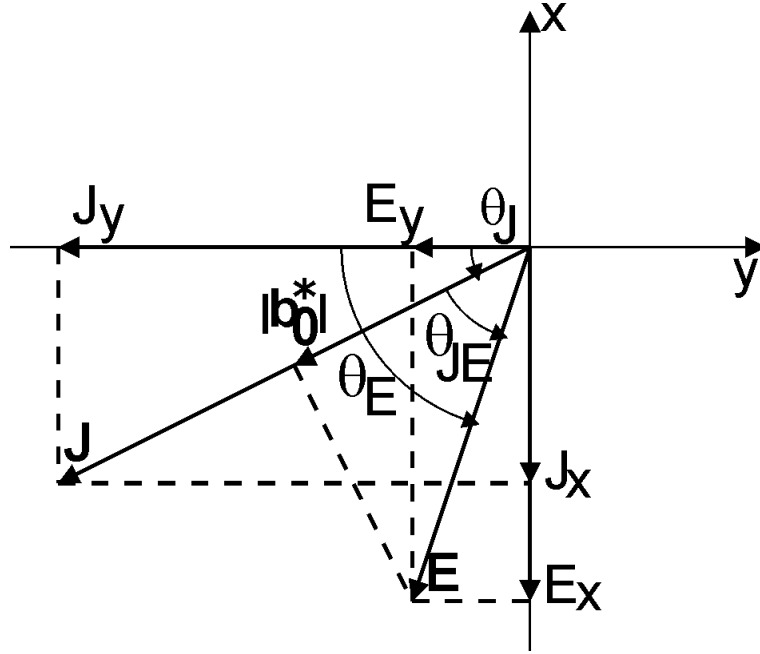
This relation can be easily demonstrated by choosing a coordinate system whose  $x$  axis is aligned with the electric field; in this system  $J_x = \Sigma_P E_x$ ,  $J_y = \Sigma_H E_y$ , and  $\tan \theta_{JE} = J_y / J_x = \Sigma_H / \Sigma_P$ . The component  $b_0^*$  of the electric field along  $J$  is given by:

$$|b_0^*| = E \cos \theta_{JE} = \frac{|E_x| \cos \theta_{JE}}{\sin(\theta_J + \theta_{JE})} = \frac{1}{\tan \theta_J + \tan \theta_{JE}} \frac{|E_x|}{\cos \theta_J} \quad (6.8)$$

Equation 6.8 can be written at any instant of time. In order to pass from  $b_0^*$  to  $b_0$  we need to change  $E_x$  with  $E_{0x}$  and  $\theta_J$  with  $|\theta_{fit}|$ . The first replacement is allowed on the ground of the mentioned global character of  $b_0$ . The second replacement can be justified by comparing the instantaneous direction of the current vector with the fitted direction of the electrojet (Fig. 6.5). By using Eq. 6.7 and choosing the right signs Eq. 6.8 transforms to:

$$b_0 = \frac{1}{\Sigma_H / \Sigma_P - \tan \theta_{fit}} \frac{E_{0x}}{\cos \theta_{fit}} \quad (6.9)$$

With  $E_{0x} = -15\text{mV/m}$  (Table 6.1),  $\tan \theta_{fit} = -0.5$ , and  $\Sigma_H / \Sigma_P = 1$ , Eq. 6.9 provides  $b_0 = -11\text{mV/m}$ , in good agreement with the values in Table 6.2. The bottom panel in the right plot of Fig. 4.2 suggests that  $\Sigma_H / \Sigma_P = 1$  is a reasonable average choice in our case.

Figure 6.6: Sketch illustrating the evaluation of  $b_0$ .

- The constant  $c_0$  is higher for the models without Hall term. This can be understood by observing that  $c_0$  has the significance of a current flowing southward, from the polar cap to the auroral oval (if positive). A negative  $b_0$  (westward electric field) drives a northward Hall current, which decreases the value of  $c_0$ . The formal expression of this argument is obtained by writing Eq. 5.27 two times, once for the model YPNH and once for the model YPYH (the demonstration for the models NPNH and NPYH is similar):

$$\begin{aligned} H_\eta^{YPNH} - J_\xi^{YPNH} &= c_0^{YPNH} \\ H_\eta^{YPYH} - J_\xi^{YPYH} &= c_0^{YPYH} \end{aligned}$$

Subtracting the second equation from the first one yields:

$$c_0^{YPNH} - c_0^{YPYH} = (H_\eta^{YPNH} - H_\eta^{YPYH}) - (J_\xi^{YPNH} - J_\xi^{YPYH})$$

The first term on the r.h.s. is positive, because of the relative orientation of the systems  $(\xi, \eta)^{YPNH}$  and  $(\xi, \eta)^{YPYH}$ , while the second term is negative, because of the Hall contribution to  $J_\xi$ . Consequently,  $c_0^{YPNH} > c_0^{YPYH}$ , in agreement with the results in Table 6.2.

- The last column of the Table 6.2 shows that the accuracy of the model (as expressed by  $\chi_{r_o}^2$ ) increases from NPNH to YPYH, with better results for higher  $n_x$  (i. e. smaller polarization scale size). However, the improvement obtained with YPNH as compared to NPYH is limited, even for large  $n_x$  (a significant decrease of  $\chi_r^2$  is seen only for  $n_x = 36$ ). The Hall current is a necessary ingredient, whose role cannot be played by polarization.

### 6.3.2 Consistency check: optical observations

The necessity of a Hall term, resulting from an arc-aligned component of the electric field, is strongly supported by the optical data (Section 3.3), which indicate a southward motion of the arc with an average velocity of  $\sim 200\text{m/s}$ , equivalent to an electric field  $E_y \approx -10\text{mV/m}$  (if the arc has no proper motion; see the discussion in Section 6.5.2). This value compares quite well with  $b_0$ . Recall, however, that  $b_0$  is actually  $E_\eta$ , which is different from  $E_y$ . This is clearly visible in the bottom right panels of Figs. 6.2 and 6.4, where  $E_y \neq -10\text{mV/m}$ .

For the model NPYH  $E_y \approx 0$ , because the contribution of  $b_0$  to  $E_y$  is almost fully compensated by the rotation of the arc (compare Eq. 5.34). This would imply that plasma has no motion in the Earth's system or, equivalently, that the arc moves with  $\sim 200\text{m/s}$  in the plasma system, which is a quite large velocity for the growth phase of a substorm (Section 3.1). The model NPYH is not likely to offer a reasonable approximation. Another argument against the model NPYH is the large  $\theta$  angle, implying that the electrojet is almost transverse to the arc.

The model YPYH compares better with the optical observation.  $E_y$  at 8:22:12, the time of the satellite encounter with the bright edge of the arc (whose motion can be followed in the TV frames, Fig. 3.12), is  $\sim 10\text{mV/m}$  westward, and it stays at  $\sim 5\text{mV/m}$  westward all over the arc. The southern edge of the arc is thus frozen in the ionospheric plasma, which is not an unusual behavior for a substorm growth phase. We cannot say too much about the rest of the arc; however, the velocity of the arc proper motion would not exceed  $100\text{m/s}$ , which could be explained in terms of the AAR motion (for further discussion see Section 6.5.2).

The optical data are unequivocal about the orientation of the arc: its alignment is roughly E–W, with a slight increase of  $\theta_{opt}$ , from  $\theta_{opt_S} \lesssim 0$  at the southern edge to  $\theta_{opt_N} > 0$  at the northern edge. The optical alignment of the arc compares well with the orientation of the FAC sheet, as it results from the magnetic data (small differences can be explained by the deviations of the magnetic field from the ideal dipole). There is, however, a clear disagreement between  $\theta_{opt}$  and  $\theta_{fit}$ . The models examined up to this point provide an ionospheric electrojet whose flow direction is not parallel to the optical arc, produced by the FAC sheet energetic electrons.

### 6.3.3 Internal consistency of the model YPYH

We shall check in more detail the electric field provided by the model YPYH. A good solution should lead to an ionospheric potential that matches the trend exhibited by the high-altitude potential (upper panel of Fig. 3.4). Besides, the results should not depend too much on the choice of the fit interval except, perhaps, for some boundary effects (see Section 6.5.3).

The comparison between the ionospheric potential, obtained for model YPYH36, and the high-altitude potential is shown in the top panel of Fig. 6.7. The origin of the potential was chosen at  $t = t_0 + 3.8$ , when the satellite encounters the first ion beam (see Fig. 3.8). The ionospheric potential is shown for the interval IALL; the high-altitude potential extends for some 15s before and after IALL. The jump in the high-altitude potential over the time interval with bad data is such that the potential drop over IALL equals 2250V. Obviously, the modeled potential fails to reproduce the measured data, in particular over the intervals I1 and I5. A satisfactory model should result in an ionospheric potential drop equal to the high-altitude one, between the boundaries of an ion beam.

The dependence of the electric field on the fit interval was examined by comparing the results obtained for the intervals I1...I5 with the results obtained for IALL (middle and bottom panels of Fig. 6.7). For the fit over IALL we took  $n_x = 36$ , whereas for the sub-intervals  $n_x = 7$ . As IALL is about 5 times longer than each of the I1...I5, this choice makes the fit resolutions comparable. Note that there is no free parameter, to allow the matching of the separate curves.

The results obtained by fitting over sub-intervals do not agree with the result of the fit over IALL. As expected from the potential calculation,  $E_x$  yielded by the fit over IALL is in strong disagreement with  $E_x$  resulted from the fit over I1 and I5. The same is true for  $E_y$ . Results obtained with YPYH using Burst data,  $n_x = 28$ , were added for I1 and I3. As the Burst rate is 4 times larger compared to the Survey rate, YPYH28 with Burst data corresponds to the same spatial frequency as YPYH7 with Survey data. The difference between the two sets is small, except for the ends of the sub-intervals, in particular the end of I3. The inaccuracy at the boundaries of the fit interval was already mentioned and will be discussed in more detail in Section 6.5.3. The large difference at the end of I3 may also be related to the abrupt decrease of the conductance to low values ( $\lesssim 1\text{mho}$ ).

More insight into the reason for the discrepancy exhibited by Fig. 6.7 can be achieved by examining the Table 6.3, which compares the parameters obtained by fit over IALL and over sub-intervals. One can see that  $\tan \theta$  and  $b_0$  are not very sensitive to the choice of the interval, but  $c_0$  has a significant variation from one interval to the other, decreasing toward north. This points to a fundamental weakness of the model YPYH: the difference  $H_\eta - J_\xi$ , which should be constant according to Eq. 5.27, actually varies across the arc. The fact that  $c_0$  is not constant cannot be explained if the coupling between the FAC and the electrojet is neglected. In the next Section, by taking the coupling into account, the results will get considerably improved.

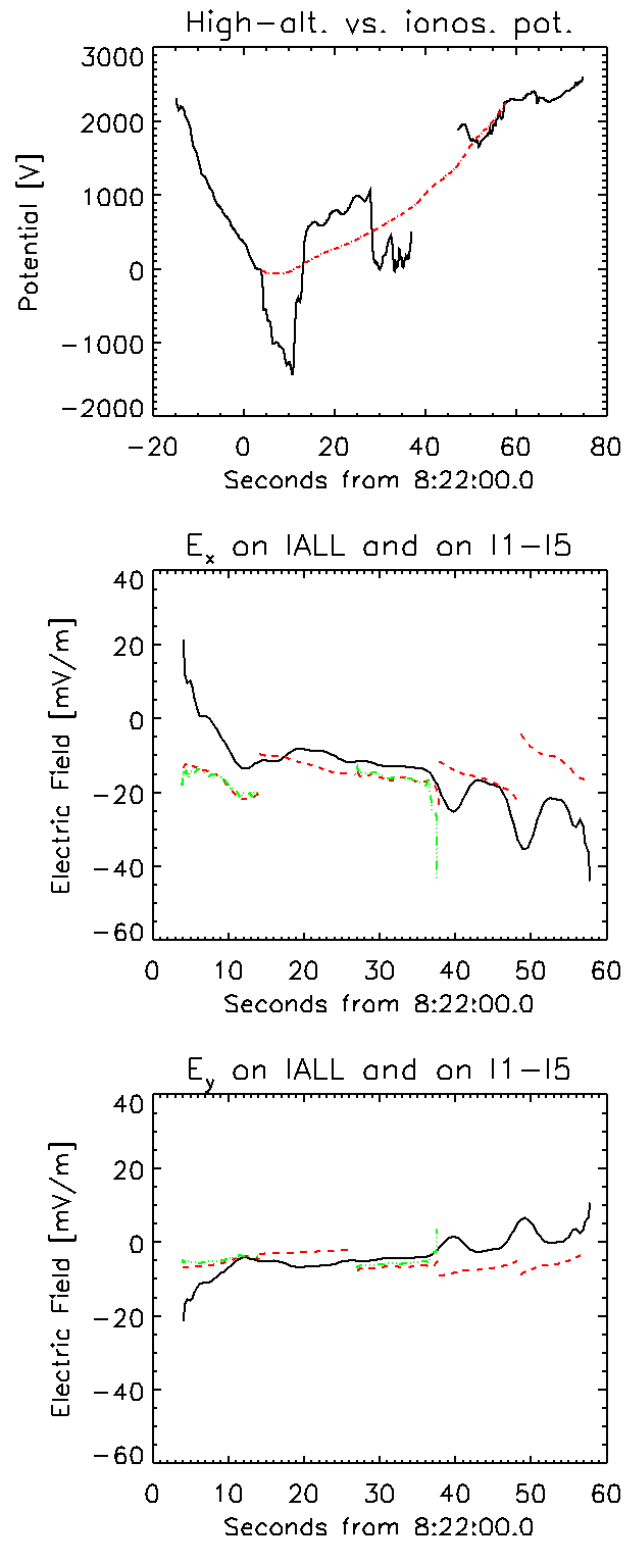


Figure 6.7: **Top:** High-altitude potential (black solid line) compared to the ionospheric potential (red dash-dotted line) obtained with model YPYH36 ( $\Delta\Phi_{\text{IALL}} = 2250\text{V}$ ). **Middle and Bottom:** IEF  $E_x$  and  $E_y$ , on IALL and on I1...I5. Model YPYH36 (black solid line) was used over IALL, model YPYH7 (red dashed line) over sub-intervals. Model YPYH28 was used with Burst data, available during I1 and I3 (green dash-dotted line).

## 6.4 Models with FAC–electrojet coupling

The results obtained in the previous two Sections, by neglecting the FAC–electrojet coupling, show that this assumption is too restrictive even for the arc geometry. In this Section we present results obtained with the models developed in Section 5.4.3. The non-linear models NPNHX, NPYHX, YPNHX, and YPYHX are discussed first. Next we address the derivation of  $\tan \theta$  from the magnetic data and examine the linear model YPYHXL.

### 6.4.1 Results obtained with the non-linear models

The improvement brought by including the FAC–electrojet coupling among the fit parameters can be easily appreciated by just qualitatively comparing the graphical representations. The new results are illustrated as follows (the figure showing the corresponding old results is indicated in brackets):

- Models NPNHX and NPYHX: Fig. 6.8 (Fig. 6.2)
- Models YPNHX and YPYHX: Fig. 6.9 (Fig. 6.4)
- Ionospheric potential (YPYHX36) and fit over I1...I5: Fig. 6.10 (Fig. 6.7)
- Ionospheric current vector (YPYHX36): Fig. 6.11 (Fig. 6.5)

Note that  $J_{ion}$  (Eq. 6.6) is now yielded by:

$$J_{ion} = J_{\xi} + c_0 + \tilde{c}_1 \xi = J_{\xi} + c_0 + c_1 x \quad (6.10)$$

The parameters were collected in the Table 6.4. Two new columns were added as compared to Table 6.2, showing the new parameter,  $c_1$ , and the difference  $H_{\eta}(L) - J_{\xi}(L) = c_0 + c_1 L$  ( $L$  is the ionospheric path length, see Table 6.1). The figures and tables presented here were obtained by using Jacobi polynomials. Using Legendre polynomials instead does not change the results, which provides a good check for the validity of the numerical algorithm (see AppendixE).

The new results are definitely better than the old ones. This can be seen by both comparing the figures and the two tables, 6.4 and 6.2. Numerically, the improvement is expressed in the  $\chi^2$  column. An interesting feature that one can notice is that the parameters do not change too much, except for  $c_0$ . On the other hand, the ionospheric potential distribution over IALL is now in good agreement with the high-altitude potential (Fig. 6.10). Consequently, the detailed balance of the current across the arc is mainly achieved through polarization. The current closure is now properly modeled:  $H_{\eta}(L) - J_{\xi}(L) = 0$ , within the experimental error (a few .01 A/m), which is the expected result at the northern boundary of the winter, nighttime auroral oval.

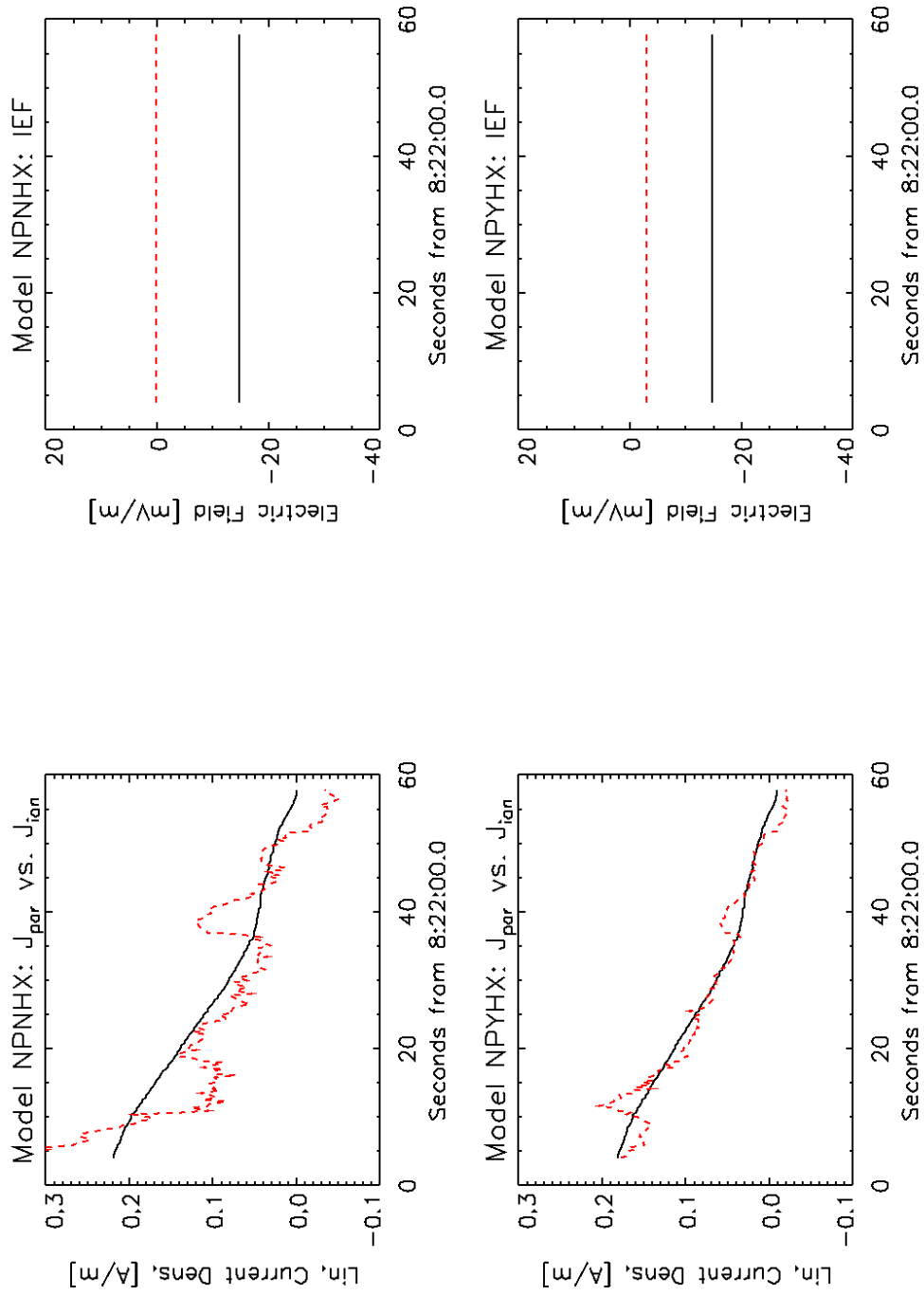


Figure 6.8: **TOP:** Model NPNHX. **BOTTOM:** Model NPYHX. Same as Fig. 6.2.

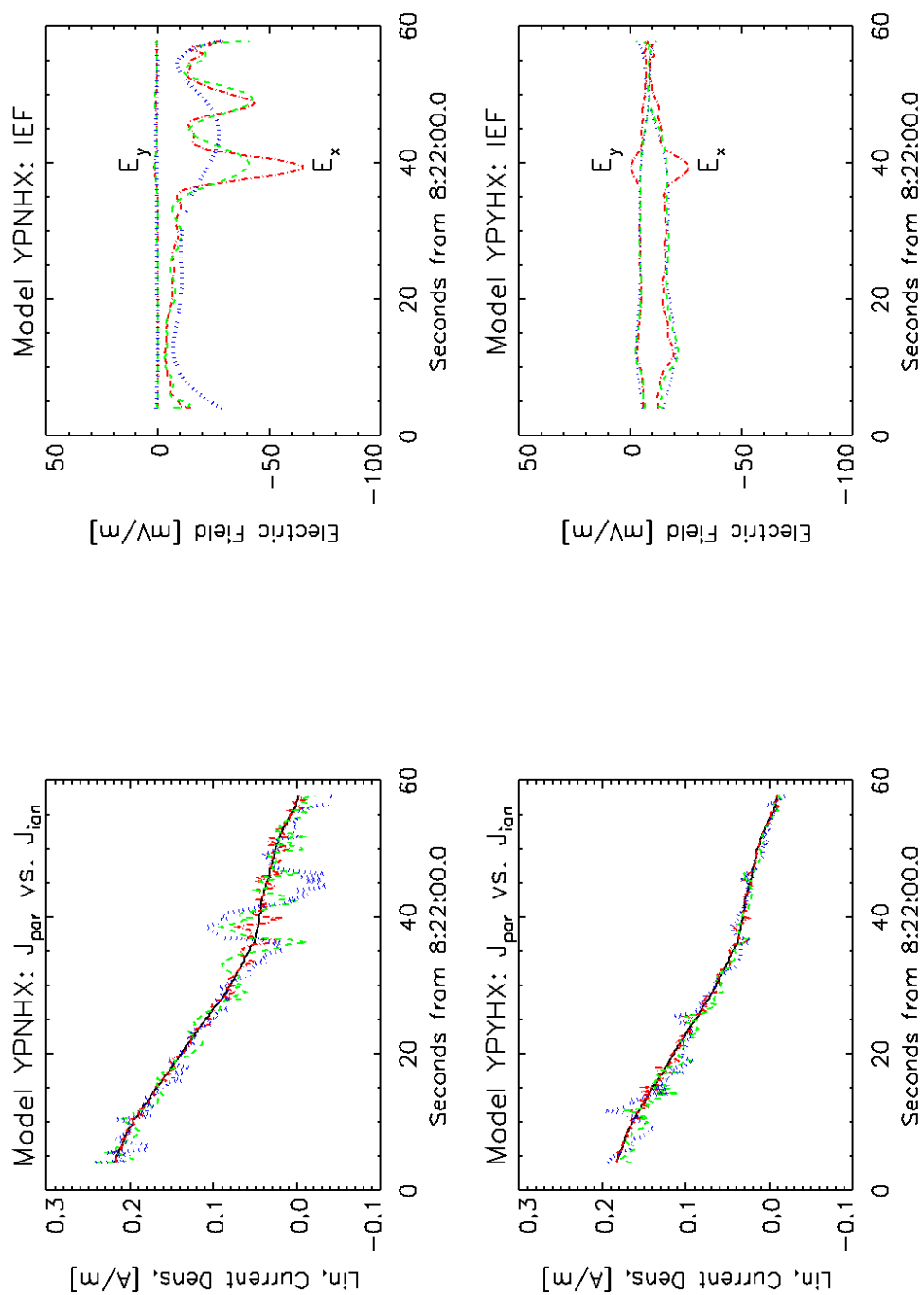


Figure 6.9: **TOP:** Model YPNHX. **BOTTOM:** Model YPYHX. Same as Fig. 6.4.



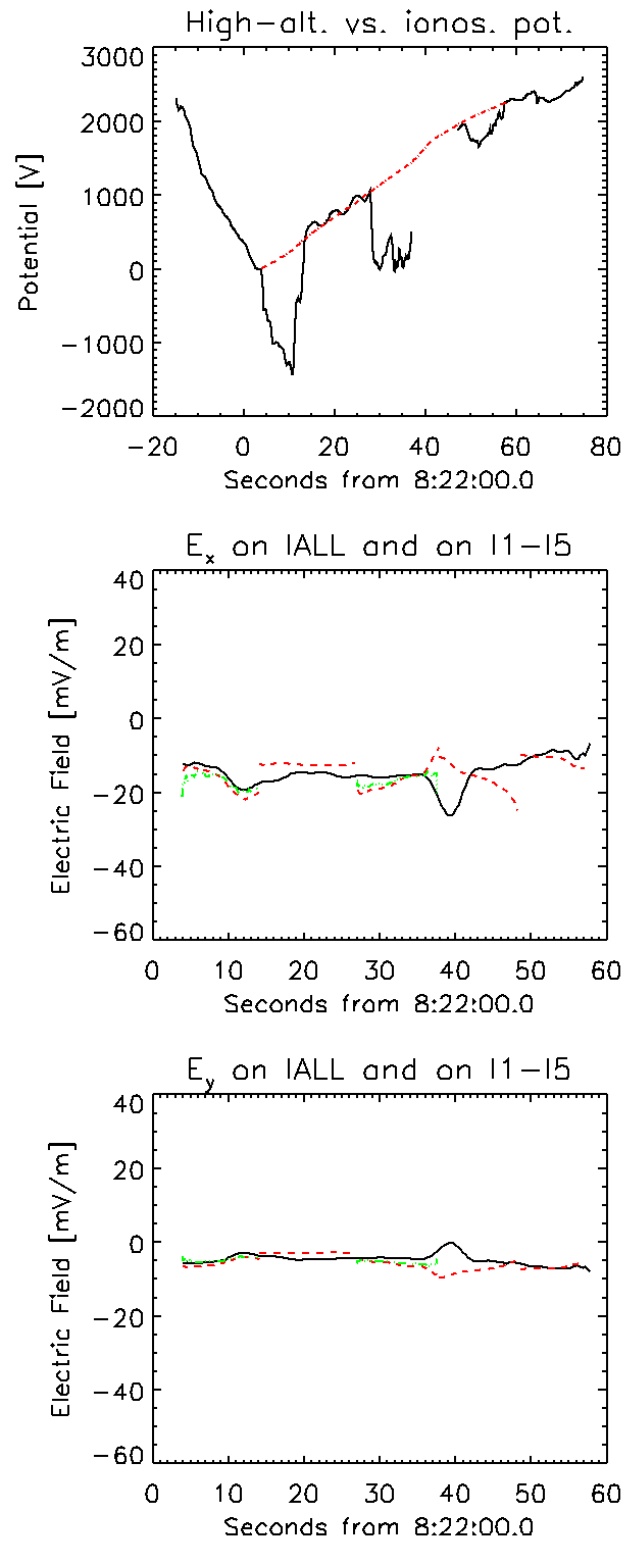


Figure 6.10: **Top:** High-altitude potential compared to the ionospheric potential obtained with model YPYHX36. **Middle** and **Bottom:** Ionospheric electric field,  $E_x$  and  $E_y$ , on IALL and on I1...I5. Same as Fig. 6.7.

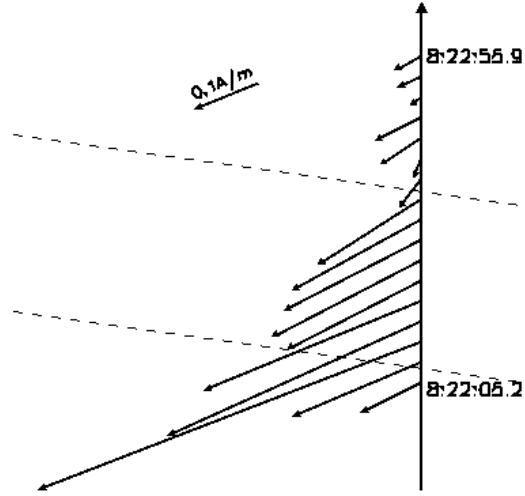


Figure 6.11: The current along the ionospheric footprint of FAST for model YPYHX36. Same format as Fig. 6.5.

The flow direction of the ionospheric current is less variable for model YPYHX36 as compared to YPYH36. The maximum ionospheric current, near the southern edge of the visible arc, is  $\sim 0.65 \text{ A/m}$  for model YPYHX36, higher than  $\sim 0.45 \text{ A/m}$  for model YPYH36. With  $J_\eta \simeq 0.3\text{--}0.6 \text{ A/m}$  (Fig. 6.11) and  $|c_1| \simeq 1\text{--}3 \mu\text{A/m}^2$  (Tables 6.4 and 6.5) the longitudinal length scale of the electrojet is  $L_\eta \simeq 200\text{--}500 \text{ km}$  (Eq. 5.48). According to Eq. 5.47  $L_\eta$  has to be corrected when  $\theta_{AF} \neq 0$ . In our case this leads to a decrease of some 10–25% in  $L_\eta$  ( $\theta_{AF} = \theta_F - \theta_A \simeq -22^\circ - 8^\circ = -30^\circ$ ,  $\sin^2 \theta_{AF} \simeq 0.25$ ,  $j_\parallel \simeq \Delta H_\eta / L \simeq -0.24 \text{ A/m} / 150 \text{ km} = -1.6 \mu\text{A/m}^2$ ; consequently  $\sin^2 \theta_{AF} \cdot j_\parallel \simeq -0.4 \mu\text{A/m}^2$ ). The strength of the electrojet increases eastward, because both  $\partial J_\eta / \partial \eta \simeq c_1$  and  $J_\eta$  are negative; this confirms the expectations for a westward electrojet at the poleward boundary of the evening auroral oval.

Further insight into the relationship between the fit parameters is provided by comparing Tables 6.3 and 6.5. Similar to the results obtained for IALL, adding the  $c_1 x$  term does not change too much the values of  $\tan \theta$  and  $b_0$ , but the variation of  $H_\eta - J_\xi$  is now reasonably continuous. This can be seen by checking the  $I_{n+1}$  value in the column  $\phi_0$  against the  $I_n$  value in the column  $c_0 + c_1 L$  (in this context  $L$  stands for the respective lengths of the sub-intervals, as read in Table 6.1). The agreement is good, within a few 0.01 A/m.

The improvement obtained by adding the term  $c_1 x$  is most convincingly expressed by the top panel of Fig. 6.10, as compared to the top panel of Fig. 6.7 (also the columns  $\Phi_{sub}$  and  $\Phi_{all}$  in Tables 6.5 and 6.3). However, the potentials are obtained by integration, which smooths out the small disagreements. To check the model in detail we have inspected the electric field on I1...I5 (middle and bottom panels of Fig. 6.10). Although the consistency of the results is now better, there are still differences, the most clear one at the boundary between I3 and I4.

Table 6.4: Models with FAC-electrojet coupling: Summary of results

Model	$\tan \theta$	$b_0$ [mV/m]	$c_0$ [A/m]	$c_1$ [ $\mu\text{A}/\text{m}^2$ ]	$c_0 + c_1 L$ [A/m]	$\chi^2_{r,i} / \chi^2_{r,o}$
NPNHX	-0.015	-	0.372	-2.51	-0.011	16579/525
NPYHX	-0.455	-7.4	0.194	-1.32	-0.007	14739/706
YPNHX3	-0.021	-	0.292	-1.71	0.031	16678/100
YPNHX7	-0.031	-	0.321	-2.05	0.009	16880/402
YPNHX12	-0.029	-	0.358	-2.41	-0.009	15007/391
YPNHX18	-0.034	-	0.258	-1.43	0.040	17300/302
YPNHX36	-0.028	-	0.258	-1.44	0.039	15873/277
YPYHX3	-0.466	-8.6	0.244	-1.90	-0.046	18569/135
YPYHX7	-0.456	-9.6	0.201	-1.51	-0.029	21101/ 31
YPYHX12	-0.497	-9.9	0.172	-1.28	-0.023	16983/ 63
YPYHX18	-0.494	-10.1	0.172	-1.28	-0.023	15099/ 58
YPYHX36	-0.413	-8.8	0.188	-1.32	-0.013	17408/ 41

Table 6.5: Model YPYHX: Parameters for the whole interval and for sub-intervals

Interval	$n_x$	$\tan \theta$	$\Phi_{sub}$ [V]	$\Phi_{all}$ [V]	$b_0$ [mV/m]	$c_0$ [A/m]	$c_1$ [ $\mu\text{A}/\text{m}^2$ ]	$c_0 + c_1 L$ [A/m]	$\chi^2_{r,i} / \chi^2_{r,o}$
IALL	36	-0.413	-	2000	-8.8	0.188	-1.32	-0.013	21262/9.0
IIS	7	-0.319	482	391	-10.3	0.204	-0.38	0.193	18902/8.0
IIB	28	-0.276	482	391	-9.1	0.233	-0.84	0.209	40268/7.7
I2	7	0.186	455	519	-5.1	0.229	-2.02	0.155	9585/2.2
I3S	7	-0.324	400	455	-8.8	0.132	-3.09	0.038	36142/3.6
I3B	28	-0.318	400	455	-8.3	0.127	-2.47	0.052	18870/1.8
I4	7	-0.372	400	474	-10.2	0.038	0.015	0.038	15970/1.7
I5	7	-0.434	292	221	-10.6	0.018	-0.76	-0.002	4605/1.5

3583/0.7  
2666/0.8

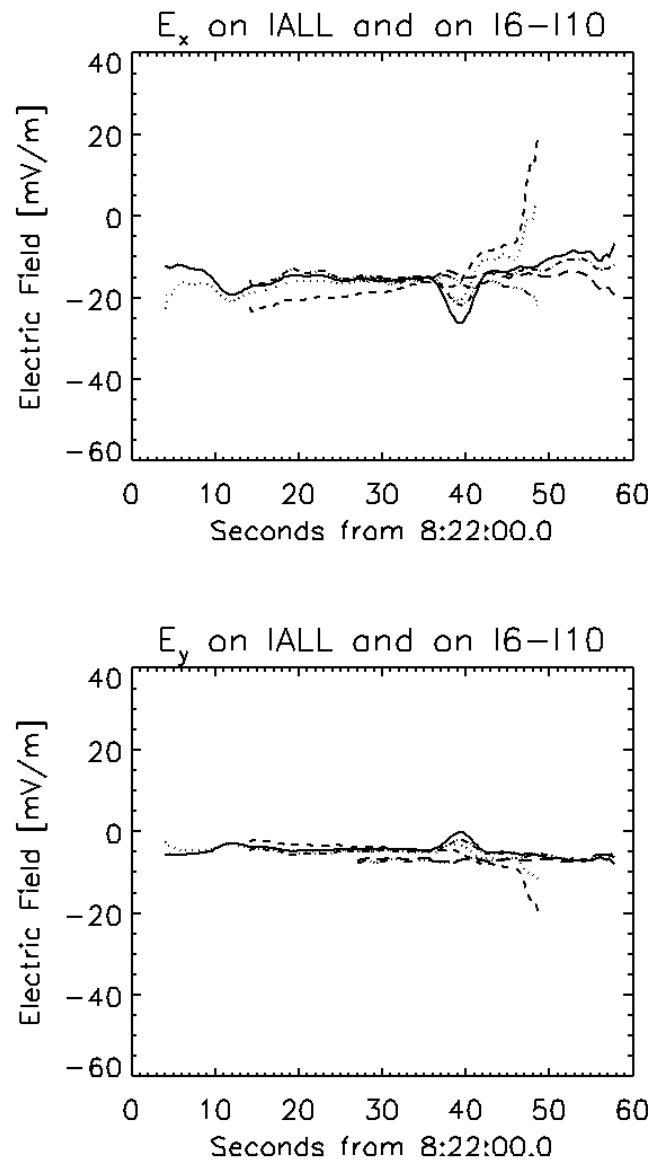


Figure 6.12: The electric field obtained by fit over the larger sub-intervals I6...I10. For the line style corresponding to each sub-interval see Table 6.6. **Top:**  $E_x$ . **Bottom:**  $E_y$ .

Table 6.6: The intervals used in Fig. 6.12

Id	$\Delta t$	$\Delta \Phi$	Line style
IALL	03.8–57.5	2250	solid
I6	03.8–48.5	1950	dotted
I7	13.8–48.5	1500	dashed
I8	13.8–57.5	1800	dash dot
I9	26.9–48.5	1000	dash dot dot dot
I10	26.9–57.5	1300	long dashes

The large disagreement around  $t_0 + 39$  is most probably a numerical effect because of having the boundary between I3 and I4 in a low conductance region. Figure 6.12 illustrates this point by showing how the results change when the fit is done on larger sub-intervals, I6...I10, that avoid the boundary between I3 and I4.  $E_x$  and  $E_y$  are quite similar to the field found by fitting over IALL, except for the already mentioned boundary effects. The time limits, the respective potential drop, and the line style used in Fig. 6.12 for each sub-interval, are listed in Table 6.6.

#### 6.4.2 Model YPYHX: Dependence of the results on the conductance pattern

In Section 4.2.1 we showed that Eqs. 4.9 are somewhat ambiguous about the pitch-angle range considered. Figure 6.13 presents  $E_x$  and  $E_y$  obtained by using the models YPYHX7, YPYHX18, and YPYHX36, with the conductance derived by integration over the full distribution and over the loss-cone. Most of the time the differences are small, implying that the choice of the pitch-angle range has secondary importance. It is only near  $t_0 + 39$ , when the conductances are very low, that the difference between the results is larger for model YPYHX36. Note that only the model YPYHX36 is able to resolve this small scale variation in conductances.

Although we have not performed a systematic study on the dependence of the derived electric field on the accuracy of the computed conductance pattern, Fig. 6.13 suggests that the error risk is increased only inside small scale regions of low conductance. On the other hand, the results are pretty close to each other e. g. during interval I1, when the conductances depend significantly on the pitch-angle range (Fig. 4.6). This remark might be useful: during I1 there is a strong gradient in the electron precipitation which leads to errors because of non-stationarity (Sections 4.4.1 and C.1). Nevertheless, the influence of these errors on the derived IEF is probably reduced.

It is interesting to compare the two sets of results from a statistical point of view. Table 6.7 lists the values  $\chi_{r_i}^2$  and  $\chi_{r_o}^2$ , obtained for  $\Delta\Phi = 2250\text{V}$ . Using the loss-cone electron population yields higher  $\chi_{r_o}^2$  (and  $\chi_{r_i}^2$ ) values, which implies a lower fit quality. This suggests that the full distribution might be a better integration domain for calculating the conductances. However, such a statistical criterion can be deceiving (see the discussion on considering  $\tan\theta$  small parameter, in the next Section) and its validation requires a more thorough check.

Table 6.7: Dependence of the fit quality on the conductance pattern.

	YPYHX7		YPYHX18		YPYHX36	
	Full distrib.	Loss-cone	Full distrib.	Loss-cone	Full distrib.	Loss-cone
$\chi_{r_i}^2$	15476	65404	16619	70233	18902	79883
$\chi_{r_o}^2$	39	135	15	46	8	17

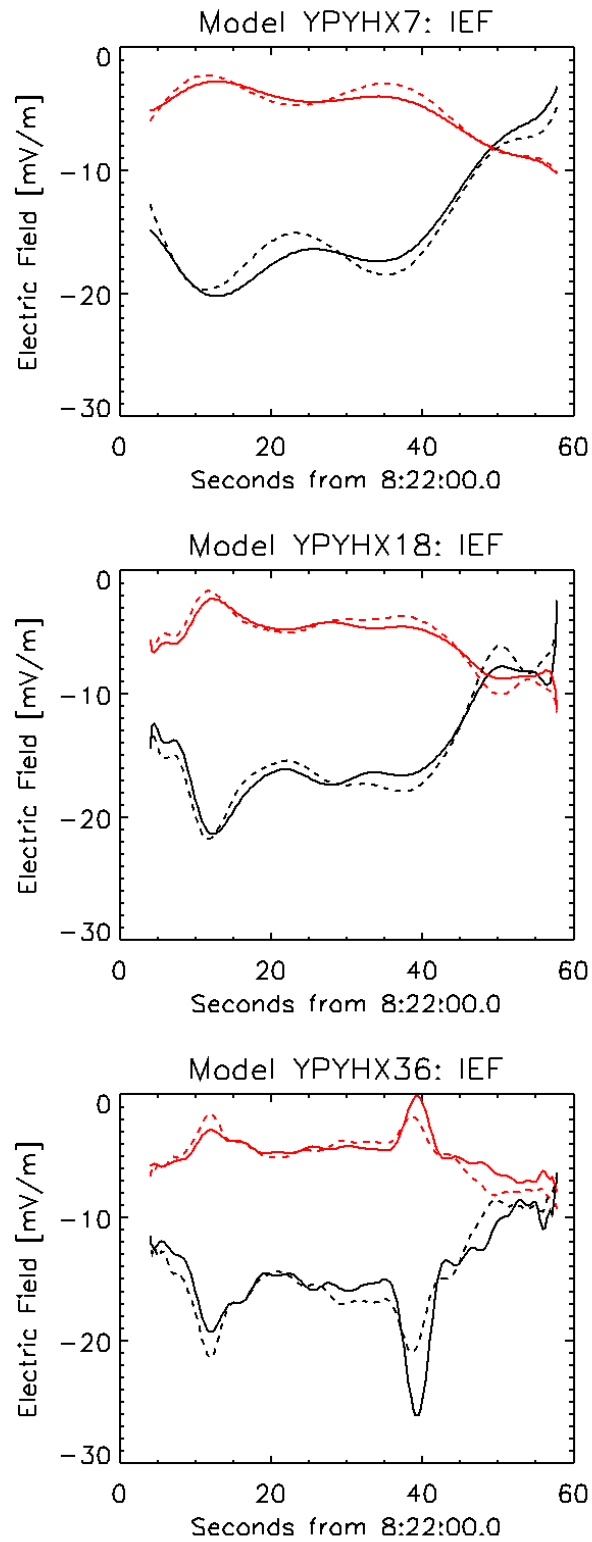


Figure 6.13: Dependence of the IEF on the conductance pattern. The model YPYHX was used with conductances derived by integration of  $J_N$ ,  $J_E$  over the full distribution (solid lines) and over the loss-cone (dashed lines).  $E_x$  is shown with black and  $E_y$  with red.

### 6.4.3 Model YPYHX: Dependence of the results on the fit formula

We shall perform some further examination of the fit formula Eq. 6.2, in order to test the dependence of the results not only on the arc model but also on the fit formula itself. More precisely, we shall look how the results change if:

- The angle  $\theta$  is considered small and Eq. 5.52 is linearized in  $\tan \theta$ . This makes sense in our case and, more generally, with polar satellites, because the satellite trajectory is presumably close to the arc normal.
- The fit formula Eq. 6.2 is not normalized by dividing it through  $\sigma^2$ .
- The FAC-electrojet coupling is modeled through a non-linear term.

#### $\tan \theta$ small parameter

In this case the definition of  $y_{ft}$  (l.h.s. of Eq. 5.52) in Eq. 6.2 reduces to:

$$y_{ft} \equiv H_x \tan \theta + \Sigma_P \sum_{i=1}^{n_x} a_i G_i - \Sigma_H b_0 + \Sigma_P b_0 \tan \theta + c_0 + c_1 x \quad (6.11)$$

The results obtained by linearizing the fit formula in  $\tan \theta$  are presented in the top panels of Fig. 6.14 and in Table 6.8. Large differences are seen to exist, as compared to the results obtained with the exact formula. The largest discrepancy is in  $\tan \theta$ , which is -3 when using Eq. 6.11 (not small at all), as compared to -0.4 when using Eq. 5.52. The flow direction of the electrojet would be practically perpendicular to the arc alignment as inferred from the optical and magnetic field data. Obviously,  $\tan \theta$  cannot be considered as a small parameter for the minimization procedure. Even if the the satellite path is almost perpendicular to the arc the angle it makes with the normal to the electrojet can be significant, which precludes the approximate formula Eq. 6.11.

An instructive remark refers to the value of  $\chi_r^2$ . The fit linear in  $\tan \theta$  is better, if judged only by the statistical criterion. The physical meaning is, however, the primary criterion to be considered.

Table 6.8: Model YPYHX36: Results obtained rigorously and with  $\tan \theta$  small

	$\tan \theta$	$b_0$ [mV/m]	$c_0$ [A/m]	$c_1$ [ $\mu$ A/m <sup>2</sup> ]	$\chi_{r_i}^2 / \chi_{r_o}^2$
Rigorous, Eq. 5.52	-0.4	-9.8	0.193	-1.34	18902/8.0
Approx., Eq. 6.11	-3.0	-3.6	0.061	-0.91	18902/1.4

### Fit formula not normalized

By neglecting the weighting factors  $1/\sigma_k^2$  the fit formula Eq. 6.2 writes:

$$f = \sum_{k=1}^N (y_{ms_k} - y_{ft_k})^2 \quad (6.12)$$

The results do not change too much. However, the weighting factors become important when the conductance drops to low values. The bottom panels of Fig. 6.14 show the electric field obtained for model YPYHX with  $n_x = 18, 36, 54$ . The higher is  $n_x$ , the smaller is the field structure that is taken into account. The interval IALL consists of 171 measuring points, each of them  $\sim 0.3s$  long. Accordingly,  $n_x = 18, 36, 54$  corresponds to resolutions of  $\sim 3s, \sim 1.5s$ , and  $\sim 1s$  respectively. The low conductance intervals,  $[t_0 + 37.5, t_0 + 41]$  and  $[t_0 + 45, t_0 + 48.5]$ , are properly modeled only for  $n_x = 36, 54$  but not for  $n_x = 18$ . If  $n_x$  is high enough to capture the small scale the neglect of the weighting factors in Eq. 6.2 artificially increases the (absolute value of the) electric field when the conductance is low, at the expense of a slight decrease for the rest of the time.

The importance of the weighting factor for low conductance intervals also points to the potentially larger error in the electric field for such intervals. The weighting factor we used is based on the error in the Pedersen conductance (Section 6.1.2). The associated relative error is not larger than  $\sim 10\%$  (Section 4.4.2), which might well be underestimated when the conductance drops below  $\sim 1\text{--}2\text{mho}$  (as it is the case in the vicinity of  $t = t_0 + 39$ ). Considering a larger error would diminish the contribution of the low conductance intervals in the fit function Eq. 6.2 and the electric field would flatten across such intervals.

When the conductance is reasonably high (exceeding a few mho) the results are relatively insensitive to the choice of the weighting factors. Taking into account that at such times the evaluation of the conductance itself is pretty accurate, it seems appropriate to conclude that our results are reliable for most of the time.

### Modeling the FAC–electrojet coupling with a non-linear term

A last check that we performed regarding the proper form of the fit function refers to the term that expresses the FAC–electrojet coupling. The results we showed are based on a linear approximation, which is the simplest modeling solution. However, there is no a priori theoretical reason to disregard other options.

A limited number of tests was performed, to see if the linear dependence is favored in some way. The answer seems to be affirmative. When choosing a quadratic or cubic dependence,  $c_1 x^2$  respectively  $c_1 x^3$  instead of  $c_1 x$ , the fit with starting point 0 does not make any change to  $c_1$



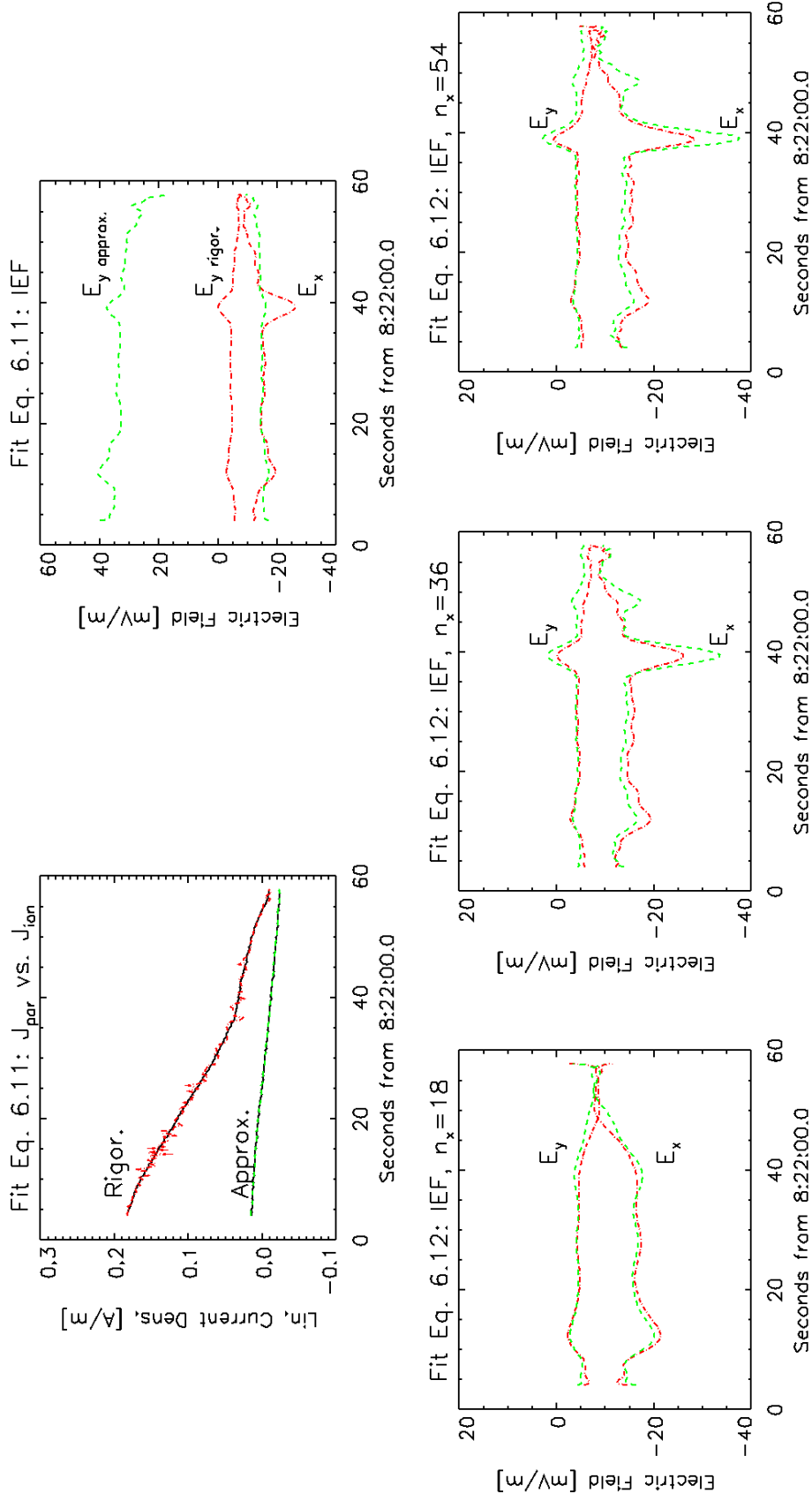


Figure 6.14: **TOP:** Comparison between the fit based on Eq. 6.11 and the exact fit for model YPYHX36. **Left:**  $J_{par}$  (black solid lines) and  $J_{ion}$ . The lower curves show the approximate results. **Right:**  $E_x$  and  $E_y$ . The red dash-dotted lines/green dashed lines show the exact/approximate results. **BOTTOM:**  $E_x$  and  $E_y$  obtained by fit with/without (red dash-dotted line/green dashed line) weighting factors in Eq. 6.2. **Left:**  $n_x = 18$ . **Middle:**  $n_x = 36$ . **Right:**  $n_x = 54$ .

(which remains 0) and the result is identical to that obtained from model YPYH. Another test was conducted by letting the exponent of  $x$  variable, that is by changing the term  $q_1 x$  to  $c_1 x^r$ . When the set of parameters provided by YPYHX was chosen as starting point, the output was essentially identical to the input (the exponent  $r$ , for example, only varied from 1 to 0.999). When the starting point was chosen to be 0 for all parameters, except for  $\eta_0 = 1$ , no useful results could be obtained because of the numerical instability introduced by the variation of  $r$ .

These limited checks suggest that the assumption Eq. 5.44 might be more than just a convenient numerical choice and the current transfer between the FAC and the electrojet could tend to proceed linearly along the arc. To clarify this issue one might have to address the M-I coupling, but a detailed investigation is beyond the scope of this work.

#### 6.4.4 Deriving $\tan \theta$ from magnetic field data

It is interesting to check how the results obtained with model YPYHX change if we use  $\tan \theta$  as provided by the magnetic field data. In this case we only have to find  $b_0$ ,  $c_0$ , and the polarization coefficients,  $a_i$ . The fit formula Eq. 5.52 does not change, except that now  $\tan \theta$  is known. Equation 5.52 becomes linear in parameters and one can use a regression method instead of non-linear minimization (the results obtained are identical, irrespective of which method is used; see Appendix F for details). We shall first address the problem of deriving  $\tan \theta$  from the magnetic data. In Section 6.4.5 we shall comment the results obtained with model YPYHXL36.

Considering both the optical (Fig. 3.12) and magnetic field (Fig. 3.4) data, one would expect to find some variation in  $\tan \theta$  across the arc. It makes sense to examine the variation of  $\tan \theta$  on a scale close to the length scale of the structure under investigation. In our case the interesting time interval was naturally divided into 5 sub-intervals, of  $\sim 10$ s each, or  $\sim 28$ km ionospheric length. One can calculate  $\tan \theta$  in 2 ways:

1. Using the variance analysis (see Appendix G). By moving a window of 10s along the interval IALL a continuous variation of  $\tan \theta$  can be obtained.
2. Recalling that  $\tan \theta = -\delta \Delta B_x / \delta \Delta B_y \approx -(\Delta B_x)' / (\Delta B_y)'$ , with  $\Delta B$  the perturbation magnetic field and  $(\Delta B)'$  the derivative with respect to  $x$ . By expanding  $\Delta B_x$  and  $\Delta B_y$  in series of Legendre polynomials one can calculate the derivatives by using an analytic expression (Eq. E.9). The scale is taken into account through the order  $n_x$  of the series. For IALL, which is 53.7s long, a scale of 10s corresponds to  $n_x \approx 5 - 6$ .

The results of the two methods are shown in Fig. 6.15. In order to illustrate the influence of the scale we show  $\tan \theta$  for  $n_x = 1, 3, 5, 7$ . The derivatives are polynomials of order  $n_x - 1$ .

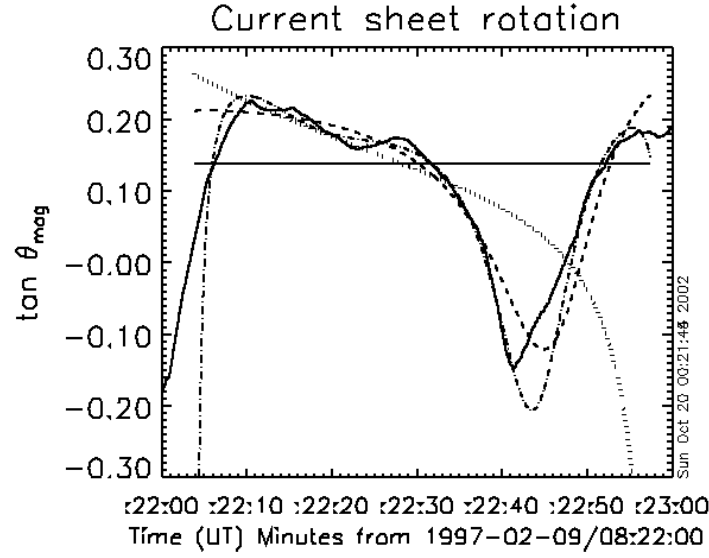


Figure 6.15: Rotation angle of the current sheet,  $\tan \theta_{mag}$ , obtained from the variance analysis (solid line) and by developing the magnetic field perturbation into Lagrange polynomials:  $n_x = 1$  (solid line, constant),  $n_x = 3$  (dotted line),  $n_x = 5$  (dashed line), and  $n_x = 7$  (dash-dotted line).

Consequently, for  $n_x = 1$  we have  $\tan \theta = \text{const}$ . One can see that  $\tan \theta$  obtained from the variance analysis with a window of 10s is somewhat 'between' the results obtained for  $n_x = 5$  and  $n_x = 7$ . Applying the variance method to the full interval IALL yields  $\tan \theta = 0.144$ , in good agreement with  $\tan \theta = 0.138$  obtained for  $n_x = 1$ . The corresponding angle is  $\theta \simeq 8^\circ$ .

#### 6.4.5 The linear model YPYHXL

Figure 6.16 shows results obtained with the model YPYHXL36 ( $\Delta \Phi = 2250\text{V}$ ). Two cases are presented: a) with  $\tan \theta$  constant and b) with  $\tan \theta$  calculated by the variance method (10s window). The parameters obtained for the two cases are compared in Table 6.9 to the parameters obtained with model YPYHX36 for both IALL and for the sub-intervals I1, ..., I5. One notes that the results are roughly insensitive to the particular form of  $\tan \theta$ . This is not surprising: the listed parameters are mainly influenced by the global change in the measured data, in particular of  $H_\eta$ , and not so much by the detailed variation, as captured by a non-constant  $\tan \theta$ .

The currents (top left panel of Fig. 6.16) exhibit a small increase as compared to model YPYHX:  $J_{par}$  (Eq. 6.5) reaches its maximum value in the AAS (that is, for model YPYHXL) and  $J_{ion}$  is accordingly increased (mainly through the increase of  $q_0$ , see Table 6.9). The orientation of the ionospheric current is substantially modified (compare Fig. 6.17 with Fig. 6.11): model YPYHXL imposes a current flow roughly parallel to the arc while for model YPYHX the dominant flow direction is determined by fit.

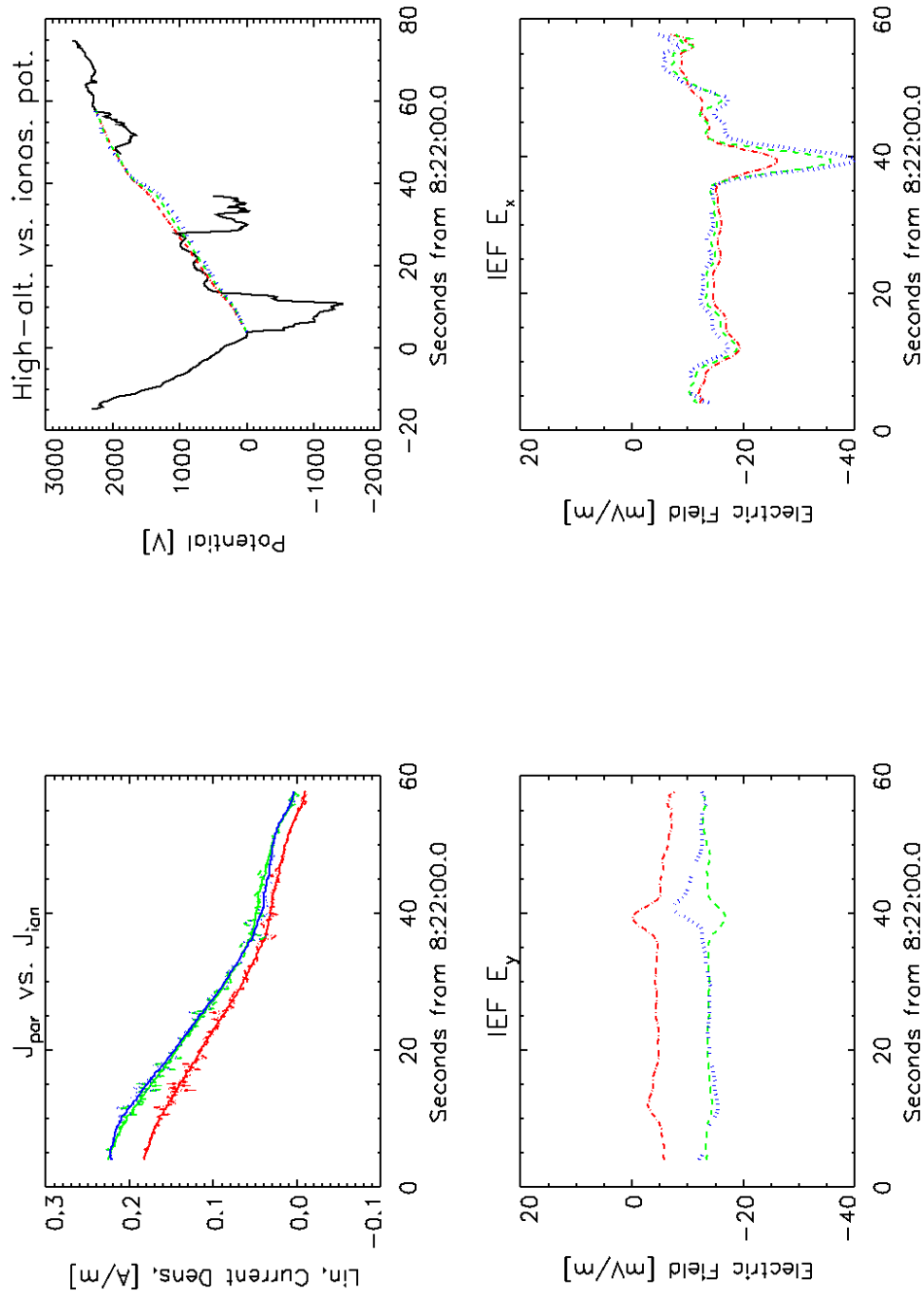


Figure 6.16: Comparison between models YPYHXL36 and YPYHX36. Model YPYHX36 is shown by red dash-dotted line. For model YPYHXL36 two cases are shown: with constant  $\tan \theta$  (green dashed line) and with  $\tan \theta$  from variance analysis (blue dotted line). **TOP Left:** Current.  $J_{par}$  is shown as solid line, observing the color code. **Right:** High-altitude and ionospheric potential ( $\Delta\Phi_{IALL} = 2250V$ ). **BOTTOM Left:**  $E_y$ . **Right:**  $E_x$ .

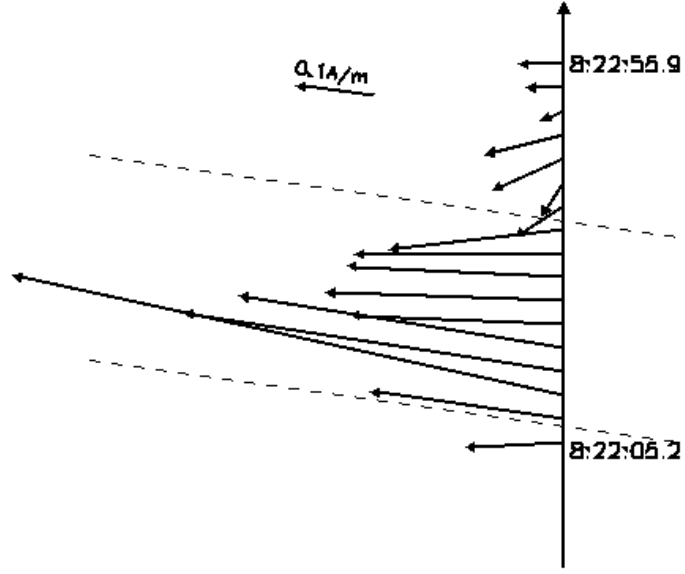


Figure 6.17: The current along the ionospheric footprint of FAST for model YPYHXL36;  $\tan \theta$  from variance analysis with 10s window. Same format as Fig. 6.5.

The  $E_x$  component of the electric field (bottom right panel of Fig. 6.16) is, for most of the time, just slightly modified. Consequently, the change in the ionospheric potential is small (top right panel of Fig. 6.16). However, the intensification of the southward IEF at  $t = t_0 + 39$  is  $\sim 2$  times stronger for model YPYHXL. This points once more to the larger uncertainty one can expect when the conductance drops to low values.

A significant difference with respect to model YPYHX36 is the  $\sim 3$  times larger westward electric field  $E_y$ . This is related to the change in the orientation of the ionospheric current, as explained by Fig. 6.18:  $\mathbf{E}_1$  and  $\mathbf{J}_1$  correspond to model YPYHX36,  $\mathbf{E}_2$  and  $\mathbf{J}_2$  to model YPYHXL36. Both vector pairs are associated with the average conductance ratio over IALL,  $\Sigma_H/\Sigma_P \simeq 1$  (implying  $\theta_1 = \theta_2 = 45^\circ$ ) and  $\mathbf{E}_1$ ,  $\mathbf{E}_2$  are related by  $E_{1x} \simeq E_{2x} \simeq E_{0x}$ . With  $\tan \theta_{J_1} = 0.5$  and  $|E_{0x}| \simeq 15 \text{ mV/m}$  one obtains  $|E_{1y}| \simeq 5 \text{ mV/m}$  and  $|E_{2y}| \simeq 15 \text{ mV/m}$ .

The goodness-of-fit as expressed by  $\chi^2_{r_o}$  in the last column of Table 6.9 suggests that the model YPYHX36 should be preferred. Metaphorically speaking, by including  $\tan \theta$  among the fit parameters a 'lower energy' configuration can be obtained, from the data point of view. However,  $E_y$  yielded by model YPYHXL36 looks better fitted for the growth phase of a substorm, as will be discussed in Section 6.5.2. In addition, we tend to regard as more credible an electrojet that flows roughly parallel to the arc. The difference  $\theta_{FA} = \theta_A - \theta_F$  ( $\approx 30^\circ$  in our case, see p. 112), between the arc and the orientation obtained by fit, might be taken as an error estimate for the flow direction of the electrojet.

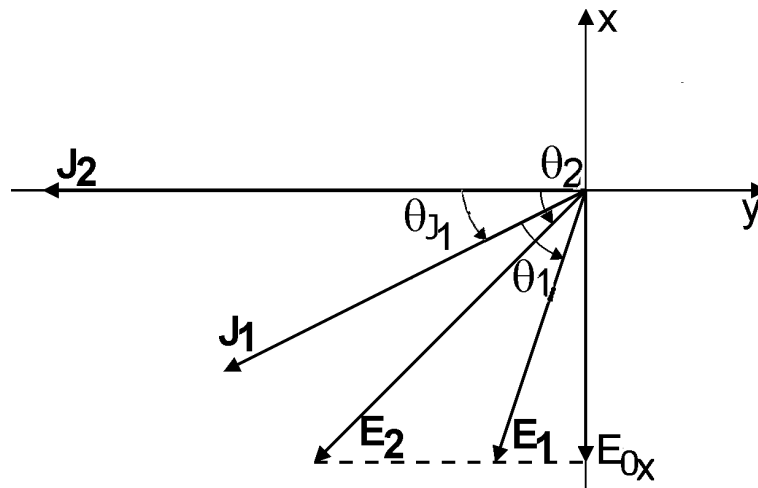
Figure 6.18: Sketch that explains the larger  $E_y$  for model YPYHXL36.

Table 6.9: Parameters obtained with model YPYHXL vs. YPYHX

Interval	Model	$b_0$ [mV/m]	$c_0$ [A/m]	$c_1$ [ $\mu\text{A}/\text{m}^2$ ]	$\chi_{r_i}^2 / \chi_{r_o}^2$
IALL	YPYHXL36 a)	-11.7	0.245	-1.55	19951/13.0
	YPYHXL36 b)	-11.4	0.245	-1.57	20283/12.8
	YPYHX36	-9.81	0.193	-1.34	18902/ 8.0
IIS	YPYHXL7 a)	-12.4	0.249	-0.04	40715/11.6
	YPYHXL7 b)	-12.5	0.253	0.07	41930/12.9
	YPYHX7	-10.3	0.204	-0.38	40268/ 7.7
IIB	YPYHXL28 a)	-10.3	0.279	-1.03	10028/ 3.0
	YPYHXL28 b)	-10.4	0.283	-1.07	10322/ 3.3
	YPYHX28	-9.1	0.233	-0.84	9585/ 2.2
I2	YPYHXL7 a)	-5.6	0.254	-2.00	37095/ 4.3
	YPYHXL b)	-5.8	0.255	-1.93	38254/ 4.6
	YPYHX7	-5.1	0.229	-2.02	36142/ 3.6
I3S	YPYHXL7 a)	-14.6	0.191	-4.57	16342/ 2.7
	YPYHXL7 b)	-14.4	0.191	-4.60	16234/ 2.7
	YPYHX7	-11.0	0.145	-3.49	15970/ 1.7
I3B	YPYHXL28 a)	-12.7	0.179	-3.30	4127/ 2.2
	YPYHXL28 b)	-12.6	0.179	-3.34	4101/ 2.2
	YPYHX28	-10.3	0.137	-2.71	3912/ 1.4
I4	YPYHXL7 a)	-18.4	0.054	0.65	3837/ 1.2
	YPYHXL7 b)	-15.7	0.048	0.41	3321/ 0.8
	YPYHX7	-12.7	0.038	0.17	3583/ 0.7
I5	YPYHXL7 a)	-17.0	0.037	-0.53	2998/ 1.7
	YPYHXL7 b)	-16.9	0.035	-0.35	2993/ 1.6
	YPYHX7	-10.6	0.018	-0.76	2666/ 0.8

## 6.5 Further discussion of the models YPYHX and YPYHXL

We shall examine in more detail some features of the models YPYHX and YPYHXL associated with uncertainties in the parameters. We shall also briefly explore some possible extensions of the fit procedure, that could lead to more accurate models of the arc.

### 6.5.1 The dependence on $\eta$ of the constant $c_0$

In Section 5.4.3 we derived the fit formula Eq. 5.52 by neglecting the dependence of  $c_0$  on  $\eta$  in Eq. 5.50. This approximation might be questioned as long as  $\Delta\eta = |\sin\theta|L$ , the variation of  $\eta$  along the satellite path, is not negligible compared to the length scale  $L_\eta$  of the electrojet. With  $L = 152\text{km}$  (Table 6.1) and  $|\tan\theta| = 0.4$  (Table 6.4) we get  $\Delta\eta = 56\text{km}$  for model YPYHX36. For model YPYHXL36  $\tan\theta = 0.14$  and  $\Delta\eta = 21\text{km}$ .  $L_\eta$  was estimated to 200–500km for model YPYHX36 (p. 112); we can keep the same estimate for model YPYHXL36, as both  $J_\eta$  and  $c_1$  are somewhat larger. Consequently, the ratio  $\Delta\eta/L_\eta$  may take values in the range 0.1–0.3 for model YPYHX36 and is probably smaller than 0.1 for model YPYHXL36.

It makes sense (in particular for model YPYHX36) to see what happens if, instead of  $c(\eta) = \text{const.} = c_0$ , we approximate  $c(\eta)$  by its Taylor expansion up to the first order:

$$c(\eta) = c_0 + \left. \frac{dc}{d\eta} \right|_{\eta=\eta_0} \Delta\eta \simeq c_0 + \frac{c_0}{L_\eta} \Delta\eta = c_0 - \frac{c_0 \sin\theta}{L_\eta} \Delta x \quad (6.13)$$

If we take  $\eta_0 = x_0 = 0$  Eq. 5.50 writes:

$$H_\eta - J_\xi = c_0 - \frac{c_0 \sin\theta}{L_\eta} x + \tilde{c}_1 \xi = c_0 + \left( c_1 - \frac{c_0 \sin\theta}{L_\eta} \right) x = c_0 + \hat{c}_1 x \quad (6.14)$$

Strictly speaking, the value obtained by fit is  $\hat{c}_1$ . The error in  $c_1$  is of the order  $\delta c_1 \simeq c_0 |\sin\theta|/L_\eta$ .

Introducing numerical values we get for model YPYHX36 an average value  $|\delta c_1| \simeq 0.2 \times 0.4/(300 \times 10^3) \simeq 0.25 \times 10^{-6}$ . The relative error in  $c_1$  is  $|\delta c_1/c_1| \simeq 0.25/1.3 \simeq 20\%$ . For model YPYHXL36 an upper estimate of the error is  $|\delta c_1| \simeq 0.25 \times 0.15/(300 \times 10^3) = 0.12 \times 10^{-6}$ . The relative error in this case is  $|\delta c_1/c_1| \simeq 0.12/1.5 \simeq 8\%$ . The variation of  $H_\eta - J_\xi$  with  $\eta$  has smaller influence on  $c_1$  for model YPYHXL36 because of the associated smaller  $\Delta\eta$ .

### 6.5.2 $E_y$ : Fit results vs. optical evidence

If we compare the electric field  $E_y \simeq -10\text{mV/m}$ , inferred from the optical data, with the results of the fit, a slight disagreement exists,  $\delta E_y \lesssim 5\text{mV/m}$ , either if we refer to model YPYHX or to model YPYHXL. For model YPYHX the resulting  $E_y$  is a little bit smaller (in absolute value) than the experimental value, while for model YPYHXL  $E_y$  is a little bit larger (bottom left panel of Fig. 6.16). There are two possible explanations for these differences:

- They could be just the effect of averaging. Although when evaluating  $E_y$  from the optical data the same  $\sim 1$  min period was used as for the fit procedure, the averaging is different:
  - The  $E_y$  provided by the optical data is based on the average velocity of the southern border of the arc
  - The  $E_y$  provided by fit is, in some sense, a spatial-temporal average over  $\sim 1$  min of FAST data, collected between points somewhat in front of the southern border and well beyond the northern border of the visible arc
- Some (or all) disagreement is real, and the arc has a proper motion, with respect to the ionospheric plasma. This topic was investigated in detail by Haerendel et al. (1993). By simultaneous measurements of plasma and arc motion, from radar and optical data respectively, these authors were able to determine the relative motion of three different arcs with respect to the plasma.

Haerendel et al. (1993) suggested that the proper motion of the arc could be initiated not only at generator but also at AAR level. In the first case one can distinguish again two possibilities: **a)** fast motions, as a result of reconnection or compressional waves at substorm onset; **b)** extremely slow motions, of the order of 10m/s (equivalent to 0.5mV/m), due to generator hot plasma transport. Neither of these two alternatives fits to our data: situation **a** is typical after the break-up, not in the growth phase, while in situation **b** the motion of the arc and the Pedersen current should point in opposite directions, not as in our case, both southward.

The proper motions generated at AAR level reflect the spontaneous propagation of the AAR into or out of the current circuit, which can be compared to a 'fracture' process (see Haerendel (1989) and references therein for details). The velocity of the motion is of the order of  $\sim 100$  m/s, equivalent to  $\sim 5$  mV/m, which compares well with our 'would be' motion. For the model YPYHX the arc travels southward somewhat faster than the plasma; according to Haerendel et al. (1993) this means that the current system shrinks and magnetic energy is released. For the model YPYHXL on the contrary, the plasma motion is faster; the current system expands and the energy is built up, in better agreement with a substorm in its growth phase.

### 6.5.3 Boundary effects

We have seen earlier in this Chapter that abrupt variations of the electric field can be sometimes noticed at the boundaries of the fit intervals (Figs. 6.7, 6.10, and 6.12). Closely related to this feature is the dependence of the derived IEF on the fit interval.



Although we do not have a good analytic proof, we feel that the origin of the problem can be traced back to the steep variation of the orthogonal polynomials at the boundaries of the interval, the steeper the higher the order of the polynomial is (see Appendix E). Small errors in the polarization coefficients  $a_i$  can combine 'in phase' with the large variations in  $G_i$ , leading to the deviations observed. It would be probably safe to disregard the 'boundaries' of the interval, i. e. the two half-periods where the steep variation is concentrated. When the conductance is small, and the errors presumably large, it may happen that the boundary errors propagate deeper inside the investigated interval (this is probably the case with interval I4).

Function expansion in series of orthogonal polynomials provides, as a rule, only convergence 'in the mean', but not uniform convergence (e. g. Courant and Hilbert, 1953, Chapter II, p. 54). The series converges to the approximated function most of the time, but there are also points of poor convergence or no convergence at all.

#### 6.5.4 Extensions of the fit procedure

The fit formula Eq. 5.52 is written in cartesian coordinates and assumes quite restrictive conditions for the electric field. In the first unit below we shall check how the fit formula changes when written in polar coordinates, which represent the simplest choice of orthogonal curvilinear coordinates. In the second unit we shall give more freedom to the electric field and derive the associated fit formula. The results from the two units can be combined increasing further the complexity of the fit formula. Note that the more general formulas to be given below were not tested with the data. They are meant to illustrate a possible continuation of the present work.

##### Fit in polar coordinates

If  $(\xi, \eta)$  are polar coordinates then  $s_\xi \equiv \xi$  and Eq. D.13 writes:

$$\frac{\partial}{\partial \xi}(H_\eta - J_\xi) - \frac{1}{R_\xi}(H_\eta - J_\xi) = \frac{\partial}{\partial s_\eta}(H_\xi + J_\eta) \quad (6.15)$$

If we set  $\partial/\partial s_\eta(H_\xi + J_\eta) = \tilde{c}_1$  Eq. 6.15 transforms to:

$$\frac{\partial}{\partial \xi}(H_\eta - J_\xi) - \frac{1}{R_\xi}(H_\eta - J_\xi) = \tilde{c}_1 \quad (6.16)$$

which is identical to Eq. 5.49 except for the second term on the l.h.s. Equation 6.16 reduces to Eq. 5.49 for  $R_\xi = \infty$ . If we assume that  $R_\xi \equiv R = \text{const.}$  Eq. 6.16 becomes linear and can be easily integrated:

$$H_\eta - J_\xi = c_0(\eta) + \tilde{c}_1 R(e^{\xi/R} - 1) \quad (6.17)$$

If  $\xi/R \ll 1$  Eq. 6.17 reduces to Eq. 5.50. This can be easily checked by writing the Taylor expansion of the exponential. The important point about Eq. 6.17 is the additional parameter  $R$ , besides the older  $c_0$  and  $\tilde{c}_1$ . Further processing yields a fit formula similar to Eq. 5.52, except for the term  $c_1 x$  which is replaced with the second term on the r.h.s. of Eq. 6.17.

### Additional degrees of freedom for the electric field

In deriving Eq. 5.52 we started from the Eqs. 5.50 and 5.33:

$$H_\eta - J_\xi = c_0 + \tilde{c}_1 \xi, \quad E_\eta = b_0$$

with the same axis,  $\eta$ , in both equations. There is, however, no imperative reason for such a constraint; the current and the electric field could, in principle, be associated with distinct axes,  $\eta$  and  $\eta_E$ . In addition, either  $E_{\eta_E}$ , or  $E_{\xi_E}$ , or both, could be variable (see Section 6.6.2); as a first approximation one may consider a linear variation. The two equations above write:

$$H_{\eta_J} - J_{\xi_J} = c_0 + \tilde{c}_1 \xi_J = c_0 + \tilde{c}_1 \cos \theta_J \cdot x = c_0 + c_1 x \quad (6.18)$$

and

$$E_{\eta_E} = b_0 + \tilde{b}_1 \eta_E = b_0 - \tilde{b}_1 \sin \theta_E \cdot x = b_0 + b_1 x \quad (6.19)$$

if  $E_{\eta_E}$  varies or, via Faraday's law

$$E_{\xi_E} = b_0 + \tilde{b}_1 \xi_E = b_0 + \tilde{b}_1 \cos \theta_E \cdot x = b_0 + b_1 x \quad (6.20)$$

if  $E_{\xi_E}$  varies. After some tedious but straightforward algebra one obtains:

$$\begin{aligned} H_x \tan \theta_J + \Sigma_P E_x (1 + \tan \theta_E \tan \theta_J) + \Sigma_H E_x (\tan \theta_J - \tan \theta_E) + \\ (-\Sigma_H + \Sigma_P \tan \theta_J) \frac{b_0 + b_1 x}{\cos \theta_E} + \frac{c_0 + c_1 x}{\cos \theta_J} = H_y \end{aligned} \quad (6.21)$$

The additional parameters are now  $\tan \theta_E$  and  $b_1$ . Equation 6.21 reduces to Eq. 5.52 if  $\theta_E = \theta_J$  and  $b_1 = 0$ . Using Eqs. 5.36 and 5.38 to replace  $E_x$  Eq. 6.21 is cast in a form appropriate for fit.

A simple and potentially interesting model is obtained by setting  $\theta_J = \theta_E = \theta_A$ , i.e. a variety of the model YPYHXL with  $E_\eta$  linearly dependent on  $x$ . Theoretically, in such a case it would not be possible to say unambiguously whether the term  $b_1 x$  originates in the variation of  $E_\eta$  (Eq. 6.19) or  $E_\xi$  (Eq. 6.20). However, the track of a polar satellite is in general roughly perpendicular to the arc,  $\theta_A \simeq 0$  and  $\cos \theta_A \gg \sin \theta_A$ ; the chance that  $b_1 x$  reflects the variation of  $E_\xi$  would be considerably higher. Conversely, if the assumption  $E_\eta = b_0 + b_1 x$  does not lead to reasonable results one might conclude that  $E_\xi$  can be considered constant along the arc, at least on a scale comparable to  $\Delta\eta = L \sin \theta_A$ , i.e. the shift associated with the satellite crossing.

## 6.6 Current configuration

The models YPYHX and YPYHXL were shown to provide consistent electric field results. In order to complete the investigation of the arc electrodynamics we concentrate now on the current flow. The ionospheric current associated with the different models was already discussed, to some extent, in the previous Sections (Figs. 6.5, 6.11, and 6.17). While our main concern there was the electric field, here the current stays in the center of interest.

We shall first perform a detailed check of the current closure equation along FAST ionospheric footprint during the ion beam period. This approach will unravel the local topology of the current flow and will give a hint about the non-local behavior. Next we shall discuss the configuration suggested by our data and emphasize its considerable departure from the standard paradigm.

### 6.6.1 Current closure along FAST ionospheric footprint

We shall evaluate the relative contributions of the FA and ionospheric currents — along and transverse to the arc — in the closure equation (Eq. 5.23). In order to calculate the ionospheric current (via Eq. 5.22) we have used the electric field derived from the model YPYHXL36; the geometry is in this case simpler and the proper motion of the arc seems to corroborate better with the substorm growth phase (Section 6.5.2).

Figure 6.19 presents the ionospheric currents,  $J_\xi$  and  $J_\eta$ , as well as the FA sheet current,  $J_\parallel$ , for the intervals IALL and I1, I2, I3 (that cover the visible arc).  $J_\xi$  and  $J_\eta$  are shown together with their Pedersen and Hall components,  $(J_{\xi P}, J_{\xi H})$  and  $(J_{\eta P}, J_{\eta H})$ .  $J_\parallel$  was calculated with:

$$J_\parallel(\xi) = \int_{\xi_0}^{\xi} j_\parallel(u) du \simeq H_\eta, \quad H_\eta \text{ at ionospheric level} \quad (6.22)$$

where  $\xi_0$  indicates the southern boundary of the downward FAC sheet. We assumed the longitudinal extension of the FAC may be approximated as infinite (see Fig. 3.4), in which case  $J_\parallel \equiv H_\eta$ .

The most important information one can extract from Fig. 6.19 is that the transverse current,  $J_\xi$ , practically vanishes at the beginning of IALL.  $J_\xi$  remains small over the whole interval, because the southward Pedersen and the northward Hall currents compensate each other. As we shall discuss in more detail next Section,  $J_\xi$  cannot provide the ionospheric connection between the downward and upward branches of the FAC. The current parallel to the arc,  $J_\eta$ , is much larger, reaching a peak value of  $\sim 0.75 \text{ A/m}$  (within the normal electrojet range).  $J_\eta$  is mostly of Hall origin, but the Pedersen contribution is not negligible (of the same order with  $J_\parallel$ ).

With the very small  $J_\xi$  it is only the variation of  $J_\eta$  that can act as source for  $j_\parallel$ . One can convince oneself about this point by checking the current continuity at ionospheric level (Eq. 5.23, re-written here in  $(\xi, \eta)$  coordinates):

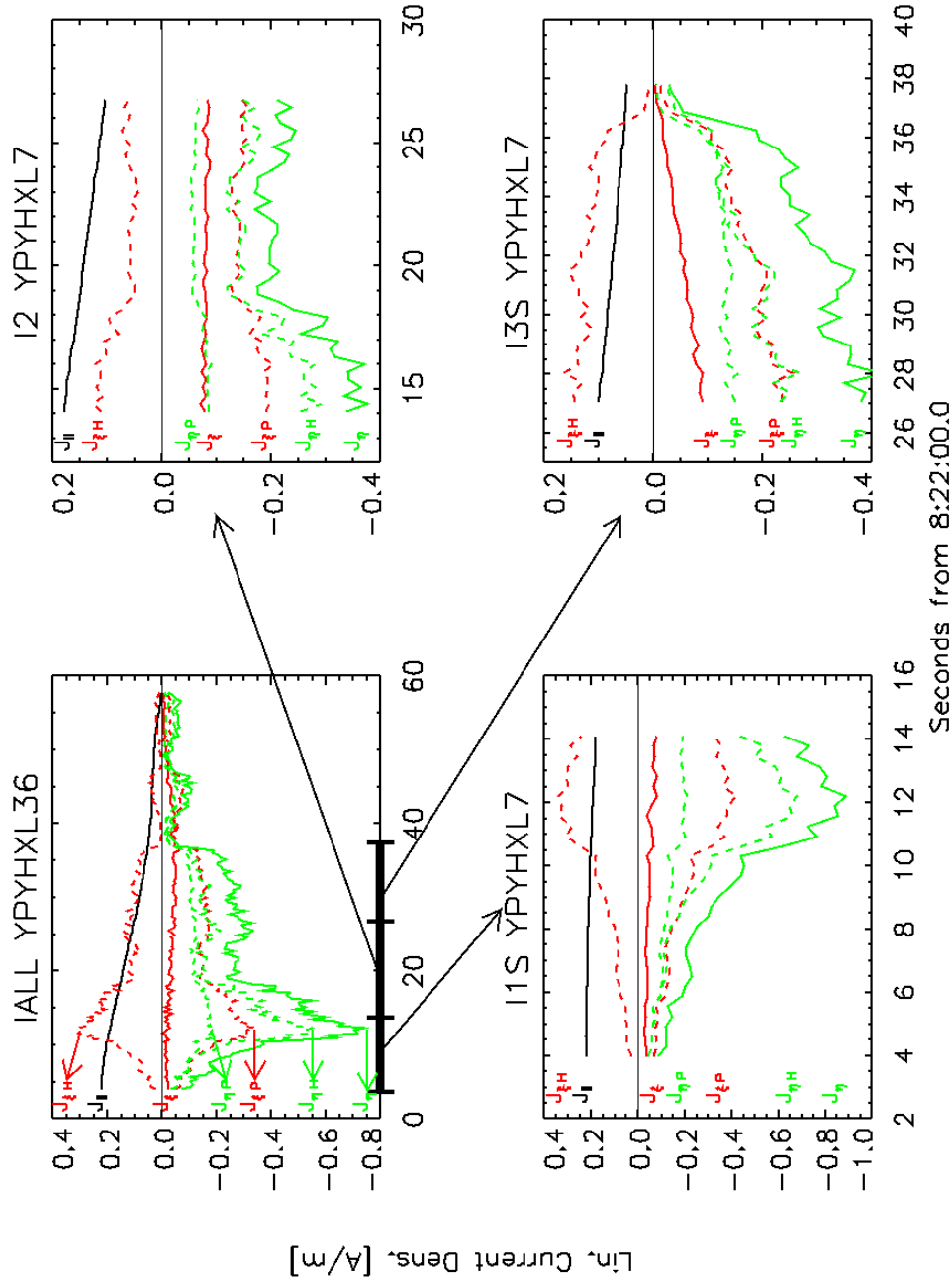


Figure 6.19: The FA and ionospheric sheet currents, along the FAST footprint, as resulted from model YPYHXL36. The Pedersen and Hall components of  $J_\xi$  and  $J_\eta$  are shown as dashed lines. **Top left:** The whole interval IALL. **Bottom and Top right:** Zoom on the intervals I1S, I3S, and I2 respectively, that encompass the visible arc. Note the very small  $J_\xi$  during I1S, which indicates that the current transfer between the downward and upward FAC regions is negligible.

$$j_{\parallel} = \frac{\partial J_{\xi}}{\partial \xi} + \frac{\partial J_{\eta}}{\partial \eta} \Rightarrow S_j \equiv \frac{\partial J_{\xi}}{\partial \xi} + \frac{\partial J_{\eta}}{\partial \eta} - j_{\parallel} = 0 \quad (6.23)$$

$S_j$  can be expressed in terms of quantities to be calculated from the experimental data:

$$\frac{\partial J_{\xi}}{\partial \xi} \simeq \frac{\Delta J_{\xi}}{L_{\xi}}; \quad \frac{\partial J_{\eta}}{\partial \eta} \simeq c_1; \quad j_{\parallel} \simeq \frac{\partial H_{\eta}}{\partial \xi} \simeq \frac{\Delta H_{\eta}}{L_{\xi}}$$

where  $L_{\xi}$  is the ionospheric length perpendicular to the current sheet,  $\Delta J_{\xi} = J_{\xi}(L_{\xi}) - J_{\xi}(0)$ , and  $\Delta H_{\eta} = H_{\eta}(L_{\xi}) - H_{\eta}(0)$ . Equation 6.23 becomes:

$$S_j \simeq S_j^{exp} = \frac{\Delta J_{\xi}}{L_{\xi}} + c_1 - \frac{\Delta H_{\eta}}{L_{\xi}} \simeq 0 \quad (6.24)$$

We checked Eq. 6.24 for the data shown in Fig. 6.19 and, in addition, for burst data, available during I1 and I3. The results obtained are collected in Table 6.10 (we used  $L_{\xi} = L \cos \theta$ , with  $L$  from Table 6.1 and  $\theta = 8^\circ$ , see Section 6.4.4). The last column proves that Eq. 6.24 is indeed verified by the data, within the experimental error. As one can see by comparing columns 3 and 4 the results obtained by fit over sub-intervals support the average trend expressed by the fit over IALL, in that the FAC is obtained at the expense of the variation in  $J_{\eta}$ . It is only for I1S (I1, Survey data) that the FAC is balanced by the variation in  $J_{\xi}$ . For I1B and I2 most of the FAC originates in the variation of  $J_{\eta}$  while for I3B and I3S  $J_{\eta}$  sources both  $j_{\parallel}$  and  $J_{\xi}$ . This last case is sketched in Fig. 6.20, which may be regarded as a graphical expression of the current continuity at ionospheric level (any other situation may be illustrated by appropriate changes of the arrows).

As our model calculations are based on the continuity equation the consistency of the results with this equation is actually not surprising. The last column of Table 6.10 just provides a good double check for the numerical method, which does not mean, however, that the results in the columns 2 and 3 are necessarily correct. The comparison of the values obtained with Survey and Burst data is significant for the errors involved. Even if one might feel reasonably confident in the tendency expressed by Table 6.10, more physical arguments, independent from the numerical processing, would be needed to improve on the credibility of these results. We shall return to this point the next Section.

Table 6.10: Check of Eq. 6.24

Interval	$\frac{\Delta J_{\xi}}{L_{\xi}}$	$c_1$	$\frac{\Delta H_{\eta}}{L_{\xi}}$	$S_j$
IALL	0.14	-1.57	-1.46	0.03
I1S	-1.55	+0.07	-1.44	-0.04
I1B	-0.37	-1.07	-1.44	0.00
I2	-0.17	-1.93	-2.18	0.08
I3S	2.93	-4.60	-1.75	0.08
I3B	1.56	-3.34	-1.75	-0.03

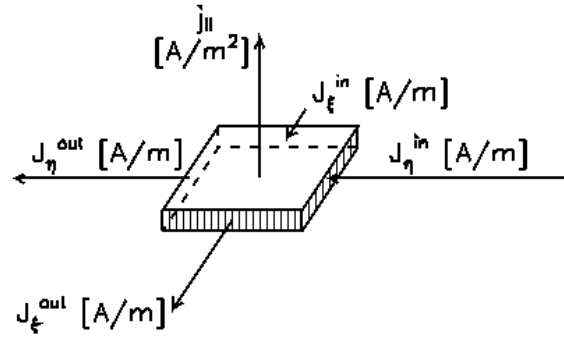
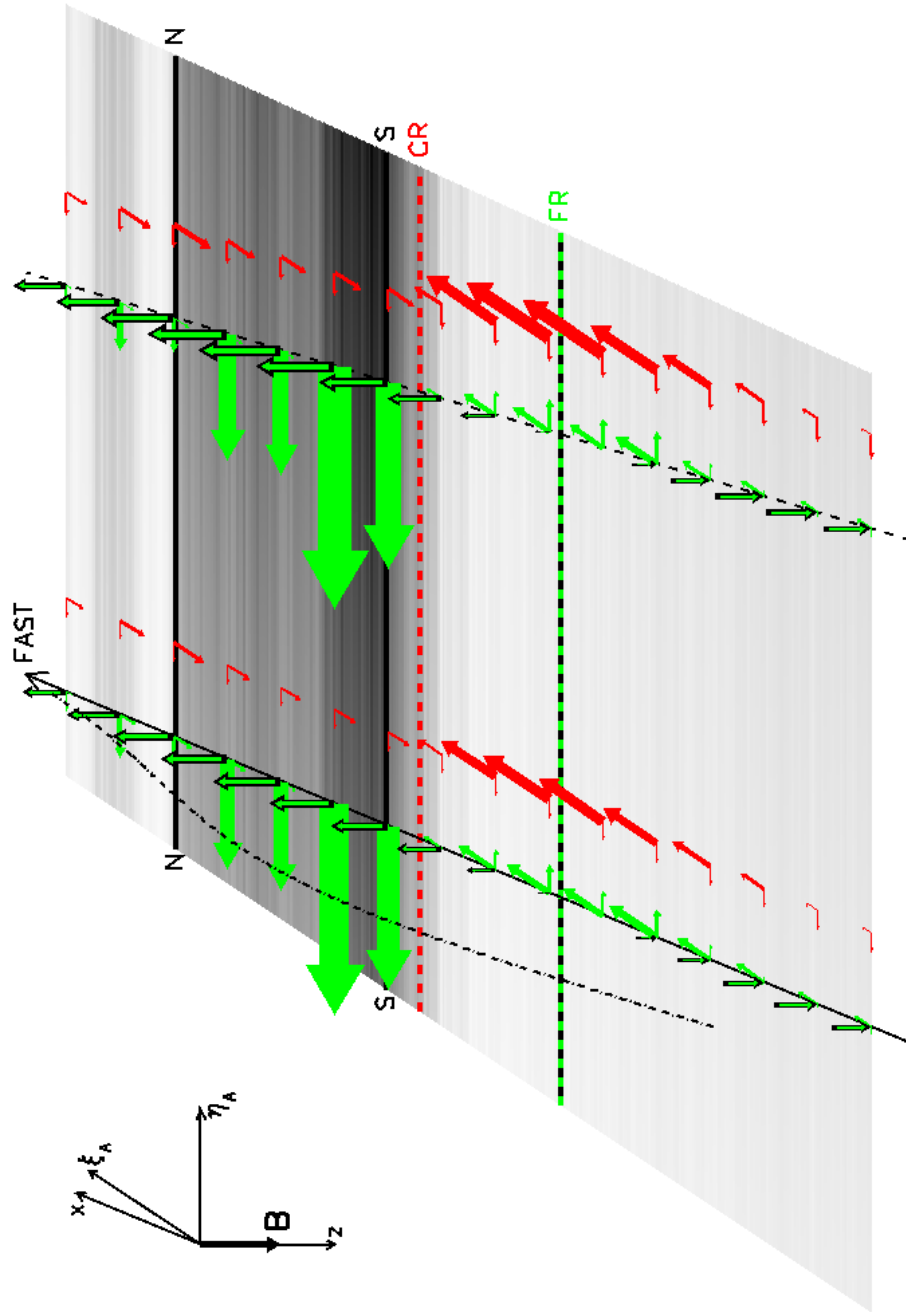


Figure 6.20: Cartoon illustrating the current conservation (Eq. 6.23). The decrease in  $J_\eta$  is the source for the increase in  $J_\xi$  and for  $j_\parallel$ . Note that  $j_\parallel$  is surface density ( $\text{A/m}^2$ ) while  $J_\xi$  and  $J_\eta$  are linear densities ( $\text{A/m}$ ).

The local closure of the current discussed above supports a 3D perspective of the arc and its surroundings as presented in Fig. 6.21. We included the currents and electric fields along FAST and an adjacent parallel track, as well as the conductance pattern, indicated by the gray background. The boundaries of the arc, the convection reversal (CR) and the FAC reversal (FR) are also shown. In the arc region the westward electrojet (WEJ) feeds the upward FAC and decreases toward west. The ionospheric current supplied by the downward FAC does not reach the upward FAC; most of it enhances the eastward electrojet (EEJ) and a small fraction crosses the CR as Hall current (see next Section) and joins the WEJ. Figure 6.21 tries to point to the possible sources for the longitudinal intensification of the electrojets:

- Enhanced precipitation (and FACs). In the arc region  $J_{\eta P}$  and  $J_{\eta H}$  point in the same direction and enhanced electron precipitation leads to the intensification of the WEJ. In the downward current region precipitating protons may carry a significant fraction of the current. However,  $J_{\eta P}$  and  $J_{\eta H}$  point in opposite directions; the EEJ does not intensify.
- Increase of  $E_\eta$ , implying a larger  $J_{\eta P}$ . The WEJ intensifies but the EEJ weakens.
- Increase of  $E_\xi$ , implying a larger  $J_{\eta H}$ . Both the WEJ and the EEJ intensify (note that here and above we refer to the absolute values of the mentioned quantities).

We suggest that the intensification of the EEJ is mainly determined by the increase in the northward electric field, while the intensification of the WEJ originates mainly in enhanced precipitation. This feature is pointed out in Section 5.4 of Kamide and Baumjohann (1993), who characterize the EEJ as “electric-field-dominant” and the WEJ as “conductivity-dominant”. Note that Fig. 6.21 is not fully consistent with our model YPYHXL, in that  $E_\xi$  is shown as variable in longitudinal direction. In the next Section we shall comment on still keeping  $E_\eta$  constant transverse to the arc.



### 6.6.2 The uncommon topology of the current flow

The comparison of the convection potential with the FAC sheet density is instrumental in understanding the closure of the current. We expanded the interval UT 8:20–8:24 of Fig.3.4 in Fig. 6.22 and chose to show again only  $\Phi$  and  $H_\eta$  in order to make clear the close proximity of the CR and FR, which is the key feature of our auroral configuration. Typically, the CR is located such way that most of the upward FAC is embedded in northward electric field and the connection between the two FAC sheets is achieved through Pedersen current — one of the two topologies discussed in the classical paper of Boström (1964). This is obviously not our case. It is only in the narrow strip between FR and CR (vertical hatching in Fig. 6.22) that the Pedersen current points to the north; the sheet upward current across this strip is, however, less than 0.02A/m. The largest part of the downward FAC injected into the ionosphere does not make it to the upward FAC. Before detailing the peculiar topology of the current flow we want to comment shortly on the position and width of the CR, as well as on the ionospheric current that crosses this boundary.

Because of the high-altitude potential structure the minimum in the potential (which is calculated from satellite data) is reached at 8:22:11 (see Fig.3.8 for a zoom). However, the trend exhibited by the potential out of the ion beams as well as our calculations (Fig.6.16) point to  $\sim$ 8:22:04 as the location of the CR. Note, however, that the electric field,  $E_x$ , that we derived is negative at this time (beginning of IALL) whereas just a few tenths of second earlier  $E_x$  is clearly positive, as indicated by the high-altitude potential. This raises the question whether such a thin CR is reasonable. Figure 6.22 suggests also that the change in the electric field is quite abrupt, while usually it is assumed that  $E_x$  has a gradual change in the vicinity of the reversal. Let us take  $E_x = 50\text{mV/m}$  south of the reversal,  $E_x = -20\text{mV/m}$  north of the reversal, and a reversal width  $W = 1\text{km}$  (we chose a conservative set of values;  $W = 1\text{km}$  corresponds to 0.35s of satellite data). The associated charge density is, in this case:

$$q_e = \frac{1}{\epsilon_0} \nabla \cdot \mathbf{E} = \frac{1}{\epsilon_0} \frac{dE_x}{dx} \simeq \frac{1}{\epsilon_0} \frac{\Delta E_x}{\Delta x} \simeq -6 \times 10^{-16} \text{C/m}^3 \quad (6.25)$$

which implies an excess of electrons  $\delta n \simeq 4 \times 10^{-3} \text{cm}^{-3}$ . This is only a small fraction ( $< 10^{-6}$ ) compared to the plasma densities to be found in the auroral region ( $> 10^4 \text{cm}^{-3}$ ). The numerical exercise above shows that the CR can be indeed very thin.

Coming to the transfer of ionospheric current through CR it is obvious that this can only be Hall current. Assuming an westward electric field of 15mV/m (as yielded by model YPYHXL36) and a Hall conductance of 4mho (Fig. 4.4), the associated northward Hall current is 0.06A/m ( $\sim 25\%$  of the current fed to the ionosphere in the downward FAC region). This current, however, does not reach the upward FAC region (Fig. 6.19) but joins the WEJ. The Hall current that crosses



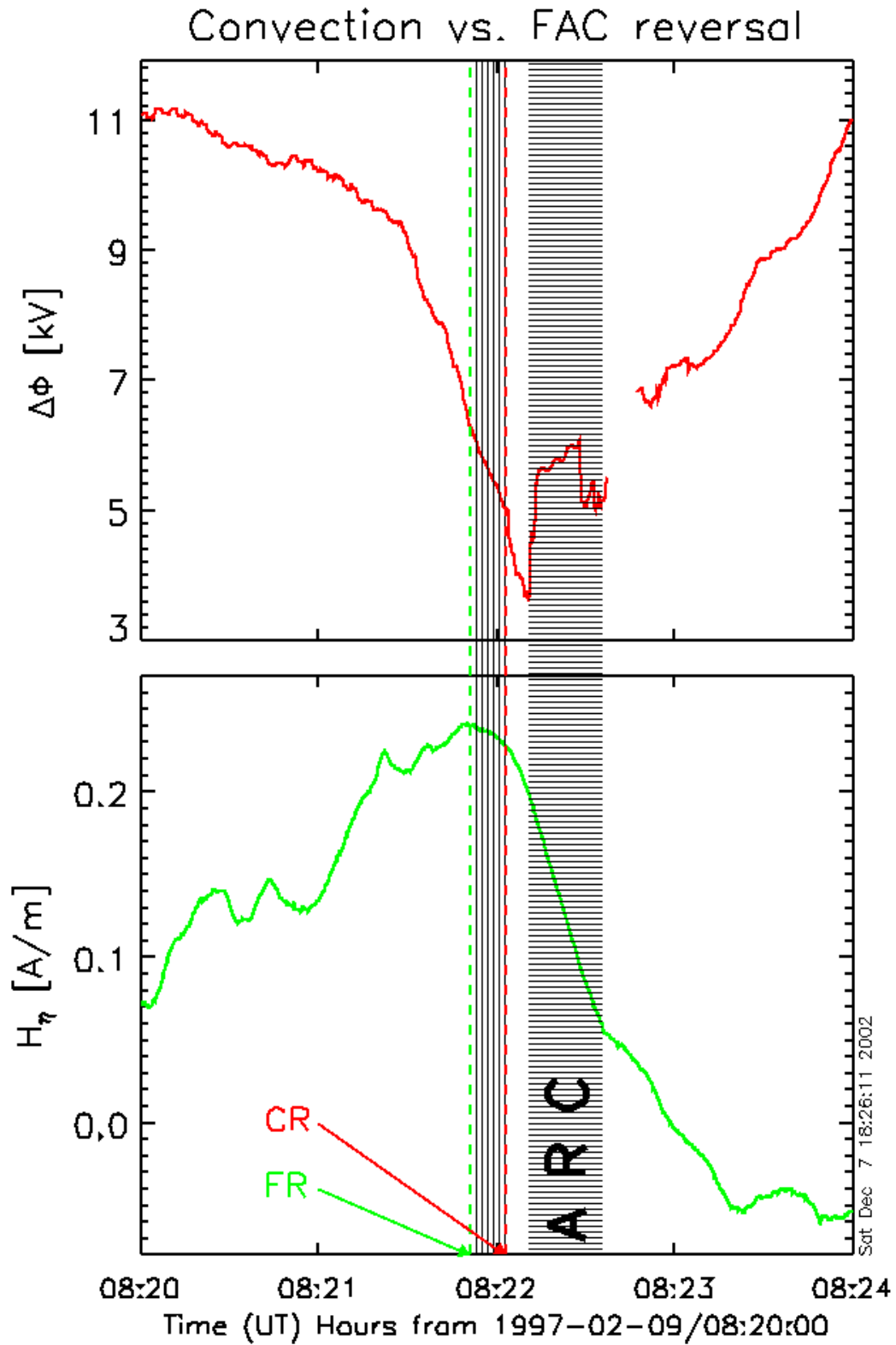


Figure 6.22: Expanded view of the interval UT 8:20–8:24 from Fig. 3.4 that shows the relative positions of the FAC reversal (FR), the convection reversal (CR), and the arc. The CR is very close to the FR and just a negligible fraction of the downward FAC returns to the magnetosphere as upward FAC.

the CR might be different if the arc is not 'frozen' in the plasma, which means that increased conductance can be carried away from the arc. In our case the distance between the peak of the electron precipitation (8:22:12, close to the southern border of the arc, indicated with horizontal hatching in Fig. 6.22) and the CR is  $\sim 20$ km. With a plasma velocity relative to the arc of  $\sim 100$ m/s (Section 6.5.2), assumed to be relatively uniform, one obtains that the precipitation peak crossed the CR  $\sim 3$ min before FAST encountered it. This time interval is longer than  $t^{(i)} \simeq 2$ min (see line 4 of Table C.2) needed for a change in plasma density from the value corresponding to the precipitation peak down to the level outside of the arc. Note that 3min before the satellite traversal the arc was less intense (frame 2 in Fig. 3.10), so that  $t^{(i)} \simeq 2$ min is a safe upper limit. We may conclude that the conductance at the CR is not significantly increased due to the relative motion of the plasma with respect to the arc.

As the charges cannot get accumulated it appears that the FACs are continued in the ionosphere with the EEJ and WEJ, as already pointed out in the previous Section. The topology of the current flow is sketched in Fig. 6.23 which can be seen as complementary to Fig. 6.21. For simplicity we neglected the small difference between AAS and SAS; below it is implied accordingly that  $x \equiv \xi$  and  $y \equiv \eta$ . Figure 6.23 also shows the electric field along the ionospheric footprint of FAST and the plasma convection, in a reference system moving with the arc. Because the westward electric field,  $E_\eta$ , does not vanish there is net plasma flux crossing the boundary of the arc and the CR; the plasma flow in Fig. 6.23 corresponds to a negative  $E_\eta$  in the arc system, as derived from model YPYHXL36. Similar results, based on the ion cloud technique, were reported already long time ago (e. g. Haerendel (1972), in particular Fig. 7, and references therein).

Figure 6.23 shows  $E_\eta$  as constant over a latitudinal extension of  $\sim 300$ km. North of the CR this assumption agrees with model YPYHXL. However, as discussed in the previous Section,  $E_\xi$  is expected to vary along  $\eta$ , at least south of the CR. Consequently, we may also expect variations of  $E_\eta$  along  $\xi$ . It is still reasonable to consider that these variations are small, at least within  $\sim 160$ km south from the CR. The ionospheric current fed by the downward FAC flows northward before joining the EEJ; a westward electric field of  $\sim 15$ mV/m drives a northward Hall current that has about the needed value to ensure the current continuity. For  $E_\eta \simeq -15$ mV/m the transverse current,  $J_\xi$ , around  $\sim 8:21:00$  is comparable to the sheet current,  $J_\parallel$ , fed by the downward FAC until this time. With  $\Sigma_P \simeq \Sigma_H \simeq 4$ mho (considering only proton induced conductance, Fig. 4.3) and  $E_\xi \simeq 10$ mV/m ( $E_\xi \simeq E_x \simeq -\Delta\Phi/\Delta x$ , with  $\Delta\Phi$  from the left third of the upper panel in Fig. 6.22) one obtains  $J_\xi \simeq 0.1$ A/m. This value compares quite well to  $J_\parallel \simeq 0.13$ A/m, read in the lower panel of Fig. 6.22).

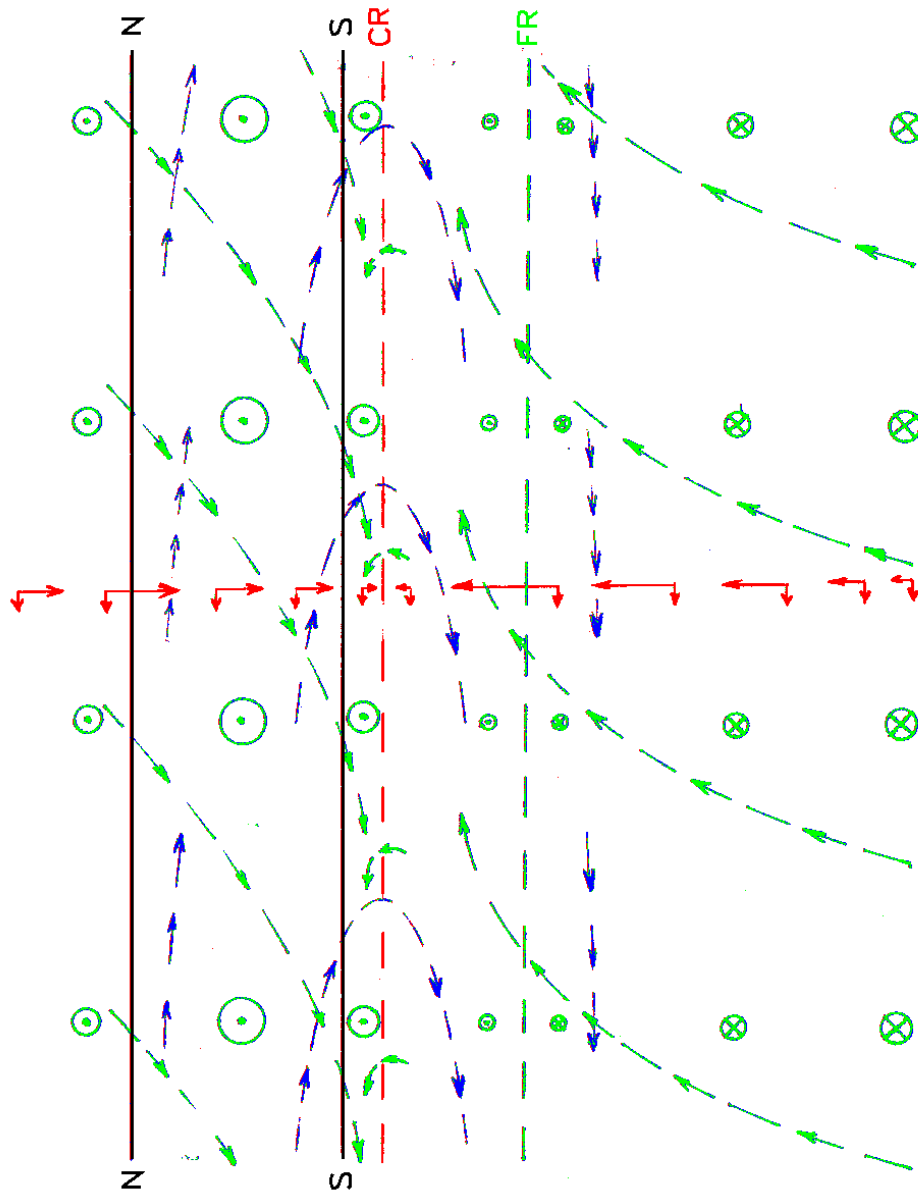


Figure 6.23: Schematic representation of the current and convection topology in the vicinity of FAST ionospheric footprint for the time interval 8:21:00–8:22:50. The ionospheric currents are shown with green arrows and the downward/upward FAC with green circled crosses/dots. The red and blue arrows show the electric field and the plasma convection respectively, in a reference system moving with the arc. The horizontal lines N–N, S–S, CR, and FR have the same significance as in Fig. 6.21. The upward FAC is fed by the WEJ. Most of the downward FAC feeds the EEJ while a small fraction crosses the CR to join the WEJ.

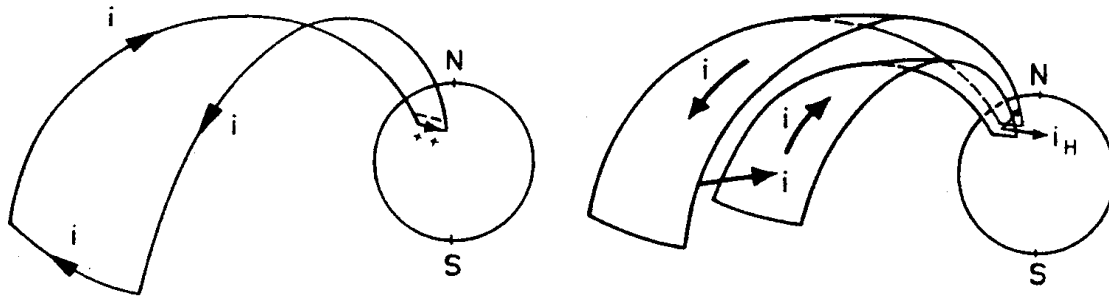


Figure 6.24: Two possible configurations of the FAC and its connection to the electrojet. **Left:** Type 1. **Right:** Type 2. Adapted from Boström (1964), Figs. 7 and 8.

We also showed  $j_{\parallel}$  as constant in Fig. 6.23. This is an immediate consequence of the current continuity Eq. 5.23 and of our assumption that  $\partial J_{\eta}/\partial \eta = \tilde{c}_1$  (Eq. 5.44 with neglect of  $\partial H_{\xi}/\partial \eta$ ), if  $\partial J_{\xi}/\partial \xi$  can be disregarded — which is reasonable close enough to CR, on its northern side, as one can read in Table 6.10. One may consider, as a first approximation, that a constant  $j_{\parallel}$  implies constant conductance. If we keep to the model YPYHXL and require  $E_{\xi}$  to be constant along  $\eta$  then the increase of both the westward and eastward electrojet toward east would require the increase/decrease of  $E_{\eta}$  north/south of the CR, with the result that  $E_{\eta}$  could no longer be constant along  $\xi$  and  $E_{\xi}$  along  $\eta$ . This reasoning illustrates the limitations of our model, which are essentially related to having data just along a 1D cut through the arc. Using these data it is possible to derive the local variation rate of the WEJ (for the EEJ the conductance might be too low for a reliable application of our method), but it is not possible to make a resolute statement about the origin of this variation. It is reasonable to expect that both the change of the conductance and of the two electric field components contribute to the variation of the WEJ, but we cannot estimate their relative importance. More involved models, as those briefly discussed in Section 6.5.4, might lead to improved results without, however, to completely eliminate this problem.

The topology of the current flow in Fig. 6.23 looks quite surprising to the reader familiar with the standard model of the auroral arc. For the first time Boström (1964) analyzed the relationship between the FACs and the auroral electrojets and pointed out the two basic configurations, Type 1 and Type 2, reproduced here in Fig. 6.24. For the Type 1 circuit the electrojet is connected with line FACs at the extremities, while for the Type 2 circuit a downward and an upward FAC sheets are connected through Pedersen current and the electrojet develops as Hall current between the two FAC sheets. Later the Type 2 circuit was associated with auroral arcs (e.g. Sesiano and Cloutier, 1976; Casserly, R.T., Jr., 1977) while the Type 1 circuit with the convection electrojets and the substorm current wedge (e.g. Baumjohann, 1983). For comprehensive reviews on the relationship between the FACs and the auroral electrojets the reader is referred

to Kamide (1982) and to Chapter 2 of Kamide and Baumjohann (1993). Considering the published material, our case is completely atypical. Although the magnetic field signature suggests a standard Type 2, the current configuration appears to consist of two times the Type 1 topology. Examination of more data is required in order to check whether this is indeed a very rare case and, if similar events are found, to determine the conditions under which they develop.

## 6.7 Summary

This Chapter was devoted to a detailed electrodynamic investigation of an arc event for which both optical and satellite data are available. We first explored the interplay between polarization and Hall current, as ionospheric carriers of the FAC supplied from the magnetosphere, within an infinite straight arc model. We found that the model was in reasonable agreement with the data, with the important exception that  $H_\eta - J_\xi = c_0$ , assumed as constant, was actually variable.

A significant improvement was obtained by taking into account the coupling between the FAC and the electrojet. The coupling was modeled as simple as possible, by just setting  $\partial J_\eta / \partial \eta \simeq \partial / \partial \eta (H_\xi + J_\eta) = \tilde{c}_1 = \text{const}$ . Even for a relatively homogeneous and quiet arc, as the one investigated here, a proper modeling is achieved only by taking into account the polarization, the Hall term, and the FAC–electrojet coupling at the same time. The results obtained in these conditions were shown to be reliable and not very sensitive to the possible error sources.

The current configuration associated with the arc, examined in the last Section, proved to be quite peculiar. Although the magnetic field signature suggests a standard current topology, with downward and upward FAC sheets connected through ionospheric Pedersen current, the two FAC regions were found to be electrically separated. North of the CR the westward electrojet feeds the upward FAC while south of the CR the downward FAC feeds the eastward electrojet; a small fraction of the downward FAC crosses the CR as Hall current, to join the westward electrojet. This uncommon behavior has its origin in the close proximity of the CR to the FR.

The consistency of the results hints to the prospect of a continuous monitoring of the high-latitude ionosphere, with medium altitude satellites like FAST, on a spatial scale of  $\sim 1\text{km}$ . By the method introduced here it becomes possible to determine both the N–S and the E–W components of the IEF with good accuracy, even at times when the satellite crosses the AAR and the electric field cannot be mapped to the ionosphere. Once the electric field is found one can also infer the 3D current flow in the vicinity of the satellite ionospheric footprint.

## Chapter 7

# Summary and future work

The central theme of the present study was to provide an accurate electrodynamic characterization of an auroral arc, by using high resolution satellite measurements and ground optical images. The method developed to determine the ionospheric electric field and current in the vicinity of the arc is based on the current continuity equation and incorporates an extended set of satellite data, taken well above the current closure region: particles (both electrons and ions), electric field, and magnetic field. The results are internally consistent and supportive for future investigations of arc electrodynamics. The optical information allows an independent check of the results.

The data examined in this work were obtained by instruments onboard the NASA satellite FAST and by a TV camera of MPE on February 9, 1997, around UT 8:22:00. After a brief presentation of the main types of data used to investigate the aurora we introduced the FAST payload, the data analysis software, and the ground optical equipment. A key point that we emphasized is the high resolution of the FAST measurements, comparable to the width of the discrete arcs.

The geophysical indices and the ground magnetograms show that the arc developed during the growth phase of a small substorm, in the most quiet period of a disturbed interval. At the time of the FAST overpass the visible arc was stable and  $\sim 70\text{km}$  wide, corresponding to the more energetic part ( $\lesssim 5\text{keV}$ ) of a broader inverted-V. A slow southward motion of the arc, equivalent to  $\sim 10\text{mV/m}$  westward IEF, is visible in the optical data. The electric field measurements locate the arc north of the CR. The associated inverted-V encompasses several ion beams, indicating alternate passes of FAST below and above the bottom side of the AAR.

The particle data enabled the calculation of the ionospheric conductance. Although both the proton and electron induced conductances were discussed, only the electrons were shown to make a significant contribution for the examined inverted-V. The solar ionization is not important during the winter time in the polar ionosphere. Special attention was given to the calculation of the

conductance during ion beam events. The errors were also carefully examined: small errors are expected inside the arc, where stationarity is a good assumption and the counting statistics of the plasma instrument is high; outside of the arc the relative errors are presumably large. Nevertheless, the arc parameters were shown to be not very sensitive to these errors.

The highly variable conductance pattern points to the need of taking into account the ionospheric polarization. Representing the auroral oval as a strip of increased, homogeneous conductance, provides a model which is good for large scale M–I coupling studies, but not to investigate small scale structures. In addition, the large scale models often neglect the longitudinal component of the electric field — and the Hall contribution to the meridional closure of the FAC — as well as the coupling between the FAC system and the electrojet. We built an arc model that depends on the following parameters: *i*) the polarization coefficients,  $(a_i)_{1 \leq i \leq n_x}$ ; *ii*) the electric field along the arc,  $b_0$ ; *iii*) the current supply transverse to the arc,  $\alpha_0$ ; *iv*) the coupling between the FAC system and the electrojet,  $\tilde{c}_1$ ; *v*) the flow direction of the electrojet,  $\theta$ . In order to clarify the importance of each parameter we explored several instances of the model, depending on reduced parameter sets.

The polarization coefficients were instrumental in expressing the variation of the IEF:  $E_x = E_{0_x} + \sum_{i=1}^{n_x} a_i G_i$ . The series expansion is based on Legendre polynomials, which satisfy the condition  $\int_{-1}^1 G_i(x) dx = 0$ . Because of this property  $E_{0_x}$  does not depend on  $n_x$  and it is equal to the average electric field, that can be computed from measured data.  $E_{0_x}$  can be found even for time periods that include intervals when the magnetic field lines below the satellite are not equipotentials — and the satellite measurements cannot be directly mapped to the ionosphere. The polarization scale size can be tuned to the data by the appropriate choice of  $n_x$ .

An important ingredient, necessary to obtain a consistent description of the arc electrodynamics, is  $E_\eta$ , the electric field parallel to the arc. Given the relative homogeneity of the arc in longitudinal direction, and the fact that the IEF can be considered, to a good approximation, as electrostatic, we took  $E_\eta = b_0 \equiv \text{const}$ . The results obtained by this choice were in reasonable agreement with the optical data and were found to be consistent with the expected relationship between electric field and current implied by Ohm's law in the anisotropic ionosphere.

A model that takes into account only the polarization and the meridional Hall current to close the FAC is not self-consistent. The parameter  $\alpha_0$  was found to vary across the arc, indicating that the FAC-electrojet coupling cannot be neglected; by taking it into account, through the parameter  $\tilde{c}_1$ , the results were radically improved. The length scale of the electrojet, related to  $\tilde{c}_1$ , was found to be in the range  $\sim 200\text{--}500\text{km}$ , in good agreement with the expectations. *The minimum set of parameters necessary to model the arc includes the polarization, the longitudinal electric field, and the FAC–electrojet coupling, even if the arc is reasonably quiet and homogeneous.*

The flow direction of the electrojet,  $\theta$ , can be either 1) determined by fit, or 2) assumed as parallel to the arc and derived from the magnetic data. Both choices led to electric fields in slight disagreement with the optical data, implying proper motion of the arc; in case 2 the proper motion corroborated better with the growth phase of the substorm. Including  $\theta$  among the fit parameters provides an additional degree of freedom and allows for an electrojet direction which is not parallel to the arc. In this case the parameter set can be found by nonlinear minimization of a  $\chi^2$  expression. When the electrojet is assumed parallel to the arc the model becomes linear and the fit problem can also be solved by regression; the results obtained by the two different methods were shown to be identical, providing a double-check for the numerical technique.

The parameters obtained in case 2 above were used to check the current configuration close to the arc. Although the magnetic field signature suggests a standard Boström Type 2 topology, the inferred configuration appears to be quite uncommon, consisting instead of two times the Boström Type 1 topology. The downward and upward FACs appear to be electrically separated in the ionosphere and the current continuity is achieved on the expense of the electrojets. This peculiar configuration is related to the close proximity of the CR and FR.

It is appropriate to conclude the whole work by pointing out some possible directions of future development. The next task to be addressed is to check whether the uncommon topology of the current flow unraveled by this case-study repeats for other FAST orbits. One could first examine only the relative position of the CR and FR. An automated software procedure could be devised allowing the efficient browsing through an extended set of orbits. Subsequently, a more detailed analysis of some selected orbits could be performed (if it is the case), by using the method introduced in this work. In parallel, the method should also be tested on a few standard cases, for which ground magnetic, radar, and/or optical data are available.

In the present study we were able to derive the parameter set for an inverted-V event, during the winter time, with the conductance induced almost exclusively by electron precipitation. More work is required to extend the method to the downward current region and/or to summer time conditions, by considering in addition the conductance induced by proton precipitation and/or solar radiation. Deriving the parameter set in the downward current region is presumably a more challenging task because of the higher uncertainty in conductance. Although in this region the precipitation is relatively flat and the polarization is expected to be less important, obtaining reliable estimates for  $b_0$  and  $\tilde{c}_1$  not only north but also south of the CR would add quantitative precision to the rather qualitative evaluation of the current flow topology.

The arc investigated in this work — as well as the associated inverted-V — was broad and stationary, features characteristic before break-up. The deviation from the ideal infinite and



straight geometry was small enough, so that a theory developed in cartesian coordinates proved to be satisfactory. Nonetheless, even for this trivial geometry, the fit procedure can still be improved. Although one cannot hope to overcome the limit imposed by the data, that lack 2D coverage, using orthogonal curvilinear coordinates and less restrictive conditions for the longitudinal electric field might lead to a more accurate modeling of the arc and, eventually, of more complicated forms.

The time dependence might also be of concern. We assumed the auroral structure to be stationary, on the  $\sim 1$  min time scale of the satellite overpass. Thus we could equate the high-altitude and the ionospheric potential drops. This procedure can lead to wrong results if the structure under investigation varies faster than the time needed by the satellite to cross it. In such a case another method to estimate the ionospheric potential drop is required.

A topic that was just touched upon refers to the relation between the ion beam energy and the FA potential drop. Once the AAR electric field is measured, and the IEF is determined with good accuracy, the FA potential drop below FAST can be readily computed. By comparing it to the ion beam energy a better characterization of the non-electrostatic interactions of particles, that take place in and below the AAR, could be obtained. The FAST data could be evaluated in conjunction with Cluster-2 measurements at higher altitude and/or low-altitude radar observations.

An important achievement of this work refers to the possibility of performing a systematic surveillance of the ionosphere, with very good spatial resolution. The method developed here is particularly appropriate for time intervals when the satellite crosses the AAR and the measured electric field cannot be simply mapped to the ionosphere. Even when the mapping is possible one could double-check the results (which are affected by measurement errors). In addition, it is possible to obtain the DC E–W electric field, which is not measured on FAST, and to evaluate the coupling between the FAC and the electrojet. The value of the results derived from satellite data would be substantially enhanced, provided that conjugated ground information is available. As a prospect for the more distant future, one could think about using ground optical information to perform systematic studies, for different classes of auroral forms.

The FAST database comprises, at present, more than 25000 orbits, with data collected during all seasons and at all local times. By extending and testing the method developed in this work one could obtain a reliable routine tool for the remote sensing of the high-latitude ionosphere. As the present case-study shows, unexpected features could be disclosed, which might shed new light on aurora and related phenomena.

# Appendix A

## Software tools

We give here a more detailed presentation of the software packages used to process the data. We only describe the end-user tools, starting with data in Level Zero Processing (LZP) files. For a more comprehensive text on the processing performed until this stage, beginning with the telemetry data, see McFadden et al. (2001).

### A.1 Science Data Tool (SDT) and Data Manager (DM)

The first evaluation of the data is done with the SDT program, developed for Sun-Solaris platform. Real Time (RT) and Data Analysis (DA) windows are available, allowing both on- and off-line inspection of the data. The RT feature was necessary in the commissioning phase and was also heavily used during campaigns. The regular processing is, however, done off-line, via menu-driven commands offered by the DA option.

An SDT session of type DA can start from scratch, by choosing the satellite, the desired data, and the time interval. SDT can access various data types from a larger number of missions (most recently electric field and ion data from Cluster were added), through decompilers that know how to read the specific data files, and how to communicate the content to SDT. Once the mission is chosen — FAST in our case — a second window opens, containing the available data types. After choosing the data types, the user has also to fix the time interval. In this way the selection basis is determined and SDT can retrieve the data from files organized according to the orbit number and to the particular data contained. For example, Survey EESA data for orbit 1859 are stored in the file *fast\_p-DSS-29-orbit1859\_r-ap1024*. The orbit is given as *orbit1859* and the data type information is coded in *ap1024*. Each particular data has an APplication IDentifier (*APID*) — for Survey EESA this is 1024. The rest of the file name gives the ground station used

to receive the telemetry flux (*DSS-29*) and some extra information related to processing done on the ground (*p* and *r*).

The management of the data files is done through a client-server system, with a central database at UCB/SSL and a client program, *datamgr* (DM), at the user site. Once the user selects the needed files, DM interrogates the central database and finds out what files are already stored on the local system and what files are missing and have to be transferred from the FAST archive. The decision on the files to be actually transferred can be tailored according to the data volume and to the local network connection. When the transfer is finished the new data is plotted by just returning the control to SDT.

Alternatively to starting from scratch, an SDT session can use an existent configuration file. When working on a certain scientific problem, once the selection of the necessary data and time intervals is done, this information can be stored and then called by just choosing the appropriate configuration file.

## A.2 General IDL routines

Interactive Data Language (IDL) is a higher level programming language, developed by Research Systems, Inc. IDL was designed to assist data processing and interpretation by offering the basic structures of a programming language, as well as a comprehensive library of routines. These routines can be further assembled into self-standing programs, to accomplish specific tasks.

The FAST software package includes a large number of IDL routines, that gives more detailed and flexible access to the data than SDT does. Here we mention some of these routines. The list is not complete and is just meant to hint upon the variety of operations that can be performed.

- Orbit related quantities, like:
  - position, velocity
  - altitude, geographic and magnetic latitude/longitude
  - model magnetic field at FAST altitude and at the ionospheric footprint

are calculated with *get\_fa\_orbit*.

- The ionospheric magnetic footprint of FAST trajectory is displayed with *plot\_fa\_crossing* (e. g. Fig. 3.2)
- The data are loaded from the SDT buffers into IDL by means of *get\_fa \** routines. For some data types there are several routines, accommodating the different time resolutions:

- *get\_fa\_ees/get\_fa\_eeb* for Survey/Burst EESA data.
  - *get\_fa\_ies/get\_fa\_ieb* for Survey/Burst IESA data.
  - *get\_fa\_tso/get\_fa\_tbo* for Survey/Burst TEAMS O+ data; for H+, He+, He++ the 'o' is changed to 'p', 'h', 'a' respectively, in the name of the routine.
  - *get\_fa\_fields* for electric and magnetic field quantities.
- With *ucla\_mag\_despin* one obtains despun components of the magnetic field in one of the following coordinate systems: Spacecraft (SC), Geocentric Equatorial Inertial (GEI), Solar Magnetic (SM), Mean Field Aligned (MFA), Satellite Associated System (SAS). The transformation matrices are also stored. The SC system has its  $x$  and  $y$  axes in the spin plane ( $x$  pointing to the sun) and  $z$  along the satellite spin axis. The GEI, MFA, and SM are well-known coordinate systems. For the definition of the SAS see p. 27. The perturbation magnetic field is obtained by subtracting the model from the measured field.
  - The electric field components  $E_{\perp}$  and  $E_{\parallel}$  (p. 17) are obtained with *ff\_despin\_svy\_long* / *fa\_fields\_despin* and *fa\_fields\_despin\_4k* / *fa\_fields\_despin\_16k*. The first two routines are used for Survey data, frequency range up to 0.25/1 kHz. The other two routines are used for Burst data, frequency range up to 4/16 kHz.
  - To get particle spectrograms one uses:
    - *get\_en\_spec* for energy spectrograms. The pitch-angle range can be chosen at will.
    - *get\_pa\_spec* for pitch-angle spectrograms. The energy range can be chosen at will.
  - Electric and magnetic field spectra are obtained with:
    - *fa\_fields\_spec* for waveform data.
    - *load\_ac\_fields* for DSP and SFA data.
  - There is a full set of routines for computing moments of the particle distributions. The energy and pitch-angle ranges can be set by the user. One can identify two groups:
    1. Routines that compute primary moments, through summation over the data:
      - *n\_2d\_fs* for density,  $n$ .
      - *j\_2d\_fs* for number flux,  $J_N$ .
      - *p\_2d\_fs* for pressure,  $p$ .
      - *je\_2d\_fs* for energy flux,  $J_E$ .

2. Routines that use the primary moments to compute derivative quantities:

- *v\_2d\_fs* for bulk velocity,  $v = J_N / n$ .
- *ec\_2d\_fs* for average energy,  $E_c = J_E / J_N$ .
- *t\_2d\_fs* for kinetic temperature,  $T = p / n$ .
- *vth\_2d\_fs* for thermal velocity,  $v_T = \sqrt{2T/m}$ .

A general frame for computing moment time series is provided through *get\_2dt*. By calling, e. g. *get\_2dt*, '*n\_2d\_fs*', '*fa\_ees*', *t1*= $\tau_1$ , *t2*= $\tau_2$ , one computes the electron density (Survey data) for the time interval  $[\tau_1, \tau_2]$ . Instead of *n\_2d\_fs* one can use any of the moment functions listed above. Other particle data types can be chosen as well, by changing '*fa\_ees*' accordingly.

- Plotting time series is done by means of the *tplot* routine. For (multi)line/spectrogram plots *tplot* calls *mplot/specplot*. A large variety of options can be set by using related routines: *options*, *tplot\_options*, *(xyz)lim*. The *tplot* quantities are stored in the heap memory, via a pointer mechanism, by using *store\_data*. To get access to *tplot* data one uses *get\_data*. The procedure *tplot\_file* enables saving/restoring *tplot* data to/from the computer hard-disk.
- Detailed views of the particle distributions are given by *spec2d/pitch2d* and *contour2d*. With *spec2d/pitch2d* one can plot energy/pitch-angle spectra, having the freedom to choose the pitch-angle/energy range and the unit for the dependent variable: counts, rate, differential flux, differential energy flux, or distribution function. With *contour2d* one can get contour plots of the distribution function, represented in either  $(W, \theta)$ , or  $(W_{\parallel}, W_{\perp})$ , or  $(v_{\parallel}, v_{\perp})$  coordinates ( $W$  is the energy,  $\theta$  the pitch-angle, and  $\parallel, \perp$  refer to the direction with respect to the magnetic field).

### A.3 Specific IDL code

New IDL code was written to accomplish the tasks implied by the present work. Some of it is listed below:

- The procedure *read\_iff* makes the reading of digitized pictures into IDL independent of the digitization software, installed at MPE on a DEC-VMS computer. By means of *read\_iff* it was possible to process the IFF image files on a Sun-Solaris machine.

- Electron and proton induced conductances (Chapter 4) are stored as tplot quantities by *store\_ph* and *store\_ph\_prot*. These routines implement the formulas given by Robinson et al. (1987) / Galand and Richmond (2001) for electron / proton Pedersen and Hall conductances.
- Error calculation sections were added to the functions computing particle moments, enumerated in Section A.2. Part of this code was necessary in the evaluation of the conductance errors (see Appendix C for details on error calculation).
- The routine *fit\_ortho* was used to approximate the conductance and magnetic field with orthogonal polynomials (Section 6.2.2); the variation of  $\chi_r^2$  with the degree of the polynomial was obtained with *rchi\_iter*.
- The IEF and the currents  $J_{par}$ ,  $J_{ion}$ , derived in Sections 6.2 and 6.4, were calculated with *ief\_nl2*. This routine has a flexible design and can easily accommodate new arc models. For each model an IDL function returning the value  $f$  (Eq. 6.2) has to be written. The user can choose which optimization routine *ief\_nl2* should call to find the minimum of  $f$  — there are three possibilities, *amoeba*, *powell*, and *dfpmin*, all of them part of the standard IDL distribution. Details on the minimization algorithms and on the structure of *ief\_nl2* are presented in Appendix F.
- Two other routines, *ief\_lin* and *ief\_iter2*, were used to make some numerical checks: *ief\_lin*, which is based on linear regression instead of non-linear minimization, was used with the linear model in Section 6.4.5; *ief\_iter2* was used to check the dependence of the results obtained by non-linear minimization, on the starting point in the parameter space. See Appendix F for more details.
- The rotation angle of the current sheet,  $\theta_{mag}$ , was found by variance analysis, implemented through the IDL routines *bvar* and *bv\_arr2* (for a short presentation of the variance analysis and of the two routines see Appendix G).

## Appendix B

# Geometric calibration of optical data

The data measured by FAST at 4000km altitude are magnetically conjugated with the light emission, which takes place at  $\sim 110$ km and is recorded on video tape. For a meaningful comparison of the two data sets one has first to find the satellite footprint at ionospheric level, and then to project it into the image plane. The operations necessary to accomplish this task are summarized in the following list (J. Vogt, personal communication):

1. Tracking the satellite position. One can either use the Satellite Situation Center web tool (SSCWeb, <http://sscweb.gsfc.nasa.gov>), or some other software available on the local machine. The general IDL FAST package (Appendix A) provides the routines *get\_fa\_orbit* and *plot\_fa\_crossing* for calculating and displaying the satellite orbit.
2. Mapping the satellite position along the magnetic field line, down to the ionosphere. One has to choose the right magnetic field model, corresponding to the epoch of the observation. Deviations as small as a fraction of a degree ( $\sim 0.1^\circ$ ) in the latitude or longitude of the projection are equivalent to distances of  $\sim 10$ km, comparable to or larger than the arc width.
3. Given the position of the observer and the position of the satellite footprint one can calculate the elevation and the azimuth of the viewing direction. These local coordinates can be further transformed to right ascension (RA) and declination (D). The RA and D are expressed in the Geocentric Equatorial Inertial (GEI) system, which is appropriate for the astronomical input data to be used for the next step.
4. Finding the correspondence between the viewing direction and the pixel position, i. e. between (RA,D) and the coordinates (x,y) in the image plane, makes use of the camera  $z$  axis direction (perpendicular to the image plane), and is based on the assumption that the transformation consists of a rotation and a radial mapping, scaled by a factor that depends on the

focal distance of the optical system. The rotation is characterized by the angle between the image y axis and the celestial North direction while the radial mapping is done with a third degree polynomial that models the distortion function of the optical system. The experimental determination of the transformation coefficients is achieved by using a calibration image, with well-known bright stars. For these stars the pixel coordinates can be read in the image whereas the RA and D can be found in catalogs or star databases. The transformation coefficients are further determined by numerical fit.

5. Using the transformation from step 4 with the (RA, D) coordinates from step 3 yields the pixel coordinates of the satellite footprint. One has to take care to add the necessary correction if the calibration image was taken at a different time as compared to the data. If the orientation of the camera in the local reference system was not changed it is only the RA that needs adjustment. In case the orientation of the camera was changed new transformation coefficients have to be found, either by calculating them from the old ones or by repeating the whole calibration procedure.



## Appendix C

# Errors associated with conductance calculation

The calculation of conductances is based on the assumption of stationarity,  $\partial/\partial t = 0$ . In the first part of the Appendix we expand the discussion on the validity of this assumption, made in Section 4.4.1. The second part details the measurement error calculation, performed in Section 4.4.2.

### C.1 Methodological errors: The assumption of stationarity

The gradients in the electron precipitation are associated with changes in the ionospheric plasma density, implying variations of conductance. As an approximate measure for the conductance variation we shall investigate the variation of the plasma density,  $n$ , at the height  $z^*$  where the ionization production maximizes. In the calculations to follow we shall disregard the variation of  $z^*$  with the energy of the precipitating electrons; nevertheless, for the numerical estimates we shall use parameters corresponding to the actual  $z^*$ . The reader is warned that the results to be obtained are not exact. A rigorous approach implies determination of the plasma density over the full ionospheric altitudinal range important for current conduction.

Considering a drifting stable arc, the spatial variation in the arc system implies a time variation at a fixed point in the ionosphere system. The width of the gradient,  $d_{jk}^{(e)}$ , and the drift velocity of the arc,  $v_a$ , provide the external time scale,  $t_{jk}^{(e)} = d_{jk}^{(e)}/v_a$ . By solving the time dependent equation Eq. 4.6 one can identify an internal time scale,  $t_{jk}^{(i)}$ , that can be associated with the change in plasma density from  $n_j$  to  $n_k$ . The smaller  $t_{jk}^{(i)}/t_{jk}^{(e)}$  is, the better  $\partial n/\partial t = 0$  holds (in the drifting arc system the quantities to be compared are  $d_{jk}^{(i)} = t_{jk}^{(i)} v_a$  and  $d_{jk}^{(e)}$ ). After giving the analytic solution of Eq. 4.6 we shall illustrate the discussion above with numerical values corresponding to our arc.

We assume that at  $t = 0$  the precipitation suddenly changes, such that the ionization production  $q$  is modified from  $q_0$  to  $q_1$ . The ionosphere is considered to be in equilibrium for  $t < 0$  and  $n_0 = \sqrt{q_0/\alpha}$ . With  $n_0$  taken as 'background' and  $q = q_1 - q_0$ , Eq. 4.6 writes:

$$\frac{dn}{dt} = (q_1 - q_0) - \alpha(n^2 - n_0^2) \quad (\text{C.1})$$

This can be easily transformed to:

$$\frac{d\hat{n}}{dt} = \frac{\kappa^2 - \hat{n}^2}{\tau_{rec0}} \quad (\text{C.2})$$

$$\hat{n} = \frac{n}{n_0}, \quad \kappa^2 = 1 + \frac{q_1 - q_0}{\alpha n_0^2} = \frac{q_1}{q_0} = \frac{n_1^2}{n_0^2}, \quad \tau_{rec0} = \frac{1}{\alpha n_0}$$

$\tau_{rec0}$  is the recombination time (Eq. 4.8) corresponding to the initial plasma density  $n_0$ .

Eq. C.2 can be solved by separation of variables:

$$\hat{n} = \hat{n}_\infty \frac{1 - \frac{\hat{n}_\infty - 1}{\hat{n}_\infty + 1} \exp - \frac{t}{\tau_{rec1}/2}}{1 + \frac{\hat{n}_\infty - 1}{\hat{n}_\infty + 1} \exp - \frac{t}{\tau_{rec1}/2}} \quad (\text{C.3})$$

$$\hat{n}_\infty \equiv \kappa = \frac{n_1}{n_0}, \quad \tau_{rec1} = \frac{\tau_{rec0}}{\hat{n}_\infty} = \frac{1}{\alpha n_1}$$

$\hat{n}_\infty$  is the value of  $\hat{n}$  at  $t = \infty$ , when  $n$  has reached the new equilibrium value  $n_1$ ;  $\tau_{rec1}$  is the corresponding recombination time. An immediate check of the solution Eq.C.3 can be done by calculating  $\hat{n}|_{t=0} = 1$  and  $\hat{n}|_{t=\infty} = \hat{n}_\infty$ . The solution is valid for both increase ( $q_1 > q_0$ ) and decrease ( $q_1 < q_0$ ) of the precipitation level. In the first case  $\hat{n}_\infty > 1$ , in the second one  $\hat{n}_\infty < 1$ .

A measure of the time necessary to change the plasma density from  $n_0$  to  $n_1$  is provided by  $\tau_{rec1}/2$ . It is interesting to remark that the increase of the plasma density is faster than the decrease; the transition time scales with the recombination time of the final state. A more accurate time constant is  $t_r$ , defined by  $|n(t_r) - n_1| = |1 - r|n_1$  (the definition holds for both  $r < 1$ , which applies when  $q_1 > q_0$ , and  $r > 1$ , which applies when  $q_1 < q_0$ ). Solving Eq. C.3 with respect to  $t$  yields:

$$t_r = \frac{\tau_{rec1}}{2} \ln \left( \frac{|\hat{n}_\infty - 1|}{\hat{n}_\infty + 1} \cdot \frac{1 + r}{|1 - r|} \right) \quad (\text{C.4})$$

A reasonable choice for the internal time scale is  $t^{(i)} \equiv t_{0.9}$ . This implies an error of  $\sim 10\%$  due to non-stationarity, which is comparable to the measurement error, as long as the precipitation level can sustain a conductance  $\gtrsim 1\text{mho}$  (Section 4.4.2). We have estimated  $t^{(i)}$  for the three intervals of precipitation gradient near to and inside our visible arc,  $I_{12}=8:22:04-8:22:12$ ,  $I_{23}=8:22:12-8:22:19$ , and  $I_{31}=8:22:35-8:22:38$ .

Table C.1: Ionospheric plasma density and recombination time

Id	Time	$\overline{E}$ [keV]	$10^{-9} \times J_N$ [cm <sup>-2</sup> s <sup>-1</sup> ]	$10^5 \times \gamma$ [cm <sup>-1</sup> ]	$z^*$ [km]	$10^{-4} \times q^*$ [cm <sup>-3</sup> s <sup>-1</sup> ]	$10^7 \times \alpha^*$ [cm <sup>3</sup> s <sup>-1</sup> ]	$10^{-5} \times n^*$ [cm <sup>-3</sup> ]	$\tau_{rec}^*$ [s]
1	8:22:00–8:22:04 8:22:38–8:22:41	1	0.5	0.2	150	0.1	1.3	0.9	88
2	8:22:12	5	1.5	5.0	120	7.5	2.8	5.0	7
3	8:22:19–8:22:35	2.5	1.0	1.0	130	1.0	2.1	2.2	22

Table C.2: Time and length scales associated with the transitions between the states listed in Table C.1

Id	Time	$t^{(i)}$ [s]	$d^{(i)}$ [km]	$t^{(e)}$ [s]	$d^{(e)}$ [km]	$t^{(i)}/t^{(e)} = d^{(i)}/d^{(e)}$
12	8:22:04–8:22:12	9	1.8	112	22.4	0.08
13	–	23	4.6	–	–	–
23	–	7	1.4	–	–	–
21	–	118	23.6	–	–	–
31	8:22:35–8:22:38	95	19.0	42	8.4	2.26
23	8:22:12–8:22:19	23	4.6	98	19.6	0.23

- The parameters required by Eq. C.4, together with the quantities necessary for their calculation, are collected in Table C.1. In the columns 3 and 4 are listed  $\overline{E}$  and  $J_N$  corresponding to the times in column 2 (outside of the visible arc, precipitation peak, and northern part of the visible arc, respectively); each of them is associated with a roughly constant precipitation level. The numbers are extracted from the left plot of Fig. 4.2 (compare also with Fig. 3.12). In columns 5 and 6 we give  $\gamma = q(z^*)/J_N$  and  $z^*$ , taken from Fig. 2 of Rees (1963). Although Rees (1963) worked with isotropic and monoenergetic distributions, his results are presumably good enough for our rough evaluation. Column 7,  $q^*$ , is obtained by multiplication of columns 4 and 5. Column 8,  $\alpha^*$ , gives the recombination coefficient (from Evans et al. (1977)), column 9,  $n^*$ , the plasma density (Eq. 4.7), and column 10,  $\tau_{rec}^*$ , the recombination time (Eq. 4.8). There is a factor of 2 variation in  $\alpha^*$  because the values correspond to the actual heights of maximum ionization production. This is not consistent with the assumption that  $\alpha$  is constant, made when solving Eq. C.2. We regard this inconsistency as tolerable for our approximate calculation.
- Table C.2 lists the time and length scales associated with the six possible transitions between the three states of Table C.1. This is meant to emphasize the substantially longer time necessary to reach the equilibrium when the precipitation decreases (the second group of three lines). The length scale  $d^{(i)}$  in column 3 and the time  $t^{(e)}$  in column 4 were calculated for a drift velocity of the arc  $v_a = 200\text{m/s}$ , as yielded by our optical data. In the columns 2, 5, 6, 7 were added entries only for the precipitation gradients actually measured.

## C.2 Measurement errors

First, the analytical formulas are processed, in order to express the number and energy fluxes,  $J_N$  and  $J_E$ , as function of the experimental quantities. Then we proceed to the calculation of the errors in  $J_N$  and  $J_E$ , that are further used to obtain the error in the average energy,  $\overline{E}$ . Finally, the relative errors in the Pedersen and Hall conductances are computed.

### C.2.1 Computation of $J_N$ and $J_E$ from the experimental data

The  $n$ -th order moment of the particle distribution is a  $n$ -rank tensor:

$$\underline{\underline{M}} = \int \mathbf{v}^n f(\mathbf{v}) d\mathbf{v}, \quad M_{i_1 \dots i_n} = \int v_{i_1} \dots v_{i_n} f(\mathbf{v}) d\mathbf{v} \quad (\text{C.5})$$

where  $f(\mathbf{v})$  is the particle distribution function and  $i_1, \dots, i_n$  are one of  $x, y$ , or  $z$ . The number and energy fluxes used in this work write as:

$$J_N = \int v_z f(\mathbf{v}) d\mathbf{v} \quad (\text{C.6})$$

$$J_E = \int \frac{m}{2} v^2 v_z f(\mathbf{v}) d\mathbf{v} \quad (\text{C.7})$$

The number flux is the first order moment (a vector) while the energy flux is the trace of the third order moment (also a vector) multiplied by  $m/2$ . We are interested only in the  $z$  components because only the fluxes along the magnetic field line reach the ionosphere and do matter for the conductance evaluation.

We shall further detail the computation of the energy flux. By expressing the integral in spherical coordinates and assuming isotropy around the field line one obtains:

$$J_E = m\pi \int_0^\infty \int_0^\pi v^5 f \sin \theta \cos \theta d\theta dv \quad (\text{C.8})$$

The upper angle integration limit,  $\pi$  instead of  $2\pi$ , takes into account the 360° FoV of the plasma instrument on FAST, in a plane that contains the magnetic field line.

Equation C.8 can be further processed by considering the relation between the distribution function and the differential number flux (e. g. Baumjohann and Treumann, 1996, p. 121):

$$f = \frac{m}{v^2} \phi_N \quad (\text{C.9})$$

By expressing  $\phi_N$  in terms of the differential energy flux,  $\phi_N = \phi_E/E$ , and by changing the integration variable from  $v$  to  $E$ , one obtains:

$$J_E = \pi \int_0^\infty \int_0^\pi \phi_E(E, \theta) \sin \theta \cos \theta d\theta dE \quad (\text{C.10})$$

If the plasma detector has I energy and K angular channels, and if the energy-angle range of the instrument fully covers the investigated distribution (which is most of the time the case for FAST, in particular for our test orbit 1859), the energy flux can be written as:

$$J_E = \pi \sum_{i,k} \int_{E_i - \frac{\Delta E_i}{2}}^{E_i + \frac{\Delta E_i}{2}} \int_{\theta_k - \frac{\Delta \theta_k}{2}}^{\theta_k + \frac{\Delta \theta_k}{2}} \phi_E(E, \theta) \sin \theta \cos \theta d\theta dE = \pi \sum_{i,k} T_{ik} \quad (\text{C.11})$$

Each of the terms  $T_{ik}$  can be calculated by using the average property of the integral:

$$T_{ik} = \phi_E(E_i^*, \theta_k^*) \int_{E_i - \frac{\Delta E_i}{2}}^{E_i + \frac{\Delta E_i}{2}} dE \int_{\theta_k - \frac{\Delta \theta_k}{2}}^{\theta_k + \frac{\Delta \theta_k}{2}} \sin \theta \cos \theta d\theta \quad (\text{C.12})$$

$$= \frac{1}{2} \phi_E(E_i^*, \theta_k^*) \Delta E_i \sin(2\theta_k) \sin \Delta \theta_k \quad (\text{C.13})$$

By dropping the index  $k$  of the angular windows (which are all equal on FAST) we get:

$$J_E = \frac{\pi}{2} \sum_{i,k} \phi_E(E_i^*, \theta_k^*) \Delta E_i \sin(2\theta_k) \sin \Delta\theta \quad (\text{C.14})$$

Equation C.14 is rigorous; no approximation has been made, except for the assumption that the energy–angle range of the detector covers the full distribution.

The terms  $\Delta E_i$ ,  $\theta_k$ , and  $\Delta\theta$  in Eq. C.14 are all known. The angular window,  $\Delta\theta$ , only depends on the geometry of the detector; the angles  $\theta_k$  are determined by the sampling rate and by the spacecraft spin phase; for a top-hat electrostatic analyzer the energy windows,  $\Delta E_i$ , are proportional to the respective middle energies,  $\Delta E_i = \kappa E_i$  (the middle energies are in turn fixed by the potential difference applied to the analyzer). See Table 2.1 for the values of  $\Delta\theta$  and  $\kappa$ .

The only unknown terms in Eq. C.14 are the differential energy fluxes,  $\phi_E(E_i^*, \theta_k^*)$ . If no assumption is made about the particle distribution over the  $(i, k)$  energy–angle bin, neither can one precisely determine  $E_i^*$  and  $\theta_k^*$ , nor can one rigorously relate  $\phi_E(E_i^*, \theta_k^*)$  to the measured counts of the detector,  $n_{ij}$ . Usually the energy–angle bin is considered to be narrow enough, so that the particle distribution can be approximated as uniform. For the calculations to come we imply this assumption is true.

If the distribution over bin  $(i, k)$  is uniform than  $E_i^* = E_i$ ,  $\theta_k^* = \theta_k$ , and the differential energy flux can be calculated from  $n_{ik}$ :

$$\phi_{E_{ik}} = \frac{n_{ik} E_i}{\Delta S_k \Delta \Omega_k \Delta E_i \Delta t} = \frac{n_{ik}}{\Delta S_k \Delta \Omega_k \kappa \Delta t} = \frac{n_{ik}}{G_{ik} \Delta t} \quad (\text{C.15})$$

with  $G_{ik}$  the geometric factor of bin  $(i, k)$  and  $\Delta t$  the sampling time (the total geometric factors for the FAST particle detectors, i. e. integrated over all angular bins, are given in Table 2.1). By using the notation  $h_{ik} = 1/(G_{ik} \Delta t)$ , the 1-count differential energy flux, we obtain the following expression for  $J_E$ :

$$J_E = \frac{\pi}{2} \sum_{i,k} n_{ik} h_{ik} \Delta E_i \sin(2\theta_k) \sin \Delta\theta = \frac{\pi}{2} \sum_{i,k} n_{ik} h_{ik} \kappa E_i \sin(2\theta_k) \sin \Delta\theta = \sum_{i,k} c_{ik}^{J_E} n_{ik} \quad (\text{C.16})$$

The  $c_{ik}^{J_E}$  coefficients are fully determined constants.

The derivation of the number flux,  $J_N$ , in terms of experimental data, is analogue to the derivation of  $J_E$ . One starts from Eq. C.6, which can be transformed to (compare with Eq. C.10):

$$J_N = \pi \int_0^\infty \int_0^\pi \frac{\phi_E(E, \theta)}{E} \sin \theta \cos \theta d\theta dE \quad (\text{C.17})$$

By assuming the distribution function is uniform over each energy–angle bin one obtains:

$$J_N = \frac{\pi}{2} \sum_{i,k} n_{ik} h_{ik} \kappa \sin(2\theta_k) \sin \Delta\theta = \sum_{i,k} c_{ik}^{J_N} n_{ik} \quad (\text{C.18})$$

with  $c_{ik}^{J_N}$  constants coefficients.

### C.2.2 Calculation of the errors in $J_E$ , $J_N$ , and $\bar{E}$

Getting the errors in  $J_E$  and  $J_N$ ,  $\sigma_{J_E}$  and  $\sigma_{J_N}$ , is a straight process. By applying the error propagation formula to Eq. C.16 one obtains:

$$\sigma_{J_E}^2 = \sum_{i,k} (c_{ik}^{J_E})^2 \sigma_{n_{ik}}^2 = \sum_{i,k} (c_{ik}^{J_E})^2 n_{ik} \quad (\text{C.19})$$

where we used the fact that  $n_{ik}$  is Poisson distributed and  $\sigma_{n_{ik}}^2 = n_{ik}$ . The error in  $J_N$  is obtained by the same equation, except for using  $c_{ik}^{J_N}$  instead of  $c_{ik}^{J_E}$ .

When calculating the error in  $\bar{E}$  one has to take into account that  $J_E$  and  $J_N$  are correlated. Intuitively, once the number flux increases, one expects that the energy flux increases as well. Consequently, one has to use the full form of the error propagation formula, which includes the correlation term,

$$\frac{\sigma_{\bar{E}}^2}{\bar{E}^2} = \frac{\sigma_{J_E}^2}{J_E^2} + \frac{\sigma_{J_N}^2}{J_N^2} - 2 \frac{\sigma_{J_E J_N}^2}{J_E J_N} \quad (\text{C.20})$$

instead of the reduced form,

$$\frac{\sigma_{\bar{E}}^2}{\bar{E}^2} = \frac{\sigma_{J_E}^2}{J_E^2} + \frac{\sigma_{J_N}^2}{J_N^2} \quad (\text{C.21})$$

which is based on the assumption that  $J_E$  and  $J_N$  are not correlated. Because of the positive correlation between  $J_E$  and  $J_N$  the error calculated correctly, with Eq. C.20, is lower than the result obtained with Eq. C.21 (one can see this in the bottom panel of Fig. 4.9).

To find the correction added by correlation, in terms of the experimental data, one has to consider the explicit dependence of  $\bar{E}$  on the counted particles,  $n_{ik}$ :

$$\begin{aligned} \bar{E} &= \frac{J_E}{J_N} = \frac{\sum_{i,k} c_{ik}^{J_E} n_{ik}}{\sum_{i,k} c_{ik}^{J_N} n_{ik}} \Rightarrow \\ \frac{\sigma_{\bar{E}}^2}{\bar{E}^2} &= \frac{J_N^2}{J_E^2} \sum_{i,k} \left( \frac{\frac{\partial J_E}{\partial n_{ik}} J_N - \frac{\partial J_N}{\partial n_{ik}} J_E}{J_N^2} \right)^2 \sigma_{n_{ik}}^2 \\ &= \frac{\sum_{i,k} \left( \frac{\partial J_E}{\partial n_{ik}} \right)^2 \sigma_{n_{ik}}^2}{J_E^2} + \frac{\sum_{i,k} \left( \frac{\partial J_N}{\partial n_{ik}} \right)^2 \sigma_{n_{ik}}^2}{J_N^2} - 2 \frac{\sum_{i,k} \frac{\partial J_E}{\partial n_{ik}} \frac{\partial J_N}{\partial n_{ik}} \sigma_{n_{ik}}^2}{J_E J_N} \\ &= \frac{\sigma_{J_E}^2}{J_E^2} + \frac{\sigma_{J_N}^2}{J_N^2} - 2 \frac{\sum_{i,k} c_{ik}^{J_E} c_{ik}^{J_N} n_{ik}}{J_E J_N} \end{aligned} \quad (\text{C.22})$$

The correlation error,  $\sigma_{J_E J_N}^2$ , is:

$$\sigma_{J_E J_N}^2 = \sum_{i,k} c_{ik}^{J_E} c_{ik}^{J_N} n_{ik} \quad (\text{C.23})$$

As the IDL routines calculating  $J_E$ ,  $J_N$ , and  $\bar{E}$ , explicitly compute the coefficients  $c_{ik}^{J_E}$  and  $c_{ik}^{J_N}$ , Eqs. C.19 and C.22 are easy to implement as add-ons to the existing code.

### C.2.3 Calculation of the errors in $\Sigma_P$ and $\Sigma_H$

As already mentioned in Section 4.4.2, we neglect the proton induced conductances. To keep this Section self-consistent, we write again the formulas for electron induced conductances (Eqs.4.9):

$$\Sigma_P = \frac{40\overline{E}}{16 + \overline{E}^2} J_E^{1/2} \quad (\text{C.24})$$

$$\frac{\Sigma_H}{\Sigma_P} = 0.45\overline{E}^{0.85} \quad (\text{C.25})$$

and for calculating  $J_E$  and  $\overline{E}$  from satellite data (Eqs. 4.15, with slightly changed notations):

$$J_E = r_B(J_E^e + J_N^e \overline{E}^i) \quad (\text{C.26})$$

$$\overline{E} = \overline{E}^e + \overline{E}^i \quad (\text{C.27})$$

The quantities on the r.h.s. of Eqs C.26 and C.27 are derived from measured satellite data;  $e$  and  $i$  identify electrons and ions respectively, while  $r_B$  is the magnetic field ratio,  $r_B = B^{ionos}/B^{sat}$ .

To calculate the errors one has to apply the error propagation formula:

- First, to Eqs. C.24 and C.25, and express  $\sigma_{\Sigma_P}$  and  $\sigma_{\Sigma_H/\Sigma_P}$  in terms of  $\sigma_{J_E}$  and  $\sigma_{\overline{E}}$ .
- Second, to Eqs. C.26 and C.27, and express  $\sigma_{J_E}$  and  $\sigma_{\overline{E}}$  in terms of the measured quantities  $J_E^e$ ,  $J_N^e$ ,  $\overline{E}^e$ , and  $\overline{E}^i$ .

A rigorous calculation should also take into account the correlation between  $J_E^e$  and  $\overline{E}^e$  in Eq. C.24, as well as the correlation between  $J_E^e$  and  $J_N^e$  in Eq. C.26. Practically, this comes to expressing the quantities entering Eqs. C.24–C.27 in terms of the primary variables,  $n_{ik}^e$  and  $n_{ik}^i$ , and then calculating the errors analogue to the procedure used for  $\sigma_{\overline{E}}$  in Section C.2.2. This task, however, is significantly more difficult and, as pointed out in Section 4.4.2, it appears that the effort is not necessary. Instead, we calculate the errors as if the implied quantities were not correlated. The resulting formulas are easy to transpose into computer code:

$$\frac{\sigma_{\Sigma_P}}{\Sigma_P} = \left( \frac{16 - \overline{E}^2}{16 + \overline{E}^2} \frac{\sigma_{\overline{E}}^2}{\overline{E}^2} + \frac{1}{4} \frac{\sigma_{J_E}^2}{J_E^2} \right)^{1/2} \quad (\text{C.28})$$

$$\frac{\sigma_{\Sigma_H/\Sigma_P}}{\Sigma_H/\Sigma_P} = 0.85 \frac{\sigma_{\overline{E}}}{\overline{E}} \quad (\text{C.29})$$

$$\sigma_{J_E} = r_B \left( \sigma_{J_E^e}^2 + J_N^{e2} \sigma_{\overline{E}^i}^2 + \sigma_{J_N^e}^2 \overline{E}^{i2} \right)^{1/2} \quad (\text{C.30})$$

$$\sigma_{\overline{E}} = \left( \sigma_{\overline{E}^e}^2 + \sigma_{\overline{E}^i}^2 \right)^{1/2} \quad (\text{C.31})$$

The error in the Hall conductance can be obtained immediately by:

$$\Sigma_H = \frac{\Sigma_H}{\Sigma_P} \Sigma_P \Rightarrow \frac{\sigma_{\Sigma_H}^2}{\Sigma_H^2} = \frac{\sigma_{\Sigma_H/\Sigma_P}^2}{\Sigma_H/\Sigma_P^2} + \frac{\sigma_{\Sigma_P}^2}{\Sigma_P^2} \quad (\text{C.32})$$



## Appendix D

# Current closure in orthogonal curvilinear coordinates

For a real arc, which is neither infinite nor straight, Eq. 5.26 can no longer be simplified to the form 5.27. Still, the ideal case of the infinite straight arc suggests a possible approach: if an orthogonal curvilinear coordinate system,  $(\xi, \eta)$ , can be found, such that the arc electrodynamics only depends on  $\xi$ , then the formalism developed in Sections 5.4.2 and 5.4.3 could be generalized.

In the following we derive a general form of the current closure equation, valid in arbitrary orthogonal curvilinear coordinates. We start from Eq. 5.19, by writing  $\nabla \cdot \mathbf{j}$  in the system  $(\xi, \eta, \zeta)$  (e. g. Morse and Feshbach, 1953):

$$\nabla \cdot \mathbf{j} \equiv \frac{1}{h_\xi h_\eta h_\zeta} \left( \frac{\partial}{\partial \xi} (h_\eta h_\zeta j_\xi) + \frac{\partial}{\partial \eta} (h_\xi h_\zeta j_\eta) + \frac{\partial}{\partial \zeta} (h_\xi h_\eta j_\zeta) \right) \quad (\text{D.1})$$

where  $h_\xi, h_\eta, h_\zeta$  are the Lamé parameters:

$$h_\xi = \left| \frac{\partial \mathbf{r}}{\partial \xi} \right|, \quad h_\eta = \left| \frac{\partial \mathbf{r}}{\partial \eta} \right|, \quad h_\zeta = \left| \frac{\partial \mathbf{r}}{\partial \zeta} \right|$$

By choosing a coordinate system with

$$x \equiv x(\xi, \eta), \quad y \equiv y(\xi, \eta), \quad z \equiv \zeta$$

the Lamé parameters become

$$h_\xi \equiv h_\xi(\xi, \eta) = \left[ \left( \frac{\partial x}{\partial \xi} \right)^2 + \left( \frac{\partial y}{\partial \xi} \right)^2 \right]^{1/2}, \quad h_\eta \equiv h_\eta(\xi, \eta) = \left[ \left( \frac{\partial x}{\partial \eta} \right)^2 + \left( \frac{\partial y}{\partial \eta} \right)^2 \right]^{1/2}, \quad h_\zeta = 1$$

and the current continuity takes the form

$$\frac{\partial j_z}{\partial z} = -\frac{1}{h_\xi h_\eta} \left[ \frac{\partial}{\partial \xi} (h_\eta j_\xi) + \frac{\partial}{\partial \eta} (h_\xi j_\eta) \right] \quad (\text{D.2})$$

Equation D.2 can be further processed to:

$$\frac{\partial j_z}{\partial z} = - \left[ \frac{1}{h_\xi} \frac{\partial j_\xi}{\partial \xi} + \frac{1}{h_\eta} \frac{\partial j_\eta}{\partial \eta} \right] - \frac{1}{h_\xi h_\eta} \left[ j_\xi \frac{\partial h_\eta}{\partial \xi} + j_\eta \frac{\partial h_\xi}{\partial \eta} \right] \quad (\text{D.3})$$

By integrating Eq. D.3 with respect to altitude (similar to the procedure used to get Eq. 5.23) one obtains:

$$j_{\parallel}^{top} = \left[ \frac{1}{h_\xi} \frac{\partial J_\xi}{\partial \xi} + \frac{1}{h_\eta} \frac{\partial J_\eta}{\partial \eta} \right] + \frac{1}{h_\xi h_\eta} \left[ J_\xi \frac{\partial h_\eta}{\partial \xi} + J_\eta \frac{\partial h_\xi}{\partial \eta} \right] \quad (\text{D.4})$$

where

$$J_\xi = \Sigma_P E_\xi - \Sigma_H E_\eta, \quad J_\eta = \Sigma_H E_\xi + \Sigma_P E_\eta$$

The first term on the r.h.s. of Eq. D.4 is the analogue of the term on the r.h.s. of Eq. 5.23, whereas the second term results because the coordinate lines are no longer straight.

An immediate check of the relation D.4 can be done by performing a particular coordinate transformation, a rotation of angle  $\theta$ :

$$\xi = \cos \theta x + \sin \theta y, \quad \eta = -\sin \theta x + \cos \theta y, \quad h_\xi = h_\eta = (\cos^2 \theta + \sin^2 \theta)^{(1/2)} = 1$$

Consequently, Eq. D.4 writes:

$$j_{\parallel}^{top} = \frac{\partial J_\xi}{\partial \xi} + \frac{\partial J_\eta}{\partial \eta} \quad (\text{D.5})$$

identical to the cartesian form Eq. 5.23

To obtain the desired generalization of Eq. 5.26, we have to express  $j_{\parallel}^{top} \equiv j_z = (\nabla \times \mathbf{H})_z$  in curvilinear coordinates as well:

$$\begin{aligned} j_{\parallel}^{top} &= \frac{1}{h_\xi h_\eta} \left[ \frac{\partial(h_\eta H_\eta)}{\partial \xi} - \frac{\partial(h_\xi H_\xi)}{\partial \eta} \right] \\ &= \frac{1}{h_\xi} \frac{\partial H_\eta}{\partial \xi} - \frac{1}{h_\eta} \frac{\partial H_\xi}{\partial \eta} + \frac{1}{h_\xi h_\eta} \left( H_\eta \frac{\partial h_\eta}{\partial \xi} - H_\xi \frac{\partial h_\xi}{\partial \eta} \right) \end{aligned} \quad (\text{D.6})$$

From Eqs. D.4 and D.6 it results:

$$\frac{1}{h_\xi} \left[ \frac{\partial}{\partial \xi} (H_\eta - J_\xi) + \frac{1}{h_\eta} \frac{\partial h_\eta}{\partial \xi} (H_\eta - J_\xi) \right] = \frac{1}{h_\eta} \left[ \frac{\partial}{\partial \eta} (H_\xi + J_\eta) + \frac{1}{h_\xi} \frac{\partial h_\xi}{\partial \eta} (H_\xi + J_\eta) \right] \quad (\text{D.7})$$

Equation D.7 takes a simpler form if one expresses the derivatives of  $h_\xi, h_\eta$  with respect to  $\xi, \eta$  through the curvature radii of the coordinate lines. In order to do this we compare the derivatives of the local unit vectors,  $\mathbf{a}_\xi$  and  $\mathbf{a}_\eta$  (Morse and Feshbach, 1953, p. 26)

$$\frac{\partial \mathbf{a}_\xi}{\partial \xi} = -\frac{1}{h_\eta} \frac{\partial h_\xi}{\partial \eta} \mathbf{a}_\eta, \quad \frac{\partial \mathbf{a}_\eta}{\partial \eta} = -\frac{1}{h_\xi} \frac{\partial h_\eta}{\partial \xi} \mathbf{a}_\xi \quad (\text{D.8})$$

with the Frenet relations

$$\frac{1}{h_\xi} \frac{\partial \mathbf{a}_\xi}{\partial \xi} = -\frac{1}{R_\eta} \mathbf{a}_\eta, \quad \frac{1}{h_\eta} \frac{\partial \mathbf{a}_\eta}{\partial \eta} = \frac{1}{R_\xi} \mathbf{a}_\xi \quad (\text{D.9})$$

where  $R_\xi, R_\eta$  are the local curvature radii of the coordinate lines. The signs are chosen such that  $R_\xi > 0$  if the arc is seen as convex when crossed in  $\xi$  direction. One obtains:

$$\frac{1}{h_\eta} \frac{\partial h_\xi}{\partial \eta} = \frac{h_\xi}{R_\eta} \quad (\text{D.10})$$

$$-\frac{1}{h_\xi} \frac{\partial h_\eta}{\partial \xi} = \frac{h_\eta}{R_\xi} \quad (\text{D.11})$$

Finally, Eq. D.7 writes:

$$\frac{1}{h_\xi} \frac{\partial}{\partial \xi} (H_\eta - J_\xi) - \frac{1}{R_\xi} (H_\eta - J_\xi) = \frac{1}{h_\eta} \frac{\partial}{\partial \eta} (H_\xi + J_\eta) + \frac{1}{R_\eta} (H_\xi + J_\eta) \quad (\text{D.12})$$

or:

$$\frac{\partial}{\partial s_\xi} (H_\eta - J_\xi) - \frac{1}{R_\xi} (H_\eta - J_\xi) = \frac{\partial}{\partial s_\eta} (H_\xi + J_\eta) + \frac{1}{R_\eta} (H_\xi + J_\eta) \quad (\text{D.13})$$

where the second form explicitly indicates that the derivatives are taken with respect to the arc elements along the coordinate lines.

## Appendix E

# Orthogonal polynomials

The concepts related to orthogonal polynomials are covered under the wider theme of series expansions of arbitrary functions. A detailed account on this topic can be found in Courant and Hilbert (1953), Chapter 2. In the first Section here we enumerate some important systems of orthogonal polynomials, explain the choice that we made for Legendre/Jacobi polynomials, and summarize some important relations. In the second Section we compare numerical results obtained by using Jacobi and Legendre polynomials.

### E.1 Brief review

Given an arbitrary interval,  $a \leq x \leq b$ , and two arbitrary piecewise continuous functions,  $f(x)$  and  $g(x)$ , the integral

$$(f, g) \equiv \int_a^b f(x)g(x) dx \quad (\text{E.1})$$

is called the *inner product* of the functions  $f$  and  $g$ . The number  $\sqrt{(f, f)}$  is called the *norm* of the function  $f$ . A system of functions  $(\phi_i)$  is called *orthogonal* if  $(\phi_j, \phi_k) = 0$ ,  $\forall j \neq k$ . If the norm  $(\phi_i, \phi_i) = 1$ ,  $\forall i$ , the system is called *orthonormal*. An example of orthonormal system over the interval  $[0, 2\pi]$  is given by the trigonometric functions:

$$\frac{1}{\sqrt{2\pi}}, \frac{\cos x}{\sqrt{\pi}}, \frac{\sin x}{\sqrt{\pi}}, \frac{\cos 2x}{\sqrt{\pi}}, \frac{\sin 2x}{\sqrt{\pi}}, \dots$$

The numbers  $c_i = (f, \phi_i)$  are called the *Fourier coefficients* of the function  $f$  with respect to the orthonormal system  $(\phi_i)$ . It can be shown that the *mean square error*,  $M$

$$M = \int_a^b \left( f - \sum_{k=1}^n \gamma_k \phi_k \right)^2 dx \quad (\text{E.2})$$

takes its minimum value for  $\gamma_k = c_k$ . If  $M$  can be made arbitrary small by increasing  $n$ , in other words if

$$\lim_{n \rightarrow \infty} \int \left( f - \sum_{k=1}^n c_k \phi_k \right)^2 dx = 0 \quad (\text{E.3})$$

the system  $(\phi_i)$  is said to be *complete*. The functions  $(\sum_{k=1}^n c_k \phi_k)_n$  are said to converge to the function  $f$  *in the mean*.

It can be shown (see Courant and Hilbert (1953) for details) that for any interval,  $a \leq x \leq b$ , and for any non-negative *weight function*,  $p(x)$ , defined over this interval, one can build a complete system of orthogonal functions,  $(\sqrt{p(x)}Q_i(x))_i$ .  $Q_i(x)$  are polynomials of degree  $i$ , termed *orthogonal polynomials belonging to the weight function  $p(x)$* , that can be determined uniquely by normalizing conditions. Some frequently used systems of orthogonal polynomials are listed below:

- Legendre polynomials,  $(P_n)$ :  $a = -1, b = 1, p(x) = 1, (P_n, P_n) = \frac{2}{2n+1}$ .
- Tchebycheff polynomials,  $(T_n)$ :  $a = -1, b = 1, p(x) = \frac{1}{\sqrt{1-x^2}}, (\sqrt{p}T_n, \sqrt{p}T_n) = \frac{\pi}{2^{2n-1}}$ .
- Jacobi (or hypergeometric) polynomials,  $(J_n)$ :  $a = 0, b = 1, p(x) = x^{q-1}(1-x)^{r-q}$  ( $q > 0, r-q > -1$ ). We are only interested in the case  $q = r = 1$ , which provides  $p(x) = 1$ . For this case  $(J_n, J_n) = \frac{1}{2n+1}$ . For the rest of this Appendix by Jacobi polynomials we understand this particular choice.
- Hermite polynomials,  $(H_n)$ :  $a = -\infty, b = \infty, p(x) = e^{-x^2}, (\sqrt{p}H_n, \sqrt{p}H_n) = 2^n n! \sqrt{\pi}$ .
- Laguerre polynomials,  $(L_n)$ :  $a = 0, b = \infty, p(x) = e^{-x}, (\sqrt{p}L_n, \sqrt{p}L_n) = (n!)^2$ .

Any finite interval,  $[s_1, s_2]$ , can be mapped to  $[0, 1]$  by  $x = \frac{s-s_1}{s_2-s_1}$ , or to  $[-1, 1]$  by  $x = 2\frac{s-s_m}{s_2-s_1}$ , with  $s_m = \frac{s_1+s_2}{2}$ .

We need orthogonal polynomials appropriate for the expansion Eq.5.38 — which implies a finite interval — constrained by the condition Eq.5.37. The finite interval rules out the Hermite and Laguerre polynomials. The condition Eq.5.37 rules out the Tchebycheff polynomials, or any other polynomials system with  $p(x) \neq 1$ . If  $p(x) \neq 1$  then

$$\int \delta E_x dx \equiv \sum_{i=1}^{n_x} a_i \int G_i dx \quad (\text{E.4})$$

is not necessarily 0 ( $(G_n)$  is a generic system) and  $E_{0_x}$  loses its meaning of average electric field, that can be calculated by  $E_{0_x} = -\Delta\Phi/L$  (Eq. 5.32). On the contrary, with  $(P_n)$  and  $(J_n)$  each term of the sum Eq. E.4 is 0. This results by just writing the definition of orthogonal polynomials

$$\int p(x)G_i(x)G_k(x) = 0, \quad \forall i \neq k \quad (\text{E.5})$$

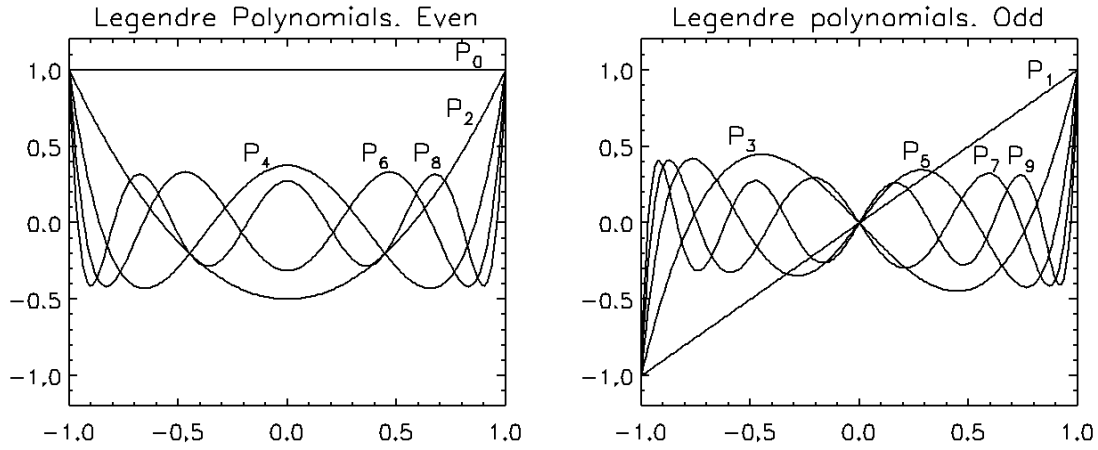


Figure E.1: Legendre polynomials,  $P_0 \dots P_9$ . **Left:** Even order. **Right:** Odd order.

for  $p(x) = 1$  and  $k = 0$ , by taking into account that  $G_0(x) = \text{const}$ . The Jacobi polynomials can be obtained from Legendre polynomials by a simple transformation:

$$J_n(x) = P_n(1 - 2x), \quad 0 \leq x \leq 1 \quad (\text{E.6})$$

One can immediately check that  $(J_n)$  defined by Eq. E.6 verifies the orthogonality relation with  $p(x) = 1$ . It may be shown further that the norm of the so defined  $(J_n)$  agrees with the general norm of Jacobi polynomials (not written in this Appendix). It results that Eq. E.6 defines indeed the Jacobi polynomials belonging to the weight function  $p(x) = 1$ , as the weight function and the norm uniquely determine the polynomial system.

The first six Legendre polynomials are listed below:

$$\begin{aligned} P_0(x) &= 1 & P_3(x) &= \frac{1}{2}(5x^3 - 3x) \\ P_1(x) &= x & P_4(x) &= \frac{1}{8}(35x^4 - 30x^2 + 3) \\ P_2(x) &= \frac{1}{2}(3x^2 - 1) & P_5(x) &= \frac{1}{8}(63x^5 - 70x^3 + 15x) \end{aligned}$$

The graphs of  $P_0 \dots P_9$  are given in Fig. E.1.

The orthogonal polynomials can be easily handled in computer codes by means of recursion formulas. For Legendre polynomials a general expression of the recursion formula is (Bundke, 1967):

$$P_{n+1}^{(m)}(x) = (1 + M_n^{(m)})xP_n^{(m)}(x) - M_n^{(m)}P_{n-1}^{(m)}(x) \text{ with } M_n^{(m)} = \frac{n+m}{n-m+1} \quad (\text{E.7})$$

where  $m = 0, 1, 2, \dots$  gives the order of the derivative and  $n = 1, 2, 3, \dots$  gives the order of the polynomial. For  $m = 0$  and  $m = 1$  Eq. E.7 reduces to, respectively:

$$(n+1)P_{n+1}(x) = (2n+1)xP_n(x) - nP_{n-1}(x) \quad (\text{E.8})$$

$$P_{n+1}' = xP_n' + (n+1)P_n \quad (\text{E.9})$$

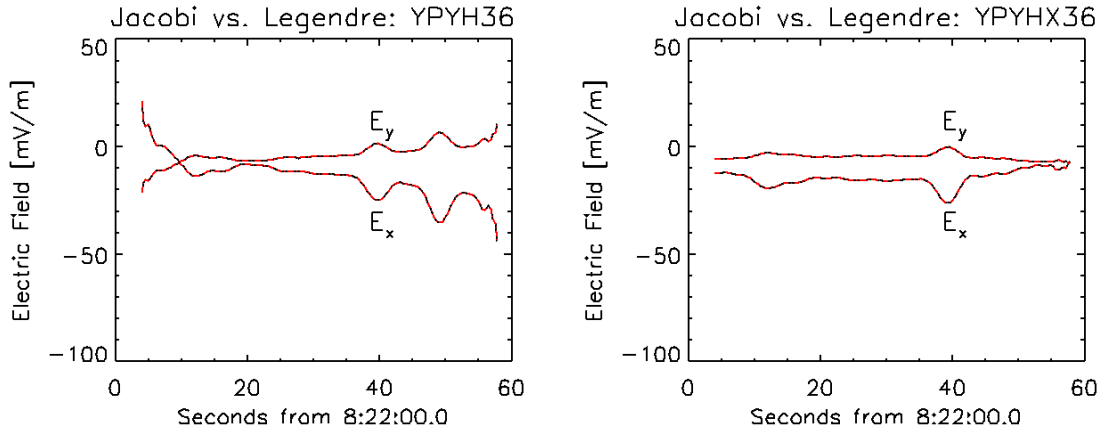


Figure E.2: The IEF obtained with Jacobi polynomials (black solid line) and with Legendre polynomials (red dash-dotted line). As the two curves are identical the result is a dashed black-red line. **Left:** Model YPYH36. **Right:** Model YPYHX36.

## E.2 Numerical results: Jacobi vs. Legendre polynomials

We consider an arbitrary point,  $P(s)$ , between the ends of the investigated interval,  $P_1(s_1)$  and  $P_2(s_2)$ . As already mentioned, the interval  $P_1P_2$  can be mapped to  $[0, 1]$  by means of:

$$x = \frac{s - s_1}{s_2 - s_1} \quad (\text{E.10})$$

and to  $[-1, 1]$  by means of:

$$\xi = 2 \frac{s - s_m}{s_2 - s_1}, \quad \text{with} \quad s_m = \frac{s_1 + s_2}{2} \quad (\text{E.11})$$

The first mapping is appropriate for using Jacobi polynomials in Eq. 5.38 and further in Eq. 5.39, the second one for using Legendre polynomials. As the two polynomial systems are related one to each other by Eq. E.6, one would expect to get identical results, irrespective of the choice made. One and the same point is mapped to either  $x$  or  $\xi$ . The quantities that depend on the point  $P$  in Eq. 5.39 are the same, either if expressed with respect to  $x$  or to  $\xi$ , and the minimization of  $f$  (Eq. 6.2) should lead to the same result.

However, a close examination of the mapping relations, Eqs. E.10 and E.11, shows that the numerical problem is not completely trivial. A simple calculation leads to  $\xi = 2x - 1 = -(1 - 2x)$ . As  $P_n(-y) = (-1)^n P_n(y)$  (Fig. E.1) it results, by using Eq. E.6, that

$$J_n(x) = (-1)^n P_n(\xi) \quad (\text{E.12})$$

Consequently, even if the minimum of function  $f$  is the same, the point in the parameter space,  $Q$ , where function  $f$  reaches his minimum should depend on the choice of the polynomial system:

$$a_{n_L} = (-1)^n a_{n_J} \quad (\text{E.13})$$

with the indices “J” and “L” standing for Jacobi and Legendre polynomials. The rest of the parameters,  $\tan \theta$ ,  $b_0$ ,  $c_0$ , and  $c_1$  (for models that take into account the FAC–electrojet coupling), should be the same.

The numerical results confirm Eq. E.13 and accordingly, the physical quantities do not depend on the choice of the polynomial system. Figure E.2 illustrates this point with the electric field obtained from the models YPYH36 and YPYHX36, by using both Jacobi and Legendre polynomials.

Comparing the results obtained by using Jacobi and Legendre polynomials provides a good analytical benchmark for the minimization procedure (to be described in Appendix F). Considering the large number of parameters (40 for model YPYHX36), the requirement Eq. E.13 is not trivial. The fact that the results obtained are in rigorous agreement with the theoretical expectation stands for the reliability of the minimization procedure.



## Appendix F

# Arc models: the numerical fit

The derivation of the ionospheric electric field and current in Chapter 6 is based on the numerical minimization of the function  $f$ , Eq. 6.2. In Section F.1 we discuss the method of least squares (MLS) and the statistical significance of  $f$ . Next, in Section F.2, we mention some of the algorithms that can be used to find the minimum of  $f$  and briefly present the computer code written to accomplish this task. The content to follow is only intended as a brief review. For more details related to Section F.1 the reader is referred to e. g. Bevington and Robinson (1992) and Press et al. (1997), Chapter 15. The theme discussed in Section F.2 is treated, e. g., in Gill et al. (1981) and Press et al. (1997), Chapter 10.

### F.1 The Method of least squares and the goodness-of-fit test

The method of least squares (MLS) is used to fit analytic functions to measured data: Considering the independent variable  $x$ , a set of measured data  $(y_i(x_i))$ , and the analytic function  $y(x; \alpha_1, \dots, \alpha_m)$ , by using the MLS one finds the parameters  $(\alpha_1, \dots, \alpha_m)$  that maximize the probability to measure the set  $(y_i(x_i))$ . Additionally, one can also evaluate if the parametrization properly models the data, by means of the goodness-of-fit test.

The MLS is appropriate for processing data whose presumed error distribution is gaussian, i. e. the probability to measure a value,  $y_i(x_i)$ , is given by:

$$p_i = \frac{1}{\sigma_i \sqrt{2\pi}} \exp -\frac{1}{2} \left( \frac{y_i - y(x_i)}{\sigma_i} \right)^2 \quad (\text{F.1})$$

where  $\sigma_i$  is the uncertainty in  $y_i$ , which depends on the measuring process. The probability,  $P$ , to measure the set  $(y_i)$  is the product of the individual probabilities,  $p_i$ :

$$\prod_{i=1}^N p_i = \prod_{i=1}^N \left( \frac{1}{\sigma_i \sqrt{2\pi}} \right) \exp -\frac{1}{2} \sum_{i=1}^N \left( \frac{y_i - y(x_i)}{\sigma_i} \right)^2 \quad (\text{F.2})$$

with  $N$  the total number of measurements. To maximize the probability  $P$  one has to minimize the exponent:

$$\chi^2 = \sum_{i=1}^N \left( \frac{y_i - y(x_i)}{\sigma_i} \right)^2 \quad (\text{F.3})$$

Minimization of  $\chi^2$  implies that its partial derivatives with respect to  $\alpha_j$  vanish:

$$\frac{\partial \chi^2}{\partial \alpha_j} = -2 \sum_{i=1}^N \left\{ \frac{1}{\sigma_i^2} [y_i - y(x_i)] \frac{\partial y(x_i)}{\partial \alpha_j} \right\} = 0 \quad (\text{F.4})$$

This is equivalent to a system of  $m$  equations for the  $m$  unknown parameters  $\alpha_j$ . If  $y$  depends linearly on all  $\alpha_j$  one obtains a linear regression problem, which can be solved by techniques based on matrix inversion. If the dependence is not linear in all the parameters, then  $\chi^2(\alpha_1, \dots, \alpha_m)$  is treated as a hyper-surface in an  $m$ -dimensional space, which is searched for the minimum. Some searching algorithms are enumerated and briefly described in the next Section.

The minimum value obtained for  $\chi^2$  provides an estimate for the quality of the fit. If the model function,  $y$ , is adequate, and if the uncertainties  $\sigma_i$  are correctly evaluated, then each term in Eq. F.3 should be, on average, close to 1. This can be easily explained intuitively: If the model function is adequate it means that  $y(x_i) \cong \langle y_i(x_i) \rangle$ , where by angular brackets we denote the mean value. If the values  $\sigma_i$  are evaluated correctly then, by the definition of the standard deviation, we get:

$$\left\langle \frac{(y_i - y)^2}{\sigma_i^2} \right\rangle \cong \frac{\langle (y_i - \langle y_i \rangle)^2 \rangle}{\sigma_i^2} = 1 \quad (\text{F.5})$$

Consequently, from Eq. F.3 we get:  $\chi^2 \cong N$ . A rigorous calculation shows that the mean value of  $\chi_r^2$  should be equal to 1, where  $\chi_r^2$  is defined by:

$$\chi_r^2 = \frac{\chi^2}{N - M} \quad (\text{F.6})$$

with  $N$  the number of measurements and  $M$  the number of parameters ( $\alpha_i$ ) (see Chapter 11 of Bevington and Robinson (1992) and references therein). If the value of  $\chi_r^2$  is significantly larger than 1 it is either because the analytic function does not correctly model the measured data, or because the uncertainties  $\sigma_i$  are underestimated, or both. If  $\chi_r^2$  is very small, then it is a good chance that the uncertainties are overestimated.

One should note that  $\chi_r^2 \cong 1$  is still not proving that the model is good, even if the uncertainties  $\sigma_i$  are correctly evaluated.  $\chi_r^2 \cong 1$  is a necessary, but not a sufficient condition, which only says that the model is compatible with the data, from a statistical point of view. An illustration for this idea can be found in the first unit of Section 6.4.3, where considering  $\tan \theta$  as small parameter leads to a better  $\chi_r^2$ , but the respective results contradict the experimental evidence (Table 6.8).

## F.2 Numerical minimization

Finding the minimum of a function comes under the larger cover of the optimization problems. In general, the minimization (or maximization) of an “objective function”,  $F(X)$ , has to be done by observing additional constraints, imposed on the value of the function and/or on the range of the independent variable  $X$  (by  $X$  we mean a point in an arbitrary, multi-dimensional space). In some cases one can obtain an unconstrained optimization problem by either disregarding the constraints or by suitable changes of variable and/or function.

For unconstrained optimization there is still a large selection of algorithms (see the references mentioned at the beginning of this Appendix). The choice is different for one-dimensional and multi-dimensional problems. One can use a method which requires the calculation of the derivative(s) or not. For the multi-dimensional case, one can make or not explicit use of a one-dimensional algorithm.

The IDL user can choose between three library routines performing unconstrained minimization in a  $n$ -dimensional space:

1. *amoeba*: The algorithm is searching for the minimum by ‘trial and error’. The name of the routine is suggestive about how the search proceeds. The function to be minimized has to be implemented as a separate IDL routine, *func*. Given the point  $X$ , the routine *func* has to return the value  $F(X)$ . The derivatives of the function are not required. *amoeba* calls *func* repeatedly, until the fractional change in  $F$  between two successive calls,  $\delta F/F$ , decreases below a predefined tolerance,  $\epsilon$  (the default tolerance is  $\epsilon = 10^{-4}$ ; this can be changed by the user). Apart from the name of the routine *func*, the user has to provide the starting point for the search,  $P_0$ , and a scale,  $\lambda$ , which determines the length of the starting search step.
2. *powell*: The algorithm is based on the Powell’s method which, at each step, chooses a set of  $n$  directions,  $(\mathbf{n}_i)$ , and performs one-dimensional minimization along each direction of the set. The key problem is to come up with a good algorithm for choosing the directions set, in order to minimize the number of steps. Powell discovered a method to produce such  $n$  “conjugate” directions, which requires only the calculation of the function value. As with *amoeba*, the user has to provide the name of the routine *func*, calculating  $F(X)$ , a starting point  $P_0$ , and a tolerance  $\epsilon$  (if different from the default one). An initial set of directions is also necessary. One common option is to take the unit vectors,  $\mathbf{e}_1, \dots, \mathbf{e}_n$ .
3. *djppmin*: The algorithm is, to some extent, similar to that used by *powell*, in that it proceeds as a sequence of one-dimensional minimizations along directions chosen in the  $n$ -dimensional

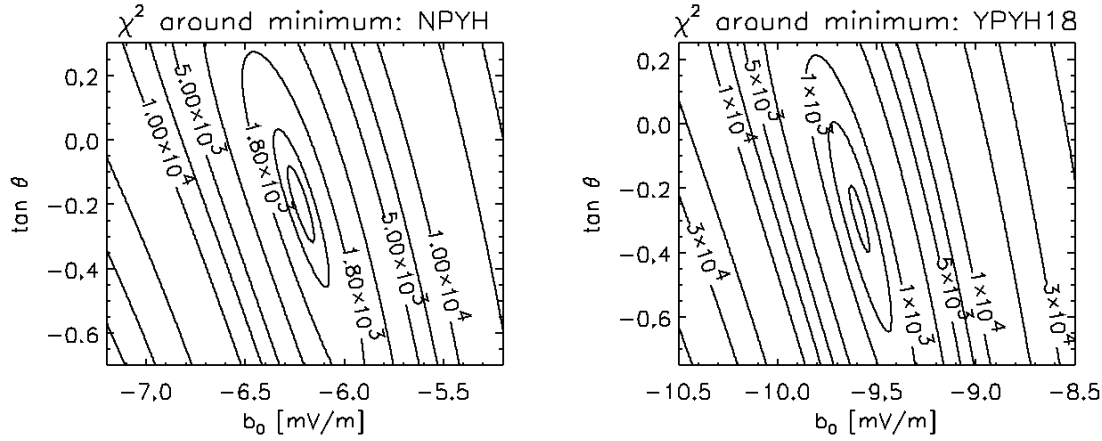


Figure F.1: Contour plots of the function  $f$  around the minimum in a  $(\tan \theta, b_0)$  2-dimensional cut. **Left:** Model NPYH. **Right:** Model YPYH18.

space. However, the choice of the direction is different and relies on the calculation of the gradient. Consequently, the user has to provide *dfpmin* the names of two functions: *func*, returning the scalar value  $F(X)$ , and *dfunc*, returning the vector  $\nabla F_X$ .

The routine *ief\_nl2* was written as an interface between the experimental data, the arc model, and the minimization procedure. The output consists of  $J_{par}$ ,  $J_{ion}$ , and the IEF, as well as the goodness-of-fit estimator  $\chi_r^2$ , which is equal to the minimized value of  $f$  divided through  $N - M$ . The operations performed by *ief\_nl2* can be summarized as follows:

- Input of the experimental data, through *ief\_nl2\_get*. The user can choose the time period and set the average electric field,  $E_{0_x}$  (this option is useful when there are gaps in the electric field data).
- Initialization of the input parameters for the minimization procedure. The following degrees of freedom can be manipulated by the user:
  - The name of the function *func* (and *dfunc*, if the minimization is done by *dfpmin*) is set according to the arc model chosen.
  - It is possible to switch on/off the use of a fit function  $f$  linearized in  $\tan \theta$  and the use of the weighting factors  $1/\sigma_k^2$  (see Section 6.4.3).
  - The starting point can be set at will. The default starting point is the origin of the parameter space.
  - If  $\tan \theta$  is determined from the magnetic data instead of considering it a fit parameter (Section 6.4.5) the user can choose the desired form of  $\tan \theta$ .

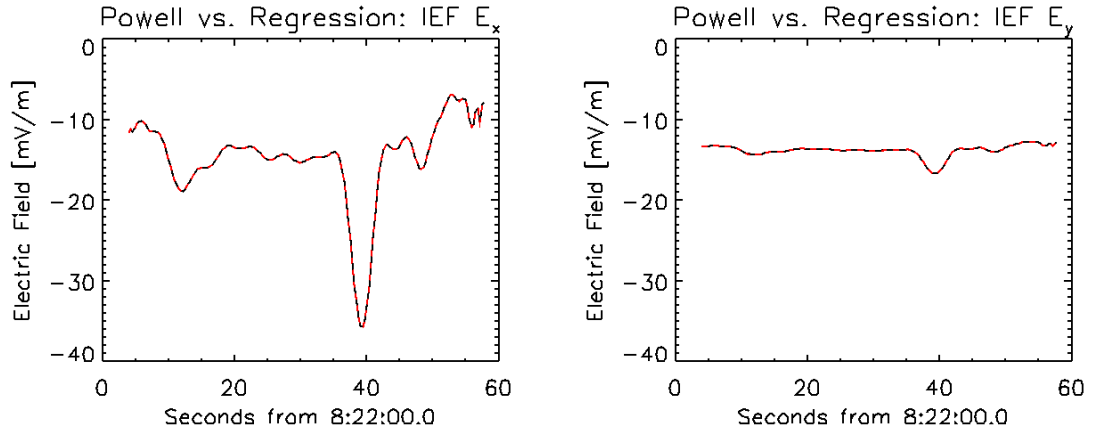


Figure F.2: The IEF obtained by non-linear minimization (black solid line) and by regression (green dashed line) with model YPYHXL36. The calculations were done by assuming  $\tan \theta = 0.14$ . The curves look bi-color because the results obtained by the two methods are practically identical. **Left:**  $E_x$ . **Right:**  $E_y$ .

- Minimization of  $f$ . The minimization algorithm can be chosen among the three options: *amoeba*, *powell*, *dffmin*.
- Calculation of  $J_{par}$ ,  $J_{ion}$ , and IEF. The output is returned as arrays that can be readily displayed in graphic form.

The results presented in Chapter 6 were obtained by using the *powell* minimization algorithm. Some of them were checked with *amoeba* but no significant difference was found. No check was done for *dffmin*. Writing the analytic form of the gradient is straight but tedious. Given the very good agreement between the results obtained with *powell* and *amoeba*, a triple check with *dffmin* was not considered necessary. As a more detailed illustration, Fig.F.1 shows 2-dimensional cuts of the parameter space, around the minimum, for the models NPYH and YPYH18.

A different test was performed with respect to the starting point. The routine *ief\_iter2* allows the user to check the results obtained when the polarization is taken into account. In this case the number of parameters can increase considerably, due to the polarization coefficients  $a_i$ , (Eq. 5.38). Consider, for example, the model YPYHX36, which depends on 40 parameters ( $\tan \theta$ ,  $(a_i)_{i=1,\dots,36}$ ,  $b_0$ ,  $c_0$ ,  $c_1$ ). At the beginning, the routine *ief\_iter2* assumes the non-polarized model NPYHX, which only depends on 4 parameters, and finds their values by starting the search from the origin of the 4-dimensional space. The result is completed with  $a_i = 0$  and used as starting point for the model YPYHX1. The process is continued iteratively: the result from model YPYHX $n$  is completed with  $a_{n+1} = 0$  and used as starting point for the model YPYHX $n+1$ . The final results were identical to that obtained with *ief\_nl2*, by starting the search from the origin of the 40-dimensional space.

When  $\tan \theta$  derived from the magnetic data is used, the  $\chi^2$  function becomes quadratic (Eq. F.3) and the system of derivatives linear in the parameters (Eq. F.4). Consequently, one should be able to derive the parameters by using linear regression instead of non-linear minimization. This task is accomplished by the routine *ief\_lin*. Its structure is similar to that of *ief\_nl2*, except for calling the IDL library function *regress* — instead of *amoeba*, *powell*, or *dfpmin*. The results obtained by using *ief\_nl2* and *ief\_lin* are practically identical (Fig.F.2), which is another confirmation that the minimization routine is reliable.

## Appendix G

### Variance analysis

One standard procedure to determine the orientation of a FAC sheet is the variance analysis. In this Appendix we only consider auroral FAC sheets at not too high altitudes (not more than  $\sim 3\text{--}4 R_E$ ), with the current flowing parallel to the quasi-dipolar magnetic field of the Earth. For a more general discussion of the variance analysis technique the reader is referred to the original paper of Sonnerup and Cahill (1967) and to the recent tutorial review, Sonnerup and Scheible (1998).

For an auroral FAC sheet the direction of the current coincides with the direction  $\mathbf{b}$  of the magnetic field. Considering a coordinate system with the  $z$  axis along  $\mathbf{b}$ , to determine the orientation of the sheet one only has to find the angle,  $\theta$ , between the normal to the sheet,  $\mathbf{n}$ , and the  $x$  axis of the coordinate system. We use the notation  $\theta_{mag}$  for the angle  $\theta$  when the  $x$  axis is perpendicular to the  $L$ -shell (see the cartoon on the right side of Fig.3.4). This particular choice of the  $x$  axis (and of the associated MFA coordinate system) is motivated by the fact that the auroral current sheets tend to be aligned with the  $L$ -shell.

The direction  $\mathbf{n}$  is determined by the condition that the component of the (measured) magnetic field along (the sought-after)  $\mathbf{n}$  direction,  $\mathbf{B} \cdot \mathbf{n}$ , has minimum variance:

$$\sigma^2 = \frac{1}{N} \sum_{k=1}^N \left( B_n^{(k)} - \langle B_n \rangle \right)^2 = \sum_{k=1}^N \left[ \left( \mathbf{B}^{(k)} - \langle \mathbf{B} \rangle \right) \cdot \mathbf{n} \right]^2 = \text{minim} \quad (\text{G.1})$$

By adding the condition  $\mathbf{n}^2 = 1$ , implemented through the Lagrange multiplier,  $\lambda$ , one comes to solving the homogeneous linear system:

$$\begin{aligned} \frac{\partial}{\partial n_x} (\sigma^2 - \lambda(n_x^2 + n_y^2)) &= 0 \\ \frac{\partial}{\partial n_y} (\sigma^2 - \lambda(n_x^2 + n_y^2)) &= 0 \end{aligned} \quad (\text{G.2})$$

After performing the differentiation the system can be written in matrix form as:

$$\begin{aligned} M_{xx}n_x + M_{xy}n_y &= \lambda n_x \\ M_{yx}n_x + M_{yy}n_y &= \lambda n_y \end{aligned} \quad (\text{G.3})$$

with

$$M_{uv} \equiv \langle B_u B_v \rangle - \langle B_u \rangle \langle B_v \rangle \quad (\text{G.4})$$

where each of  $u$  and  $v$  stands for either  $x$  or  $y$ . Solving the system G.3 is equivalent to finding the eigenvalues and the eigenvectors of the matrix  $M$ . As  $M$  is symmetric (Eq. G.4), the eigenvalues,  $\lambda_1 < \lambda_2$ , are real, and the respective eigenvectors,  $\xi$  and  $\eta$ , are orthogonal. The normal  $\mathbf{n}$  is identical to  $\xi$ , the eigenvector corresponding to  $\lambda_1$ . Both eigenvalues are positive and equal to the variance of the magnetic field along the direction of the respective eigenvector. This can be checked by writing the matrix  $M$  in the coordinate system  $(\xi, \eta)$ , where it takes the diagonal form

$$M = \begin{pmatrix} \lambda_1 & 0 \\ 0 & \lambda_2 \end{pmatrix} \quad (\text{G.5})$$

Once the eigenvectors were determined, the angle  $\theta_{mag}$  can be found by using either  $\xi$  or  $\eta$ :

$$\tan \theta_{mag} = \frac{\xi_y}{\xi_x} = -\frac{\eta_x}{\eta_y} \quad (\text{G.6})$$

We implemented the variance analysis through the IDL routine *bvar*. The code is based on the library function *eigenql* which computes the eigenvalues and eigenvectors of real, symmetric matrices. The user has to supply the magnetic data and the time limits for the investigated current sheet, and has the option to choose between 2D and 3D calculation (the routine can be used not only for auroral FAC sheets but also for the more general case of finding the normal to an arbitrary layer, like discontinuities or current sheets in the distant magnetosphere). For the 3D case the calculation proceeds analogous to the 2D one, except for the matrix  $M$  which has  $3 \times 3$  elements and is built by using the full set of magnetic data.

By means of the IDL routine *bv\_arr2* the variance analysis can be performed on a continuous basis: given the magnetic data, the time limits,  $t_1$  and  $t_2$ , and a temporal window,  $\tau$ , *bv\_arr2* calls *bvar* for each interval  $\tau$  obtained by moving the window between  $t_1$  and  $t_2$ . The temporal window can be chosen equal to the time scale of a characteristic structure embedded in the current sheet. Thus, one can check for the variability of the current sheet on that particular time scale.



# Bibliography

- Aikio, A., Opgenoorth, H., Persson, M., and Kaila, K., Ground-based measurements of an arc-associated electric field, *J. Atmos. Terr. Phys.*, *55*, 797–808, 1993.
- Akasofu, S.-I., The development of the auroral substorm, *Planet. Space Sci.*, *12*, 273–282, 1964.
- Akhiezer, A., Akhiezer, I., Polovin, R., Sitenko, A., and Stepanov, K., *Plasma Electrodynamics. I. Linear Theory*, vol. 68 of *International Series on Monographs in Natural Philosophy*, Pergamon, Oxford, 1975.
- Albert, R., Nearly monoenergetic electron fluxes detected during a visible aurora, *Phys. Rev. Lett.*, *18*, 369–372, 1967.
- Alfvén, H., A theory of magnetic storms and of the aurorae, *Kungl. Sv. Vetensk.-Akad. Handlingar III*, *18*, 1939.
- Alfvén, H., On the motion of a charged particle in a magnetic field, *Ark. Mat. Astr. Fys.*, *27A*, 1–20, 1940a.
- Alfvén, H., A theory of magnetic storms and of the aurorae; 2. The aurorae; 3. The magnetic disturbances, *Kungl. Sv. Vetensk.-Akad. Handlingar III*, *18*, 1940b.
- Alfvén, H., On the existence of electromagnetic-hydrodynamic waves, *Ark. Mat. Astr. Fys.*, *29B*, 1–7, 1942.
- Alfvén, H., On the theory of magnetic storms and aurorae, *Tellus*, *10*, 104–116, 1958.
- Amm, O., Direct determination of the local ionospheric Hall conductance from two-dimensional electric and magnetic field data: Application of the method using models of typical ionospheric electrodynamic situations, *J. Geophys. Res.*, *100*, 21 473–21 488, 1995.
- Amm, O., Method of characteristics in spherical geometry applied to a Harang-discontinuity situation, *Ann. Geophys.*, *16*, 413–424, 1998.

- André, M., Norqvist, P., Andersson, L., Eliasson, L., Eriksson, A., Blomberg, L., Erlandson, R., and Waldemark, J., Ion energization mechanisms at 1700 km in the auroral region, *J. Geophys. Res.*, 103, 4199–4222, 1998.
- Atkinson, G., Auroral arcs: Result of the interaction of a dynamic magnetosphere with the ionosphere, *J. Geophys. Res.*, 75, 4746–4755, 1970.
- Baumjohann, W., Ionospheric and field-aligned current systems in the auroral zone: A concise review, *Adv. Space Res.*, 2, 55–62, 1983.
- Baumjohann, W. and Treumann, R., *Basic Space Plasma Physics*, Imperial College Press, London, 1996.
- Baumjohann, W., Pellinen, R., Opgenoorth, H., and Nielsen, E., Joint two-dimensional observations of ground magnetic and ionospheric electric fields associated with auroral zone currents: Current systems associated with local auroral break-ups, *Planet. Space Sci.*, 29, 431–447, 1981.
- Bevington, P. and Robinson, D., *Data reduction and error analysis for the physical sciences*, McGraw-Hill, New York, 2 edn., 1992.
- Borovsky, J., The production of ion conics by oblique double layers, *J. Geophys. Res.*, 89, 2251–2266, 1984.
- Boström, R., A model of the auroral electrojets, *J. Geophys. Res.*, 69, 4983–4999, 1964.
- Boström, R., Ionosphere–magnetosphere coupling, in *Magnetospheric physics*, edited by B. McCormac, vol. 44 of *Astrophysics and Space Science Library*, pp. 45–59, D. Reidel, Dordrecht, 1974.
- Brekke, A. and Egeland, A., *The Northern Light*, Springer, Berlin, 1983.
- Brekke, A. and Moen, J., Review paper — Observations of high latitude ionospheric conductances, *J. Atmos. Terr. Phys.*, 55, 1493–1512, 1993.
- Brekke, A., Doupnik, J., and Banks, P., A preliminary study of the neutral wind in the auroral *E* region, *J. Geophys. Res.*, 78, 8235–8250, 1973.
- Brekke, A., Doupnik, J., and Banks, P., Incoherent scatter measurements of *E* region conductivities and currents in the auroral zone, *J. Geophys. Res.*, 79, 3773–3790, 1974.
- Bundke, W., *12 stellige Tafel der Legendre-Polynome*, vol. 320 of *Hochschultaschenbücher*, Bibliographisches Institut, Mannheim, 1967.

- Bythrow, P., Heelis, R., Hanson, W., and Power, R., Simultaneous observations of field-aligned currents and plasma drift velocities by Atmosphere Explorer C, *J. Geophys. Res.*, 85, 151–159, 1980.
- Carlqvist, P. and Boström, R., Space-charge regions above the aurora, *J. Geophys. Res.*, 75, 7140–7146, 1970.
- Carlson, C., Curtis, D., Paschmann, G., and Michael, W., An instrument for rapidly measuring plasma distribution functions with high resolution, *Adv. Space Res.*, 2, 367–370, 1983.
- Carlson, C., Pfaff, R., and Watzin, J., The Fast Auroral SnapshoT mission, *Geophys. Res. Lett.*, 25, 2013–2016, 1998a.
- Carlson, C., McFadden, J., Ergun, R., M.Temerin, Peria, W., Mozer, F., Klumpar, D., Shelley, E., Peterson, W., Möbius, E., Kistler, L., Elphic, R., Strangeway, R., Cattell, C., and Pfaff, R., FAST observations in the downward auroral current region: Energetic upgoing electron beams, parallel potential drop, and ion heating, *Geophys. Res. Lett.*, 25, 2017–2021, 1998b.
- Carlson, C., McFadden, J., Turin, P., Curtis, D., and Magoncelli, A., The electron and ion plasma experiment for FAST, *Space Sci. Rev.*, 98, 33–66, 2001.
- Casserty, R.T., Jr., Observation of a structured auroral field-aligned current system, *J. Geophys. Res.*, 82, 155–163, 1977.
- Cattell, C., The relationship of field-aligned currents to electrostatic ion cyclotron waves, *J. Geophys. Res.*, 86, 3641–3645, 1981.
- Chamberlain, J., *Physics of the aurora and airglow*, vol. 2 of *International Geophysics Series*, Academic Press, New York, 1961.
- Chapman, S. and Cowling, T., *The Mathematical Theory of Non-Uniform Gases*, Cambridge Monographs on Mechanics and Applied Mathematics, Cambridge University Press, Cambridge, 1939.
- Chiu, Y. and Schulz, M., Self-consistent particle and electrostatic field distributions in the magnetospheric-ionospheric auroral region, *J. Geophys. Res.*, 83, 629–642, 1978.
- Chiu, Y., Cornwall, J., Fennell, J., Gorney, D., and Mizera, P., Auroral plasma in the evening sector: Satellite observations and theoretical interpretations, *Space Sci. Rev.*, 35, 211–257, 1983.
- Comfort, R., Wu, S., and Swenson, G., An analysis of auroral *E* region neutral winds based on incoherent scatter radar observations at Chatanika, *Planet. Space Sci.*, 24, 541–560, 1976.

- Coroniti, F. and Kennel, C., Polarization of the auroral electrojet, *J. Geophys. Res.*, 77, 2835–2851, 1972.
- Courant, R. and Hilbert, D., *Methods of mathematical physics*, Interscience, New York, 1953.
- de la Beaujardière, O., Vondrak, R., and Baron, M., Radar observations of electric fields and currents associated with auroral arcs, *J. Geophys. Res.*, 82, 5051–5062, 1977.
- de la Beaujardière, O., Vondrak, R., Heelis, R., Hanson, W., and Hoffman, R., Auroral arc electrodynamic parameters measured by AE-C and the Chatanika radar, *J. Geophys. Res.*, 86, 4671–4685, 1981.
- Debye, P. and Hückel, E., Zur Theorie der Elektrolyte, *Phys. Z.*, 24, 185–206, 1923.
- Eather, R., Auroral proton precipitation and hydrogen emissions, *Rev. Geophys. Space Phys.*, 5, 207–285, 1967.
- Elphic, R., Bonnell, J., Strangeway, R., Kepko, L., Ergun, R., McFadden, J., Carlson, C., Peria, W., Cattell, C., Klumpar, D., Shelley, E., Peterson, W., Möbius, E., Kistler, L., and Pfaff, R., The auroral current circuit and field-aligned currents observed by FAST, *Geophys. Res. Lett.*, 25, 2033–2036, 1998.
- Elphic, R., Means, J., Snare, R., Strangeway, R., and Kepko, L., Magnetic field instruments for the Fast Auroral Snapshot explorer, *Space Sci. Rev.*, 98, 151–168, 2001.
- Ergun, R., Carlson, C., McFadden, J., Mozer, F., and Strangeway, R., Parallel electric fields in discrete arcs, *Geophys. Res. Lett.*, 27, 4053–4056, 2000.
- Ergun, R., Carlson, C., Mozer, F., Delory, G., Temerin, M., McFadden, J., Pankow, D., Abiad, R., Harvey, P., Wilkes, R., Primbsch, H., Elphic, R., Strangeway, R., Pfaff, R., and Cattell, C., The FAST satellite fields instrument, *Space Sci. Rev.*, 98, 67–91, 2001.
- Evans, D., Maynard, N., Troim, J., Jacobsen, T., and Egeland, A., Auroral vector electric field and particle comparisons 1. Electrodynamics of an arc, *J. Geophys. Res.*, 82, 2235–2249, 1977.
- Fälthammar, C.-G., Magnetic-field-aligned electric fields, *ESA J.*, 7, 385–404, 1983.
- Föppl, H., Haerendel, G., Haser, L., Loidl, J., Lütjens, P., Lüst, R., Melzner, F., Meyer, B., Neuss, H., and Rieger, E., Artificial strontium and barium clouds in the upper atmosphere, *Planet. Space Sci.*, 15, 357–372, 1967.
- Frank, L. and Ackerson, K., Observations of charged particle precipitation into the auroral zone, *J. Geophys. Res.*, 76, 3612–3643, 1971.

- Frey, H., Lieb, W., Bauer, O., Höfner, H., and Haerendel, G., CCD-camera system for stereoscopic optical observations of the aurora, in *Current developments in optical design and engineering VI*, vol. 2863 of *SPIE Proceedings*, pp. 460–466, SPIE, 1996.
- Fukushima, N., Generalized theorem for no ground magnetic effect of vertical currents connected with Pedersen currents in the uniform-conductivity ionosphere, *Rep. Ionos. Space Res. Jpn.*, 30, 35–40, 1976.
- Galand, M. and Richmond, A., Ionospheric electrical conductances produced by auroral proton precipitation, *J. Geophys. Res.*, 106, 117–125, 2001.
- Galand, M., Fuller-Rowell, T., and Codrescu, M., Response of the upper atmosphere to auroral protons, *J. Geophys. Res.*, 106, 127–139, 2001.
- Gill, P., Murray, W., and Wright, M., *Practical Optimization*, Academic Press, New York, 1981.
- Glassmeier, K.-H., Ground-based observations of field-aligned currents in the auroral zone: Methods and results, *Ann. Geophys.*, 5A, 115–126, 1987.
- Gold, T., Motions in the magnetosphere of the earth, *J. Geophys. Res.*, 64, 1219–1224, 1959.
- Greenwald, R., Weiss, W., Nielsen, E., and Thomson, N., STARE: A new radar auroral backscatter experiment in northern Scandinavia, *Radio. Sci.*, 13, 1021–1039, 1978.
- Gurnett, D., Electric field and plasma observations in the magnetosphere, in *Critical problems of magnetospheric physics*, edited by E. Dyer, pp. 123–138, National Academy of Sciences, Washington D.C., 1972.
- Gurnett, D. and Frank, L., Observed relationship between electric fields and auroral particle precipitation, *J. Geophys. Res.*, 78, 145–170, 1973.
- Haerendel, G., Plasma drifts in the auroral ionosphere derived from barium releases, in *Earth's magnetospheric processes*, edited by B. McCormac, pp. 246–257, D. Reidel, 1972.
- Haerendel, G., Cosmic linear accelerators, in *Proc. Varenna-Abastumani Int. School & Workshop on Plasma Astrophysics*, pp. 37–44, ESA SP-285, Varenna, Italy, 1989.
- Haerendel, G., Field-aligned currents in the Earth's magnetosphere, in *Physics of magnetic flux ropes*, edited by C. Russell, E. Priest, and L. Lee, vol. 58 of *Geophysical Monograph*, pp. 539–553, AGU, 1990.

- Haerendel, G., Rieger, E., Valenzuela, A., Föppl, H., Stenbaek-Nielsen, H., and Wescott, E., First observation of electrostatic acceleration of barium ions into the magnetosphere, in *European Programmes on sounding-rocket and balloon research in the auroral zone*, SP-115, ESA, Neuilly, France, 1976.
- Haerendel, G., Buchert, S., La Hoz, C., Raaf, B., and Rieger, E., On the proper motion of auroral arcs, *J. Geophys. Res.*, 98, 6087–6099, 1993.
- Hallinan, T. and Davis, T., Small-scale auroral arc distortions, *Planet. Space Sci.*, 18, 1735, 1970.
- Hoffman, R. and Evans, D., Field-aligned electron bursts at high latitudes observed by OGO 4, *J. Geophys. Res.*, 73, 6201–6214, 1968.
- Holzworth, R. and Meng, C., Mathematical representation of the auroral oval, *Geophys. Res. Lett.*, 2, 377, 1975.
- Iijima, T. and Potemra, T., Large-scale characteristics of field-aligned currents associated with substorms, *J. Geophys. Res.*, 83, 599–615, 1978.
- Inhester, B., Untiedt, J., Segatz, M., and Kürschner, M., Direct determination of the local ionospheric Hall conductance distribution from two-dimensional electric and magnetic field data, *J. Geophys. Res.*, 97, 4073–4083, 1992.
- Kamide, Y., The relationship between field-aligned currents and the auroral electrojets: A review, *Space Sci. Rev.*, 31, 127, 1982.
- Kamide, Y. and Baumjohann, W., *Magnetosphere–Ionosphere Coupling*, vol. 23 of *Physics and Chemistry in Space*, Springer, Berlin, 1993.
- Kamide, Y., Richmond, A., and Matsushita, S., Estimation of ionospheric electric fields, ionospheric currents, and field-aligned currents from ground magnetic records, *J. Geophys. Res.*, 86, 801–813, 1981.
- Kelley, M., *The Earth's Ionosphere*, vol. 43 of *International Geophysics Series*, Academic Press, San Diego, California, 1989.
- Kertz, W., *Einführung in die Geophysik. II. Obere Atmosphäre und Magnetosphäre*, vol. 535 of *Hochschultaschenbücher*, Bibliographisches Institut, Mannheim, 1971.
- Kintner, P., Kelley, M., and Mozer, F., Electrostatic hydrogen cyclotron waves near one Earth radius altitude in the polar magnetosphere, *Geophys. Res. Lett.*, 5, 139–142, 1978.

- Kintner, P., Kelley, M., Sharp, R., Ghielmetti, A., Temerin, M., Cattell, C., Mizera, P., and Fennell, J., Simultaneous observations of energetic (keV) upstreaming ions and electrostatic hydrogen cyclotron waves, *J. Geophys. Res.*, *84*, 7201–7212, 1979.
- Klumpar, D., Möbius, E., Kistler, L., Popecki, M., Hertzberg, E., Crocker, K., Granoff, M., Tang, L., Carlson, C., McFadden, J., Klecker, B., Eberl, F., Künne, E., Kästle, H., Ertl, M., Peterson, W., Shelley, E., and Hovestadt, D., The Time-of-flight Energy, Angle, Mass Spectrograph (TEAMS) experiment for FAST, *Space Sci. Rev.*, *98*, 197–219, 2001.
- Knight, S., Parallel electric fields, *Planet. Space Sci.*, *21*, 741–750, 1973.
- Kosch, M., Amm, O., and Scourfield, M., A plasma vortex revisited: The importance of including ionospheric conductivity measurements, *J. Geophys. Res.*, *105*, 24 889–24 898, 2000.
- Küppers, F., Untiedt, J., Baumjohann, W., Lange, K., and Jones, A., A two-dimensional magnetometer array for ground-based observations of auroral zone electric currents during the International Magnetospheric Study (IMS), *J. Geophys.*, *46*, 429–450, 1979.
- Langmuir, I., The interaction of electron and positive ion space charges in cathode sheaths, *Phys. Rev.*, *33*, 954–989, 1929.
- Lühr, H., Warnecke, J., Zanetti, L., Lindqvist, P.-A., and Hughes, T., Fine structure of field-aligned current sheets deduced from spacecraft and ground-based observations: Initial Freja results, *Geophys. Res. Lett.*, *21*, 1883–1886, 1994.
- Lund, E., Möbius, E., Klumpar, D., Kistler, L., Popecki, M., Klecker, B., Ergun, R., McFadden, J., Carlson, C., and Strangeway, R., Direct comparison of transverse ion acceleration mechanisms in the auroral region at solar minimum, *J. Geophys. Res.*, *104*, 22 801, 1999.
- Lysak, R., Coupling of the dynamic ionosphere to auroral flux tubes, *J. Geophys. Res.*, *91*, 7047–7056, 1986.
- Lysak, R., Electrodynamics coupling of the magnetosphere and ionosphere, *Space Sci. Rev.*, *52*, 33–87, 1990.
- Maggs, J. and Davis, T., Measurements of the thicknesses of auroral structures, *Planet. Space Sci.*, *16*, 205–209, 1968.
- Marghitu, O., Blagau, A., Vogt, J., Klecker, B., Haerendel, G., Möbius, E., McFadden, J., Carlson, C., Strangeway, R., and Elphic, R., Observational evidence for a potential relationship between visible auroral arcs and ion beams — a case study, *Phys. Chem. Earth*, *26*, 223–228, 2001.

- Marklund, G., Auroral arc classification scheme based on the observed arc-associated electric field pattern, *Planet. Space Sci.*, 32, 193–211, 1984.
- McFadden, J., Carlson, C., R.E.Ergun, Mozer, F., Temerin, M., Peria, W., Klumpar, D., Shelley, E., Peterson, W., Möbius, E., Kistler, L., Elphic, R., Strangeway, R., Cattell, C., and Pfaff, R., Spatial structure and gradients of ion beams observed by FAST, *Geophys. Res. Lett.*, 25, 2021–2024, 1998.
- McFadden, J., Carlson, C., and R.E.Ergun, Microstructure of the auroral acceleration region as observed by FAST, *J. Geophys. Res.*, 104, 14 453–14 480, 1999.
- McFadden, J., Ergun, R., Carlson, C., Herrick, W., Loran, J., Verneti, J., Teitler, W., Bromund, K., and Quinn, T., Science operations and data handling for the FAST satellite, *Space Sci. Rev.*, 98, 169–196, 2001.
- McIlwain, C., Direct measurement of particles producing visible auroras, *J. Geophys. Res.*, 65, 2727–2747, 1960.
- McIlwain, C., Coordinates for mapping the distribution of magnetically trapped particles, *J. Geophys. Res.*, 66, 3681–3691, 1961.
- Meng, C.-I. and Akasofu, S.-I., The relation between the polar cap auroral arc and the auroral oval arc, *J. Geophys. Res.*, 81, 4004–4006, 1976.
- Mishin, V., Bazarzhapov, A., and Shpynev, G., Electric fields and currents in the Earth's magnetosphere, in *Dynamics of the Magnetosphere*, edited by S.-I. Akasofu, vol. 78 of *Astrophysics and Space Science Library*, pp. 249–268, D. Reidel, Dordrecht, 1980.
- Mizera, P., Gorney, D., and Fennell, J., Experimental verification of an S-shaped potential structure, *J. Geophys. Res.*, 87, 1535–1539, 1982.
- Morse, P. and Feshbach, H., *Methods of theoretical physics*, International Series in pure and applied physics, McGraw-Hill, New York, 1953.
- Mott-Smith, H. and Langmuir, I., The theory of collectors in gaseous discharges, *Phys. Rev.*, 28, 727–763, 1926.
- Mozer, F., Origin and effects of electric fields during isolated magnetospheric substorms, *J. Geophys. Res.*, 76, 7595–7608, 1971.
- Mozer, F. and Kletzing, C., Direct observation of large, quasi-static, parallel electric fields in the auroral acceleration region, *Geophys. Res. Lett.*, 26, 1629–1632, 1999.



- Mozer, F., Carlson, C., Hudson, M., Torbert, R., Parady, B., Yatteau, J., and Kelley, M., Observations of paired electrostatic shocks in the polar magnetosphere, *Phys. Rev. Lett.*, 38, 292–295, 1977.
- Mozer, F., Cattell, C., M.K. H., Lysak, R., Temerin, M., and Torbert, R., Satellite measurements and theories of low altitude auroral particle acceleration, *Space Sci. Rev.*, 27, 155–213, 1980.
- Opgenoorth, H., Pellinen, R., Baumjohann, W., Nielsen, E., Marklund, G., and Eliasson, L., Three-dimensional current flow and particle precipitation in a westward travelling surge (observed during the Barium-GEOS rocket experiment), *J. Geophys. Res.*, 88, 3138–3152, 1983.
- Opgenoorth, H., Häggström, I., Williams, P., and Jones, G., Regions of strongly enhanced perpendicular electric fields adjacent to auroral arcs, *J. Atmos. Terr. Phys.*, 52, 449–458, 1990.
- Paschmann, G., Fazakerley, A., and Schwartz, S., Moments of plasma velocity distributions, in *Analysis methods for multi-spacecraft data*, edited by G. Paschmann and P. Daly, vol. 1 of *ISSI Scientific Reports*, chap. 6, ISSI/ESA, Bern, Switzerland, 1998.
- Pfaff, R., Borovsky, J., and Young, D., eds., *Measurement Techniques in Space Plasmas. Particles*, no. 102 in Geophysical Monograph, AGU, Washington, D.C., 1998a.
- Pfaff, R., Borovsky, J., and Young, D., eds., *Measurement Techniques in Space Plasmas. Fields*, no. 103 in Geophysical Monograph, AGU, Washington, D.C., 1998b.
- Pfaff, R., Carlson, C., Watzin, J., Everett, D., and Gruner, T., An overview of the Fast Auroral SnapshoT (FAST) satellite, *Space Sci. Rev.*, 98, 1–32, 2001.
- Press, W., Teukolsky, S., Vetterling, W., and Flannery, B., *Numerical recipes in C — The art of scientific computing*, Cambridge University Press, Cambridge, 2 edn., 1997.
- Rees, M., Auroral ionization and excitation by incident energetic electrons, *Planet. Space Sci.*, 11, 1209–1218, 1963.
- Reiff, P., Models of auroral zone conductances, in *Magnetospheric currents, Geophysical monograph* 28, edited by T. Potemra, p. 180, AGU, Washington, 1984.
- Rich, F., Cattell, C., Kelley, M., and Burke, W., Simultaneous observations of auroral zone electrodynamics by two satellites: Evidence for height variations in the topside ionosphere, *J. Geophys. Res.*, 86, 8929–8940, 1981.
- Richmond, A. and Kamide, Y., Mapping electrodynamic features of the high-latitude ionosphere from localized observations: Technique, *J. Geophys. Res.*, 93, 5741–5759, 1988.

- Richmond, A., Kamide, Y., Ahn, B.-H., Akasofu, S.-I., Alcaydé, D., Blanc, M., de la Beaujardière, O., Evans, D., Foster, J., Friis-Christensen, E., Fuller-Rowell, T., Holt, J., Knipp, D., Kroehl, H., Lepping, R., Pellinen, R., Senior, C., and Zaitzev, A., Mapping electrodynamic features of the high-latitude ionosphere from localized observations: Combined incoherent-scatter radar and magnetometer measurements for January 18–19, 1984, *J. Geophys. Res.*, **93**, 5760–5776, 1988.
- Rishbeth, H. and Garriott, O., *Introduction to ionospheric physics*, Academic Press, New York, 1969.
- Robinson, R., Vondrak, R., Miller, K., Dabbs, T., and Hardy, D., On calculating ionospheric conductances from the flux and energy of precipitating electrons, *J. Geophys. Res.*, **92**, 2565–2569, 1987.
- Rothwell, P., Silevitch, M., and Block, L., A model for the propagation of the westward traveling surge, *J. Geophys. Res.*, **89**, 8941–8948, 1984.
- Sato, M., Kamide, Y., Richmond, A., Brekke, A., and Nozawa, S., Regional estimation of electric fields and currents in the polar ionosphere, *Geophys. Res. Lett.*, **22**, 283–286, 1995.
- Sato, T., A theory of quiet auroral arcs, *J. Geophys. Res.*, **83**, 1042–1048, 1978.
- Sesiano, J. and Cloutier, P., Measurements of field-aligned currents in a multiple auroral arc system, *J. Geophys. Res.*, **81**, 116–122, 1976.
- Sharp, R., Johnson, R., and Shelley, E., Observation of an ionospheric acceleration mechanism producing energetic (keV) ions primarily normal to the geomagnetic field direction, *J. Geophys. Res.*, **82**, 3324–3328, 1977.
- Shelley, E., Sharp, R., and Johnson, R., Satellite observations of an ionospheric acceleration mechanism, *Geophys. Res. Lett.*, **3**, 654–656, 1976.
- Smiddy, M., Burke, W., Kelley, M., Saflekos, N., Gussenhoven, M., Hardy, D., and Rich, F., Effects of high-latitude conductivity on observed convection electric fields and Birkeland currents, *J. Geophys. Res.*, **85**, 6811–6818, 1980.
- Sofko, G., Greenwald, R., and Bristow, W., Direct determination of large-scale magnetospheric field-aligned currents with SuperDARN, *Geophys. Res. Lett.*, **22**, 2041–2044, 1995.
- Sonnerup, B. and Cahill, L., Magnetopause structure and attitude from Explorer 12 observations, *J. Geophys. Res.*, **72**, 171–183, 1967.

- Sonnerup, B. and Scheible, M., Minimum and maximum variance analysis, in *Analysis methods for multi-spacecraft data*, edited by G. Paschmann and P. Daly, vol. 1 of *ISSI Scientific Reports*, chap. 8, ISSI/ESA, Bern, Switzerland, 1998.
- Stern, D., A brief history of magnetospheric physics before the spaceflight era, *Rev. Geophys.*, **27**, 103–114, 1989.
- Stern, D., A brief history of magnetospheric physics during the space age, *Rev. Geophys.*, **34**, 1–31, 1996.
- Sugiura, M., A fundamental magnetosphere-ionosphere coupling mode involving field-aligned currents as deduced from DE-2 observations, *Geophys. Res. Lett.*, **11**, 877–880, 1984.
- Sugiura, M., Maynard, N., Farthing, W., Heppner, J., Ledley, B., and L.J. Cahill, Jr., Initial results on the correlation between the magnetic and electric fields observed from the DE-2 satellite in the field-aligned current regions, *Geophys. Res. Lett.*, **9**, 985–988, 1982.
- Temerin, M., Cerny, K., Lotko, W., and Mozer, F., Observations of double layers and solitary waves in the auroral plasma, *Phys. Rev. Lett.*, **48**, 1175–1179, 1982.
- Tonks, L. and Langmuir, I., Oscillations in ionized gases, *Phys. Rev.*, **33**, 195–210, 1929.
- Untiedt, J. and Baumjohann, W., Studies of polar current systems using the IMS Scandinavian magnetometer array, *Space Sci. Rev.*, **63**, 245–390, 1993.
- Vickrey, J., Vondrak, R., and Matthews, S., The diurnal and latitudinal variation of auroral zone ionospheric conductivity, *J. Geophys. Res.*, **86**, 65–75, 1981.
- Vlasov, A., On vibrational properties of the electron gas (in Russian), *J. Exp. Teor. Phys. USSR*, **8**, 291–318, 1938.
- Vogt, J., Haerendel, G., and Glassmeier, K.-H., A model for the reflection of Alfvén waves at the source region of the Birkeland current system: The tau generator, *J. Geophys. Res.*, **104**, 269–278, 1999.
- Wallis, D. and Budzinski, E., Empirical models of height integrated conductivities, *J. Geophys. Res.*, **86**, 125–137, 1981.
- Zmuda, A., Armstrong, J., and Heuring, F., Characteristics of transverse magnetic disturbances observed at 1100 km in the auroral oval, *J. Geophys. Res.*, **75**, 4757–4762, 1970.



# Acknowledgment

The present work was accomplished at the Max-Planck-Institut für extraterrestrische Physik in Garching and at the Institute for Space Sciences in Bucharest, and benefited from a visit at the Space Sciences Laboratory of the University of California at Berkeley. I had the privilege to meet highly dedicated and qualified scientists. At the same time I had the chance to take part, together with a small but enthusiastic group, in opening a new research area in my native country. I am grateful to all my teachers and colleagues for everything I learned in the past few years.

It is a pleasure for me to thank Prof. Dr. Gerhard Haerendel, who enabled my work at MPE through a stipend of the Max Planck Society. Among his many duties Prof. Haerendel agreed to act as Ph.D. adviser and the several discussions we had improved my understanding on the auroral physics.

This work would not have been possible without the constant encouragement and effective support from Dr. Berndt Klecker. I am grateful to Berndt not only for his competent advice, but also for the many occasions when he tactfully helped me to overcome difficulties. Berndt provided ample logistic assistance, including several travels and the acquisition of a Sun Station that was finally donated to ISS.

I owe many thanks to Dr. Joachim Vogt for valuable suggestions and useful comments. Joachim performed the geometrical calibration of the optical data. He also introduced me at the Institut für Geophysik und Meteorologie in Braunschweig and, in a discussion that we had there, pointed out the important role played by the ionosphere in the auroral phenomena.

I am pleased to thank Prof. Dr. Karl-Heinz Glaßmeier, whose kind help was instrumental in making the graduation process smooth, for the hospitality and cordial atmosphere that I found at IGM.

In evaluating the FAST data I got advice from Dr. Charles Carlson, Dr. Jim McFadden, and Dr. Robert Ergun, PIs of the FAST mission and of the plasma and electric field experiment. I owe special thanks to Jim for friendly support, valuable insight, and for the full access to the FAST database. Ken Bromund and Jack Verneti were always prompt in answering my questions related to the FAST software.

The fruitful discussions that I had with colleagues from MPE and SSL — Drs. Joshua Semeter, Andris Vaivads, Mårten Blixt, Harald Kucharek, Alexander Bogdanov, Thomas Leuschacher, Harald Frey, Laura Peticolas, and John Bonnell — enlightened some of the many facets of aurora. I am thankful to Joshua for organizing a pleasant visit at the Center for Geospace Studies of SRI International.

The effort to build up a space plasma group in Bucharest started with the pioneering work of Dr. Mircea Ciobanu and got support from Dr. Maria Haiduc and Dr. Dumitru Haşegan. Several young physicists — Marius Echim, Oana Bălan, Adrian Blăgău, Horia Comişel, and Dragoş Constantinescu — joined this effort after 1990. Most of them are still actively involved in space physics projects. I thank them all for their dedication, for the team spirit, for everything they taught me during these years.

Although I spent much of the last few years away from home, part of it was always with me thanks to Gerry, Mona, Doina, Anna, and Nelu, to their warm hospitality and friendship.

Most of all, I am grateful to my mother and my sister for their love, understanding, and patience. And to my father, for making us a family.



## **Lebenslauf**

von

### **Octav Marghitu**

Geboren am 28. Oktober 1966 in Bukarest

#### *Eltern:*

Valentin Marghitu, Ingenieur

Silvia Marghitu, geb. Plăviciosu, Ingenieurin

#### *Schulbildung:*

Sep. 1973 – Juni 1981	Elementarschule, Bukarest
Sep. 1981 – Juni 1985	Nicolae Bălcescu Gymnasium, Bukarest

#### *Wehrdienst:*

Sep. 1985 – Juni 1986	Mediaş
-----------------------	--------

#### *Universitätsstudium:*

Sep. 1986 – Juni 1991	Universität Bukarest, Studienfach Physik. Diplomarbeit: Bildverarbeitung – allgemeine Grundregeln und Anwendungen
Sep. 1991 – Juni 1997	Universität Bukarest, Studienfach Mathematik

#### *Anstellungen:*

Okt. 1991 – Aug. 1995	Assistent, Ökologie-Universität, Bukarest
Nov. 1994 – Apr. 1998	Forschungsassistent, Institut für Raumwissenschaften, Bukarest
Apr. 1998 –	Wissenschaftler, Institut für Raumwissenschaften, Bukarest

#### *Stipendien:*

September 1993	CERN Advanced Accelerator School, Rhodos, Griechenland
September 1995	IPP Summer University for Plasma Physics, Garching
März 1997	Installation von FAST software am MPE
Okt. 1997 –	Mehrere Promotionsstipendien für Ausländer am MPE: Untersuchung der polaren Beschleunigungsgebiete mit Hilfe von FAST Daten
Juni 2001	FAST Daten Auswertung am Space Sciences Laboratory, U.C. Berkeley